Effects of cement organic additives on the adsorption of uranyl ions on calcium silicate hydrate phases : experimental determination and computational molecular modelling

Iuliia Androniuk

UNIVERSITE BRETAGNE LOIRE

IMT Atlantique
Bretagne-Pays de la Loire
École Mines-Télécom

Thèse de Doctorat

Iuliia ANDRONIUK

Mémoire présenté en vue de l'obtention du
grade de Docteur de l'IMT Atlantique (Bretagne - Pays de la Loire)
sous le sceau de l'Université Bretagne Loire

École doctorale : *ED3MPL*

Discipline : *Chimie théorique, physique, analytique*
Unité de recherche : *Subatech, UMR 6457*

Soutenue le *20/02/2017*
Thèse N° : *2017IMTA0007*

Effects of cement organic additives on the adsorption of uranyl ions on calcium silicate hydrate phases: experimental determination and computational molecular modelling

JURY

Rapporteurs :	**Ali ZAOUI**, Professeur, Université de Lille 1 **David READ**, Professeur, University of Surrey
Examinateurs :	**Abdesselam ABDELOUAS,** Professeur, Subatech, l'IMT Atlantique **Barbara LOTHENBACH,** Ingénieure de recherche, EMPA **Alena KREMLEVA**, Chercheur, Technical University of Munich **Rémi MAURICE,** Chargé de recherche CNRS, Subatech
Invité :	**Pierre HENOCQ**, Ingénieur de recherche, Andra
Directeur de Thèse :	**Andrey KALINICHEV**, Directeur de Recherche, Subatech, l'IMT Atlantique
Co-encadrant de Thèse :	**Catherine LANDESMAN**, Ingénieure de recherche CNRS, Subatech

Acknowledgments

I would like to express my heartfelt gratitude for giving me the opportunity to conduct my doctoral work in Subatech laboratory at Institut Mines-Télécom Atlantique (former Ecole des Mines de Nantes). The study was supported by ANDRA. This work would never have come about without the help, support and collaboration of many people over the last three years.

I would like to thank the following people for their contribution to the success of this work:

Andrey Kalinichev for the help he has given me, for the patience he has displayed, for the confidence he has shown throughout my work and ultimately for his great availability. I also thank him for encouraging me to submit the results of my work to international conferences and journals.

Catherine Landesman for her help through the many shared discussions on Thursday mornings, her encouragement, advice, good humor, and her judicious remarks for the improvement of this work.

Rémi Maurice and Pierre Henocq, the members of my committee, for their time, patience, insights, and support in overcoming obstacles I have been facing during my studies.

Also, I would like to express my gratitude to Dr Mélanie Legros from the Institut Charles Sadron (Strasbourg) for polymer characterisation and to Dr Stéphane Gaboreau from BRGM (Orléans) for solid state NMR analysis.

Generous allocations of supercomputing resources at the CCIPL, GENCI and TGCC supercomputing facilities (projects x2014096921, x2015096921, and t2016096921) are also most gratefully acknowledged.

I would like to thank all my colleagues from Radiochemistry group in Subatech for their unswerving encouragement and positive outlook. I am very grateful for their many counsels, for their confidence, for their skills that they put at my service.

Lastly, I would like to thank my family for their kind support and encouragement, and for always being there for me even when I am 2,600 km away from home.

Without all of you, this would not have been possible.

Abstract and keywords

Cementitious materials are extensively used in the design and construction of radioactive waste repositories. One of the ways to enhance their performance is to introduce organic admixtures into the cement structure. However, the presence of organics in the pore water may affect the radionuclide mobility: organic molecules can form water-soluble complexes and compete for sorption sites. This work was designed to get detailed understanding of the mechanisms of such interactions on the molecular level. The model system has three components. First, pure C-S-H phases with different Ca/Si ratios were chosen as a cement model. Secondly, gluconate (a simple well-described molecule) is selected as a good starting organic additive model to probe the interaction mechanisms on the molecular scale. A more complex system involving polycarboxylate superplasticizer (PCE) was also tested. The third, U (VI), is a representative of the actinide radionuclide series. The development of description of the effects of organics for radioactive waste disposal applications was the primary objective of this work. The study of binary systems provides reference data for the investigation of more complex ternary (C-S-H / organic / U(VI)). The interactions are studied by means of both experimental and computational molecular modelling techniques. Data on sorption and desorption kinetics and isotherms for additives and for U (VI) on C-S-H are acquired and analysed in this work. In parallel, atomistic models are developed for the interfaces of interest. Structural, energetic, and dynamic aspects of the sorption processes on the surface of cement are quantitatively modeled by molecular dynamics computer simulations.

Keywords: Calcium silicate hydrate (C-S-H); Uranium (VI); gluconate; adsorption; molecular dynamics

Résumé et mots-clés

Les matériaux cimentaires sont largement utilisés dans la conception et la construction des sites de stockage géologique de déchets radioactifs. Ces matériaux jouent un rôle important dans le conditionnement de certains déchets de moyenne activité, dans la fabrication des massif de scellement pour des alvéoles de stockage, et sont également essentiels pour la construction des galeries et puits d'accès aux installations de stockage. Lors de la conception du stockage géologique des déchets radioactifs, de nombreux facteurs doivent être pris en compte de façon à garantir la sûreté à long terme: les propriétés du site choisi telles que la disponibilité des ressources naturelles, la stabilité sismique et volcanique, la chimie des eaux souterraines…etc., ainsi que la nature et le type de déchets radioactifs, des colis de déchets, et les propriétés des matériaux utilisés pour la construction des barrières ouvragées. Par conséquent, même si les matériaux cimentaires sont choisis pour leurs propriétés physiques et mécaniques, ils peuvent également contribuer au confinement de la radioactivité et à l'étanchéité des alvéoles de stockage après leur fermeture. La capacité de confinement de la radioactivité de ces matériaux découle de leurs propriétés chimiques (eau porale à pH élevé, présence de phases minérales chargées de surface spécifique élevée), ce qui leur confère une grande affinité avec de nombreux radionucléides qui peuvent être retenus par différents mécanismes (sorption, incorporation ou précipitation).

Lors de la fabrication de pâte de ciment, des additifs organiques (comme des superplastifiants) sont souvent utilisés afin d'améliorer les propriétés mécaniques du matériau de final. La présence de ces produits chimiques potentiellement réactifs peut affecter la mobilité des radionucléides. Même si la quantité d'additifs organiques utilisée est généralement faible, les mécanismes de leurs interactions avec tous les composants du système de stockage des déchets doivent être systématiquement étudiés, décrits et compris.

Ce travail propose une double approche expérimentale et de modélisation moléculaire permettant de décrire quantitativement, à l'aide de systèmes représentatifs réalistes, les interactions des radionucléides avec les matériaux cimentaires et les molécules organiques. Le système modèle comporte trois composantes principales. Tout d'abord, des phases pures de silicate de calcium hydraté (C-S-H) contenant différentes compositions en Ca/Si choisies comme phase modèle d'un ciment, puis, le gluconate (molécule simple et bien décrite) choisi comme bon représentant d'additifs organiques pour sonder les mécanismes d'interaction à l'échelle moléculaire, enfin, l'uranium choisi d'une part comme représentant des

radionucléides de la série des actinides et d'autre part, parce qu'il est l'un des radionucléides pour lequel les interactions avec les matériaux cimentaires ont fait l'objet de nombreuses d'études. Bien qu'il puisse exister sous différents états d'oxydation, l'uranium est présent en milieu oxique sous forme d'uranium(VI), très mobile en milieu aqueux. Dans les systèmes cimentaires, l'uranium(VI) existe sous forme de cation dioxouranyl aqueux (UO_2^{2+}) et sa stabilité a été confirmée par des expériences XANES (Sylwester et al., 2000). Le motif linéaire de dioxouranyle linéaire UO_2^{2+} peut se lier à des ligands organiques chargés négativement dans le plan équatorial.

L'objectif principal de ce travail a consisté à développer une description des effets des additifs organiques sur les propriétés des pâtes de ciment dans le cadre de leur utilisation pour le stockage des déchets radioactifs. Les plastifiants (superplastifiants) sont utilisés pour améliorer l'hydratation du ciment, améliorer l'ouvrabilité et la fluidité des pâtes de ciment sans ajouter d'eau supplémentaire et sans changer le rapport eau/ciment. Ces additifs peuvent également améliorer la résistance à la compression des matériaux cimentaires. Les superplastifiants les plus répandus sont des polyélectrolytes organiques à masse moléculaire élevée, comprenant principalement des polymères à structure en peigne (tels que les acides polycarboxyliques) et des copolymères.

Des systèmes binaires ont été initialement étudiés de façon à obtenir des données de référence pour l'investigation de systèmes ternaires (C-S-H/adjuvant organique/U (VI)). Les systèmes ternaires sont destinés à mimer les processus "réels" où la matière organique résiduelle interagit avec les radionucléides potentiellement relâchés par les déchets. Les interactions ont été étudiées par des techniques expérimentales complémentaires et de modélisation moléculaire. Les phases C-S-H synthétisées ont été caractérisées pour obtenir les véritables rapports Ca/Si et vérifier les contaminations possibles des échantillons. De plus, c'est une validation des résultats obtenus par rapport aux données de la littérature et aux données de référence des expériences sur les systèmes binaires et ternaires.

L'étude de systèmes binaires a été réalisée de façon à obtenir des données de référence pour l'investigation de systèmes ternaires (C-S-H/adjuvant organique/U(VI)), destinés à mimer les processus "réels" où la matière organique résiduelle interagit avec les radionucléides potentiellement relâchés par les déchets. La méthodologie choisie repose sur une approche complémentaire liant expériences et modélisation moléculaire. Les phases C-S-H ont été synthétisées par réaction en phase aqueuse et caractérisées par Diffraction des Rayons X (DRX) et RMN-MAS du solide avant la réalisation des expériences de sorption. Leurs

solutions d'équilibre caractérisé par ICP-MS quadrupolaire et par chromatographie à échange d'ion (HPIC). Les expériences ont consisté en la détermination des cinétiques et d'isothermes de sorption et de désorption de molécules organiques (Gluconate et PCE) et de U(VI) sur les phases C-S-H. La cinétique rapide d'adsorption des molécules organiques (gluconate et PCE) montre que la nature de l'interaction d'adsorption est principalement électrostatique, les cations Ca^{2+} présents au niveau l'interface liquide-solide jouant le rôle de médiateurs (ponts cationiques). Les résultats montrent que l'addition d'ions gluconate peut significativement augmenter la sorption d'un radionucléide (U(VI)) dans les phases de C-S-H.

De plus, un effet notable du rapport Ca/Si sur la sorption du gluconate sur les C-S-H est observé, avec une sorption plus forte pour des rapports Ca/Si élevés. En effet, l'augmentation du rapport Ca/Si est corrélée au changement de signe de la charge de surface des phases C-S-H (de négatif à positif) du à la surcharge par Ca^{2+} (Viallis-Terrisse et al., 2001; Jonssön et al., 2005; Labbez et al., 2011). Parallèlement, la charge du groupement fonctionnel des molécules organiques est négatif en solutions alcalines (par ex. le pKa du groupe carboxyl de l'ion Gluconate est de 3,86) donc son adsorption serait dans ce cas principalement gouvernée par des forces d'attraction. Ceci pourrait signifier qu'avec le temps, la dégradation d'une pâte cimentaire caractérisée par des rapports Ca/Si (des phases C-S-H) plus faibles, pourrait favoriser le relâchement des molécules des surfaces cimentaires vers l'eau porale. L'évolution des concentrations des ions majoritaires et du pH a été mesuré à chaque étape des expériences avec le gluconate de façon à obtenir une vue détaillée des processus. Les concentrations à l'équilibre de Si and de Ca^{2+}ainsi que le pH, restent stables quels que soient les échantillons étudiés.

L'ion sodium a été ajouté au système en tant que contre-ion du gluconate (sel de sodium de l'acide gluconique). Une expérience spécifique a été réalisée pour étudier l'influence de la présence d'ions sodium sur le processus d'adsorption dans le système binaire C-S-H/gluconate. L'ion sodium, chargé positivement, est connu pour être sorbé sur les C-S-H de faibles rapports Ca/Si (Stade, 1989; Hong and Glasser, 1999; Viallis et al., 1999). Nos résultats montrent que son addition, en concentration relativement faible, n'affecte pas l'état d'équilibre des C-S-H: le pH et les concentrations de Ca et de Si restent constants pour tous les échantillons.

L'ion gluconate est une petite molécule qui est un bon modèle de départ pour l'étude à l'échelle moléculaire du mécanisme d'interaction C-S-H/organique. Cependant, on peut se poser la question de savoir si ce même mécanisme fonctionne pour des molécules organiques

plus complexes. Par conséquent, il a été testé un autre système avec le superplastifiant à base d'acides polycarboxyliques (PCE), une molécule typique d'un adjuvant industriel.

Il a été confirmé expérimentalement que l'interaction PCE et les C-S-H est aussi principalement électrostatique et déterminée par l'attraction du cation Ca^{2+} présent à la surface. La différence de sorption de PCE entre C-S-H de rapports Ca/Si variable (1 et 1,4) existe, mais les valeurs des rapports de distribution (Rd) calculés sont trop proches pour que ces différences soient considérées comme significatives : Rd (PCE/C-S-H) = 35-50 L/kg. Les molécules de PCE n'interagissent pas de la même manière (que l'ion de gluconate) avec la surface des C-S-H, leur cinétique d'adsorption est légèrement plus lente que pour de plus petites molécules organiques. Contrairement au gluconate, PCE n'affecte pas la sorption de l'Uranium(VI) aux C-S-H. Ceci peut s'expliquer par la différence de masse moléculaire et de configuration moléculaire de la molécule organique étudiée. Une étude serait nécessaire pour étudier l'influence de la masse moléculaire ainsi que de la structure des molécules organiques sur les mécanismes de sorption de l'Uranium(VI). De plus, l'utilisation de PCE marqué isotopiquement par ^{14}C pourrait être utilisée pour améliorer les expériences à faibles concentrations en polymère dans le but d'exclure les interactions des molécules organiques les unes avec les autres.

Les techniques de chimie analytique liquide permettent d'identifier les principales tendances du comportement des espèces étudiées à la surface des phases de C-S-H mais ne permettent pas de montrer quel est le mécanisme moléculaire impliqué. Ainsi, la modélisation moléculaire devient un outil utile pour l'interprétation d'évènements macroscopiques.

En parallèle, des modèles atomistiques ont été développés pour toutes les surfaces d'intérêt. La technique de dynamique moléculaire (DM) a permis de modéliser les aspects structuraux, énergétiques et dynamiques des processus de sorption sur les surfaces des phases C-S-H. Des simulations DM non contraintes ont été réalisées. Les défauts existant dans les chaines de silicate des C-S-H peuvent constituer de potentiels sites de surface pour les espèces considérées. L'intérêt de la dynamique moléculaire prend alors tout son sens puisqu'elle permet d'obtenir une image à l'échelle atomique des interactions de surface. A des fins de cohérence, le travail de modélisation a porté sur la caractérisation des mêmes systèmes binaires et ternaire que ceux étudiés expérimentalement. La solution aqueuse de gluconate, trois phases C-S-H possédant des rapports Ca/Si différents et leurs interfaces en solution ont ainsi été étudiés.

Dans ce travail, la sorption des ions d'intérêt sur différents sites de surface a été évaluée. Une comparaison détaillée entre les surfaces des phases C-S-H en contact avec des solutions contenant ou non des ions U(VI) a permis d'identifier et de décrire des sites de sorption potentiels, structurellement différents en fonction des rapport Ca/Si modélisé. Plusieurs sites de sorption pour les ions uranyle existent les surfaces des C-S-H ; des complexes mono- et bidentates peuvent être formés avec les oxygènes déprotonés de la surface. De plus, les ions calcium s'adsorbant sur ces mêmes sites, une compétition Ca^{2+}/UO_2^{2+} pour ces sites peut être attendue.

Pour des cas bien sélectionnés, des simulations de DM avec contraintes ont été réalisées afin de déterminer les profils d'énergie libre d'adsorption via des calculs de potentiel de force moyenne et d'estimer les constantes de complexation. Pour les phases C-S-H de rapport Ca/Si = 0,83, deux sites de sorption énergétiquement égaux ont été trouvés pour Ca^{2+} dont un seul accessible aux ions UO_2^{2+}. Un modèle de phases C-S-H, incluant des défauts dans la structure et possédant avec une charge négative plus élevée, conduit à obtenir, à partir des profils PMF calculés, des sites présentant une adsorption plus forte pour les cations. En solution aqueuse, les ions gluconate forment des complexes avec les cations Ca^{2+} et UO_2^{2+}. La complexation avec le calcium s'est révélée être plus favorable que celle avec les ions uranyl. Les résultats obtenus sur l'environnement structurel local des cations sont en accord avec les données de la littérature. Les ions gluconate s'adsorbent sur les phases C-S-H par l'intermédiaire du groupement fonctionnel carboxyle et du cation pontant formant ainsi des complexes de sphère interne et externe avec la surface.

La combinaison des résultats expérimentaux et de modélisation obtenue dans ce travail, conduit à faire l'hypothèse du mécanisme d'interaction moléculaire suivant pour le système ternaire modélisé. Les énergies libres d'adsorption des cations Ca^{2+} et UO_2^{2+} sont assez similaires, ce qui conduit à une potentielle compétition pour les sites de sorption de surface. Le rôle de médiateur des ions Ca^{2+} dans la sorption du gluconate a été confirmé et il a été démontré que l'ajout de composés organiques affaiblissait la liaison des cations avec les sites de surface. En conséquence, une diminution de l'énergie libre d'adsorption du complexe Ca-gluconate pourrait faciliter l'échange avec les ions UO_2^{2+} sur le même site de sorption et pourrait ainsi expliquer l'augmentation de l'adsorption de UO_2^{2+} observée expérimentalement dans le système ternaire.

Mots clés: Silicate de calcium hydraté, Uranium (VI); gluconate; adsorption; dynamique moléculaire

Table of Contents

List of tables

List of figures

List of Annexes

List of abbreviations

C-S-H	Calcium silicate hydrate
CM	Colloidal model (CM-I and CM-II)
EXAFS	Extended X-ray absorption fine structure spectroscopy
FTIR	Fourier-transform infrared spectroscopy
HCP	Hydrated cement paste
HLW	High level waste
IC	Ion exchange chromatography
ICP-MS	Inductively coupled plasma – mass spectrometry
ILW	Intermediate level waste
IR	Infrared specroscopy
LAMMPS	Large-scale atomic/molecular massively parallel simulator
L/S	Liquid to solid ratio
LL	Long-lived (waste)
LLW	Low level waste
LSC	Liquid scintillation counting
MASA	Sodium methallyl sulfonate
MD	Molecular dynamics
MM	Molecular mechanics
NAMD	Nanoscale molecular dynamics
NEXAFS	Near edge X-ray absorption fine structure spectroscopy (also XANES)
NMR	Nuclear magnetic resonance spectroscopy
PCE	Polycarboxylate superplasticiser
PDI	Polydispersity index
PEGMEMA	Poly(ethylene glycol methyl ether methacrylate)
PMF	Potential of mean force
PPCO	Polypropylene copolymer
PTFE	Polytetrafluoroethylene
QM	Quantum mechanics
RCN	Running coordination number
RDF	Radial distribution function
RESP	Restrained electrostatic potential VLLW Very low level waste
SANS	Small angle neutron scattering
SFMC	Sulfonated melamine formaldehyde polycondensates
SL	Short-lived (waste)
SPC	Simple point charge
TEM	Transmission electron microscopy
TOC	Total organic carbon
VDW	Van der Waals
XRD	X-ray diffraction
WHAM	Weighted histogram analysis method

Introduction

Radioactive waste is the waste that contains radionuclides with activity defined and regulated by country authorities. Radioactive waste is originated from nuclear power plants, industrial, medical, scientific and military activities and is generated in various forms with specific radionuclide compositions.

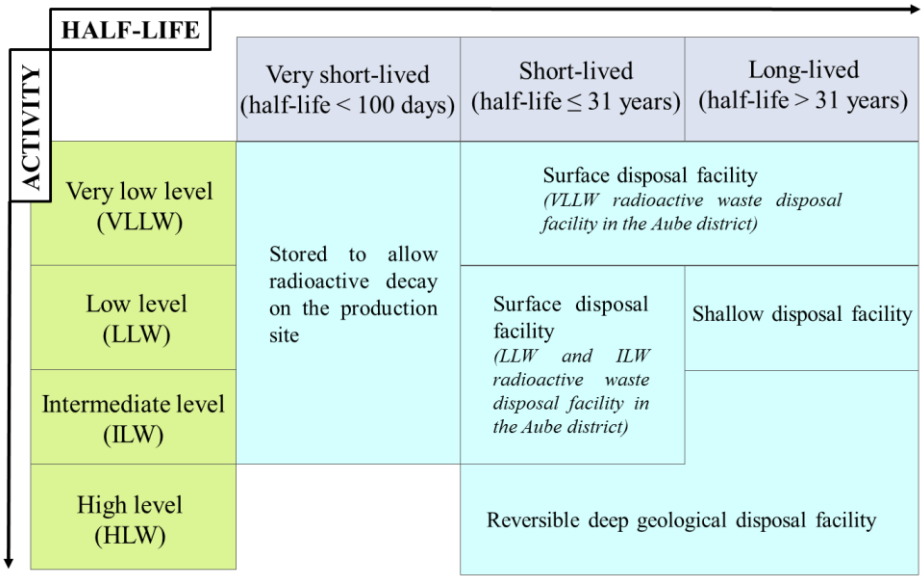

Figure 1. *French classification for radioactive waste from Andra website (English version, 07/01/2017, radioactive waste/classification, with permission).*

In France radioactive waste is classified according to its activity level and half-life (Fig. 1):

1. ***Very low level waste*** (VLLW) has an activity level close to that of naturally occurring radioactivity (1-100 Bq/g). It does not require high level isolation and can be stored in near surface landfill disposals (Andra CSTFA disposal facility located in the Aube district). Soils, sludge and rubbles are a typical waste in this group.

2. ***Low-level long-lived waste*** (LLW-LL) represents a broad range of waste including radium-bearing and graphite waste. LLW-LL contains mostly long lived radionuclides (Ra, U, Th) with half-lives that are more than 31 years. It requires higher isolation and can be stored in engineered near surface disposals.

3. ***Low and intermediate level short-lived waste*** (LILW-SL) contains short-lived radionuclides (^{60}Co, ^{137}Cs) with half-life ≤ 31 years, and limited amounts of long-lived radionuclides. Waste is managed at the Andra CSFMA waste disposal facility located in the Aube district.

4. ***Intermediate-level long-lived waste*** (ILW-LL) is mostly composed of metal structures used in the fuel recycling process. It has radionuclides with long half-lives (more than 31 years) and will be stored in the deep geological disposal facility.

5. ***High level waste*** (HLW) – waste that can generate a lot of heat during decay process. It contains fission products (^{134}Cs, ^{137}Cs, ^{90}Sr), activation products (^{60}Co) and actinides (^{244}Cm, ^{241}Am). Stable deep geological disposals are normally considered for storage.

The main idea of managing and storing radioactive waste is to protect people and environment from its harmful influence. This means isolation and/or processing of radionuclides in a way that no damage is done when they return to the biosphere. Unlike other hazardous waste the level of danger for radioactive waste reduces with time and eventually all of it decays into non-radioactive elements.

In France, Andra (Agence nationale pour la gestion des déchets radioactifs) is a public body in charge of the long-term management of all radioactive waste, it works under the supervision of the Ministry of Ecology, Energy, Sustainable Development and the Sea and the Ministry of Research. Andra is in charge of a project of deep geological waste disposal (Cigeo) for HLW-LL and ILW-LL wastes generated by French nuclear power plants. The facility will be situated in northeastern France on the border of Meuse and Haute-Marne regions and will include both surface and underground installations (e.g., Grambow, 2016). The underground disposal will be built at a depth of approximately 500 meters in the layer of impervious clay rock (Callovo-Oxfordian clay formation) as it is shown in Fig. 2-B.

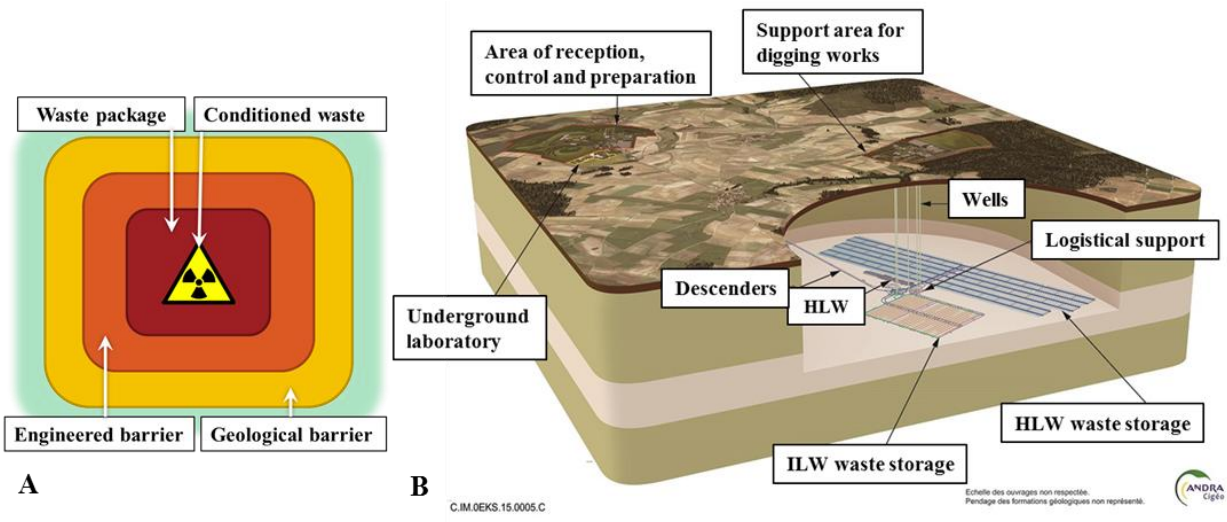

Figure 2. *The multi-barrier concept of radioactive waste disposal (A) and 3D diagram of Cigeo facility design (B, image adopted from Andra with permission).*

The multi-barrier concept is adopted and applied for different types of radioactive waste. In principle, the multi-barrier consists of three successive barriers: waste packages, the engineered structure and the geological formation of the site that together provide physical and environmental levels of protection (Fig. 2-A). The first barrier is the conditioned immobilized waste typically through cementation (ILW-LL) or vitrification (HLW-LL). The second one is the corrosion-resistant canisters (e.g., carbon steel for HLW-LL) that contain the immobilised waste. The last barrier is the host rock together with the disposal structure, which ensures isolation, stability and safety of the radioactive waste over a very long period of time.

Many factors should be taken into account when the long-term safety of radioactive waste disposal is considered: both natural site properties, such as availability of natural resources, seismic and volcanic stability, ground water chemistry, etc., and engineered properties including waste forms, waste packages, and construction materials.

Cement and concrete play an important role in the design of the radioactive waste disposal. It can be both part of the packaging for some intermediate level waste or part of the sealing material for HLW storage cells, and also a construction material for the galleries and access shafts (Fig. 3) of the waste disposal facility. As a result, even if cement materials have been chosen for their mechanical and physical properties, they may also contribute to the containment of radioactivity and the control of the water flow into the repository after closure. These materials have a high affinity with a lot of radionuclides which can be retained through different mechanism (sorption, incorporation or precipitation) due to their chemical properties (high pH porewater, presence of charged phases with high surface area).

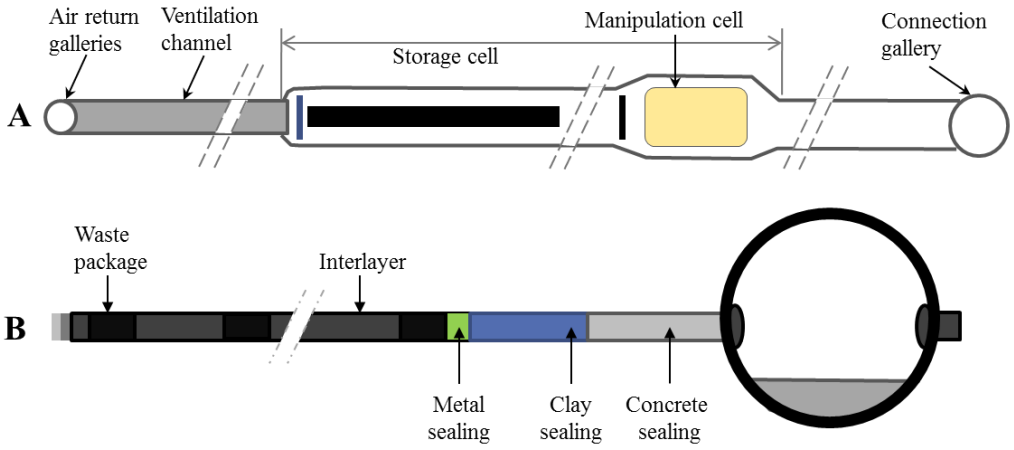

Figure 3. *Design of storage cells for ILW (A) and HLW (B) (based on Andra, 2009).*

During cement paste production, organic additives (e.g., superplasticisers) are typically used to enhance mechanical properties of the final cement material. Of course, the presence of potentially reactive chemicals may cause additional safety concerns. So, even though the amount of additives is usually small, the mechanisms of their interactions with all components of the waste disposal system should be systematically studied, described and understood.

This work is therefore a part of a global approach that proposes to describe, using model systems, the interactions between organic molecules and cementitious materials with radionuclides. Uranium(VI) has been then selected as a representative radionuclide because it is one of the most studied elements with a lot of data available in literature.

The work consists of four chapters. The first chapter presents a literature survey on the key points of the study. The primary and secondary objectives are formulated accordingly. The second chapter provides information on materials and methods used and experimental results of materials characterisation. The third and fourth chapters present the results and conclusions for the two complementary approaches used in the work: wet chemistry experiments and computational molecular modelling.

Chapter 1

Background and Motivation

1.1. Cement

Cement is a complex material that consists of hydrated clinker (calcium silicates, aluminates, alumoferrites) and gypsum. The production of cement is huge (more than 4000 million metric tons were produced worldwide in 2015). It is one of the most used building materials and obviously will be used in the design and construction of deep geological waste repositories. Cement raw clinker materials are geologically available and resources exhaustion is unlikely in the future. In the concept of radioactive waste disposal, cements are a part of both the repository infrastructure (walls of the galleries, access shafts) and the waste packaging (intermediate level long living radionuclides).

In cement chemistry it is common to use the first letter of the oxide to describe the chemical formula in a simplified way: C = CaO; S = SiO_2; A = Al_2O_3; F = Fe_2O_3; M = MgO; H = H_2O, and so on. This notation should not be confused with chemical elements. So, C-S-H should be understood as CaO-SiO_2-H_2O or calcium silicate hydrate (Taylor, 1990).

Cement clinker is made by pyroprocessing (T = 1450°C) of homogeneous mixture of limestone and alumo-silicates (clays). After heating the formed nodules are finely ground and calcium sulfate (gypsum) is added to control the setting rate of cement during the hydration process. Clinker typically consits of alite, belite, aluminates, and alluminoferrites.

Alite, or tricalcium silicate (Ca_3SiO_5), is the major component of clinker in most of the conventional cements. Pure alite consists of 73.3 wt. % of CaO and 26.3 wt. % of SiO_2, but the oxides of Na, K, Mg, Al, P, S, and Fe are also present in clinker (up to 4 wt. % in total). Alite is rapidly hydrated, it dictates the setting time and is responsible for the short-term strength development of the material (Taylor, 1990).

Belite (dicalcium silicate, Ca_2SiO_4, often its β-polymorph) reacts with water much slower and is reposible for the strength development at the later phases of cement formation (up to one year). Pure belite contains 65.1 wt. % of CaO and 34.9 wt. % of SO_2, while oxide substitutions of up to 6% (mostly oxides of Al and Fe) are also observed in clinker (Taylor, 1990).

Nearly 10% of clinker are constituted by the aluminate phase ($Ca_3Al_2O_6$). Aluminate is the most reactive phase in cement clinker and its hydration causes exotermic “flash set” (immediate set). This process is not desirable and is typically deactivated through the addition of gypsum, $CaSO_4 \cdot 2H_2O$. With sulfates addition, the ettringite phase

($3CaO \cdot Al_2O_3 \cdot 3CaSO_4 \cdot 32H_2O$) is formed on the surface of aluminates decreasing their reactivity. Slow hydration of aluminates creates sulfoaluminate phases such as AFm ($CaO \cdot Al_2O_3 \cdot CaSO_4 \cdot 12H_2O$).

Another typical clinker component is tetracalcium aluminoferrite (Ca_2AlFeO_5). Aluminate and ferrite rapidly form various metastable hydrate phases that further trasnform with time into more stable cubic structure (Taylor, 1990; Ridi et al., 2011).

Based on the composition, there are different types of cements. Portland cement is the most common type of cement in general use with clinker compositions that typically consist of 45–75 wt. % of alite, 7–32 wt. % of belite, 0–13 wt. % of aluminates, 0–18 wt. % of alumoferrites, and 2–10 wt. % of gypsum. Depending on the desired physical and chemical peformance, different types of cement blends are designed. The most known are cement blends with blast-furnace slag (sulfate-resisting and low-heat cement), fly ash (low cost cement with early strength developpement), silica fume (exceptionally high strength cement), metakaolin. Other types of cements include pozzolan-lime (ground pozzolan and lime) cements, slag-lime (ground granulated blast-furnace slag and lime) cements, supersulfated cements (80 wt. % ground granulated blast furnace slag, 15 wt. % gypsum or anhydrite, ordinary Portland cement clinker or lime) and calcium sulfoaluminate cements (ye'elimite-based clinker).

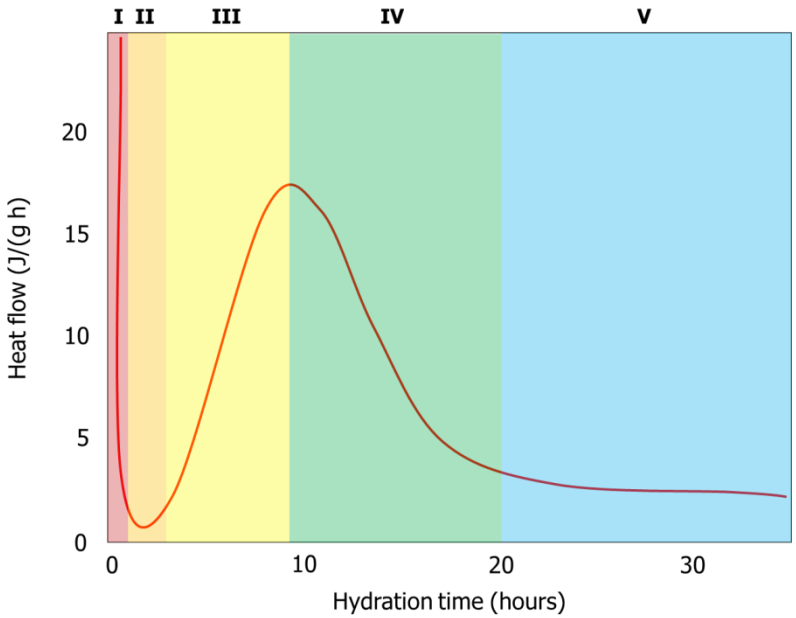

Figure 4. *Typical evolution of the heat flow for the hydration process of a cement/water paste (Ridi et al., 2011; Taylor, 1990).*

When water is added to clinker, the hydration process starts. The mechanisms of cement hydration were extensively studied (e.g., Bentz, 1997; Pane and Hansen, 2005; Bullard et al., 2011; Scrivener et al., 2004, 2015; Trauchessec et al., 2015; and many others). Due to the complex chemical composition of cement, the hydration is typically described as a five step (sometimes four step) process (Fig. 4):

(I) ***Dissolution*** **–** the silicate and aluminate phases dissolve, a saturated calcium hydroxide solution is formed (pH=12);
(II) ***Induction*** **–** a dormant period of a few hours long;
(III) ***Acceleration*** **–** a precipitation of silicate and aluminate hydrates, further dissolution of the anhydrous phases;
(VI) ***Deceleration*** **–**a strong decrease of the hydration rate;
(V) ***Slow ongoing hydration*** **–** a diffusion-controlled process.

In cement materials, calcium silicate hydrate (C-S-H) phases are formed as a result of hydration of alite (Ca_3SiO_5) and industrial belite (Ca_2SiO_4), the two silicates that are the essential constituents of clinker of most cements (Taylor, 1990). Synthetic pure C-S-H phases can be also produced by the pozzolanic reaction: ($CaO + SiO_2 + 2\ H_2O$) → ($Ca(OH)_2 + H_4SiO_4$) → ($CaH_2SiO_4 \cdot 2H_2O$). Because of its critical role, C-S-H was chosen as the cement model in this work.

In natural environments and with time cementitious materials become a subject to degradation processes. One of the most significant degradation scenarios is decalcification (leaching of calcium and hydroxide ions from the cement pore solution). Decalcification can cause severe alteration in cement structure and change the properties of the hydrated phases (Glasser et al., 2008). There are obviously various processes that cause cement degradation (irradiation, heating cycling, mechanical damage, etc.), but in this work only decalcification is considered out of all possibilities.

1.2. Calcium Silicate Hydrate

1.2.1. C-S-H structure and properties

An accurate nano-scale description of C-S-H phases is very challenging and the interest in understanding their structure and the nature of structural disorders continues to be strong. A

significant amount of research has been done in the last decades to address these issues using various experimental and theoretical methods. Some of the C-S-H characteristic features can be found in the short summary table below (Table 1).

Table 1. Experimental characterisation of C-S-H

Method	Selected key points	References
Rietveld analysis of powder X-ray diffraction (XRD) data	- a nano-crystalline material with turbostratic structure; - long range crystallographic order; - XRD pattern is close to tobermorite 11 Å (Ca/Si = 0.8).	Grangeon et al., 2013
Nuclear magnetic resonance spectroscopy (NMR)	- tobermorite-like structure for high Ca/Si; - average silicate chain length in C-S-H depends on Ca/Si ratio; - structure of C-S-H is not altered by the presence of organic polymers during hydration step and it is proved by ^{1}H and ^{29}Si NMR studies.	Cong and Kirkpatrick, 1996 Brunet et al., 2004 Richardson et al., 2010 Bosque et al., 2016 Rottstegge et al., 2006 Tajuelo Rodriquez et al., 2015
Raman spectroscopy	- synthetic C-S-H has a tobermorite-like structure	Richardson et al., 2010
Fourier-transform infrared spectroscopy (FTIR)	- C-S-H has features of jennite structure at high Ca/Si ratio (more than 1.3)	Yu et al., 1999
Transmission electron microscopy (TEM)	- C-S-H is a layered material; - crystals have size of 10-50 nm; - the basal distance for Ca/Si = 0.8 is 11 Å; - synthetic C-S-H can include amorphous phases rich on Ca; - synthetic C-S-H has a foil like morphology.	Richardson et al., 2010 Tajuelo Rodrigues et al., 2015 Grangeon et al., 2013
Small angle neutron scattering (SANS)	- in hydrated cement the formula is $(CaO)_{1.7}(SiO_2)(H_2O)_{1.8}$; - in hydrated cement C-S-H density is 2.604 mg/m^2; - three H_2O types are present: interlayer bonded, adsorbed on the surface, liquid in nanopores.	Allen et al., 2007

Studies were also performed using extended X-ray absorption fine structure spectroscopy (EXAFS) (Lequeux et al., 1999), near edge X-ray absorption fine structure spectroscopy

(NEXAFS) (Mendes et al., 2011), and molecular dynamics simulations (Faucon et al., 1997; Kalinichev and Kirkpatrick, 2002; Kalinichev et al., 2007; Churakov et al., 2014; Dongshuai, 2014).

All of the essential C-S-H compositional and structural features listed above are carefully taken into account when the atomistic computational models were constructed in the present work.

Tobermorite is a rare natural layered mineral, a calcium silicate hydrate compound that consists of CaO polyhedral layers parallel to the (001) crystallographic plane with attached silicate layers on both sides. Silicate is present in the form of infinite "dreierketten" type chains (chains of triplets, Fig. 5). There are two types of silicate tetrahedra: nonbridging tetrahedra (connected with CaO layer via two shared oxygens) and bridging tetrahedra (connects two nonbridging tetrahedra, points towards the interlayer and possesses a silanol group). H_2O molecules and Ca^{2+} ions are present in the interlayer and provide the structure its unique properties (Dongshuai, 2014). Several tobermorite crystal structures with varying basal spacing are identified: clinotobermorite, tobermorite 9 Å, tobermorite 11 Å, and tobermorite 14 Å (different water content, degree of silicate chain polymerisation, abundance of interlayer calcium) (Merlino et al., 1999; Biagioni et al., 2015).

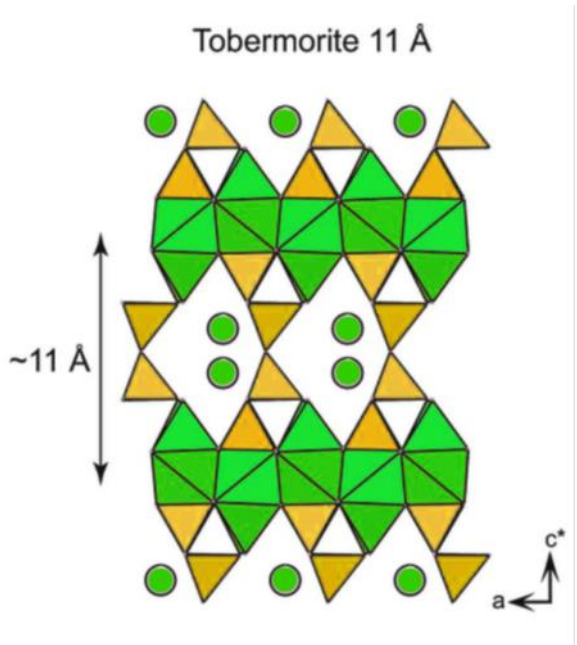

Figure 5. *A three dimensional view of the tobermorite structure using the orthorhombic axis a/2 = 5.58 Å, b = 7.39 Å, and c/2 = 11.389 Å (Hamid, 1981; Grangeon, 2013).*

Ca/Si ratio of C-S-H is an important parameter to consider since it can significantly influence chemical and physical properties of cement (e.g., pH of the pore water, the surface charge, equilibrium ion concentrations). Despite the fact that in ordinary Portland cement we can observe predominantly C-S-H phases with Ca/Si ratios higher than 1.5, lower ratios appear in cement with added fly ash and silica fume, and in degraded pastes because of the decalcification.

1.2.2. C-S-H models

Due to the compositional and structural diversity of cement phases, modelling of cementitious materials is quite challenging, and even the most advanced models represent significant simplifications of the real systems. One of the useful ways to categorise the cement models is by their characteristic length scale (Dolado and van Breugel, 2011) (Fig. 6).

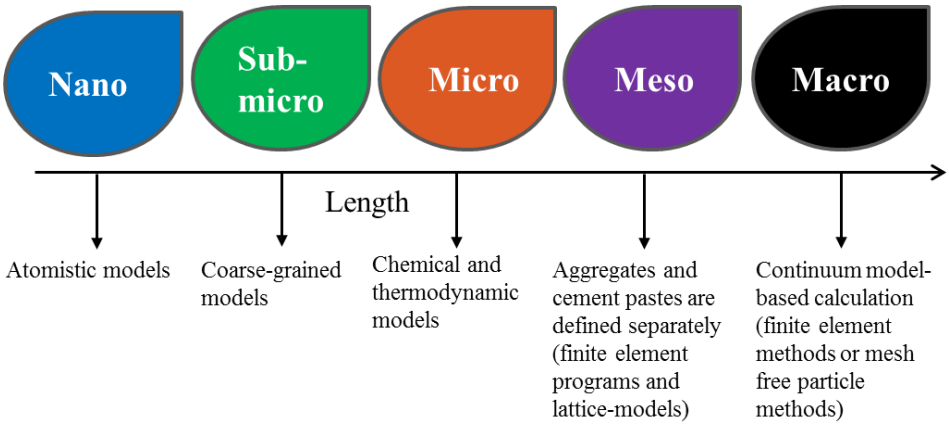

Figure 6. *Classification of the models of cementitious materials based on their characteristic length scale (Dolado and van Breugel, 2011).*

A nanoscale colloidal model of C-S-H (CM-I and CM-II) was developed a decade ago (Allen et al., 2007; Jennings, 2008). The elementary units of this model are non-spherical particles (named as "globules") with nanometer dimensions and an internal sheet-like structure. The particles are charged and anisotropic, they aggregate forming typically disordered mesostructure (Delhorme et al., 2016; Bonnaud et al., 2016). Water is found in the interlayer and intraglobular spaces, distributed in small and large gel pores. It is mostly adsorbed at the surfaces of C-S-H particles and within the intraglobule spaces (Fig. 7). The colloidal model explains the behaviour of water in C-S-H phases and predicts some of the mechanical properties of cement. However, the focus of the present work is not in the bulk properties of

C-S-H, but rather in the molecular level quantification of the interaction mechanisms that occur at the C-S-H surfaces.

The first atomistic models of C-S-H were based on the crystal structure of tobermorite (e.g., Faucon et al., 1997; Bell and Coveney, 1998; Kalinichev and Kirkpatrick, 2002; Gmira et al., 2004; Kalinichev et al., 2007). Although the structure of this mineral is very similar to C-S-H, it is desirable to introduce some elements of structural disorder and defects that bring models closer to reality. Indeed, numerous defect-containing tobermorite models are developed. Tobermorite modifications provide possibilities to model different Ca/Si ratios and better predict the processes that occur in degraded cement or cement with high silica content.

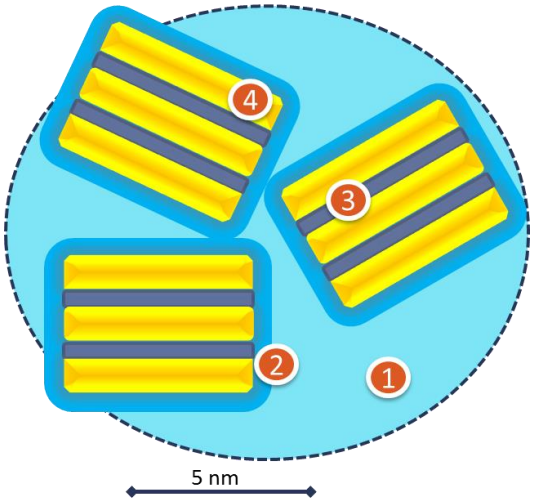

Figure 7. *A schematic nanoscale model of C-S-H particles (based on Allen et al., 2007) with different types of water identified: 1 – nanopore water; 2 – adsorbed water; 3 – interlayer water, 4 – layered calcium silicate nanoparticles.*

Richardson and Grooves (1992) proposed a generalized model which represented C-S-H particles as nanostructures composed of silicate chains (with different length and different amount of silanol groups) in contact with $Ca(OH)_2$. The structural formula is derived from tobermorite and can be expressed as $\{Ca_{2n}H_wSi_{(3n-1)}O_{(9n-2)}\}\cdot(OH)_{w+n(y-2)}\cdot Ca_{0.5ny}\cdot mH_2O$, where w is the number of silanol groups and w/n is the degree of protonation. The model assumed a certain amount of missing bridging silica tetrahedra, an addition of Ca^{2+}, and a variable degree of protonation of the silanol groups. A similar model of defect tobermorite structure was proposed by Cong and Kirkpatrick (1996) based on the assumption that the charge of the deprotonated nonbridging oxygens of the silicate layer is compensated by Ca^{2+} ions through the formation of Si-O-Ca links. Additionally, C-S-H structure description was developed by Nonat and Lecoq (1998) who assumed the absence of silanol groups but the presence of Ca^{2+}

and OH^- ions in the C-S-H interlayers. Depolymerisation of silicate chains as the main mechanism of increasing the Ca/Si ratio of C-S-H was also pointed out by Yu et al. (1999) who used infrared spectroscopy to study the structure of C-S-H.

A significant advance in the C-S-H atomistic description has been made by Pellenq et al. (2009) using a bottom-up modelling approach (Fig. 8 (left)). This model provides realistic Ca/Si ratios and density values for C-S-H. Moreover, it was validated by reproducing various macroscopically measurable physical properties of C-S-H (mechanical stiffness and strength, hydrolytic shear response); and provided a good agreement with other experimental characterisations (Si-NMR, EXAFS, XRD, IR). Further, the atomic order-disorder structure had been quantified by Bauchy et al. (2014) who demonstrated how the C-S-H structure can be described as an intermediary between full crystallinity and entirely amorphous glass. Another atomistic model of C-S-H ($Ca_{1.67}SiH_x$) has been proposed by Kovačević et al. (2015) with a view on how silica oligomers are distributed in the structure. The most stable model was the one where only bridging silica tetrahedra were removed, thus breaking infinite silica chains into dimers and pentamers (Fig. 8 (right)). As a result, the approach of adjusting the lengths and shapes of the C-S-H silica chains to conform with available Si-NMR data was adopted for the model construction in the present work.

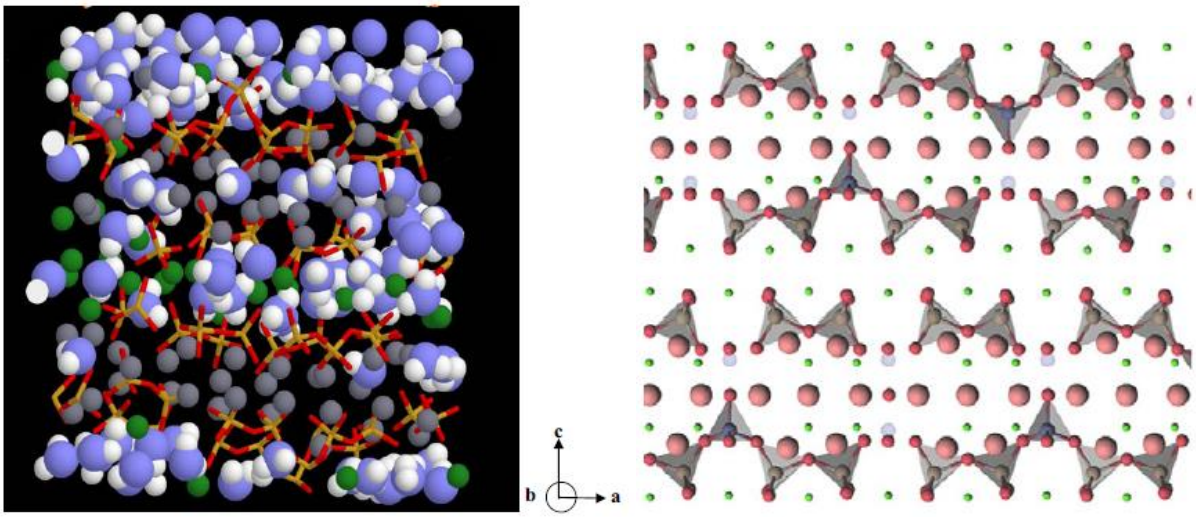

Figure 8. *Examples of atomistic models of the C-S-H.* ***Right****: Ca/Si = 1.75 (Pellenq et al., 2009); the blue and white spheres are O and H atoms of H_2O molecules, respectively; the green and grey spheres are inter and intra-layer Ca ions, respectively; yellow and red sticks are Si and O atoms in silica tetrahedra.* ***Left****: Ca/Si = 1.67 (Kovačević et al., 2015); the grey and blue spheres are Si, the red and pink spheres are O in silica tetrahedra and of water, respectively; the green spheres are Ca ions. Images adapted with permission.*

The exact structure of C-S-H is still not completely defined and various models are still being developed. Yet, as it can be seen, all presently available models share certain basic features. The model of the C-S-H surface developed in this work should also not be taken as an absolutely correct description of C-S-H. This model was theoretically developed based on the experimental observations discussed above in order to provide relative simplicity and to facilitate better quantitative understanding of the molecular mechanisms of interaction among different chemical species near the surface of C-S-H.

1.3. Uranium sorption on C-S-H

Uranium has been selected as the model radioelement in the current work. A significant amount of research has already been done to describe its behaviour in cementitious materials.

Uranium can be found in different oxidations states. Under oxic conditions it is typically present as U(VI), which is highly mobile in the aqueous environment. In cementitious systems, uranium exists in the form of aqueous uranyl cation (UO_2^{2+}), and its stability was confirmed by XANES experiments (Sylwester et al., 2000). In the same study, it was reported that uranium uptake is caused by the inner-sphere complexation with cement mineral phases. In the absence of CO_2 and at pH >10 (characteristic to cement pore water), the dominating hydroxo complexes of UO_2^{2+} should be $UO_2(OH)_3^-$ and $UO_2(OH)_2^0$, but other coordinations are also possible (Prikyl et al., 2001). Numerous studies have shown that the C-S-H phase of the hydrated cement paste is the preferential binding surface for uranyl cations (Wieland et al., 2010).

Several batch U(VI) sorption experiments on synthesised C-S-H phases were performed by Pointeau et al. (2004), Tits et al. (2008, 2011) revealing rapid kinetics (a stable state reached within approximately 10 days) and a very strong uranium uptake (10^3 l/kg – 10^6 l/kg). Measured sorption isotherms (Fig. 9) showed a significant dependence of U(VI) uptake by C-S-H on the Ca/Si ratio, pH, and on the presence of alkali ions in the studied systems. As many other cation species, U(VI) sorbs better when Ca/Si and pH are lower. Cation-exchange properties of C-S-H phases with low Ca/Si ratios are already well-known (Viallis-Terrisse et al., 2001; Ochs et al., 2006; Pointeau et al., 2006).

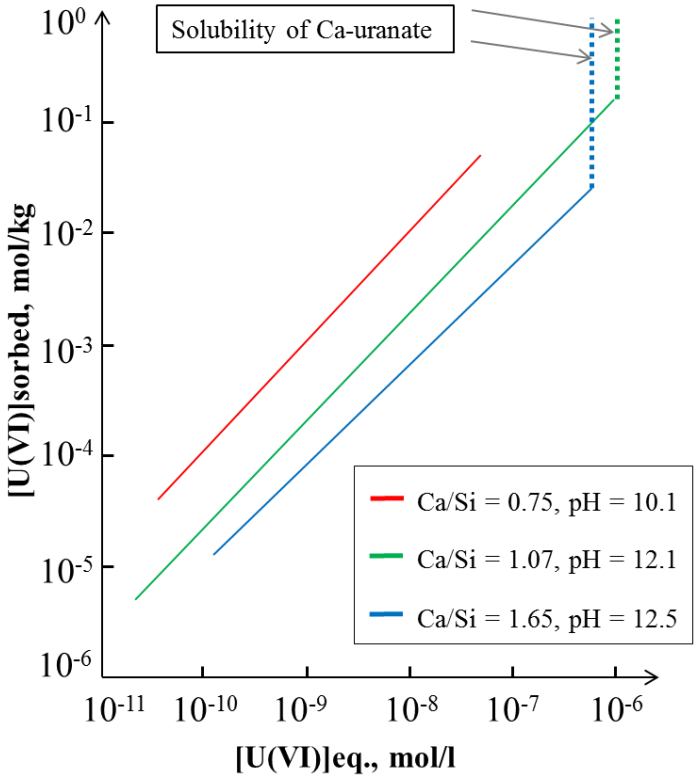

Figure 9. *Isotherms of U(VI) sorption on C-S-H with various Ca/Si ratios (data taken from Tits et al., 2011).*

The detailed mechanisms of U(VI) immobilisation have been studied by Macé et al. (2013) using extended X-ray absorption fine structure spectroscopy (EXAFS). The uranium coordination environment was found to be independent of the initial reaction conditions. At a higher concentration of uranyl ions (13.6-45 mg/g) the formation of calcium-uranate precipitate has been observed. In the proposed mechanisms, binding to a single Si of the surface was stated with a high probability of U(VI) incorporation into the C-S-H structure. A better description of a UO_2^{2+} local environment in C-S-H (and also in hydrated cement paste) can be found in the more recent work of Tits et al. (2015). Three distinguishable types of U(VI) species in the cementitious systems can be identified: (i) surface complexed; (ii) incorporated; (iii) precipitated. The incorporation should happen in the C-S-H interlayer space as shown in Fig. 10-b (Gaona et al., 2012; Macé et al., 2013). Once the ion is incorporated, it is no longer in contact with pore water and should not interact with solution ions present there. Thus, incorporated U(VI) will not be considered in this work.

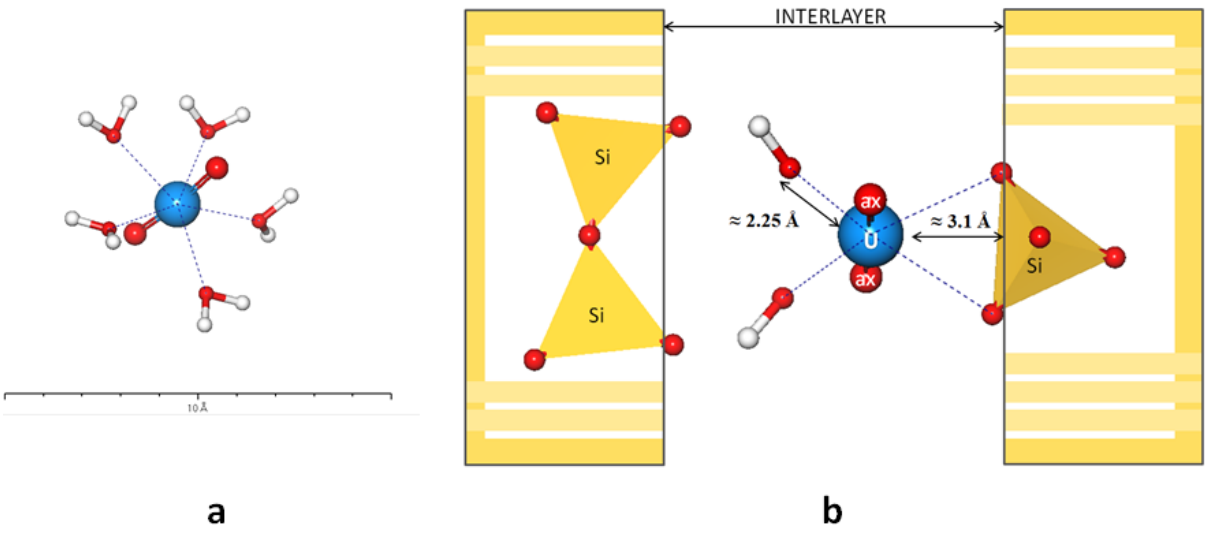

Figure 10. *a – Uranyl cation (UO_2^{2+}) with its hydration shell; b – An interlayer incorporation model for $UO_2(OH)^{2-}$ in C-S-H proposed by Macé et al. (2013).*

It is also important to keep in mind that the solvent can influence the interaction between the uranyl cation and the ligands (organic ions) (Buhl et al., 2006). In carbonate systems, complexation has been observed (Richter et al., 2016) causing reduced sorption of U(VI) on minerals under high pH conditions. A CO_2-free inert atmosphere should help to avoid a process like this for the model systems in the current work.

The interactions between U(VI) and organic ligands are of particular interest in the scope of this work (see more details in section 1.4), and gluconate anion is introduced here as a model of organic compound present in cement.

The interaction between U(VI) and organic molecules has already attracted attention and an extensive amount of research has been conducted on the structure and reactivity of uranium complexes in various reactive media (Kakihana et al., 1987; Nguyen-Trung et al., 1992; Quiles et al., 1998; Groenewold et al., 2010; Birjkumar et al., 2011; Birjkumar et al., 2012). It is interesting to note that the presence of organics can even enhance the sorption of U(VI) on mineral surfaces at highly alkaline conditions (Baston et al., 1992, 1994).

The linear dioxouranyl cation, UO_2^{2+}, can coordinate negatively charged ligands in the equatorial plane. Uranyl can form a complex with more than one gluconate ion both under acidic conditions (Zhang et al., 2009), and under alkaline conditions (Birjkumar et al., 2011; Colàs et al., 2013). The coordination is mostly happening with deprotonated carboxyl groups of gluconate, but at high pH (pH > 13.9), only solution hydroxyls are present in the first

hydration shell of the uranyl cation, deprotonation of the gluconate hydroxyl group can also take place, making the interaction with uranyl more probable (Fig. 11).

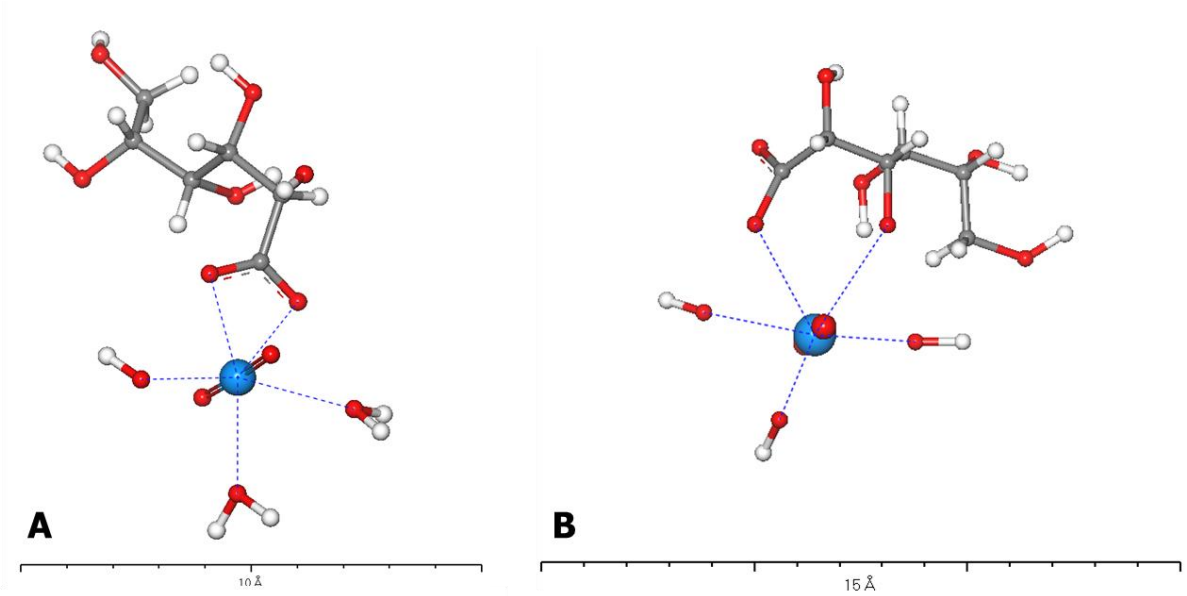

Figure 11. *UO_2^{2+} / gluconate ion complexation (ratio 1:1): A – at pH < 13.9; B – at pH > 13.9 (Birjkumar et al., 2011).*

At excess of ligand, more gluconate molecules can be present in the first solvation shell of UO_2^{2+}. In addition, complexation with larger organic molecules (polyacrylic and fulvic acids) has been studied (De Stefano et al., 2011), and it was shown that carboxyl groups are the binding sites and the density of them in the molecule greatly affects the UO_2^{2+} complexation. The higher the number of carboxyl groups present in the organic ligand, the higher is the sequestration of radionuclides. This may raise concern that the presence of organic ligands with multiple carboxyl groups can negatively affect UO_2^{2+} uptake by cementitious materials.

1.4. Cements and organic compounds

Organics can be brought into the cement structure and its interfaces as organic cement additives or as part of the radioactive waste. Organic additives are introduced to alter various properties of cement. Based on their function the cement admixtures are classified into five main groups: air-entraining, water-reducing, retarding, accelerating, and plasticisers (superplasticisers) (Kosmatka et al., 2002).

Air entraining additives (surfactants) – allow incorporating small air bubbles (Ø < 1mm) into the structure of cement during mixing. They increase freeze resistance, durability and workability of the resulting cement. These organic compounds are mostly represented by salts

of wood resins, petroleum acids, proteinaceous material, fatty and resinous acids and their salts, alkylbenzene sulfonates (Geraldi et al., 2016; Šeputytė-Jucikė et al., 2016).

Water reducers are used to decrease cement porosity, water permeability and diffusivity. They provide the possibility to control the plasticity of cement in time. Most common agents in this group are lignosulfonates and hydrocarboxylic acids (Geraldi et al., 2016; Phan et al., 2006).

Retarders are added to slow down the rate of concrete setting and to maintain the workability of the mix at high-temperature conditions. Retarders can be both organic and inorganic (Zuo et al., 2014; Papageorgiou et al., 2005). The most known among such organic additives are the salts of lignosulfonic acids, citric acid monohydrate, sodium gluconate.

Accelerating additives (coagulants) are used when rapid cement setting is needed. They increase construction safety and promote the development of high early-strength (Won et al., 2012). Triethanolamine and calcium formate are representatives of the group.

Plasticisers (superplasticisers) are used to enhance cement hydration, improve the workability and fluidity of cement pastes without the addition of extra water and without changing the water/cement ratio. These additives can also improve the compressive strength of cement materials. The most widespread superplasticisers are organic polyelectrolytes with high molecular mass, mainly comb polymers and copolymers (Fig. 12).

The dosage of superplasticiser in cement depends on different factors: water/cement ratio, cement composition, admixture characteristics. In most cases, it is in the range of 0.1 - 2 % w.t. (Yamada et al., 2000; Yoshioka et al., 2002; Herterich et al., 2003; Winnefeld et al., 2007; Ridi et al., 2013). Thus, their residual concentration in the pore water of cement should not be very high.

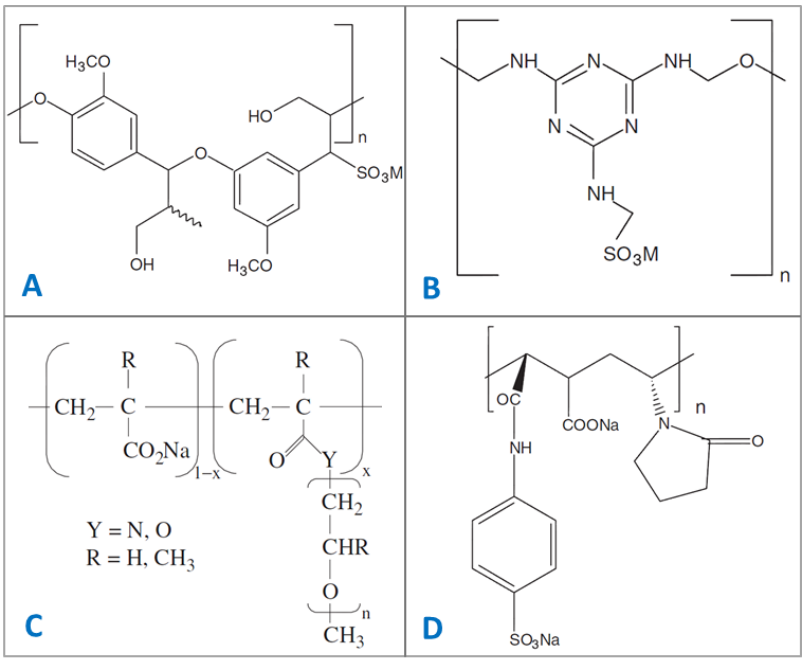

Figure 12. *Selected examples of industrial superplasticisers (Giraudeau et al., 2007): A – lignosulfonates; B – sulfonated melamine formaldehyde polycondensates (SFMC); C – polycarboxylates; D – vinyl copolymers.*

The molecules of superplasticisers adsorb on the surface of cement particles and cause repulsive interactions between them through the formation of a steric layer (Fig. 14). The effects of superplasticisers on the hydration processes have been studied (Pourchet et al., 2006; Giraudeau et al., 2007; Autier et al., 2013; Cappelletto et al., 2013), but more detailed understanding is still needed about their behaviour on the surface of cement and in the pore water.

Under conditions of close proximity of the organic polymer additives to the cement surface (~10 nm), it can be suggested that organics is immobilised by adsorption or incorporation into the hydrated cement phase (Rottstegge et al., 2006).

Electrostatic interactions play one of the key roles in the admixture-cement system. It was shown that the higher is the amount of negatively charged functional groups in the polymer (e.g. deprotonated carboxylic groups) the higher is its sorption on cement phases. Moreover, the addition of any of the polycarboxylate additives generates a slight positive increase of ζ-potential, regardless of the specific types of the superplasticiser and cement to which it was added (Alonso et al., 2013). In the same work, PCE adsorption isotherms have been described for cements of different types (Fig. 13), and it was shown that the cement surface reaches saturation at [PCE] > 2 mg/g cement.

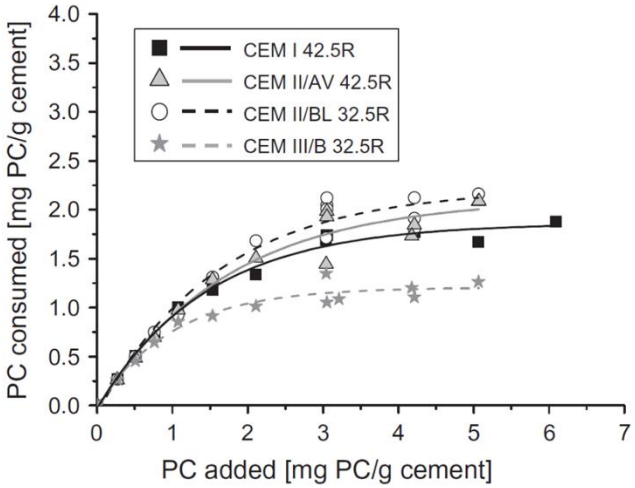

Figure 13. *Isotherms of PCE (Mw = 60 kDa, PDI = 1.7) adsorbed by four types of cement (image taken from Alonso et al., (2013) with permission).*

Measurements of ζ-potential are frequently used to characterise the forces acting between particles. Chemical composition of the solvent is one of the major factors determining ζ-potential along with other important parameters, such as ionic strength, nature of the ionic species, and their charge. The ζ-potential can be accurate and precise only when the solvent properties are well-defined.

It is found that mineral phases with a negative or neutral ζ-potential do not adsorb large amounts of organic admixtures. As a result, positive ζ-potential is crucial for their sorption. Measured ζ-potential of ordinary Portland cement was reported to be +12 mV at pH 12 (Nagele, 1986). In a 0.1 M potassium hydroxide solution and in a synthetic pore solution, the ζ-potential of C-S-H is slightly positive and is around +0.25 mV (Zingg et al., 2008). The ζ-potentials of alite and belite were reported to be negative (-5 mV) (Yoshioka et al., 2002).

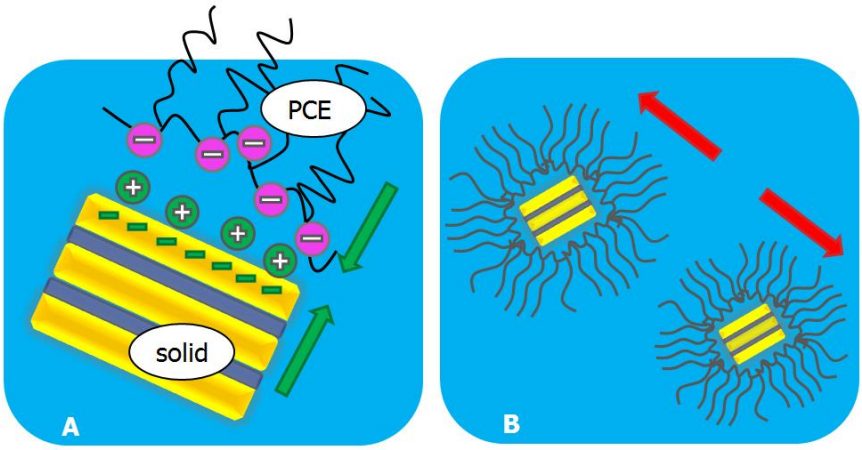

Figure 14. *Scheme of superplasticisers action in the cementitious system. A – Sorption of superplasticiser on the particle surface. B – Repulsion between cement particles.*

Table 2. Zeta potentials of cement phases

Cement phase	Zeta potentials, mV	Specific conditions	Reference
Ordinary Portland cement	+12	pH =12	Nagele et al., 1986
Ordinary Portland cement	-17	pH=13.3 (fresh HCP state)	Pointeau et al., 2006
	+20	pH=12.65	
	-8	pH=11 (degraded state)	
Ordinary Portland cement	-10	Suspension in water, high pH	Elakneswaran et al., 2009
Slag cement paste	-12	Suspension in water, high pH	
Ground granulated blast furnace slag	-35	Suspension in water, high pH	
Hydrated cement paste	-8	Suspension in water, high pH	
Ettringite	+4.15		Plank et al., 2007
Monosulfate	+2.84		
Syngenite	+0.49		
Portlandite	-4.4		
Gypsum	-0.06		
Alite	+10		Zingg et al., 2008
Alite	-10	With superplasticiser mV immediately after mixing	Yoshioka et al., 2002
Alite, belite	-5		
C-S-H	-25 - +25	As a function of the calcium concentration in solution	Viallis-Terrisse et al., 2001
C-S-H	+0.25	0.1 M KOH solution and in synthetic pore solution	Zingg et al., 2008

The values of C-S-H ζ-potential as a function of calcium hydroxide concentration in solution were reported by Viallis-Terrisse et al. (2001). It was confirmed that calcium determines the potential of the double layer at the interface with a solution (see Fig. 15). The point of zero charge is found to be around $[Ca^{2+}]$ = 2 mmol/L. When the concentrations of calcium are very low and there are no other special ions present at the surface, the silica layers are partially deprotonated (pH 10.5–11) increasing the negative surface charge and leading to an overall negative ζ-potential. When the concentration of calcium is much higher (more than 2

mmol/L), the adsorption of cations compensates the negative charge to a considerable degree, so that the absolute values of ζ-potential are lower. For the high concentration of calcium (around lime saturation, 22 mmol/L) with pH in the range of 12–12.5, the surface ionisation will be greater. Nonetheless, in the case when the calcium concentration is too high the adsorption of calcium compensates the negative surface charge and causes the reversal of the ζ-potential. This surface of positive charge is neutralised by hydroxyl ions present in the diffuse layer (in the concept of the electrical double layer, it is a second layer in which free interfacial ions are moving near the surface influenced by electrostatic attraction and thermal motion).

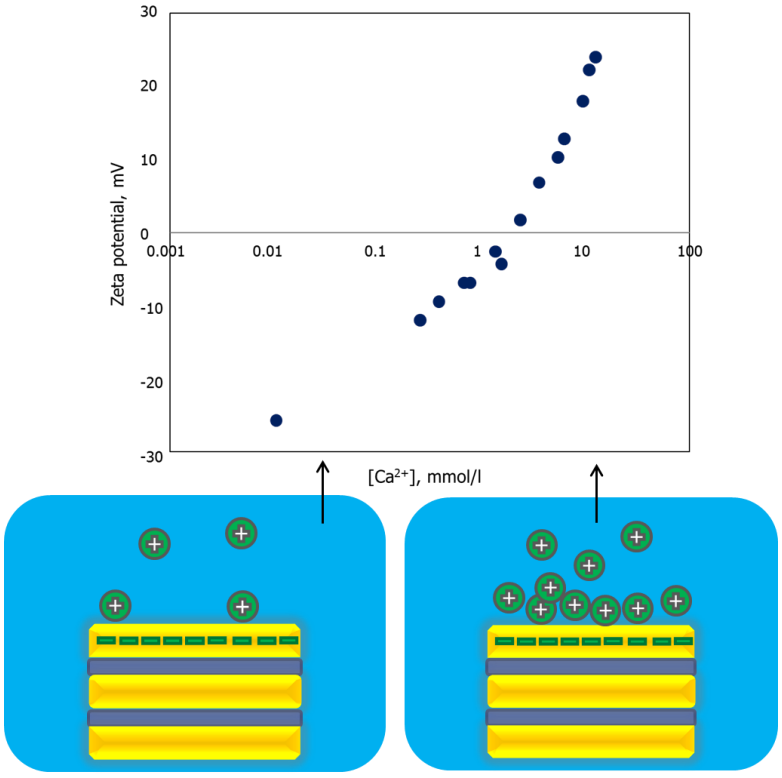

Figure 15. *Zeta potential of C-S-H phase as a function of the calcium concentration in solution (data are taken from Viallis-Terrisse et al., 2001). The schemes below illustrate the view of C-S-H surfaces at different Ca^{2+} concentrations.*

Different organic molecules may affect ζ-potentials of component minerals to a different degree. The ζ-potential of alite with superplasticisers is approximately -10 mV immediately after mixing. For other mineral phases it is approximately -15 mV. In general, with the addition of superplasticisers all component minerals are have negative ζ-potentials (Yoshioka et al., 2002). It was reported that independent of the solution, ζ-potentials of tricalcium silicate and C–S–H in synthetic pore solutions are not significantly influenced by the addition of

polycarboxylates. With increasing concentration of the additive, ζ-potential of the suspension remains constant and positive (Zingg et al., 2008).

Cement may undergo degradation when put into contact with organic acids as it was shown by Larruer-Cayol et al. (2011) on the example of oxalic, citric and tartaric acids. Organic acids form complexes with Ca^{2+} and cause significant decalcification. Also, it was observed that decalcification increases for polyacidic compounds, and it can be a good reason to take a closer look at the interaction between polycarboxylic superplasticisers and cement.

1.5. Objectives of the project

It can be concluded from the above discussion, that there exists more or less sufficient understanding of the molecular processes in the binary systems (C-S-H – U(VI); C-S-H – organic ion; organic complexing agent – U(VI)). Essentially, the next step is to move to system combinations of multiple components present in the system together. This constitutes the primary objective of the present work.

The defects in C-S-H surface silicate chains can serve as potential sorption sites for the interfacial species. This is where the computational molecular modelling becomes very helpful by providing a quantitative atomic scale picture of the interfacial interactions. The sorption of ions of interest on different surface sites is evaluated in this project.

The interactions between complexing agents and radionuclides and the processes affecting the solubilisation of radionuclides can be described by the general scheme as shown in Fig. 16 (Keith-Roach, 2008):

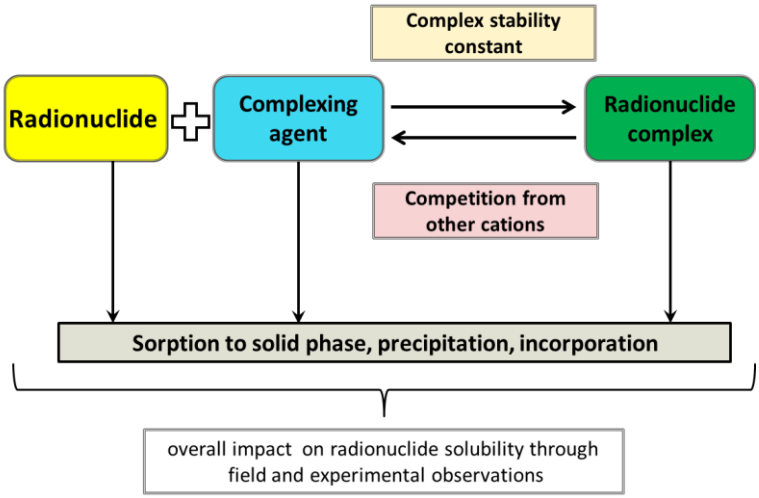

Figure 16. *The general scheme of radionuclide-admixture interaction (from Keith-Roach, 2008; with permission).*

Another important issue is that the presence of organic molecules on the surface of cementitious particles can influence the diffusion of ions to the sorption sites, and they can form complexes of different stability with metal cations present in the solution.

In the scope of this project the following principal questions can be asked:

→ How does gluconate sorb on C-S-H surfaces and how much it is different from the sorption on hydrated cement paste?

→ What is the effect of Ca/Si ratio of C-S-H on the behaviour of interfacial organic ions or how sorption properties of cement might develop in time (as a result of degradation)?

→ Does the presence of gluconate on the surface affects the adsorption of U(VI) on the C-S-H phases?

→ What could be the molecular mechanisms involved?

→ Do the same mechanisms work for more complex organic molecules, such as polycarboxylate polymer? How does it sorb and how does it affect the radionuclide behaviour?

In conclusion, the primary objective of this work is to identify and describe the most probable molecular mechanisms of interaction in the three-component model system (C-S-H/organic additive/U(VI)). The secondary objective includes the comparison of the results obtained for simplified components with the data obtained for more complex, real-life materials (polymer superplasticiser, hydrated cement paste).

Chapter 2

Materials and Methods

2.1. Experimental methods

2.1.1. Methodology

To facilitate the description of complex processes, a number of simplifications of the investigated systems are introduced. The detailed reasoning was given in Chapter 1. To sum up, cement is modelled as represented by pure C-S-H phases and its degradation is represented by varying the Ca/Si ratio (Ca/Si of 0.83, 1.0, and 1.4) of the C-S-H phase. Organic additives are studied on the example of simple gluconate ion and polymeric synthesised polycarboxylate. Out of all possible radioelements, ^{238}U is selected a model.

First, binary systems are in focus of the investigation since they provide the essential reference information for understanding the behaviour of the ternary systems (Fig. 17). A comparison between sorption on C-S-H and HCP is also done to check if the results are transferable to more realistic cement systems. The experiments on U(VI) sorption on C-S-H are performed to verify the reproducibility and to serve as a reference.

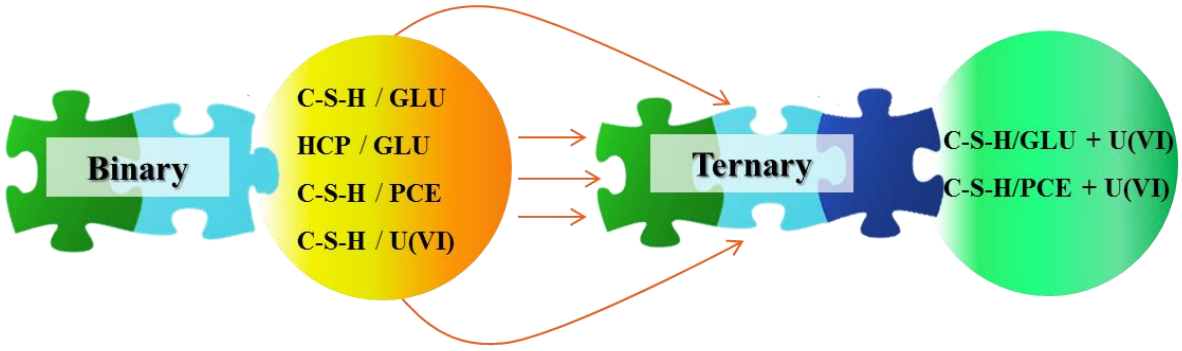

Figure 17. *Model systems.*

The ternary systems are designed to mimic the "real" processes when residual organics, present in cement pore water after the hydration process, may interact with radionuclides potentially released by the wastes. Thus, in the present experiments the C-S-H phases are equilibrated with organic components prior to their exposure to U(VI).

Eventually, four binary and two ternary systems were studied. The experimental models are summarised in Fig. 17.

2.1.2. Synthesis of C-S-H

C-S-H phases prepared by alite hydration can be inhomogeneous having local regions with different Ca/Si ratios, and also the kinetics of hydration is much slower than the kinetics of direct reaction, so pure synthetic phases were chosen for this study (Fig. 18).

Degasified water was prepared by heating (T=50°C) and steering under partial vacuum of Milli-Q® ultrapure water (>18.2 MΩ·cm). The synthesis was performed in the absence of carbon dioxide in a glove-box under inert atmosphere (argon). Synthetic C-S-H gels were prepared individually in PPCO centrifuge tubes (Nalgene™) by the direct reaction of calcium oxide (Sigma Aldrich, ≥ 99.9%) and silica fume (Aerosil® 200, Evonik) in degasified water with solid-to-water ratios of 2×10^{-2} kg/l. This method gives opportunity to obtain C-S-H gels with different Ca/Si ratios by controlling the amount of initial reagents. Three compositions of calcium silicate hydrates were synthesised corresponding to three values of Ca/Si ratio (0.83, 1.0 and 1.4) in order to be able to compare the sorption properties of pure hydrate phases and those of the degraded cement.

After an aging period of 1 month, the synthesised suspensions were centrifuged (4000 rpm, 40 min) and filtered through 0.22 μm PTFE syringe membrane filters (VWR).

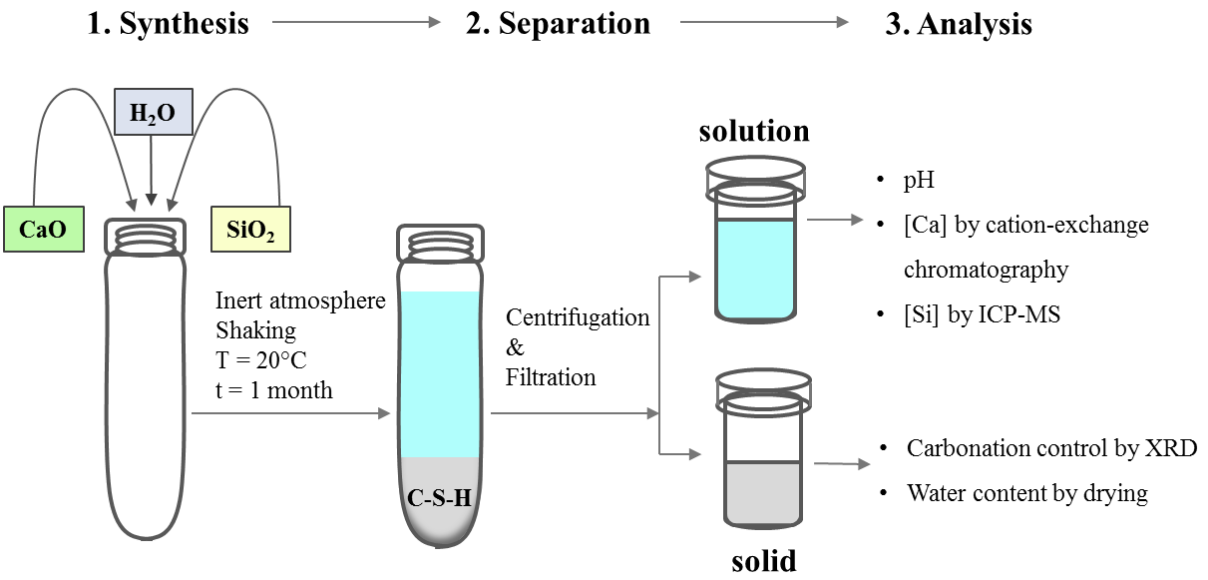

Figure 18. *The general scheme of C-S-H synthesis and characterisation.*

2.1.3. C-S-H characterisation

Synthesised C-S-H phases have to be characterised in order to obtain actual Ca/Si ratios and to control the sample for possible contaminations. Moreover, it is a validation of the obtained results with respect to the available literature data and reference information for the experiments on binary and ternary systems.

2.1.3.1. Characterisation of the solid phase

Separated solids, from samples dedicated for solid analysis, were analysed by XRD to control purity and to confirm the absence of crystalline phases such as portlandite (excess of calcium) and calcite (carbonation). Carbonation (formation of calcium carbonate) can cause significant complications in quantifying the amount of calcium that participates during the synthesis of C-S-H phases and therefore should be avoided. To limit this issue a homemade protective sealed XRD cell has been used during the sample analysis (Fig. 19). The diffractograms were registered on a D5000 diffractometer (Bruker) using Cu K_α line (λ = 1.54184 Å) in the standard Bragg-Brentano ($\theta/2\theta$) geometry (angular range: 5-51°; angular step: 0.02°; total duration: 12 hours).

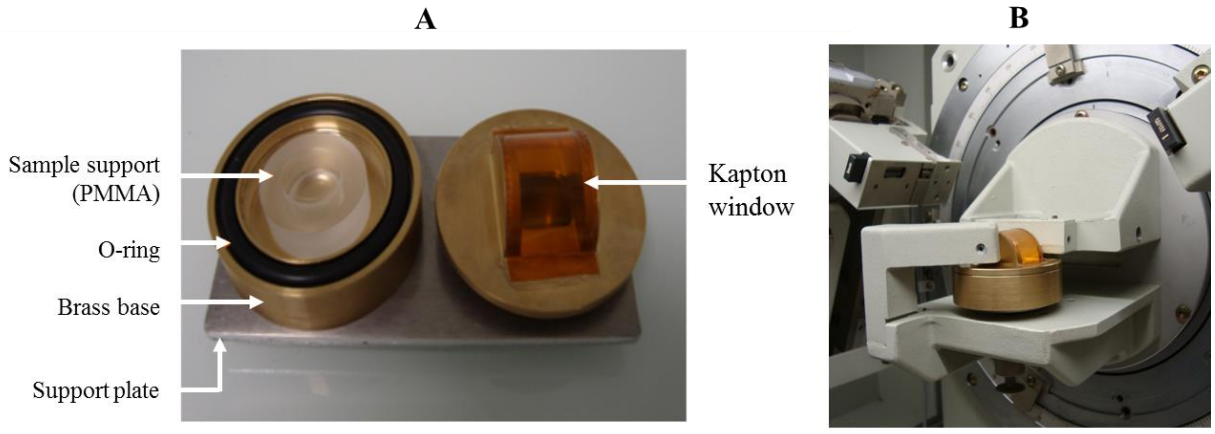

Figure 19. *Protective XRD cell for powder analysis: A – cell design; B – instrumental arrangement.*

The solids for the analysis were dried in the inert atmosphere over silica gel for 2 weeks. All C-S-H samples were prepared at the same time and conditions and only differed by their Ca/Si ratios. The resulting diffractograms were analysed with the *EVA* software (V12.0 rev0 +Diffract Plus release 2006) and compared to the reference patterns from the ICDD-PDF database. All samples show X-ray diffraction patterns typical for C-S-H phases with maxima

at 16.7°, 29.1°, 32°, and 49°. Unfortunately, the diffraction maximum at 7° related to the basal plane reflection (001) is not well defined (Fig. 20). Broad and weak diffraction peaks are characteristic of amorphous (nanocrystalline) phases and they become sharper with increasing Ca/Si ratio (more ordered structure (Grangeon et al., 2013)). It can be seen that there is a slight carbonation of the samples used for the XRD analysis. The samples were not completely dry ("soft" drying on silica gel) and the protective XRD cell could not completely assure that there is no exchange with the atmosphere during 12 hours of the data collection. The carbonation results have no impact on those C-S-H samples that were kept in the glove-box and were used for the sorption/desorption experiments.

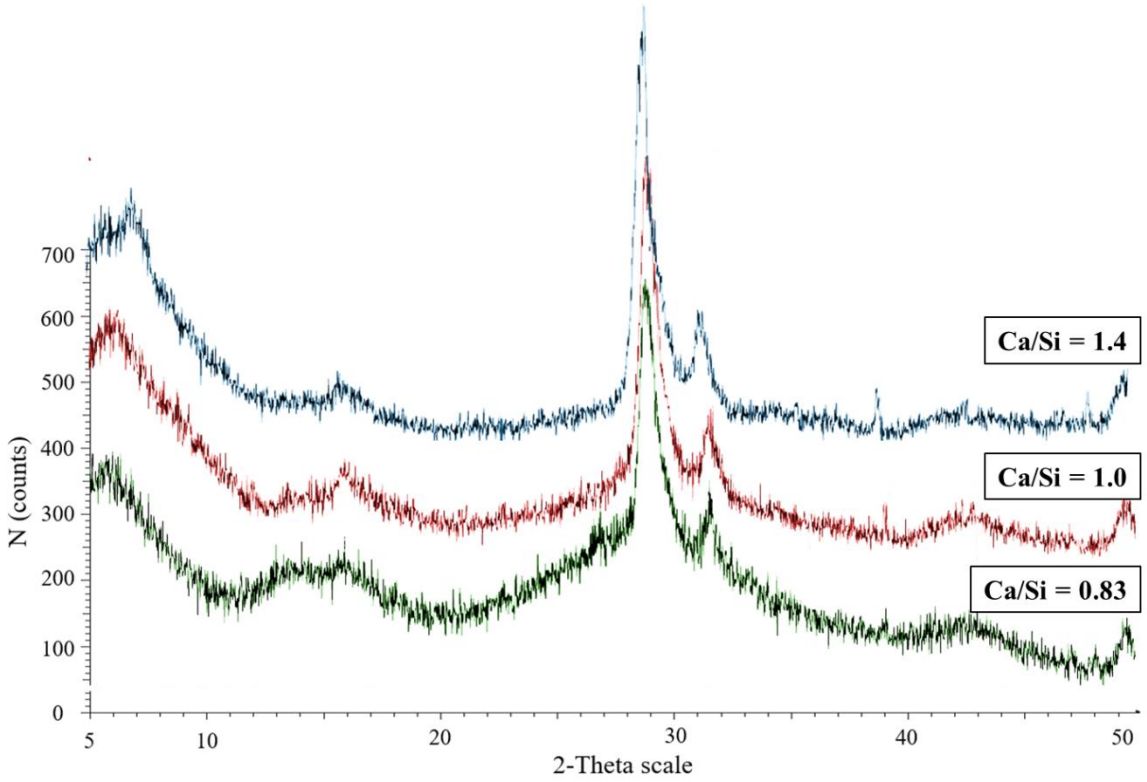

Figure 20. *XRD patterns of the solid phase of C-S-H with Ca/Si: 0.83; 1.0; and 1.4.*

The determination of C-S-H water content is a complicated task since many factors can influence the accuracy of the final results (drying conditions). The amount of water present in the synthesised C-S-H phases was evaluated by two-step drying (Table 3). First, a measured mass of the C-S-H sample was heated at T = 60 °C. The sample mass was periodically monitored until it reached a constant value. The heating at mild temperatures allows

estimating the amount of free water that does not belong to the C-S-H phase. As a second step, heating at T = 105 °C was performed.

Table 3. The C-S-H water loss during heating.

Temperature	Time, hours	Ca/Si = 0.83 m (C-S-H), g	Ca/Si = 1.0 m (C-S-H), g	Ca/Si = 1.4 m (C-S-H), g
	↓ Initial mass (wet solid) ↓			
T = 60°C	0	3.151	3.224	2.744
	5	0.382	0.374	0.354
	8	0.374	0.376	0.312
	24	0.354	0.354	0.310
	30	0.355	0.354	0.310
	48	0.355	0.354	0.311
Loss of free water:		Δ = 2.796 g	Δ = 2.890 g	Δ = 2.434 g
T = 105°C	72	0.276	0.344	0.294
	80	0.275	0.344	0.294
	96	0.275	0.344	0.294
↑ Final mass (dried solid) ↑				

The results of water loss for three C-S-H phases are presented in Table 3. The results on the free water content were further used for the calculation of liquid-to-solid ratio of the individual samples.

2.1.3.2. Solid state NMR analysis

Solid state NMR analysis of the samples was performed and interpreted at the CEMTHI Laboratory (Orléans, France). ^{29}Si MAS NMR spectra were acquired on a Bruker Advance 400 MHz (B_0=9.4 T) operating at a Larmor frequency of 79.4 MHz and with a spinning rate of 12 kHz. Each spectrum is the sum of 30,000 to 40,000 transients accumulated with a recycling delay of 10 s ensuring complete magnetization relaxation. ^{29}Si chemical shifts are given relative to tetramethylsilane (TMS) at 0 ppm. The spectra were deconvoluted using the *Dmfit* program (Massiot et al., 2002), into individual Gaussian–Lorentzian peaks, whose integration corresponded to the relative amount of differently coordinated species. This deconvolution was performed using the minimum possible number of component peaks to describe the spectrum accurately, based on the information available in the literature for cement (Colombet et al., 1998).

The ^{29}Si MAS spectra acquired for the three different C-S-H phases (chemical shift range: -70 ppm to-105 ppm) are reported in Fig. 21. They show typical patterns for C-S-H phases with several peaks varying with the Ca/Si ratio.

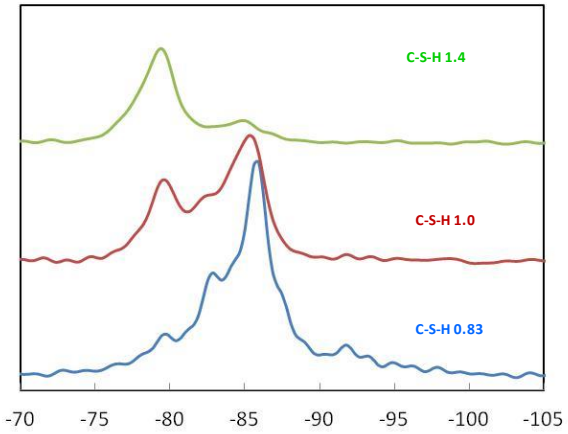

Figure 21. *^{29}Si MAS NMR spectra of the different C-S-H phases.*

The ^{29}Si chemical shifts were attributed based on the connectivity of silicon tetrahedra in the C-S-H structure as described by Roosz (2016) (Fig. 22).

Thus, five main chemical shifts are reported at -77.88, -79.5, -82.5, -84,0 and -85,0 ppm which can be related to the different polymerization degrees of silicon tetrahedra Q^{1br}, Q^1, Q^{2i}, Q^{2br} and Q^2 respectively (Fig. 23).

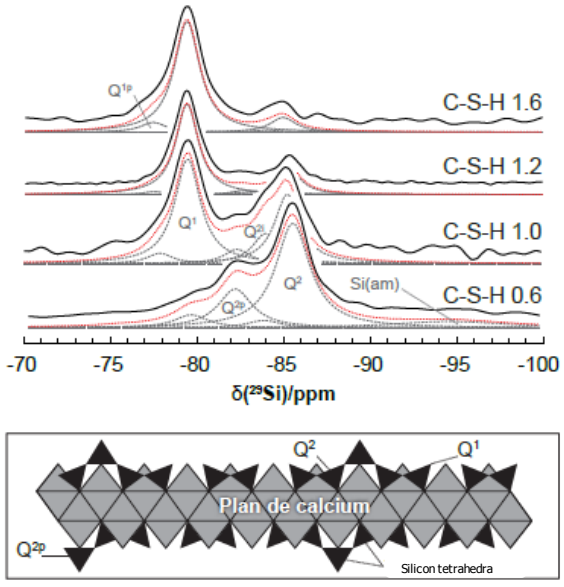

Figure 22. *Deconvolution of ^{29}Si MAS NMR spectra in C-S-H structure and silicon tetrahedra connectivity Q^n (from Roosz, 2016; with permission)*

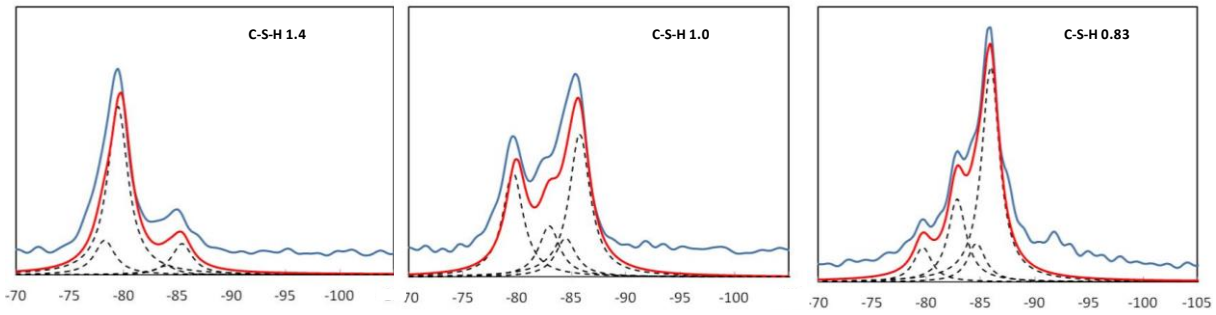

Figure 23. *Gaussian/Lorentzian deconvolution of ^{29}Si RMN spectra for each C-S-H phase: experimental spectra (blue line); individual contribution (black dashed line); calculated spectra (red line).*

The identification of the Q^1 and Q^2 tetrahedra and the absence of Q^4 related to amorphous silica (residual silica fume) show that the hydration reaction (synthesis) is fully completed. The deconvolution procedure gives the individual contributions of each Q^n tetrahedra to the total spectrum area. The ratio Q_R, $Q^1/\sum Q^n$, is an indicator of silicate chain polymerization and can also be used to estimate the Ca/Si ratio. Those data are reported in Table 4.

Table 4. Contribution of each Q^n tetrahedra and Q_R ratio for C-S-H phases.

		δ ^{29}Si (ppm)					
		-77,88	-79,5	-82,5	-84	-85	
Ca/Si	Sample	$Q1_{br}$	Q1	$Q2_i$	$Q2_{br}$	Q2	QR
0,8	C-S-H0.8		9,31	22,26	10,46	57,98	0,09
1	C-S-H1.0		30,86	15,13	11,6	42,42	0,31
1,4	C-S-H1.4	14,16	69,53		3,56	12,75	0,84

The results obtained on the samples in this work show a classical trend. As the Ca/Si ratio increases, Q^2 contributions diminish and Q^1 contributions increase, which is consistent with the depolymerisation of the silica chains and the formation of dimers for C-S-H with Ca/Si>1. Moreover, the Q_R values, obtained in this work, were compared with the data compilation of C. Roosz (Fig. 24) (Roosz, 2016).

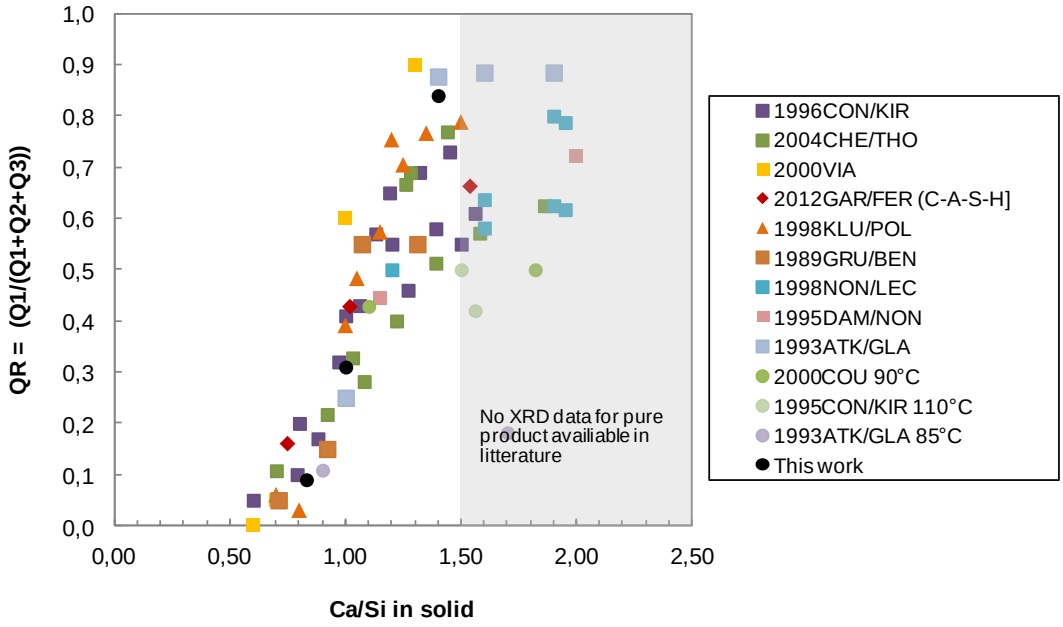

Figure 24. *Correlation of Q_R value with Ca/Si ratio in the C-S-H structure (adapted from Roosz, (2016) with permission)*

The results obtained for C-S-H phases with Ca/Si < 1, are totally consistent with what can be found in the literature and give a strong confidence in the quality of the C-S-H phases synthetized. However, as reported in Fig. 24, for Q_R values above 0.7, the correlation is not so good. The discrepancy is mostly due to the use of different protocols for the C-S-H synthesis. As a consequence, Q_R value is then much less accurate for a precise estimation of the Ca/Si ratio. Taking this into account, the C-S-H phase with Ca/Si = 1.4 in the present work is consistent with literature data.

2.1.3.2. Characterisation of the liquid phase

pH values were measured using a combined microelectrode (PHM220, Radiometer, pH range 0-14) calibrated with buffer solutions of 9.18 (pH9.180, Radiometer Analytical) and 12.45 pH (pH12.45, Radiometer Analytical) at room temperature (t = 23°C). The concentrations of Si and Ca in solutions were measured by quadrupole inductively coupled plasma - mass spectrometry (XSeries II ICP-MS, Thermo Fisher Scientific) and cation-exchange ion chromatography (ICS1000, Thermo Scientific Dionex). The equilibrium characteristics of the prepared system provide an understanding of the C-S-H structure and a correlation between pH, Ca and Si concentrations and Ca/Si ratio, as has already been described thoroughly (Chen et al., 2004; Lothenbach and Nonat, 2015).

The real Ca/Si ratios were calculated from the difference between the initial amounts of Ca and Si and the measured concentrations of these elements in the equilibrated solutions (Table 5). It was confirmed that synthesised C-S-H phases have Ca/Si ratios that correspond to the target ones and the resulting equilibrium characteristics agree well with the data available in the literature (Chen et al., 2004; Lothenbach and Nonat, 2015).

Table 5. Characterisation of C-S-H equilibrated solutions.

Ca/Si ratio (target)	pH value	[Si] equilibrated in solution, mol/l	[Ca] equilibrated in solution, mol/l	Ca/Si ratio (calculated)
0.83	10.24±0.05	$(2.68\pm0.31)\times10^{-3}$	$(1.25\pm0.12)\times10^{-3}$	0.85±0.05
1.0	11.51±0.05	$(0.42\pm0.63)\times10^{-4}$	$(2.10\pm0.12)\times10^{-3}$	0.98±0.05
1.4	12.32±0.05	$(1.70\pm0.71)\times10^{-5}$	$(11.10\pm0.12)\times10^{-3}$	1.38±0.05

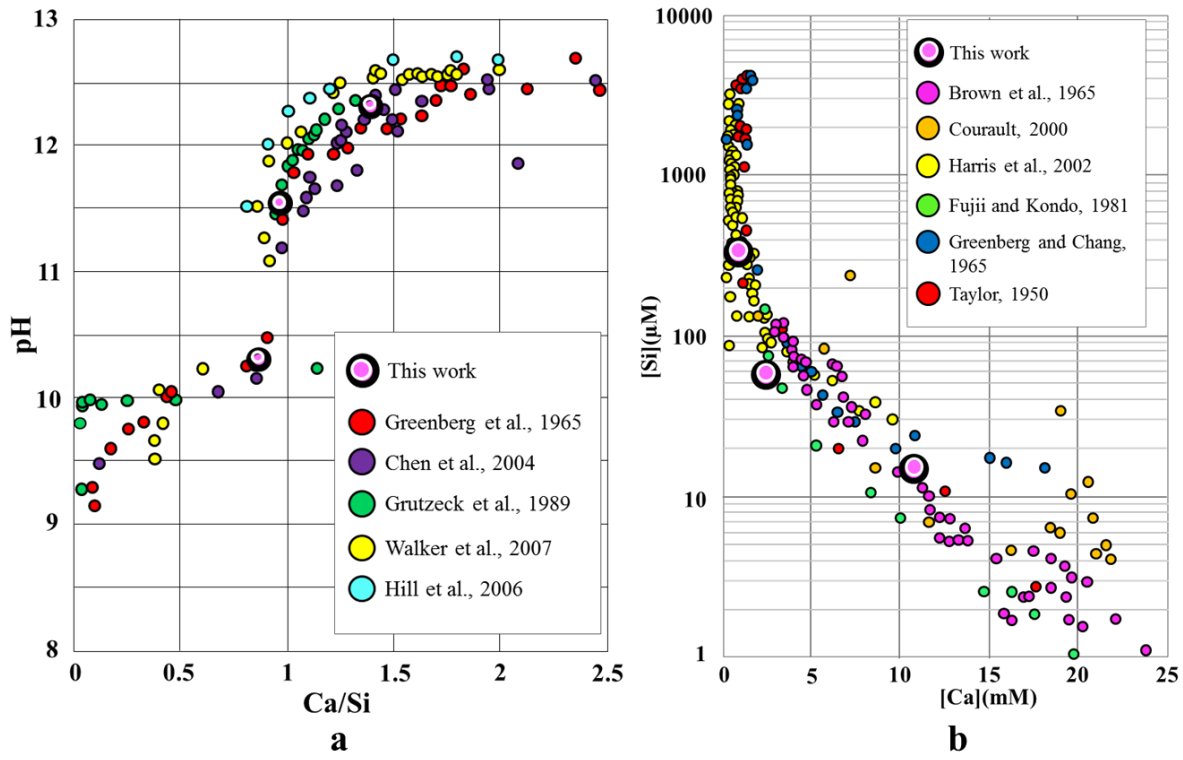

Figure 25. *Characteristics of C-S-H equilibrated solution: **a** – pH as a function of Ca/Si ratio; **b** – concentration of Si as a function of Ca concentration in equilibrated solution.*

2.1.4. Gluconate sorption on C-S-H

Gluconate uptake by the C-S-H phases was studied using classical sorption/desorption experiments. First, the kinetics of sorption was studied to get the initial understanding and to

estimate the contact time for further study of the corresponding isotherms. A sorption experiment is typically followed by a desorption experiment (kinetics and desorption isotherm).

The uncertainties of each experimental step were calculated (micropipettes, scales, ICP-MS, IC, LSC, etc.) and the error propagation formula (eq. 1.) was applied with an assumption of independent variables (Ku, 1966):

$$s_f = \sqrt{\left(\frac{\partial f}{\partial x}\right)^2 s_x^2 + \left(\frac{\partial f}{\partial y}\right)^2 s_y^2 + \left(\frac{\partial f}{\partial z}\right)^2 s_z^2 + \cdots} \quad (1)$$

where, x, y, z are variables at each experimental step with the uncertainty of s_x, s_y, and s_z respectively. The results are expressed at the uncertainty level of 95% (k = 2).

A general scheme of the gluconate sorption and desorption experiment is presented in Fig. 26.

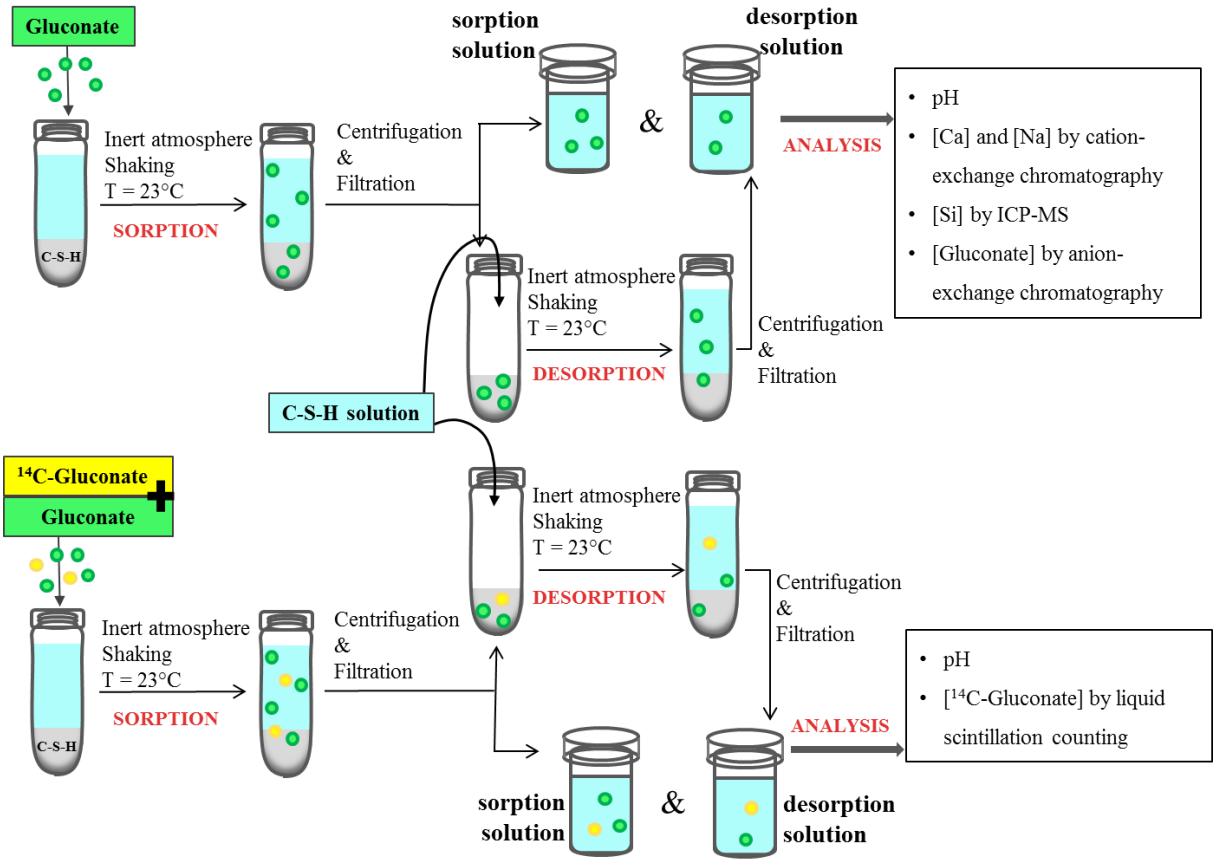

Figure 26. *The general protocol of gluconate sorption and desorption experiment.*

2.1.4.1. Sorption experiments

The sorption process is classically described by an isotherm (concentration of species sorbed as a function of species concentration in equilibrated solution). A series of batch experiments was performed to evaluate the sorption of gluconate (D-Gluconic acid sodium salt, ≥ 99%, Sigma-Aldrich) on C-S-H with various Ca/Si ratios by measuring the concentration depletion in the solution:

$$[\text{Gluconate}]_{\text{sorbed}} = ([\text{Gluconate}]_{\text{initial}} - [\text{Gluconate}]_{\text{solution}}) \text{ x} \times (V/Q(\text{Si})_{\text{C-S-H}}) \quad (2)$$

where

$[\text{Gluconate}]_{\text{sorbed}}$: concentration of gluconate on the solid (mmol/mol of Si);

$[\text{Gluconate}]_{\text{initial}}$: concentration of gluconate initially present in solution (mmol/l);

$[\text{Gluconate}]_{\text{solution}}$: concentration of gluconate in solution at equilibrium (mmol/l);

V is the solution volume (l);

$Q(\text{Si})_{\text{C-S-H}}$ is the amount of Si in C-S-H (mol);

To study a wide range of concentrations, stable and radio-labelled gluconate was used. The amount of C-S-H was estimated from the amount of Si in the solid because its estimation from water loss introduces higher uncertainties. The following formula (3) was used:

$$Q(\text{Si})_{\text{C-S-H}} = Q(\text{Si})_{\text{initial}} - Q(\text{Si})_{\text{solution}} \quad (3)$$

where,

$Q(\text{Si})_{\text{C-S-H}}$: concentration of Si in the solid (mol);

$Q(\text{Si})_{\text{initial}}$: concentration of Si initially added during C-S-H synthesis (mol);

$Q(\text{Si})_{\text{solution}}$: concentration of Si in solution at equilibrium (mol).

Sorption can be characterised by the distribution ratio (*Rd*), describing the distribution of the species of interest between the solid phase and the liquid phase in a batch sorption experiment:

$$\text{Rd (l/kg}_{\text{solid}}) = ([\text{Gluconate}]_{\text{sorbed}} / [\text{Gluconate}]_{\text{solution}}) \text{ x L/S} \quad (4)$$

where *L/S* is the liquid to solid ratio (l/kg). For the *L/S* calculation the amount of solid was estimated after drying the C-S-H samples at t = 60°C for 48 hours.

For sorption experiments, initial gluconate concentrations were in the range of 10^{-5} to 10^{-2} mol/l. Non-radioactive (stable) gluconate was analysed by DIONEX ICS-1000 ion chromatography system (IonPac AS18 hydroxide-selective anion-exchange column coupled

with a conductivity detector, see Annexe 2 The eluent consisted of a 5mM KOH solution at a flow rate of 1 ml/min. Gluconate standard solutions (D-Gluconic acid sodium salt, ≥ 99%, Sigma Aldrich) were used for the calibration curve in the range from 0.5 to 10 mg/l. An injection loop of 100 µl was used to lower the detection limit for gluconate (0.5 mg/l of gluconate).

The kinetics of adsorption was studied by measuring the evolution of gluconate concentration in the contact solution after 0.5, 1, 3, 7, 15 and 30 days of reaction (for the initial gluconate concentration of 1.03×10^{-3} mol/l). Full ion composition analysis with ion chromatography was performed for all samples to provide a complete system description. Sodium concentrations were additionally analysed for the reason that Na^+ was added to the systems as a counterion of gluconate.

2.1.4.2. Desorption experiments

The solid separated at the end of the sorption experiment was used for desorption studies (kinetics and isotherm of desorption). 25 ml of the organics-free solutions with pH and concentrations of Ca and Si defined by the C-S-H equilibrium state (Table 4) were added to the samples. The gluconate concentration at the end of the desorption step was calculated as:

$$[\text{Gluconate}]_{\text{desorption}} = [\text{Gluconate}]_{\text{sorbed}} - [\text{Gluconate}]_{\text{desorbed}} \quad (5)$$

where

$[\text{Gluconate}]_{\text{desorption}}$: concentration of gluconate on the solid at the end of the desorption step (mmol/mol of Si);
$[\text{Gluconate}]_{\text{sorbed}}$: concentration of gluconate on the solid at the end of the adsorption step (mmol/mol of Si);
$[\text{Gluconate}]_{\text{desorbed}}$: concentration of gluconate in solution at the equilibrium at the end of the desorption step (mmol/mol of Si).

The calculation of $[\text{Gluconate}]_{\text{desorbed}}$ included an evaluation of the residual amount of solution left after separation. The water content for each C-S-H phase was calculated by weight loss during drying at 60°C (see Table 3).

2.1.4.3. Liquid Scintillation Counting Analysis

Sorption of gluconate using gluconic acid isotopically labelled with ^{14}C (D-[1-^{14}C], > 99%, ARC) was studied in the range of particularly low concentrations: 10^{-9} to 10^{-6} mol/l. ^{14}C has a

half-life of 5730 years and decays by beta-emission (E_{max} = 156 keV, E_{av} = 49.44 keV) to the stable nuclide ^{14}N:

$$^{14}_{6}C \rightarrow {}^{14}_{7}N + e^{-} + \bar{\nu}_e \quad (6)$$

The equilibrated solutions were analysed by liquid scintillation counting (Tri-Carb 3170 TR/SL, PerkinElmer) in order to determine the residual amount of the radioactive tracer (see Annex 1 for more details). Ultima Gold LLT was used as an LSC cocktail. It is a multipurpose liquid scintillation cocktail for a wide range of aqueous samples. The sample-to-cocktail proportion was 1:10.

When radiotracers were added, the adsorption values were calculated from the ratio of the activity of ^{14}C in the solid phase and its activity in solution assuming an equilibrium isotopic exchange between the ^{14}C labelled and inactive gluconate in the C-S-H system:

$$C_{eq} = \frac{C_{ini} * A_{eq}}{A_{ini}} \quad (7)$$

where, C_{ini} and A_{ini} are the initial concentration and activity, C_{eq} and A_{eq} – their values in the equilibrium solution.

The difference between the actual activity of a sample and the activity measured by the instrument is caused by the process called quenching. A part of the energy is typically absorbed by the solvent and, thus, it is not registered by the scintillator. To introduce quench correction an external standard spectrum analysis was performed. The counting efficiency (ε) was evaluated to determine the activities of the samples:

$$\varepsilon = \frac{A_m}{A_0} \text{ x } 100\% \quad (8)$$

where, A_0 is the known activity of a standard solution, A_m is the activity measured by LSC. The activity in the sample (A_{sample}) is calculated by the following equation:

$$A_{sample} = \frac{A_m - A_{BG}}{\varepsilon} \quad (9)$$

where A_{BG} – background activity (cps, counts per seconds), ε – counting efficiency. For solutions of ^{14}C-labelled gluconate, the counting efficiency was (83 ± 0.5) %.

2.1.5. Gluconate sorption on HCP

Sorption and desorption of gluconate on HCP were measured in addition to the experiments with pure C-S-H phases. Hydrated CEM I (from Lafarge, Val d'Azergues factory) have been

taken for the experiment. 200 g of HCP were mixed with 800 ml of decarbonized and degasified water.

At selected conditions, the ion chromatography method was found to be unsuitable for the analysis of gluconate in HCP equilibrated solutions since the solution is rich on anions with very high retention times. So, ^{14}C-labelled gluconate was used to study the entire concentration range. The initial concentrations of gluconate were in the range from 10^{-8} to 10^{-3} mol/l.

The procedure of sample preparation and analysis was the same as for the sorption experiments on pure C-S-H phases.

2.1.6. Synthesis and characterisation of polycarboxylate superplasticiser

Polycarboxylate (PCE) is a representative of commonly used industrial superplasticiser. Since the exact composition of the manufactured product is usually not known and often masked with additional agents, it was decided to synthesise pure PCE for the current project in order to describe the mechanisms of interactions clearly.

PCE was synthesised by radical polymerization in aqueous solution following the protocol described by Plank et al. (2008) with several modifications proposed by M. Isaacs. 10 mL of deionized water, monomer, the macromonomer and chain transfer agent dissolved in 26.3 mL of deionized water were initially mixed in the reaction vessel. pH is specified at 9 and an aqueous solution of 0.25 g initiator in 1.5 mL of deionized water was added to start the polymerization (Fig. 27). The reaction was performed at 80 °C.

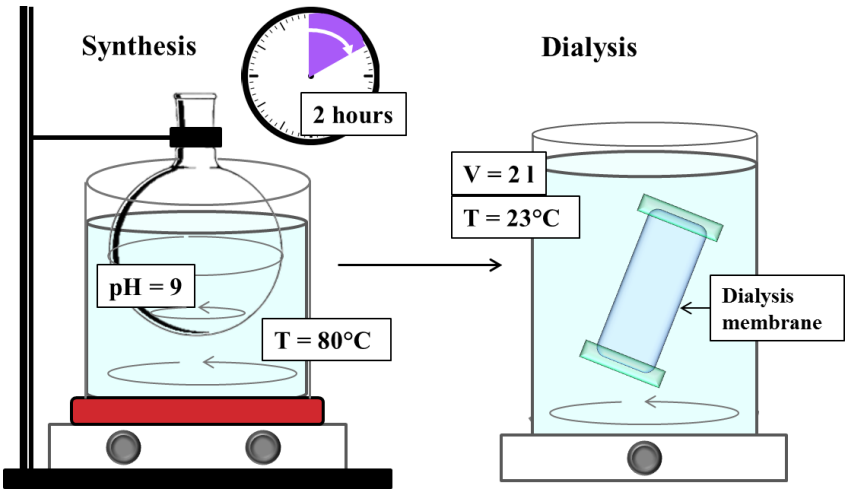

Figure 27. *PCE synthesis and the purification step.*

Reagents used:

1. ***Monomer***: sodium methacrylate (Sigma-Aldrich). The monomer is the building block of the negatively charged backbone of PCE superplasticiser.

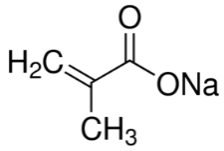

2. ***Macromonomer***: PEGMEMA, with number-average molecular mass (Mn) of 950 (Sigma-Aldrich), -CH_3 terminated. The macromonomer forms the brush-like structure of the polymer causing sterical hindrance between cement particles when sorbed.

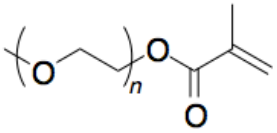

3. ***Chain transfer agent***: sodium methallyl sulfonate (MASA) (FLUKA). It is a chemical compound that possesses a weak bond that helps to transfer the growth of the polymer chain to another molecule. Often it is called regulator or modifier. It also adds a certain amount of negatively charged groups to the polymer backbone (sulfonate groups) but the small quantity used here enables to ignore the contribution.

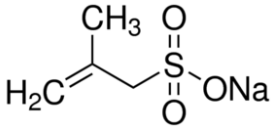

4. ***Initiator***: sodium persulfate (Sigma-Aldrich). Persulfates produce free radicals when heated and in the presence of monomers act as a polymerisation initiators to form polymer molecules.

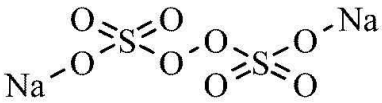

Thus, the total scheme of PCE polymerisation can be expressed like this:

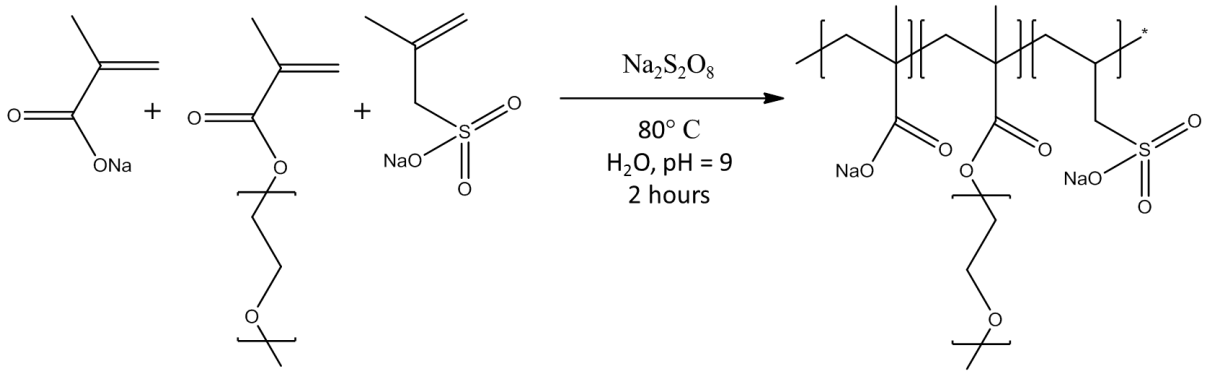

The purification was performed by dialysis tubing method using hydrophilic membranes with a typical molecular weight cut-off of 14 000 Da (dialysis tubing cellulose membrane, Sigma-Aldrich). The reaction solution was placed into the pre-washed dialysis tube and put into a large volume of distilled water (2 litres). Water was changed after 5 hours and the tube was left for another 24 hours. The dialysed polymer was collected and freeze dried as a next step.

The synthesised PCE was analysed using size exclusion chromatography (the analysis was performed by Dr. Mélanie Legros from the Institut Charles Sadron, Strasbourg, which is a CNRS unit specialising in polymer science):

Molecular mass: M_n = 33 700

M_w = 92 500

Polydispersity: M_w/M_n = 2.75

M_n is the number average molecular mass of a polymer containing N_i molecules of mass M_i, an arithmetic average of the molar mass distribution:

$$M_n = \frac{\sum M_i N_i}{\sum N_i} \tag{10}$$

M_w is the mass average molecular mass, the sum of the products of the fractional molar mass multiplied by the weigh factor. It presents the distribution of molar mass in polymer:

$$M_w = \frac{\sum M_i^2 N_i}{\sum M_i N_i} \tag{11}$$

The ratio of Mw to Mn characterises polydispersity, and the broader is the molecular mass distribution in the polymer the higher is its polydispersity.

PCE is well-soluble in aqueous solution. The concentrations of polycarboxylate are identified by Total Organic Carbon analysis (Annexe 4).

2.1.7. Sorption of PCE on C-S-H

A series of test batch experiments were performed to evaluate the sorption of synthesised polycarboxylate on C-S-H phases with Ca/Si = 1.0 and Ca/Si = 1.4 using the same procedure as for the gluconate sorption experiments described above:

$$[PCE]_{sorbed} = ([PCE]_{initial} - [PCE]_{solution}) \times L/S \quad (12)$$

The kinetics of adsorption was studied by measuring the evolution of polycarboxylate concentration in the contact solution after 1, 3, 7, 14, 28 days of reaction. The initial PCE concentration of 0.77 g/l was used in the experiment.

For sorption experiments, the initial PCE concentrations were in the range of 0.01 to 10 g/l. The samples were left to equilibrate with regular shaking for a period of one week. After that, they were centrifuged and the solution was separated and filtrated. pH was measured following a standard protocol.

In parallel, high solubility of PCE in aqueous solution was studied and confirmed: with the highest concentration used for adsorption experiment ([PCE] = 10 g/l) no precipitation was observed after 1 week.

The concentrations in solution were analysed by Total Organic Carbon (TOC) analysis (Shimadzu TOC-V_{CSH} analyser with non-dispersive infrared detector). To measure the sample concentration, a correlation between the total carbon concentration and peak area (calibration curve) is predetermined using a standard solution. Subtracting the inorganic carbon concentration, measured by the analyser, from the total carbon concentration, determines the total organic carbon concentration. Samples with lower polymer concentration that required less dilution were neutralised by H_3PO_4 titration as required for the TOC analysis.

2.1.8. Uranium (VI) sorption on C-S-H

C-S-H with Ca/Si = 1.4 was used for the U(VI) sorption experiment. Figure 28 presents the general approach of the experiment. The initial concentrations in sorption experiments were in

the range of 10^{-5} to 10^{-2} mol/l. Mother solution of $^{238}U(VI)$ (from CERCA, Areva) had initial concentration of 0.181 mol/l in HCl 0.01 mol/l. For each concentration, an appropriate volume of ^{238}U solution in 10^{-2} mol/l hydrochloric acid was added to the C-S-H suspension. A contact time of 2 weeks was used. The range of concentrations was selected following the protocol given by Tits et al. (2011), to avoid the major formation of a U(VI) precipitate ([U] < 10^{-2} mol/l). Similar to the gluconate study, full ion analysis (U, Si, Ca, pH) was performed and the concentrations of U(VI) were measured using ICP-MS.

A series of batch experiments were performed to evaluate the sorption of $^{238}U(VI)$ on C-S-H with various Ca/Si ratios by ratios by measuring the concentration depletion in the solution:

$$[U(VI)]_{sorbed} = ([U(VI)]_{initial} - [U(VI)]_{solution}) \times L/S \quad (13)$$

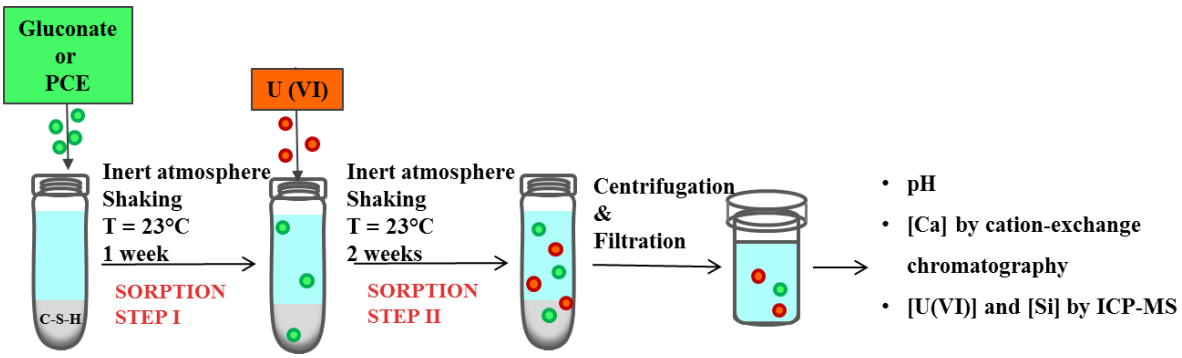

Figure 28. *Scheme for the ternary system experiment.*

To study the interaction mechanism of U(VI) with C-S-H phases in the presence of organic molecules two ternary systems were developed. The experiment with the ternary system containing gluconate ion was performed in parallel to the study of U(VI) on C-S-H without the organic additives. C-S-H with Ca/Si = 1.4 was selected to study both ternary systems. First, C-S-H has been equilibrated with gluconate of a defined concentration (0.35 mM) for 1 week (based on the results of adsorption kinetic study) prior to the addition of the Uranium(VI). The prepared "binary" C-S-H was further used to study the isotherm of adsorption of U(VI). The same protocol was applied to the system involving polycarboxylate. The general scheme of the ternary system experiment is presented in Fig. 28.

2.2. Computational methods

2.2.1. Molecular dynamics simulations

2.2.1.1. Method introduction

In general, computational modelling can be used on different length and time scales as it is represented by the scheme in Fig. 29. Molecular modelling allows mimicking and interpretation of the processes that are happening on the time scale from femtoseconds to hundreds of nanoseconds (~10^{-15} – 10^{-7} s; i.e., on the scale characterising molecular vibrational, rotational, and slow diffusional motions) and on the length scale from Angstroms to tens of nanometers (~0.1 – 100 nm; i.e., from the scale of individual chemical bonds to almost macroscopic scale of nano- and micro-particles). There are two main techniques that can be applied for that: quantum mechanics and molecular mechanics (Fig. 29).

In quantum mechanics (QM) simulations electrons are explicitly taken into account and thus a study of chemical reactions becomes possible. Quantum calculations are computationally very demanding and are often performed for a relatively small number of atoms and molecules. As discussed above, C-S-H gels have disordered structure and larger system sizes are necessary in order to realistically model the behaviour of these materials. In most cases, this makes use of quantum simulations for C-S-H interfaces computationally prohibitively expensive, if not completely impossible.

Molecular mechanics (MM, empirical force-field-based method) considers the model system considering as consisting only of atoms. Different from QM, the electronic structure of the system is empirically modeled by distributions of partial atomic charges, and the interactions between atoms in MM are described in a simplified way, such that each molecule is seen as a system of atoms of certain masses and charges connected by spring-like bonds. This system can move in space, rotate and vibrate according to the forces acting between atoms and described by a set of empirical functions often collectively called a “force field”.

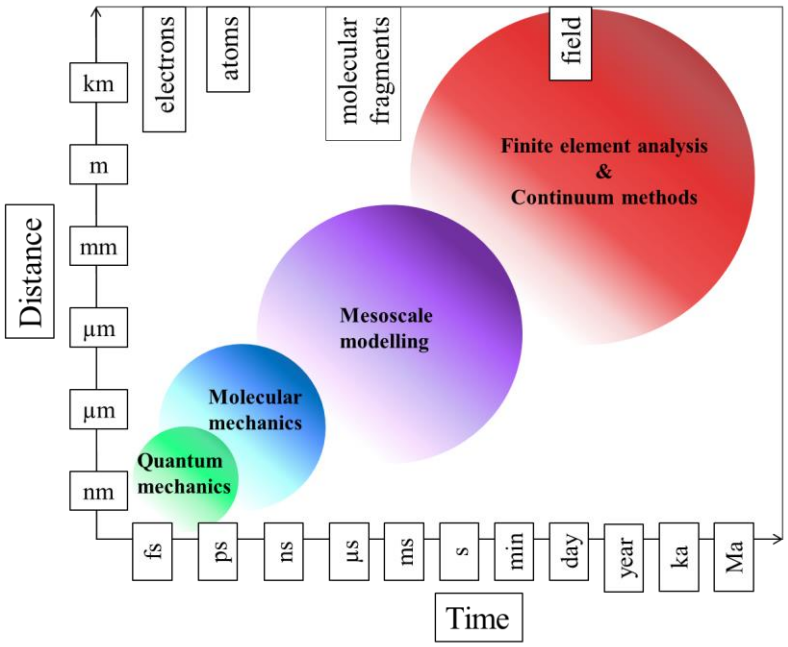

Figure 29. *Computational modelling methods.*

Classical molecular dynamics computer simulation is a method in which Newton's equations of motion are numerically solved for a system of interacting atoms:

$$\mathrm{F_i} = \mathrm{m_i a_i} = \mathrm{m_i} \frac{\mathrm{d^2 r_i}}{\mathrm{dt^2}} \tag{14}$$

$$\mathrm{F}_i = -\frac{\mathrm{d}}{\mathrm{dr}_i}\mathrm{U(r}_i) \tag{15}$$

where F_i and a_i are functions of the position of the atom i at every instant, m_i is the mass of the atom, $U_i\ (r)$ is potential energy of its interaction with other atoms in the system. The simulation data in the form of dynamic trajectories of all atoms in the system can then be analysed with the help of statistical mechanics in order to obtain many molecular properties of the system.

Molecular modelling allows interpretation of the observed interfacial behaviour on the atomic and molecular scale considering the effects of the structure and composition of the surface on the interaction. Thus, molecular dynamics can be a bridge between theoretical hypotheses and experimental observations.

2.2.1.2. Building C-S-H models

The realistic atomistic description of a C-S-H phase is much more challenging than a description of common crystalline phases. Numerous experimental studies (neutron scattering (Allen, 2007), ^{43}Ca NMR (Bowers and Kirkpatrick, 2009), ^{29}Si NMR (Brunet et al., 2004), XRD, TEM, EXAFS (Grangeon et al., 2013)) suggested that the crystal structure of tobermorite is one of the closest to real cement hydrate. The unit cell parameters and atomic coordinates of tobermorite-11 Å (Hamid, 1981) were used as the basis of our models.

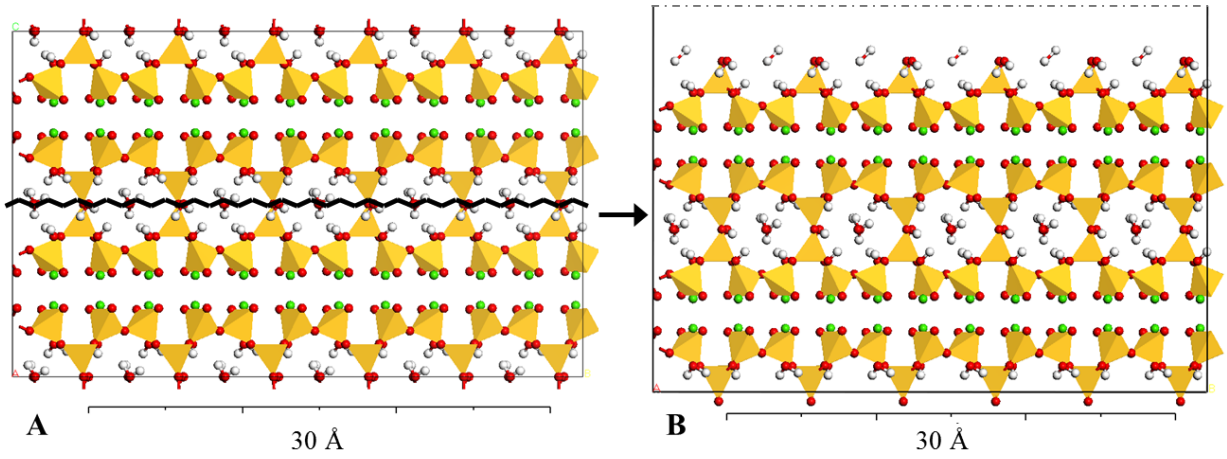

Figure 30. *The building of C-S-H surface. A – supercell (6 x 6 x 1) of tobermorite-11 Å; B – cleaved surface along (0 0 1) plane. Colour scheme: yellow – Si tetrahedra, red – O, green – Ca, white – H.*

The simulation supercell was then formed by unit cell multiplication along *x* and *y* crystal axes. The size of the system is chosen in such a way that the introduced defects would not create an excessively ordered regular pattern when periodic boundary conditions (PBC) are applied. In PBC, the modelled system is described as a unit cell infinitely replicated in all three dimensions in space, and thus surrounded by an infinite number its self-images. At the same time, the system should be relatively small to require reasonable computational time to calculate its properties. As a result, four C-S-H models with approximately 40 × 40 Å^2 surface areas were constructed.

The bulk tobermorite supercell of 6 × 6 × 1 (40.2 × 44.4 × 22.5 Å^3) was then cleaved along the (0 0 1) crystallographic plane – a typical cleavage plane for tobermorite (in the middle of interlayer) to create a basic model of the C-S-H surface which was then further modified to construct models of C-S-H surfaces with various Ca/Si ratios. Since the surface is the primary object of interest in our study it was decided that only the top layers of the cleaved crystal

(those in direct contact with the model solutions) would be modified to produce the required Ca/Si ratios, leaving the initial stoichiometric tobermorite in the middle of the model structure (Fig. 30). The statistical accuracy of the calculated properties is improved by a factor of two through the creation of identical defects on the two cleavage surfaces of C-S-H.

The model structures with different Ca/Si ratios can be constructed in two ways (Fig. 31) by randomly removing silica tetrahedra from the crystalline tobermorite structure (using the data from ^{29}Si MAS NMR studies for C-S-H as a guidance (Cong and Kirkpatrick, 1996; Beaudoin et al., 2009) and by introducing additional Ca^{2+} cations into the interlayer.

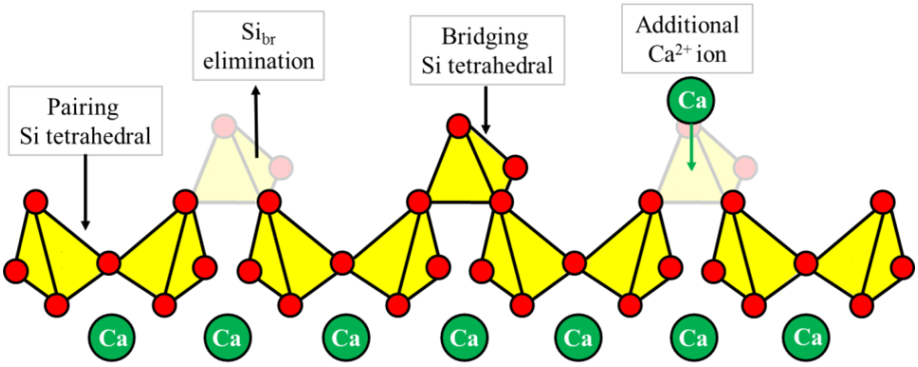

Figure 31. *The scheme of Ca/Si ratio modification of the tobermorite fragment.*

To achieve higher Ca/Si ratios, bridging tetrahedra were extracted randomly taking into account that a dimer is the most abundant of all silicate species in C-S-H and a linear pentamer is the second most abundant (Richardson et al., 2010; Sáez del Bosque et al., 2016). The formation of defects in the silicate chains can result in extra adsorption of water molecules at the surface. At the same time, H_2O dissociation in reactive media leads to the formation of additional hydroxyl groups on the surface and protons that bind at the sites of missing silicon tetrahedra. Different cases of surface site protonation (Churakov et al., 2014) should be considered since they can result in the accumulation of different surface charge (see Fig. 32).

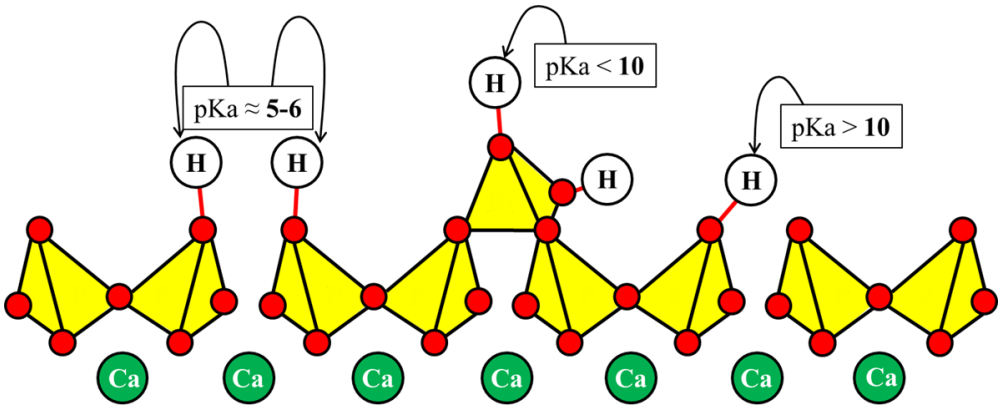

Figure 32. *Different types of silanol groups on C-S-H surface and their intrinsic acidity constants (Churakov et al., 2014).*

Aqueous hydroxyl ions were added to the system in order to maintain the total electrostatic neutrality of the models. For the C-S-H model with the lowest Ca/Si ratio, all silanol groups of bridging Si and one of the pairing Si (replacing the introduced defect) were deprotonated; for the C-S-H models with high Ca/Si ratio, all of the surface silanol groups were deprotonated. The deprotonated oxygens of the surface were assigned a higher partial charge (q = -1.3|e|) than the protonated ones, following the atomistic models of kanemite (Kirkpatrick et al., 2005). Aqueous hydroxyl ions were added to the system in order to maintain the total electrostatic neutrality of the models. Three dimensional periodic boundary conditions were applied to the constructed model interfaces, and for each Ca/Si ratio three such interfaces were simulated: C S H/water, C-S-H/uranyl solution, and C-S-H/gluconate solution..

Most interatomic interaction parameters, including the partial atomic charges for C-S-H, H_2O, and Ca^{2+} ions were taken from the ClayFF parameterization (Cygan et al., 2004) and its later modifications for cement systems (Kirkpatrick et al., 2005; Kalinichev et al., 2007). The interaction parameters for uranyl ions used in this work (Guilbaud and Wipff, 1993, 1996) are also consistent with ClayFF (Teich-McGoldrick et al., 2014). For organic gluconate, the GAFF set of parameters was used (Wang et al., 2004).

2.2.1.3. Force field choice

The inter- and intra-molecular forces are defined by the force field which is a set of functions and parameters that together specifies potential energy of interatomic interactions in the system. The total potential energy of the system is expressed as a sum of all individual contributions from several types of terms (Fig. 33):

$$\mathbf{E_{total}} = E_{Coul} + E_{VDW} + E_{bond\ stretch} + E_{angle\ bend} + E_{torsion} + E_{improper} + E_{out\text{-}of\text{-}plane} \quad (16)$$

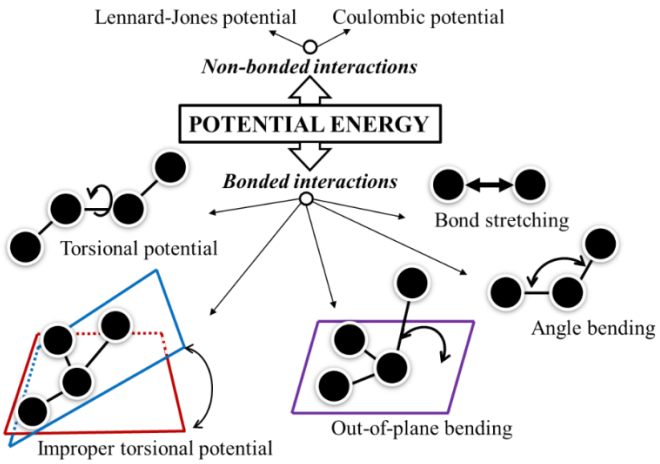

Figure 33. *Main contributions to a MM force field.*

These parameters are empirical and they are typically obtained through fitting experimental data (usually various spectroscopic or diffraction results) and/or using quantum chemical calculations. The parameters derived from experimental data for small molecules can be further extrapolated (transferred) to larger molecules with similar atomic structures. The results of molecular modelling strongly depend on the choice of the force field and its accuracy for a given problem. One of the primary difficulties in simulating mineral-organic systems is defining a force field that is consistent with the interactions between minerals and organics (Freeman et al., 2007).

ClayFF (Cygan et al., 2004) is an empirical force field developed and used for mineral and mineral-like water-solid interfaces and has been successfully applied for simulations of cement materials (Kalinichev and Kirpatrick, 2002; Kalinichev et al., 2007; Kumar et al., 2007; Shahsavari et al., 2011; Kalinichev, 2014). In ClayFF only oxygen-hydrogen and oxygen-uranium bonds are explicitly defined (bond-stretch and angle bending terms), all other interactions are treated as non-bonded and quasi-ionic (defined only by electrostatic and van-der-Waals terms).

In ClayFF the partial charges of atoms are used rather than full formal charges (see Table 5). Parameters for uranyl atoms are taken from Guilbaud and Wipff (1993, 1996). They are defined through quantum mechanical calculations and represent empirical parameters that are used to fit the potential energy surface due to the actual electron structure of the system.

Table 6. Atom types and their partial charges in ClayFF (Cygan et al., 2004).

Atom species and force field notations	Charge/e-
Water hydrogen (h*)	0.41
Water oxygen (o*)	-0.82
Bridging oxygen (ob)	-1.05
Oxygen of hydroxyl group (oh)	-0.95
Oxygen of aqueous hydroxyl (oh-)	-1.41
Deprotonated oxygen of silanol group (onb)	-1.358
Tetrahedral silicon (st)	2.1
Octahedral calcium (cao)	1.36
Interlayer calcium and aqueous calcium ion (Ca)	2.0
Hydrogen of hydroxyl group (ho)	0.425
Uranium in uranyl ion (uo)	2.5
Uranyl oxygen (ou)	-0.25

Electrostatic interactions are calculated by the Coulomb law:

$$E_{Coul} = \frac{e^2}{4\pi\epsilon_0}\sum_{i\neq j}\frac{q_i q_j}{r_{ij}} \quad (17)$$

where q_i and q_j are the partial charges of the atoms, r_{ij} – separation distance between the charges (i and j). For calculation of short-range repulsion and longer-distance dispersive attraction (often called the van der Waals term) the Lennard-Jones (12-6) function is commonly used:

$$E_{VDW} = \sum_{i\neq j} D_{0,ij}\left[\left(\frac{R_{0,ij}}{r_{ij}}\right)^{12} - 2\left(\frac{R_{0,ij}}{r_{ij}}\right)^{6}\right] \quad (18)$$

where $D_{0,ij}$ (energy parameter) and $R_{0,ij}$ (distance parameter) are empirical constants. When interaction between a pair of unlike atoms is calculated, D_0 for this pair is defined through the geometric mean rule and R_0 through the arithmetic mean rule (Lorentz-Berthelot mixing rules):

$$D_{0,ij} = \sqrt{D_{0.i}D_{0,j}} \quad (19)$$

$$R_{0.ij} = \frac{R_{0,i}+R_{0,j}}{2} \quad (20)$$

H_2O molecule, the hydroxyl group and the uranyl ion bonds in ClayFF are additionally explicitly defined by simple bond-stretch and angle-bend harmonic terms:

$$E_{\text{bond stretch (ij)}} = k_{bs}(r_{ij} - r_0)^2 \quad (21)$$

$$E_{\text{angle bend (ijk)}} = k_{ab}(\theta_{ijk} - \theta_0)^2 \quad (22)$$

where, k_{bs} and k_{ab} are force constants, r_0 and θ_0 are equilibrium values of the bond and angle, respectively. Between the explicitly bonded atoms electrostatic and VDW interactions are assumed to be excluded.

Based on the recent study of clay-organic force field combinations (Szczerba and Kalinichev, 2016), it was decided to use the general AMBER force field (GAFF, Wang et al., (2004)) for the description of gluconate and its interactions with the C-S-H surface. GAFF contains parameters for a wide variety of organic molecules composed of different types of atoms (C, H, O, N, P, S, halogens), and it is highly consistent with ClayFF in its functional form. When an organic molecule is included in the model system, additional potential energy terms are used to describe its intra-molecular motions and interactions. Figure 34 shows the structure of the gluconate molecule with its bonds and angles that require special force field parameters. $E_{torsition}$, $E_{improper}$, $E_{out\text{-}of\text{-}plane}$, typical terms for organic molecules, are added here to the general energy expression. The "torsion" (also known as "dihedral") angle energy parameter defines intramolecular rotations:

$$E_{torsion} = \sum \frac{V_n}{2}(1 + \cos(n\varphi - \gamma)) \quad (23)$$

The "improper angle" term has the same functional expression as torsion, and it is used to ensure the planarity of the defined functional groups (e.g. deprotonated carboxyl group of the gluconate ion).

SPC (simple point charge) model for H_2O molecules was used as in the original ClayFF. In GAFF partial charges on atoms are assigned by the restrained electrostatic potential fit model (RESP).

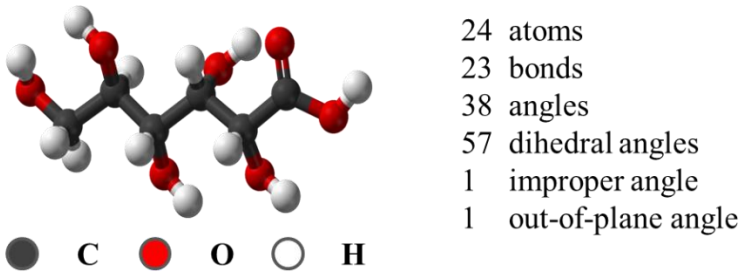

Figure 34. *The ball and stick model of gluconate and its structural characteristics.*

2.2.1.4. General simulation protocol

A molecular dynamics simulation is generally divided into three stages: initialisation, equilibration, and production. The first step is to define initial positions and velocities for all atoms in the simulation box. Once this is set, the system equilibration is necessary in order to bring the simulated molecular system to the required state of thermodynamic equilibrium.

The standard distance cut-off of 15 Å was used to calculate short-range Lennard-Jones interactions to the potential energy. Long-range electrostatic forces were evaluated by means of the Ewald summation method. Materials Studio software package (BIOVIA, San Diego, CA, USA) was used to prepare the simulation models and to visualise the results, but all large-scale equilibration and production MD runs were carried out with the LAMMPS (Plimpton, 1995) and NAMD (Phillips et al., 2005) software packages.

The structural models cannot be considered as thermodynamically equilibrated from the beginning. So, as the first step geometry optimisation of each model structure was performed using the Polak-Ribiere version of the conjugate gradient algorithm of energy minimization with tolerance thresholds of 10^{-6} kcal/mol for energy and 10^{-8} kcal/mol-Å for forces. Thus optimised structures were then used in molecular dynamics (MD) simulations. The Verlet leapfrog algorithm was used to numerically integrate the equations of motion with a timestep $\Delta t = 1$ fs. In the leapfrog scheme the velocity (v) is defined at half steps ($\delta t/2$) while the positions (r) are defined at whole steps of δt (Verlet, 1967):

$$v(t + \delta t) = v\left(t - \frac{\delta t}{2}\right) + a(t)\delta t \tag{24}$$

$$r(t + \delta t) = r(t) + v\left(t + \frac{\delta t}{2}\right)\delta t \tag{25}$$

The selected timestep ensures a reasonable accuracy and numerical stability of the integration algorithm.

Severe artefacts may occur in the system if the nonbonded long-range interactions have an abrupt cut-off. To avoid such behaviour, Ewald summation approach was used. It is a computational algorithm to accurately determine the contributions to the potential energy due to the long-range electrostatic interactions in the system with periodic boundary conditions. It uses the expression that is a sum of Coulomb terms in direct (real-space) and reciprocal space, and three (sometimes four) correction terms. The point charges are represented as a Gaussian charge density (exponential decay).

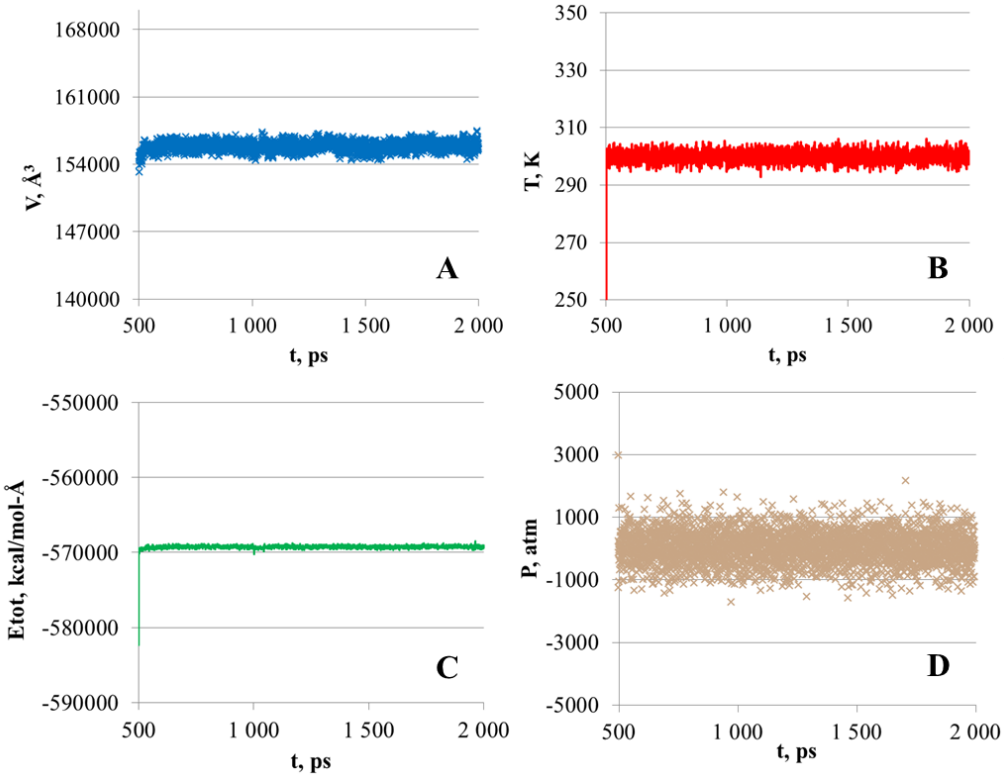

Figure 35. *An example of parameter monitoring during equilibration stage: A – cell volume, B – temperature; C – total potential energy; D – pressure.*

During the pre-equilibration MD run performed for each model system, several parameters were carefully monitored: individual components of the potential energy, density, stabilisation of system atomic configuration (Fig. 35). Once these parameters attained their stable values, the system was considered to reach a required thermodynamic equilibrium and the main MD production run could be started. All simulations were run for 2 ns (*NPT*-ensemble) after an equilibration period of 1 ns (*NVT*-ensemble). In the *NPT*-ensemble (isothermal–isobaric

ensemble), number of atoms (*N*), pressure (*P*), and temperature (*T*) are conserved using a Nose/Hoover temperature thermostat and Nose/Hoover pressure barostat (Nosé, 1984; Hoover, 1985). In the *NVT*-ensemble (canonical ensemble), number of atoms (*N*), volume (*V*) and temperature (*T*) are kept constant. Ambient conditions (T = 300 K, P = 0.1 MPa) were assumed in all MD runs.

2.2.2. Simulation analysis

2.2.2.1. Atomic radial distribution functions and coordination numbers

Calculation of radial distribution functions (also known as pair distribution functions or pair correlation functions) helps to describe local structural properties of the studied systems, particularly liquids and solid-liquid interfaces. It shows a normalised probability of finding an atom (A) at a certain distance (r_{AB}) from another atom B (Fig. 36).

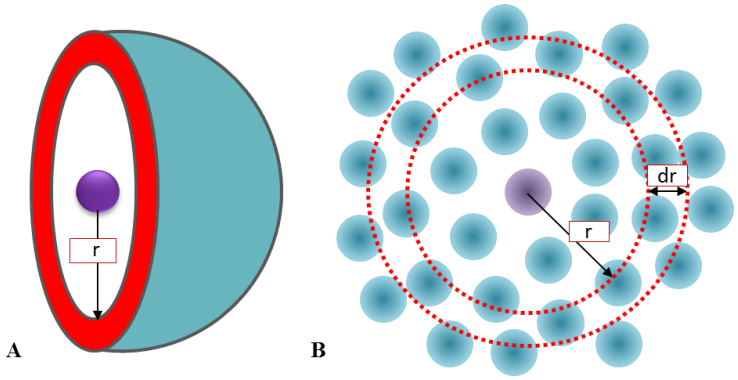

Figure 36. *Radial distribution function: schematic spherical shell (A) and its 2D projection (B).*

To calculate the radial distribution function (RDF) for a pair of atomic types in the system from an MD-generated trajectory, the distances between all possible pairs of these atoms are sorted into distance bins (dr) and averaged over the total simulation time and over all pairs of such atoms in these atoms.

In other words, quantitatively, RDF (g(r)) is a dimensionless function that shows a normalized probability of finding an atom (A) at a distance (r_{AB}) from another atom (B) compared to a completely random distribution of atoms in space (e.g., in ideal gas):

$$g_{AB}(r_{AB}) = \frac{\bar{N}_{AB}}{4\pi\rho_B r_{AB}} \quad (26)$$

where $\bar{N}_{AB}$ is an average number of atoms B at the distance r_{AB} from the atom A, ρ_B is the number of atoms B per volume unity (number density). The calculated results can be usually compared with experimental data from X-ray or neutron diffraction measurements (if available), which provide experimentally measured structure factors of the system that can be Fourier-transformed into the corresponding RDFs.

Integration of the given RDF provides the running coordination number. It is an average number of atoms B within a sphere of a defined radius r_{AB} from atom A:

$$n_{AB} = 4\pi\rho_B \int_0^{r_{AB}} g_{AB}(r) r^2 dr \quad (27)$$

In our case, the most important RDFs were characterizing the local structural environments of Ca^{2+} and UO_2^{2+} (when present) cations and various oxygen species: oxygens of H_2O, of solution OH^- groups, protonated and deprotonated silanol groups of the surface, oxygens of the carboxyl and hydroxyl groups of gluconate molecules, and uranyl oxygens. These functions provide time-averaged information on the composition of the first solvation shell of the ion and help to evaluate the strength of their complexation or adsorption to a studied substance or surface.

The solvation shell is the shell composed of the solvent and present dissolved chemical species that surround a selected atom or molecule. If the solvent is water, the shell is often called hydration shell.

2.2.2.2. Atomic density profiles

The structure of solutions at a solid-liquid heterophase interface can give an insight into the nature of interactions between species of interest and their spatial distribution within the interface.

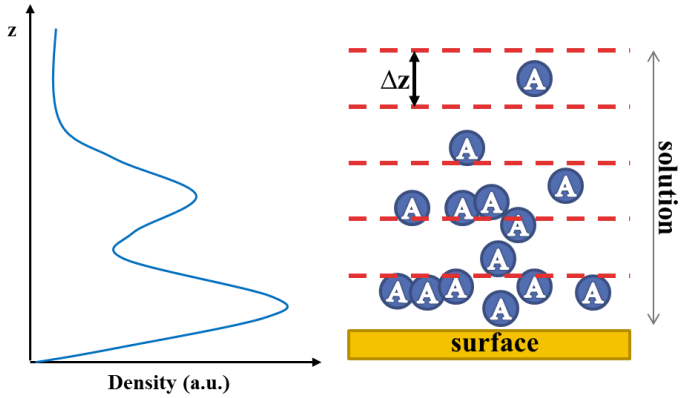

Figure 37. *Calculation of atomic density profiles.*

Calculation of atomic density profiles in the direction perpendicular to the surface is done through evaluation of the average number of atoms of a certain type ($\bar{N}_A$) found, on average, at a certain distance z (i.e, within the range of distances from z to z+Δz) parallel to the surface (Fig. 37):

$$\text{density}_A\,(z) = \frac{\bar{N}_A(\Delta z)}{V} \tag{28}$$

where *V* is the total system volume.

In this work, the atomic density distributions were typically calculated through the statistical analysis of 2000 atomic configurations in thermodynamic equilibrium for the systems without organic molecules and 4000 configurations in the presence of gluconate. The consecutive configurations were separated in time by 0.5 ps and selected from the entire length of the equilibrium production MD run.

2.2.2.3. Surface atomic density maps

The distribution of atoms can also be analysed within a layer of solution parallel to the surface at a certain distance from the surface (two-dimensional distribution in the xy plane). These distributions are defined by the probability of finding an atom of type A at a position (x,y) above the surface within a range of distances from z to (z+Δz):

$$\text{surface density}_A\,(x,y) = \bar{N}_A(\Delta x \Delta y) \tag{29}$$

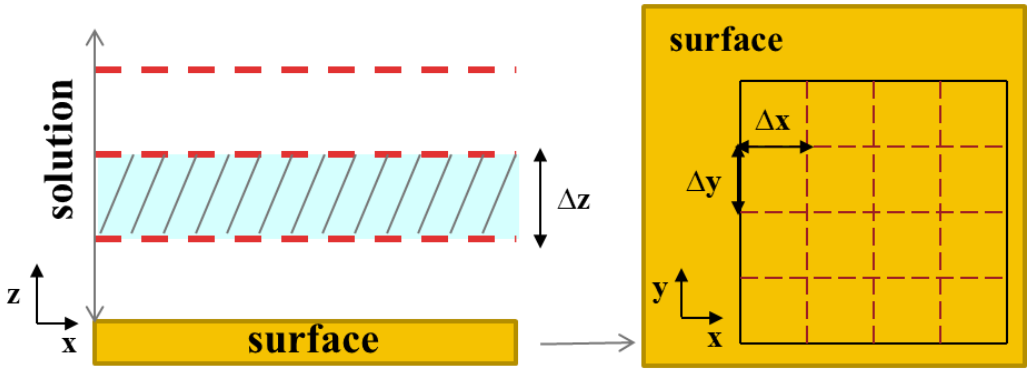

Figure 38. *The scheme of a surface density map calculation.*

This type of trajectory analysis allows determining preferential sorption sites of solution species of interest. As in the case of atomic density profile calculations, the surface density maps in this study were typically calculated through the statistical analysis of 2000 equilibrium atomic configurations for the systems without organic molecules and 4000 configurations in the presence of gluconate.

The consecutive configurations were separated in time by 0.5 ps and selected from the entire length of the equilibrium production MD run.

2.2.2.4. Potentials of mean force and the calculations of adsorption free energies

Free energy (F) can be evaluated when the canonical partition function (Q) of the system is known:

$$F = -\frac{1}{\beta}\ln Q \tag{30}$$

with $\beta = 1/k_B T$, where k_B is the Boltzmann constant and T is absolute temperature. The canonical partition function (NVT ensemble) can be obtained through the integration over the phase space of the system:

$$Q = \int \exp[-\beta U(r)] d^N r \tag{31}$$

where U(r) is the potential energy, N is a number of degrees of freedom.

The change of free energy is the driving force of any process, such as a chemical reaction. In the case of sorption processes, the differences in free energy between different states of the system (surface-ion) along a distance coordinate can quantitatively characterise the strength of

sorption sites of interest. Free energy is related to the probability distribution along the reaction coordinate. When reaction coordinate (x) is defined, the energy calculation takes the form:

$$F(x) = -\frac{1}{\beta}\ln\frac{\int \delta(x(r)-x)\exp((-\beta U)d^N r)}{\exp((-\beta U)d^N r)} \quad (32)$$

F(x) also is known as the potential of mean force (PMF). In computer simulations, direct phase-space integrals cannot be accurately calculated, instead, time averaging is used assuming that the system is ergodic (so, P(x) = Q(x)):

$$P(x) = \lim_{t\to\infty}\frac{1}{t}\int_0^t \rho\big(x(t')\big)dt' \quad (33)$$

where *t* is time, *ρ* is a number of appearances of *x* in the given reaction interval. As a result, a statistical analysis of an MD simulation trajectory enables the calculation of free energy changes in the system.

For our practical application, the NAMD open source code (Phillips et al., 2005) was used to perform umbrella sampling (biased MD simulation method) and the simulation results have then been processed by the WHAM algorithm (Kastner, 2011) to calculate the potential of mean force, thus providing a free energy profile of adsorption along the selected coordinate (in our case – normal to the surface).

The umbrella sampling algorithm was initially developed by Torrie and Valleau (1974; 1977). Its practical implementation using the weighted histogram analysis method (WHAM) was later developed by Ferrenberg and Swenden (1989) and further generalised by Kumar et al. (1992). The umbrella sampling method uses the molecular configurations from MC or MD computer simulations to determine the probability for the system to be in a given conformation or a structural state. With this method, it is possible to overcome high energy barriers and to perform sampling of unfavourable atomic configurations of the system with statistical accuracy which otherwise would not be possible.

The energy barriers along the reaction coordinate can make a process of sampling very difficult, thus, an additional term of potential energy can be added to ease the transition across the barrier. The total PMF calculation in our case consists of a series of individual MD runs during which a selected ion is restrained at a certain distance from the surface within a

defined range of distances (window). In each simulation window, this distance is restrained at its required value using a harmonic restraint, $U_{bias}(x)$, to allow the system to sample all possible configurations at that particular reaction coordinate. At each time step during the simulation, the force required to keep the molecules at the constraint distance was defined (typically, k = 100-250 kcal/mol- Å^2 for 1.0 Å < x < 6.0 Å; k = 25-100 kcal/mol- Å^2 for 6.0 Å < x < 15.0 Å). The biasing potential is described by the formula:

$$U_{bias}(x) = k(x - x_0)^2 \quad (34)$$

where x_0 – target distance; k – force constant.

$$P(x) = \frac{\sum_{i=1}^{Nsim} n_i(x)}{\sum_{i=1}^{Nsim} N_i exp([F_i - U_{bias,i}(x)]/k_B T)} \quad (35)$$

$$F_i = -k_B T ln\{\sum_{xbins} P(x) exp[-U_{bias,i}(x)/k_B T]\} \quad (36)$$

where N_{sim} is number of simulations, $n_i(x)$ is number of counts in the histogram bin associated with x, $U_{bias,i}$ and F_i are the biasing potential and the free energy shift from simulation, $P(x)$ is the estimate of the unbiased probability distribution. A detailed description of the umbrella sampling and WHAM algorithms used here can be found elsewhere (Kastner, 2011).

PMF calculations were applied here to obtain a quantitative description of the adsorption free energy profiles of Ca^{2+} and UO_2^{2+} cations as a function of their distance from the C-S-H surfaces of varying Ca/Si ratios and at the interfaces with aqueous solutions of various compositions using the recently developed approach (Loganathan and Kalinichev, 2017). A complete calculation requires a number of separate simulations. For each PMF curve obtained, approximately 60-70 biased MD simulations were run in NVT ensemble (T = 300 K) for 1000 ps time. All MD simulations at defined windows are independent thus they could be run in parallel.

Before the WHAM code has been applied, all histograms of the simulation series had been carefully monitored to ensure adequate and relatively uniform sampling of the reaction coordinate as it shown in Fig. 39. The sampling windows had sufficient overlaps with each other ensuring proper recovering of the unbiased PMF curve from the ensemble of the histograms. PMF calculations strongly depend on the way the umbrella sampling is performed and artefacts may occur if data in a particular window are missing or insufficient (Souaille and Roux, 2001).

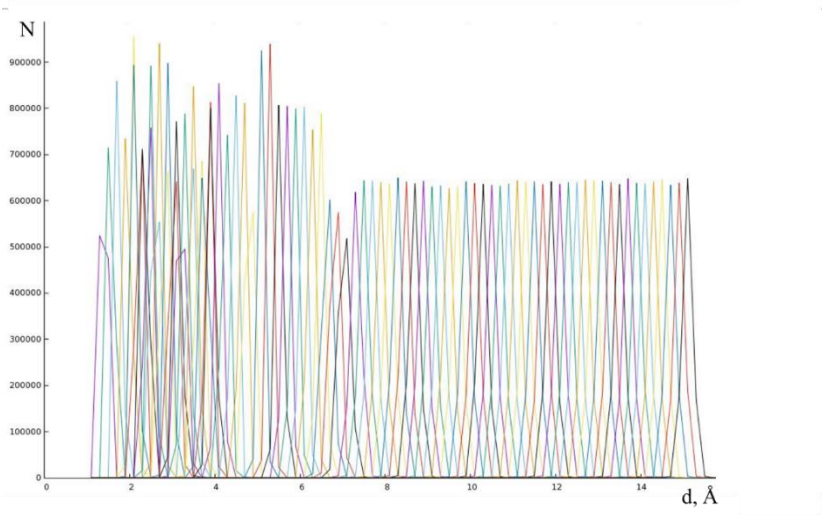

Figure 39. *The typical histogram of umbrella sampling.*

The *z* distance between the ion of interest and the C-S-H surface was constrained. The constraint distances were probed from 1 to 15 Å with a step of 0.2 Å.

To keep the atom at defined sorption site and not to allow its significant drift in directions parallel to the surface, an additional xy constrain was applied as a "soft cylindrical wall" of a defined diameter, as shown in Fig. 40 (Loganathan and Kalinichev, 2017). No additional force restraint has been applied in this case.

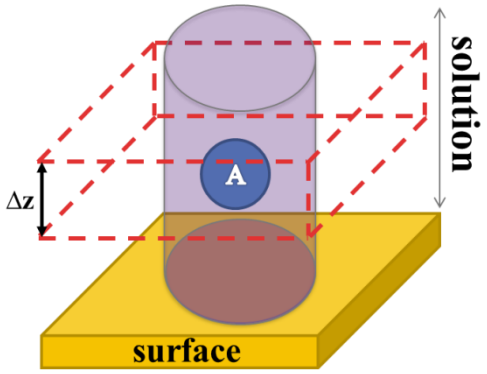

Figure 40. *Schematical presentation of constrains for PMF calculations.*

The free energy of adsorption strongly depends on the surface structure and composition. The PMF between ions of the solution (Ca^{2+}, UO_2^{2+}, gluconate) and C-S-H surfaces were calculated for several specific adsorption sites identified during the previous unconstrained MD simulations. The reference atoms were selected in such a way that the centre of mass was

located in the projection of the atom of interest on the surface where zero is defined as the average z-coordinate of deprotonated oxygens of the pairing tetrahedra. Practically, the biasing potential applied was different for every sorption site studied; its value was continuously monitored and adjusted during the umbrella sampling simulations to achieve the desired level of statistical accuracy.

Chapter 3

Results and Discussion: Experimental Study

3.1. Gluconate sorption on C-S-H

3.1.1. Sorption experiments

3.1.1.1. Kinetics of gluconate adsorption

The kinetics of gluconate adsorption on C-S-H has been studied and Figure 41 shows the measured evolution of gluconate concentration in supernatant solution with time for an initial concentration of 1.03×10^{-3} mol/l. Full tabulated results for this and other experiments can be found in the Annex 5. For all selected C-S-H compositions the adsorption of gluconate was relatively fast, with the reactions almost completed within 1 day and reaching a steady state in 3 days. Thus, the contact time of 3 days for isotherm studies was selected for all C-S-H phases studied. Also, it has been shown that Ca/Si ratio affects the gluconate uptake but does not affect the kinetic rates of sorption.

Quantitatively, more gluconate was adsorbed on C-S-H with Ca/Si = 1.4 than on the other two compositions. Fast kinetics is generally interpreted as evidence of surface sorption when the adsorption is limited by electrostatic interactions. Assuming that C-S-H should be the main responsible phase of gluconate uptake, the obtained kinetic results can be compared with the ones from Glaus et al. (2006). In their work, it was shown that a steady state is reached after 1 day of equilibration and the difference in gluconate equilibrium concentration in solution for 1 and 3 days stays in the range of measurement uncertainties.

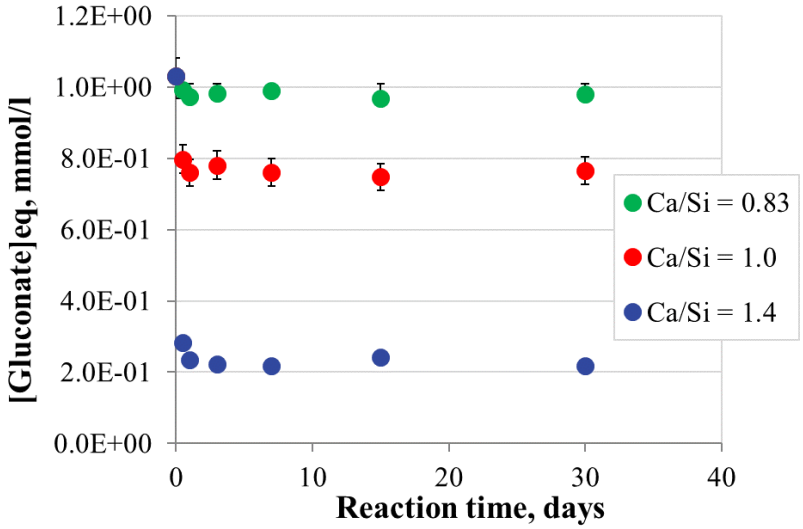

Figure 41. *The kinetics of gluconate adsorption on C-S-H phases with three Ca/Si ratios (0.83, 1.0, 1.4), S/L = 20 g/l.*

3.1.1.2. Isotherms of gluconate adsorption

Figure 42 presents combined results of two sorption experiments performed with ^{14}C-labelled gluconate for the range of very low concentrations and with stable gluconate for higher concentrations. The results expressed as a log[Gluconate]$_{solid}$ / log[Gluconate]$_{solution}$ show the influence of the Ca/Si ratio on the gluconate adsorption by C-S-H phases. For three Ca/Si compositions studied, the sorption gradually increases in the entire concentration range used, and the higher the ratio the higher the sorption is. The lowest adsorption was observed for C-S-H with Ca/Si = 0.83. The sample with Ca/Si = 1.4 showed stronger adsorption of gluconate than the one with Ca/Si = 1.0. The data overlap demonstrates good reproducibility of the results obtained with two different analytical techniques (IC and LSC).

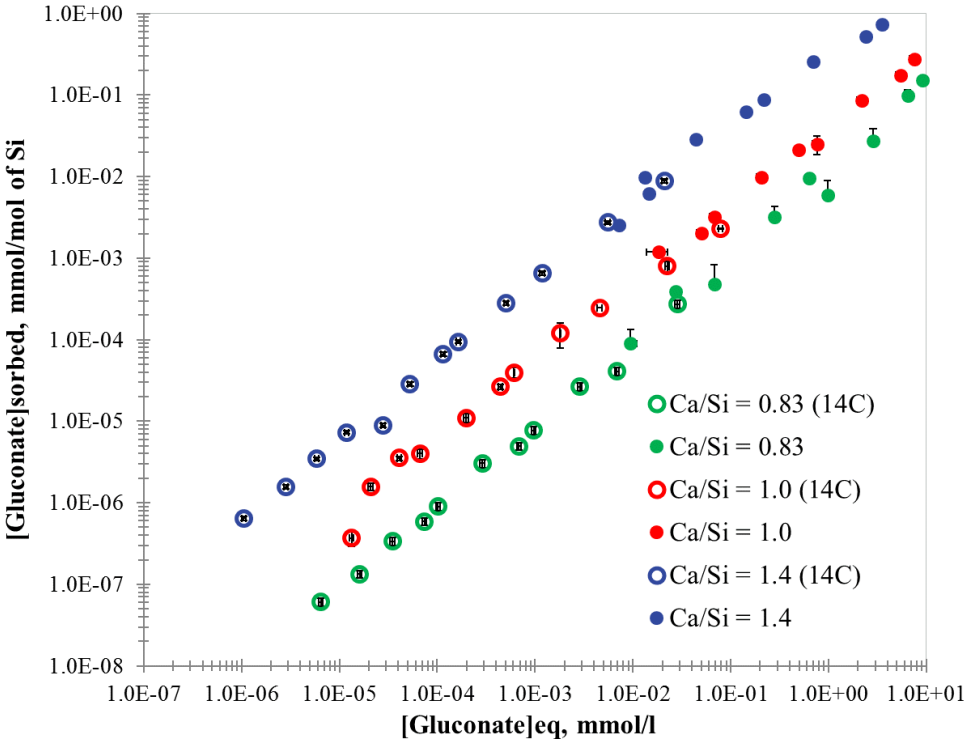

Figure 42. *The isotherms of gluconate adsorption for C-S-H phases with three Ca/Si ratios (0.83, 1.0, 1.4), S/L = 20 g/l.*

The isotherms of adsorption in the low concentration range tend to be linear and the trends are similar for all C-S-H compostions studied. Linear sorption often can be an indication of the existence of only one type of preferential sorption sites or the existence of several sites with equal probability of adsorbate attraction. Linear sorption is the first stage of gluconate sorption process, further saturation of sites causes a decrease in gluconate uptake by C-S-H

phases. The saturation stage can be easier identified (C-S-H with Ca/Si = 1.4) when the isotherm is expressed as Rd (l/kg) as a function of $[Gluconate]_{solution}$.

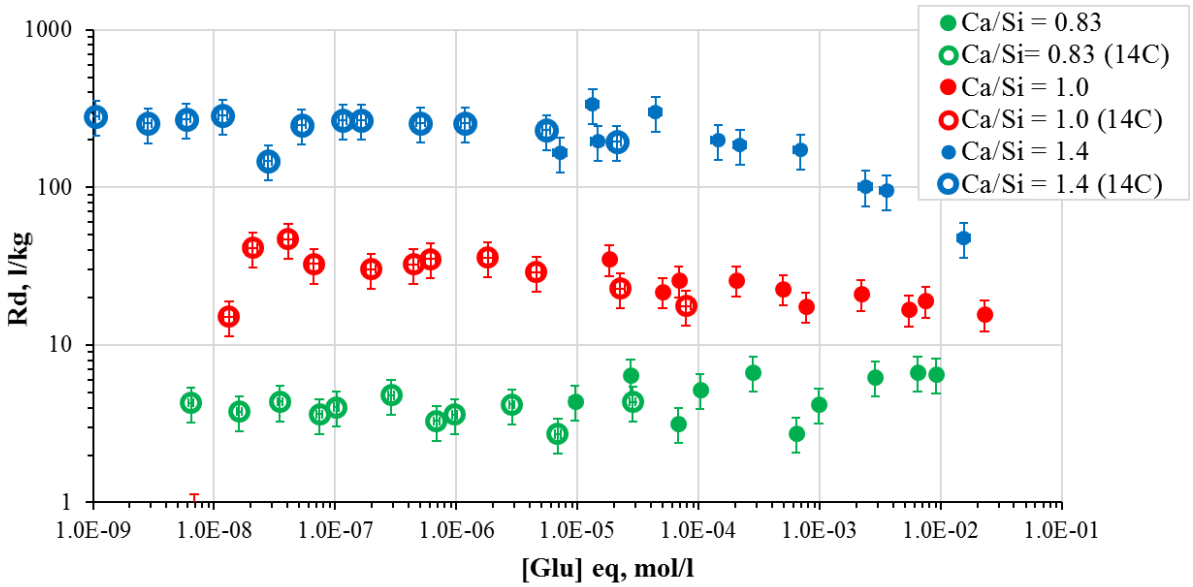

Figure 43. *The distribution ratio (Rd) for gluconate adsorption on C-S-H phases with three Ca/Si ratios.*

The distribution coefficients (Rd) were calculated with the maximum Rd value of approximately 285, 40, and 4.5 l/kg for C-S-H samples with Ca/Si = 1.4, 1.0, and 0.83, respectively (Fig. 43). The saturation of sorption sites can be clearly identified: the Rd values are decreasing at high gluconate loadings for the C-S-H sample with the highest Ca/Si (1.4). The saturation of other C-S-H phases studied has not been observed at the selected experimental conditions.

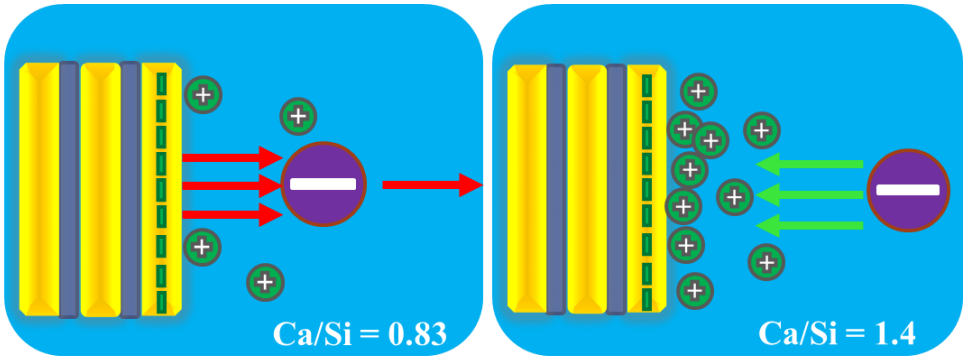

Figure 44. *The mechanism of gluconate/C-S-H interaction. Yellow bricks – C-S-H particles, green circles – Ca^{2+} cations, violet cirle – gluconate anion.*

The gradual increase in the amount of gluconate sorbed on C-S-H can be explained by electrostatic interactions between the adsorbate and the C-S-H surface (Fig. 44). As it has been already mentioned, with the increase of Ca/Si ratio, the surface charge changes from negative to positive due to Ca^{2+} overcharging (Viallis-Terrisse et al., 2001; Jonssön et al., 2005; Labbez et al., 2011).

At the same time, the nature of the interacting organic functional groups plays a very important role in the adsorption. In alkaline solutions, gluconate is deprotonated and exists in the form of a negatively charged ion (pKa of the gluconate carboxyl group is 3.86), so its adsorption would be mostly driven by electrostatic forces. The rapid kinetics of adsorption also validates this assumption: a steady state is reached only after one day of contact.

Furthermore, it has been shown by Pallagi et al. (2013; 2014) that in highly alkaline solutions gluconate anions bind Ca^{2+} cations to form different types of complexes. In their study, multinuclear complexes containing more than one molecule of gluconate were suggested as dominant (Fig. 45). Nevertheless, the concentrations of gluconate used here are far too low to observe such complexation, taking into account that the highest initial gluconate concentration was 0.01 M (20 times lower than in the work of Pallagi et al. (2014)).

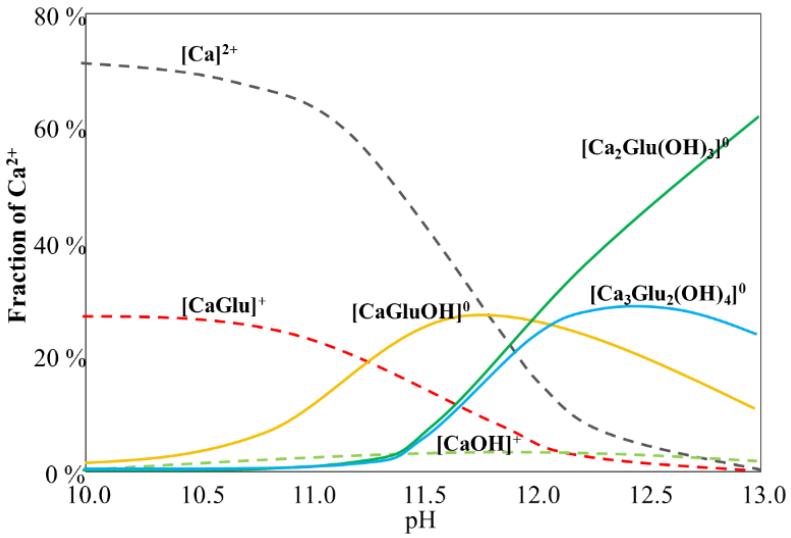

Figure 45. *The species distribution diagram for Ca-gluconate system ($[Ca^{2+}]$ = 0.06 M; $[Gluconate^{-}]$ = 0.19 M) as a function of pH (image taken from Pallagi et al., 2014).*

For a complete description of the studied systems, a full cation and anion analysis was performed for each sample: pH, [Ca], [Si], [Gluconate], [Na]. No change in pH values was

observed for all C-S-H phases studied (see Annexe 5). The results for major cations are presented in Fig. 46. No significant changes in concentration were observed. The addition of gluconate within the selected concentration range does not affect the Si content in the C-S-H solution in the stable state. The results of [Si] evolution agree with conclusions made by Nalet and Nonat (2016) that D-gluconate does not show strong complexing abilities with silicate cations. At the same time, as expected, higher gluconate concentration causes a slight increase in Ca concentration due to the strong complexation.

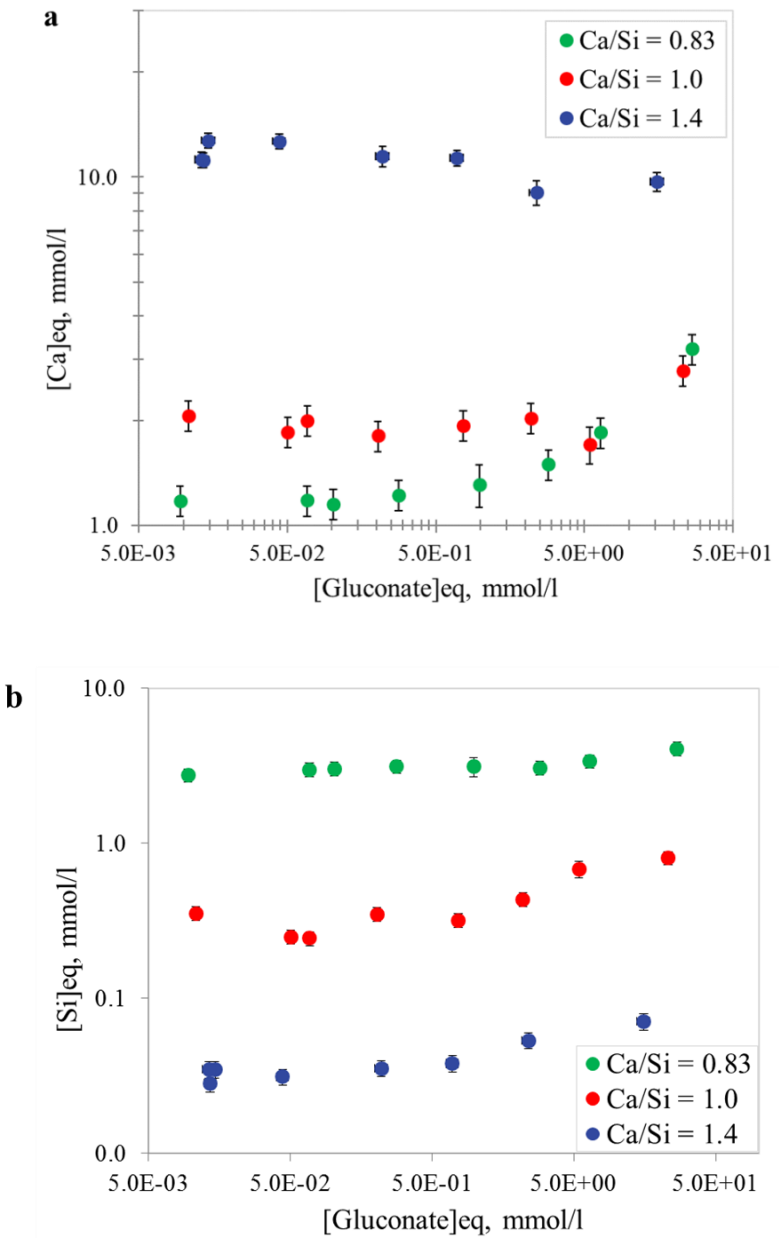

Figure 46. *The evolution of Ca (**a**) and Si (**b**) concentrations in the C-S-H equilibrated solution as a function of gluconate concentration at steady state.*

3.1.1.3. Influence of sodium on gluconate sorption

Sodium was added to the system as a counterion of gluconate (sodium salt of gluconic acid). A separate experiment was performed to investigate if its presence can affect the adsorption processes in the C-S-H/gluconate binary system.

The experiment on adsorption of inactive gluconate on C-S-H phases with various Ca/Si ratios was repeated following the same protocol. The results of these repeated expeirments of gluconate adsorption (named Na experiment here) agree with the previous study reported in Fig. 47.

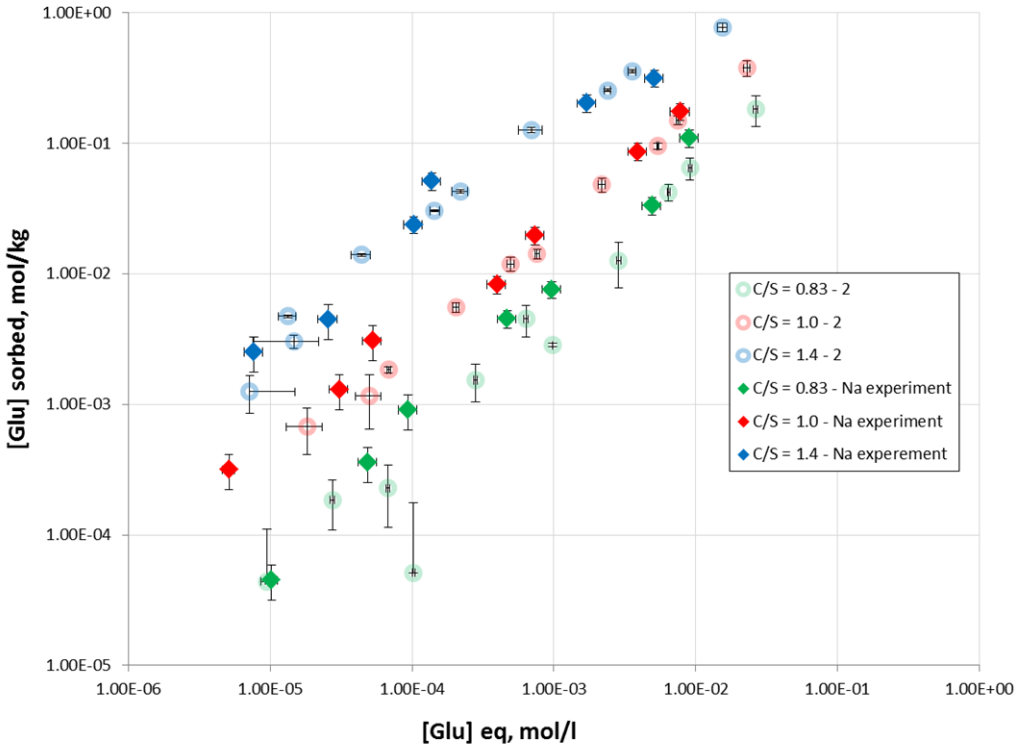

Figure 47. *The isotherm of gluconate adsorption on C-S-H with different Ca/Si. The results of the previous study are shown for comparison (labeled by -2 here).*

The evolution of Na concentration in solution as a function of the initial amount of Na introduced to the system was monitored. It was shown that sodium sorbs on the C-S-H phase with lower Ca/Si ratios and does not sorb on the C-S-H phase with Ca/Si = 1.4.

Being a positively charged cation, sodium is known to be sorbed on C-S-H phases with low Ca/Si ratios (Stade, 1989; Hong and Glasser, 1999; Viallis et al., 1999). Alkali cations (Na, K) can compete with Ca for negative surface sorption sites of C-S-H phases (Labbez et al.,

2011). The competition when Ca^{2+} concentration increases as a result of substitution by Na^{+} and K^{+} can only be observed for C-S-H phases with low Ca/Si.

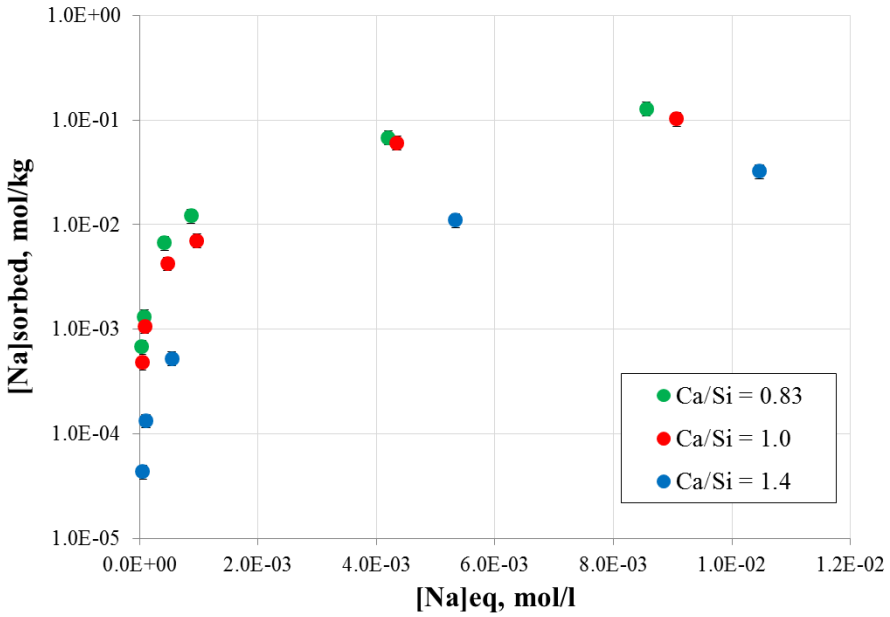

Figure 48. *Sorption of Na^{+} on C-S-H with different Ca/Si ratios (0.83; 1.0; and 1.4).*

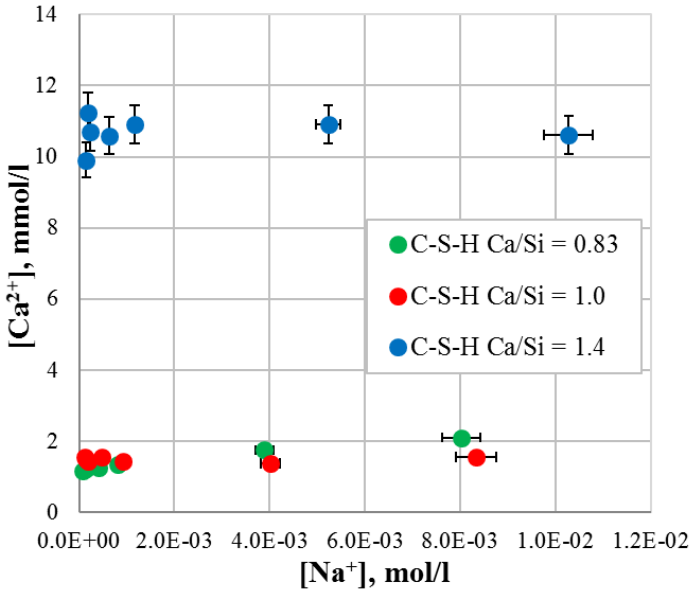

Figure 49. *Concentrations of Ca^{2+} in the C-S-H equilibrated solution as a function of the Na^{+} addition.*

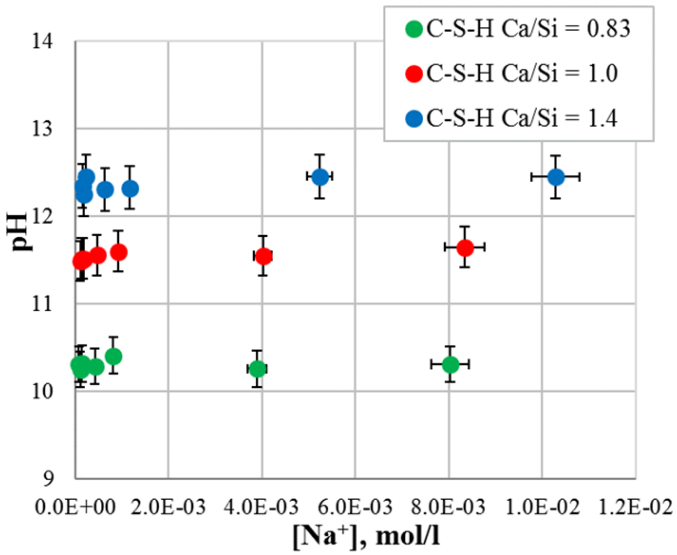

Figure 50. *The pH values in the C-S-H equilibrated solution as a function of the Na^+ addition.*

The results of sodium adsorption on C-S-H phases are presented in Fig. 48. The highest uptake was observed for the C-S-H sample with Ca/Si = 0.83. It was shown that the addition of Na^+ in relatively small amounts does not affect the equilibrium state of C-S-H: pH, Ca, and Si concentrations stay constant for all samples (Fig. 49 and 50).

3.1.2. Desorption experiments

The results of experiments on the desorption kinetics and isotherms of gluconate from C-S-H are presented in Fig. 51. All systems reached a steady state in 1 day, so the reaction time of 3 days was selected for the desorption experiments. It was shown that the desorption process is not reversible for all studied C-S-H phases indicating that additional processes or chemical reactions occur. It can be seen that the hysteresis is more prominent for the C-S-H composition with lower Ca/Si ratio, while the sorption for the sample with Ca/Si = 1.4 is reversible within the stated levels of uncertainty for both experiments. The observed desorption hysteresis can also be a result of the sorption non-equilibrium. The uncertainties in desorption calculations are high since it is an experiment which consists of multiple consecutive steps. The "real" uncertainty can be underestimated. It may be assumed that the steady state has been reached but post-adsorption transitions of gluconate molecules on the C-S-H surface take place.

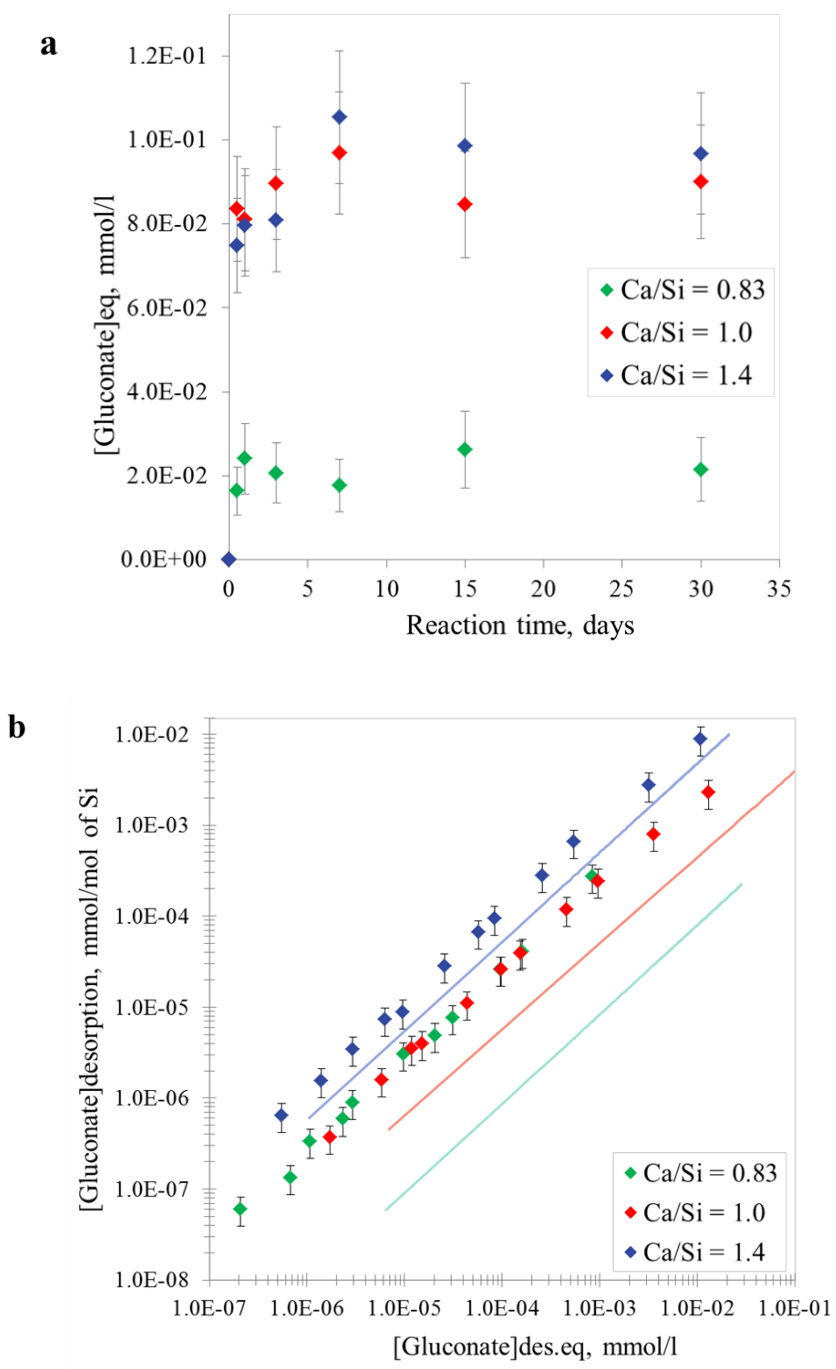

Figure 51. *The kinetics of gluconate desorption from C-S-H (**a**) and isotherms of gluconate desorption (**b**) from C-S-H phases with three Ca/Si ratio (0.83, 1.0, 1.4), S/L = 20 g/l. Lines only show the averaged position of the sorption isotherms.*

The C-S-H surface provides different sorption sites for organic anion that have to be studied (see the molecular modelling section below). Also, some of the hydroxyl groups of gluconate may participate in the sorption process and contribute to its stronger binding to the C-S-H surface. The calculated uncertainties are large due to the propagation of errors through numerous steps of the desorption experiment. Wet chemistry experiments allow identification

of the main trends in the behaviour of the investigated species on C-S-H surfaces, but they do not provide sufficient information on the molecular mechanisms involved. Thus, computational molecular modelling was further used here as a tool for the interpretation of macroscopic observations.

3.2. Gluconate sorption and desorption on HCP

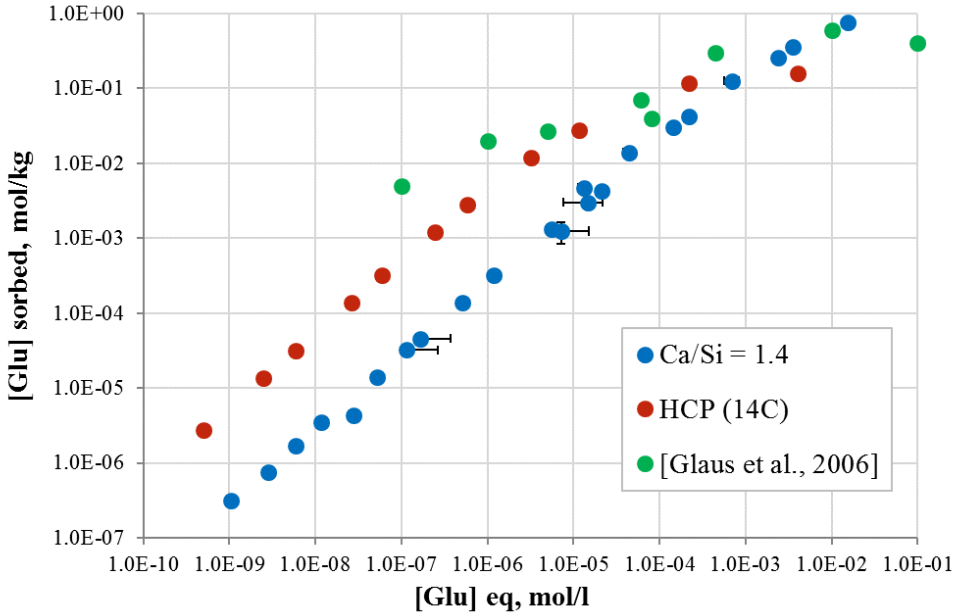

Figure 52. *The isotherm of gluconate adsorption on hydrated cement paste (CEM I, S/L=20 g/l).*

To the best of our knowledge, the desorption processes of gluconate from C-S-H phases have never been studied before, and only a comparison with the data from Glaus et al. (2006) for hydrated cement paste is then possible (the only data reported in the literature). It should be kept in mind that the Ca/Si ration of HCP is around 1.6 and it contains up to 70% of C-S-H phase. An isotherm of ^{14}C-labelled gluconate adsorption on hydrated cement paste is presented in Fig. 52.

Glaus et al. (2006) classically identified two sorption sites for gluconate: a strong site (with the sorption affinity constant K_{strong} = (2±1) x 10^6 l/mol and sorption capacity q_{strong} = (0.04 ± 0.02) mol/kg) and a weak site (with K_{weak} = (2.6 ± 1.1) x 10^3 l/mol and q_{weak} = (0.7 ± 0.3) mol/kg, accordingly). The sorption was found to be reversible for both sites: directly (as a result of gluconate desorption experiment) for the weak site, and indirectly for the strong site based on the experimental results of α-isosaccharinic acid (α-ISA, a structurally similar

polyhydroxycarboxylic acid) desorption from HCP (Van Loon et al., 1997). The sorption capacity of HCP and affinity constant for α-ISA are as follows: q_{strong} = (0.1 ± 0.01) mol/kg, and K_{strong} = (1730 ± 385) l/mol; q_{weak} = (0.17 ± 0.02) mol/kg and K_{weak} = (12 ± 4) l/mol. It can be seen that the binding of α-ISA to HCP is much weaker and it cannot be treated as a complete analogue of gluconate in desorption experiments. Also, the strutural nature of the weak and the strong sites remained undefined.

The obtained results are compared both with the published data and the results from the current work for the C-S-H phase with the highest Ca/Si ratio (1.4). Ca/Si ratio of HCP is 1.6 and, according to the presented trend for C-S-H phases, more gluconate should be sorbed on the hydrated cement phase. But the sorption on the hydrated cement paste (CEM I) is much higher than on pure C-S-H. It can be suggested that the C-S-H phase can be considered as the main adsorber of organic anions from solution, but even this assumption is not enough to fully explain the sorption on HCP.

The isotherm of gluconate desorption was measured for the hydrated cement paste as well, as can be seen in Fig. 53. The desorption from the hydrated cement paste was found to be fully reversible since the desorption isotherm follows the sorption isotherm below $[\text{Gluconate}]_{\text{des.eq}}$ = (2 x 10^{-4}) mol/l. The results also agree with the observed trend of increasing reversibility of gluconate uptake with the increase of Ca/Si ratio of C-S-H.

The obtained desorption results can't be directly compared with the ones of Glaus et al. (2006) since numerical data are missing, and the concentration ranges of the two experiments seem to overlap for only two experimental points ([Gluconate] > 10^{-4} mol/l).

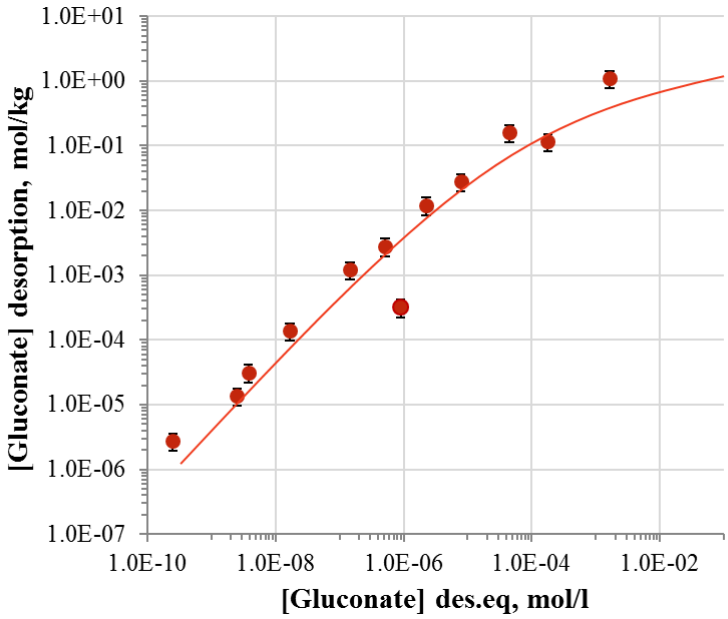

Figure 53. *The isotherm of ^{14}C-labelled gluconate desorption from hydrated cement paste (S/L = 20 g/l). The orange line only shows the average position of sorption isotherm.*

3.3. Sorption of PCE on C-S-H

The adsorption of PCE on a charged surface is energetically favourable, and for molecules with long side chains it occurs because of a significant entropy gain, as it was shown by Plank et al. (2010). Generally, the adsorption of polymers is mostly controlled by the diffusion of the molecule to the surface of interaction. The rate of diffusion depends on the molecular mass, molecular structural properties (e.g., side chain lengths, polymer conformation), and the interaction with ions present in the solution. The probability of polymer incorporation into C-S-H interlayers has been studied by Popova et al. (2000) using XRD and ^{29}Si NMR analysis, and no significant change in the basal spacing has been found after the addition of polymer additives. So, only superficial adsorption is considered in this work.

The data on the kinetics of adsorption for synthesised polycarboxylate on two C-S-H phases illustrated in Fig. 54, with the initial polymer solution concentration equivalent to 0.77 g/l.

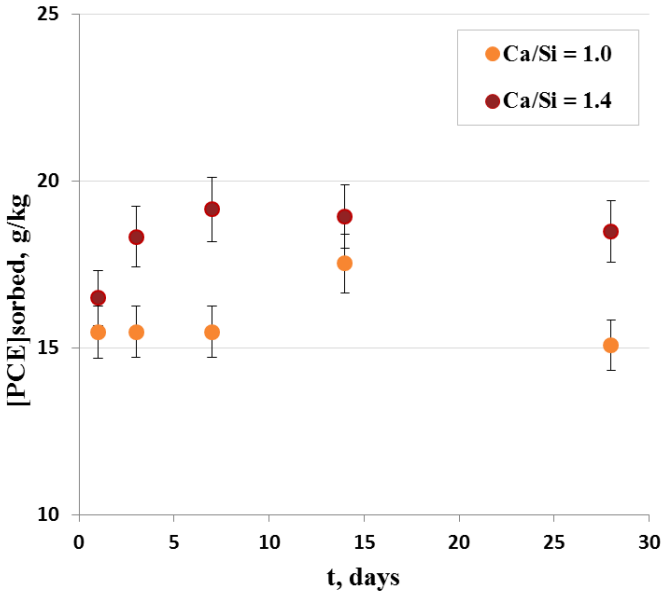

Figure 54. *The kinetics of polycarboxylate adsorption on C-S-H with Ca/Si = 1.0 and 1.4.*

The steady was reached in one week of reaction time for both C-S-H phases studied and remained constant over a time period of one month. There is a difference in sorption of PCE on C-S-H with Ca/Si = 1.0 and Ca/Si = 1.4, but the calculated Rd values are very close to each other: R_d (PCE/CSH) = 35-50 l/kg.

PCE does not react with the C-S-H surface in the same manner as gluconate ions, and its adsorption rate is somewhat slower comparing to what was observed for smaller organic molecules: a steady state is reached in 1 week for C-S-H with Ca/Si = 1.4 while for gluconate it was only 0.5 day.

The measured PCE adsorption isotherms on two C-S-H phases are presented in Fig. 55. No difference in PCE sorption for lower concentrations ($[PCE]_{eq}$ < 2 g/l) was observed between the two C-S-H phases studied: there is an overlap between the isotherms. The influence of Ca/Si ratio of C-S-H on the PCE adsorption is, thus, negligible.

Polycarboxylate molecules tend to be adsorbed on positively charged surfaces because of their negatively charged backbone functional groups (Flatt and Houst, 2001; Kauppi et al., 2005; Plank and Winter, 2008; Ferrari et al., 2010; Lesage et al., 2014). It was previously confirmed that the higher the carboxylate group content in the superplasticiser, the greater is its uptake, because the admixture adsorption by cement particles is mediated by carboxylic groups (Yamada et al., 2000; Yamada et al., 2001; Alonso et al., 2013). This interaction can also explain the main mechanisms of PCE sorption on C-S-H phases.

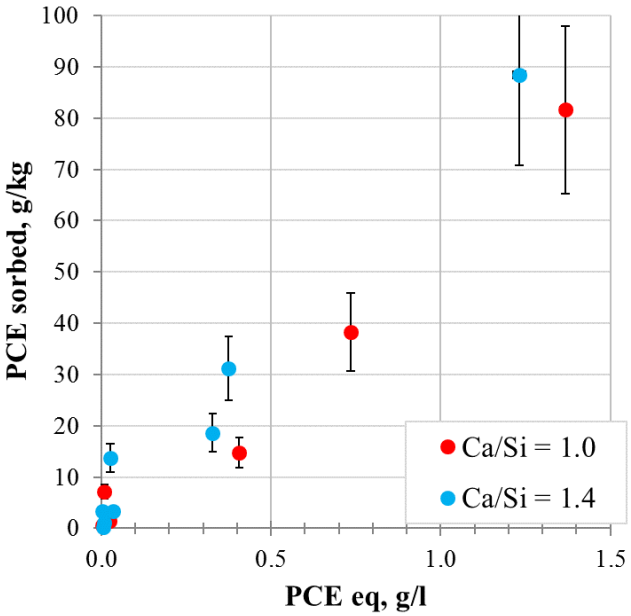

Figure 55. *The isotherms of PCE adsorption on C-S-H phases with Ca/Si = 1.0 and Ca/Si = 1.4.*

The results do not show the same trend as those described by Alonso et al. (2013) for PCE consumption by cement pastes. The term is "consumption" often used to describe the uptake of PCE since it is difficult to separate pure sorption mechanisms for polymer molecules from other processes that can decrease the concentration of organics in the solution. Alonso et al. (2013) have studied the PCE sorption on CEM I, and it was shown that the cement surface reaches saturation at [PCE] ≈ 2 g/kg. In this work, only synthetic C-S-H with its equilibrated solution is present, and the saturation stage, characteristic for cement, has not been clearly identified. A large amount of sorbed PCE on C-S-H phases can be explained by multiple layer adsorption, PCE aggregation (formation of micelles) or overestimated concentration decrease due to the centrifugation step.

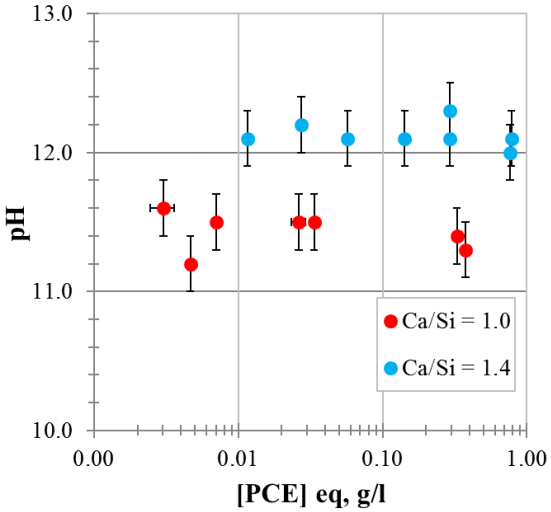

Figure 56. *pH values of C-S-H equilibrated solutions as a function of the PCE concentration in the steady state.*

For all samples, the solution pH was measured after PCE adsorption (Fig. 56). It was found that the addition of polycarboxylate polymer does not affect pH of the equilibrated solution.

The method used to evaluate PCE adsorption does not allow to distinguish the concentration depletion due to the sorption process and due to the probable confinement of PCE molecules in the solid phase between C-S-H particles after centrifugation (Ferrari et al., 2011). Surface polymer precipitation can also be suggested as it was done by Houst et al. (2007) for the interpretation of linear adsorption for the range of added PCE concentrations for a model surface (MgO). Additionally, it can be suggested that association with Ca^{2+} cations can decrease the anionic charge on the molecule (Plank et al., 2010) or they can form multicore intramolecular complexes with polymer molecules, increasing their consumption, as shown schematically in Fig. 57.

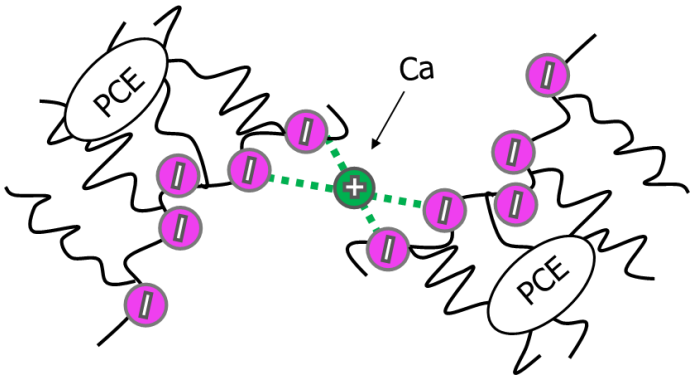

Figure 57. *The multicore intramolecular complex of PCE molecules with Ca^{2+}.*

The primary uptake mechanism of PCE is also accepted to be Ca^{2+}-mediated surface sorption, as in the case of gluconate (Plank et al., 2008; Turesson et al., 2014; Liu et al., 2015). It is important to note that at the solution/C-S-H interface the polymer molecules might compete with simple ions that modify polymer conformation. In highly alkaline solutions, the deprotonated carboxyl groups of the polymers potentially can either connect through hydrogen bonding to the surface sorption sites (-surface-OH_2^+) or complex via the interfacial Ca^{2+} cations (Houst et al., 2007).

It can be seen that the behaviour of PCE molecules on C-S-H interfaces is much more complex than the behaviour of gluconate. The data on other ions present in the system is necessary (Ca, Si) as well as an additional study of sorption at the range of lower concentrations.

As a next step, PCE is added to C-S-H to study its potential influence on the adsorption behaviour of U(VI). The lowest PCE concentration used in the sorption study is used for equilibration.

3.4. Uranium sorption on C-S-H

3.4.1. Binary system: U(VI)/C-S-H

Uranium (VI) exists in aqueous solutions in the form of uranyl cation, UO_2^{2+}, and in alkaline solutions it forms hydroxo complexes of different stoichiometry with a general formula $(UO_2)_m(OH)_n^{2m-n}$ (Krestou and Panias, 2004).

Adsorption is one of the main reactions that control the mobility of radionuclides in cement phases. A strong sorption of U(VI) on C-S-H has already been demonstrated by Tits et al. (2011). In the present work, the behaviour of the binary C-S-H/U(VI) system was investigated for the C-S-H phase with the highest Ca/Si ratio at a solid-to-liquid ratio of 20 g/l. It was assumed that the U(VI) binding by C-S-H is mostly occuring due to surface sorption and might also involve Ca uptake (Tits et al. (2011)).

The highest sorption is under alkali-free conditions, and it was found to be dependent on pH and on the C-S-H composition (Tits et al., 2011). The results obtained in the current study for isothermal adsorption in the absence of organic molecules (Fig. 58) reveal linear adsorption

(slope of ≈ 1) with the same trends reported earlier for C-S-H phases with various Ca/Si ratios under alkali-free conditions (10.1 < pH < 12.5) (Tits et al., 2011).

Pointeau et al. (2004) have shown that Rd values for U(VI) adsorption on C-S-H phases are very similar after 9 days and 21 days of contact time. The reported fast sorption kinetics and the linear sorption behaviour suggest that the uptake of U(VI) might happen due to adsorption involving only one major sorbed species and a major single sorption site (or several sites with equal sorption affinities).

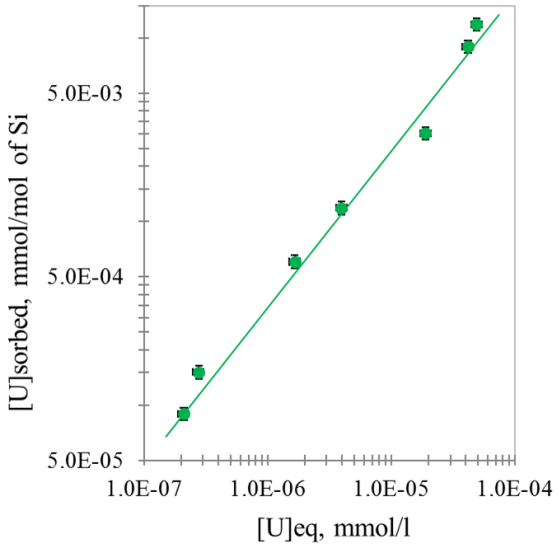

Figure 58. *The isotherm of U(VI) adsorption on C-S-H with Ca/Si = 1.4, S/L = 20 g/l.*

No considerable changes in the measured pH, Si, and Ca concentrations values were observed in our experiments (Annex 5). These results agree with Tits et al. (2011) and indicate that the addition of U(VI) does not affect much the equilibrium state of the C-S-H phase.

The results of this experiment are the reference for the interpretation of U(VI) sorption behaviour in ternary systems.

3.4.2. Ternary systems: Gluconate/U(VI)/C-S-H and PCE/U(VI)/C-S-H

Sorption of U(VI) on C-S-H with Ca/Si = 1.4 in the presence of organic molecules (gluconate and PCE) has been investigated and compared with the results for the U/C-S-H binary system. The measured isotherms are presented in Fig. 59 including the results of U(VI) adsorption as a blank experiment for better comparison. The concentrations of organic molecules were selected to be as low as possible to ensure undersaturated conditions with monolayer

adsorption on the surface: 0.35 mmol/l of gluconate and 0.01 g/l of polycarboxylate accordingly. The choice of concentrations was guided by the measured adsorption isotherms and by the detection limits of analytical instruments used.

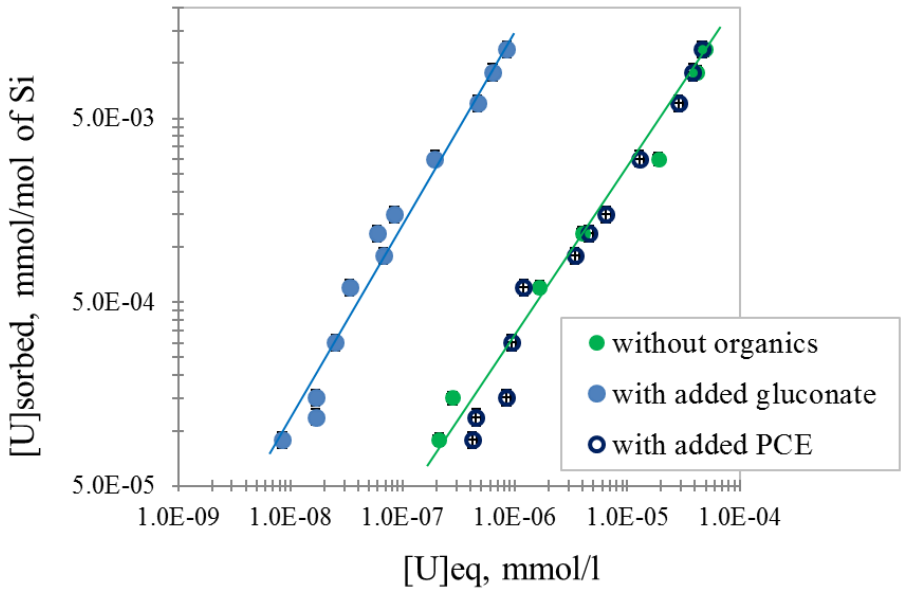

Figure 59. *The isotherm of U(VI) adsorption on C-S-H with Ca/Si = 1.4 (S/L = 20 g/l) in the presence of gluconate and PCE (ternary systems).*

It can be clearly seen that the pre-equilibration of C-S-H with gluconate causes a significant change in the uptake values for the model radioelement: U(VI) sorbs better for over the entire range of concentrations studied. At the same time, the addition of polycarboxylate does not affect the U(VI) sorption on a macroscopic level and the results for the C-S-H/PCE/U(VI) ternary system do not differ much from the binary C-S-H/U(VI).

The ion analysis (Ca, Si, U and pH) in the ternary system with gluconate was performed (Annexe 5), and similar to the results on the binary system, the values pH, Si and Ca concentrations in the ternary system all remained stable. These data reveal that the formation of a U(VI) precipitate can be excluded in the concentration range of the present work (less than 10^{-7} mol/l in equilibrium). U(VI) solubility in C-S-H systems is determined by Ca–uranate (Tits et al., 2008) and it varies between 10^{-5} mol/l and 10^{-7} mol/l depending on the Ca equilibrium concentration and pH (Tits et al., 2011).

The concentration of gluconate in equilibrium was also analysed for all the samples. Its evolution as a function of U(VI) concentration is reported in Fig. 60. It can be concluded that

there is no evident competition between gluconate ions and uranyl cations for the sorption sites on C-S-H: the adsorption of gluconate does not change for $[U]_{eq}$ below $5x10^{-5}$ mol/l.

The method of solution depletion cannot provide enough information to identify the processes causing the uptake of particular species. Even though the total concentration of gluconate in the steady state did not change, it could partially participate in complexation of uranyl cations. Colàs et al. (2013) have studied the complexation of gluconate with U(VI) in alkaline solution. They suggested a $UO_2(OH)_2(Gluconate)^{2-}$ complex to be a stable species formed at high pH (pH=12) as a result of UV–Vis absorbance experiment. In our work, both gluconate and uranyl are present at low concentrations, and the formation of polynuclear complexes is less probable.

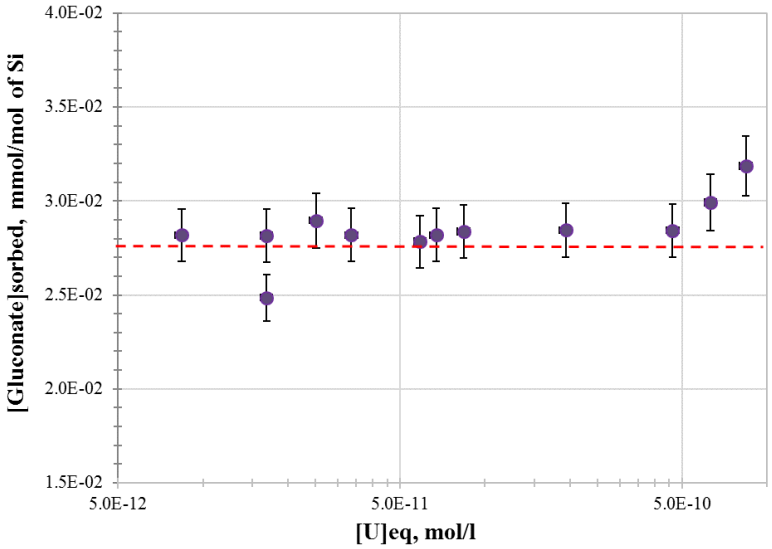

Figure 60. *The concentration of gluconate in the C-S-H equilibrated solution as a function of the U(VI) addition ($[Gluconate]_{initial}$=0.35 mmol/l, the red dashed line represents the permanent state concentration of gluconate in the absence of U(VI); S/L = 20 g/l, Ca/Si=1.4).*

It is known that superlasticisers can increase the solubility of some radioelements (Eu(III), Th(IV), Ni(II), U(VI), Pu(IV)) and decrease their sorption on cement (CEM I, CEM V) (McCrohon and Williams, 1997; Greenfield et al., 1998; Dario et al., 2003; Young et al., 2013). However, the decrease of U(VI) sorption on C-S-H phases has not been observed. The comparison of the present results with literature findings is not straightforward since only pure C-S-H phases were studied, but not real cement pastes. Also, the strongest effect of superplasticisers on the radionuclide solubility is reached when they are introduced in solution

but in the current work it was previosly sorbed on the solid. Another important factor to consider is the concentration: the effects on the radionuclide sorption on cement are observed for $[PCE]_{initial} > 0.1$ % (Dario et al., 2003; Young et al., 2013).

It can also be expected that the molecular mass of the organic molecule can influence the mechanisms of interaction. Both of the presently studied organic molecules (gluconate and PCE) have shown rapid kinetics of adsorption that is typically interpreted as an electrostatic mechanism of uptake. Evidently, gluconate ion is much smaller and thus much more mobile than a polymer, and, as a result, gluconate ion can approach closer to the surface and might more easily create stable complexing configurations with cations. So, The results of the gluconate study should be extrapolated with certain caution.

3.5. Chapter conclusions

The measurements of gluconate sorption on pure C-S-H phases with three Ca/Si ratios (0.83, 1.0, 1.4) were performed with all C-S-H phases carefully analysed to ensure the desired Ca/Si ratios and purity prior to all wet chemistry experiments. It was shown that sorption of gluconate is a rapid process which is not fully reversible. The adsorption of gluconate is affected by the Ca/Si ratio of C-S-H: the sorption ability of C-S-H increases for higher Ca/Si ratios showing trends similar to the ones that are reported in the literature.

The evolution of major ion concentrations and pH were measured at every stage of experiments with gluconate to get a detailed understanding of processes involved. The concentration of Si and Ca in the equilibrated solutions and their pH values did not change for any sample used in the study.

New data on gluconate sorption and desorption on HCP at low concentrations have been obtained. The results confirm that the C-S-H phases are primarily responsible for the adsorption of organic anions.

The rapid kinetics of adsorption of both gluconate and PCE polymer molecules indicates that the nature of adsorption interaction is mainly electrostatic and it is occuring through the mediation of Ca^{2+} cations present at the solution-solid interface.

The presence of organics in the system can influence the uptake mechanisms of metal cations by C-S-H phases. It was shown that the addition of gluconate ion increases significantly the

sorption of Uranium (VI). At the same time, an experiment with polycarboxylate ion did not reveal any differences in the surface sorption of the metal ion. It may be explained by the difference in molecular masses and molecular configurations of the organic molecule studied.

Wet chemistry experiments allowed to identify the main trends in the behaviour of the studied species on C-S-H surfaces, but they do not explicitly indicate what are the molecular mechanisms involved. Thus, molecular modelling becomes a helpful tool here for the interpretation of the macroscopic observations. The results of molecular modelling on the sorption of gluconate and uranyl ions are presented and discussed in the next chapter.

Chapter 4

Results and Discussion: Molecular Modelling

4.1. Bulk aqueous gluconate solutions

To be able to characterise the behaviour of gluconate ions with cations on the surface of C-S-H phases the reference system should be studied first. The presence of Ca^{2+} can influence the adsorption of UO_2^{2+} in different ways: (i) competing with UO_2^{2+} for surface sorption sites; (ii) changing the surface charge; (iii) affecting aqueous speciation of U(VI) through the formation of calcium uranate complexes. So, a description and interpretation of UO_2^{2+} sorption on C-S-H phases can't be complete without a comparison with models that include calcium cations. Solutions of the calcium salt of gluconic acid (2,3,4,5,6-pentahydroxyhexanoic acid) were studied by classical MD simulations using the LAMMPS open source code (Plimpton, 1995).

The chemical structure of gluconic acid consists of a six-carbon zigzag backbone chain with five hydroxyl groups and terminated by a carboxylic acid group. Different spatial arrangements (conformations) of gluconic acid are possible due to rotations about the single bond between carbons with sp^3 hybridization (Littleton, 1953; Lys, 1984). Several conformations were initially built and went through the geometry optimisation step to obtain the most probable molecular configuration. Potentials from ClayFF were used for the inorganic part of the simulated systems, and potentials from GAFF – for gluconate (see Section 2.2.1.3. for more details). The models of bulk aqueous solutions were built next:

1. Gluconate with calcium cations: 3809 water molecules, 8 gluconate molecules, 4 Ca^{2+}.
2. Gluconate with calcium cations and aqueous hydroxyls: 3809 water molecules, 8 gluconate molecules, 8 Ca^{2+}, 8 OH^-(aq).
3. Gluconate with calcium, uranyl cations, and aqueous hydroxyls: 3809 water molecules, 8 gluconate molecules, 6 Ca^{2+}, 12 OH^-(aq), 4 UO_2^{2+}.

First, a potential energy minimization (geometry optimisation) and further equilibration using *NPT*-ensemble MD simulation (1 bar, 300K) were performed (equilibration time: 1000 ps). It was followed by an unconstrained MD simulation for another 1000 ps in the equilibrium thermodynamic state (recording system coordinates every 0.5 ps). Radial distribution functions and running coordination numbers were calculated for different pairs of atoms present in the system (calcium cations, gluconate oxygens, atoms of the uranyl cation, H_2O and OH^-).

The properties of hydrated Ca^{2+} ions have already been studied using experimental and computational techniques (Probst et al., 1985; Ohtaki and Radnai, 1993; Jalilehvand et al., 2001; Tommaso et al., 2014). Ca^{2+} is typically coordinated by 7-8 oxygens in the first solvation shell: carboxyl oxygens of gluconate at $r \approx 2.6$ Å, water oxygens at $r \approx 2.5$ Å, and aqueous hydroxyl oxygens at $r \approx 2.4$ Å.

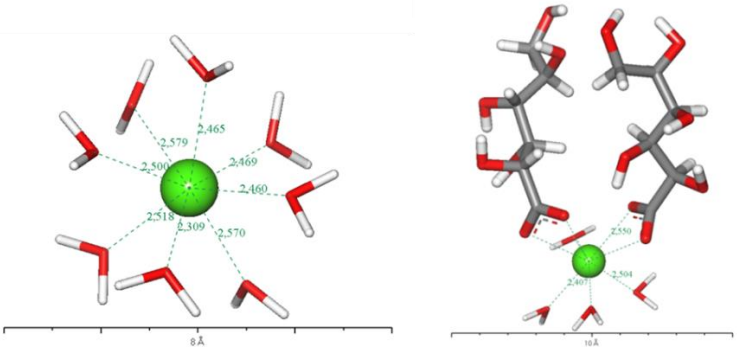

Figure 61. *Simulation snapshots of the Ca^{2+} hydration shell and the complex with gluconate ions.*

Oxygen atoms of the first shell are coordinated with other solution molecules through hydrogen bonding to the second solvation shell at distances around 3.5 - 4.5 Å, but in the current work, these less important details will not be considered. Ca^{2+} can form monodentate and bidentate complexes with gluconate depending on the concentration of both ions in solution (Fig. 61).

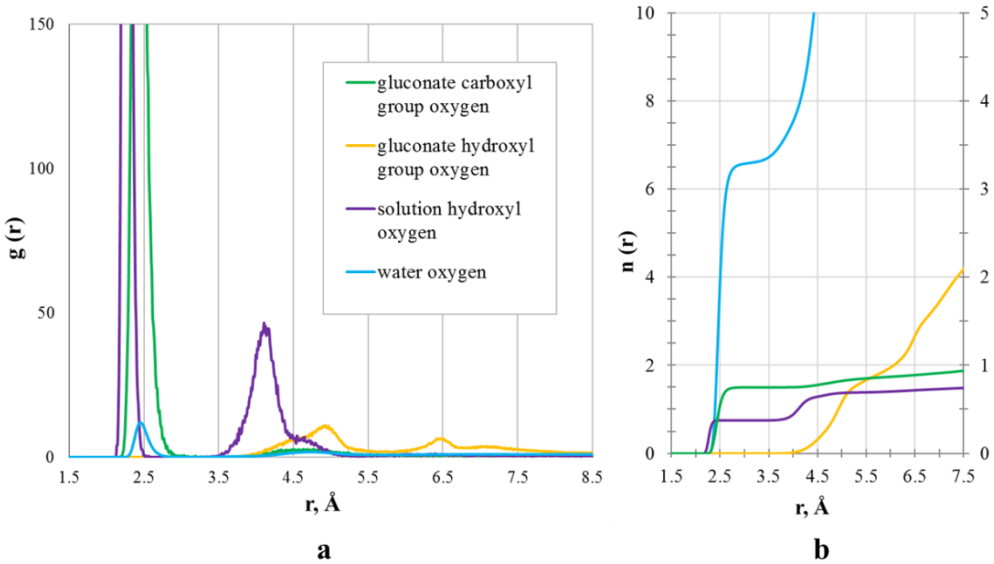

Figure 62. *Local structural properties of calcium gluconate solution: **(a)** - radial distribution functions for Ca-O pairs; **(b)** – running coordination numbers.*

There is a low probability of binding of Ca^{2+} with hydroxyl group of gluconate in the first solvation shell: no peak can be seen for the interval of distances 2.2 Å < *r* < 2.7 Å (Fig. 62-b). On all RCN plots in this chapter the data for the water oxygen is presented on separate scale (left) for clarity.

Predominant formation of multinuclear complexes of Ca^{2+} and polyhydroxy carboxylates like gluconate in hyperalkaline solution has been proposed by Pallagi et al. (2014) with a high probability of Ca^{2+} coordination by oxygens of the second and third carbon of the organic molecule (binuclear $[Ca_2Gluc(OH)_3]^0$ and trinuclear $[Ca_3Gluc_2(OH)_4]^0$ complexes). According to previously presented distribution diagram (Fig. 45 in Chapter 3) in the pH range of 10.5-12.5 for solutions with excess of gluconate ions ([Gluconate]:$[Ca^{2+}]$ = 3:1) the following complexes coexist in an approximate proportion: ~30% of mononuclear $[CaGlucOH]^0$, ~20% of binuclear and ~20% of trinuclear, ~30% of unreacted Ca^{2+}. In the current work, the simulation models consisted of ions at lower concentrations with the ligand-to-cation proportion of 1:1, only carboxyl groups were considered deprotonated, and possible effects of polarisability of the gluconate hydroxyl groups could not be included. Under these assumptions, only mononuclear complexes were observed.

UO_2^{2+} is coordinated by 5 oxygens of the solution species (H_2O molecules and OH^- ions, Fig. 63) at average distances of about 2.4 Å, which is close to the experimental and theoretical estimates (Aaberg et al., 1983; Druchok et al., 2005; Hagberg et al., 2005; Gutowski and Dixon, 2006).

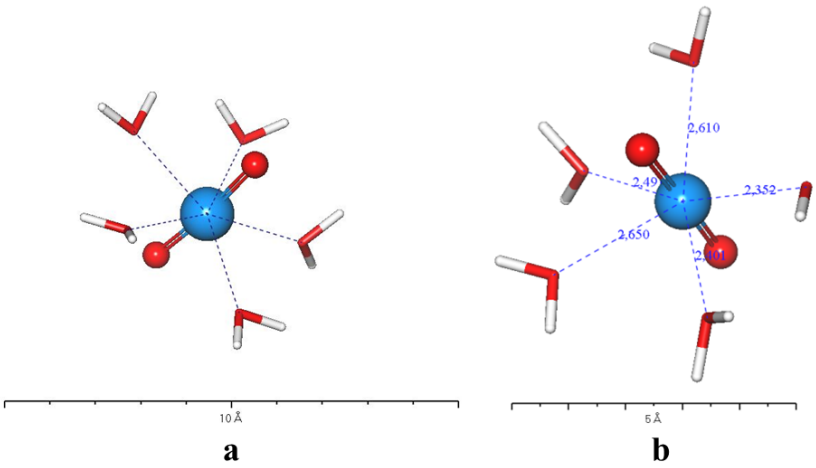

Figure 63. *Simulation snapshots of the UO_2^{2+} hydration shell:* **(a)** *– with waters only;* **(b)** *– with one water molecule substituted by aqueous hydroxyl.*

Aqueous hydroxyls, if present in solution, can easily replace H_2O molecules in the first hydration shell of both Ca^{2+} and UO_2^{2+} cations. As it can be seen from the time averaged radial distribution functions (Fig. 64 (c) and (d)), there is a low probability of binding between UO_2^{2+} and gluconate (both hydroxyl and carboxyl functional groups) in the first solvation shell.

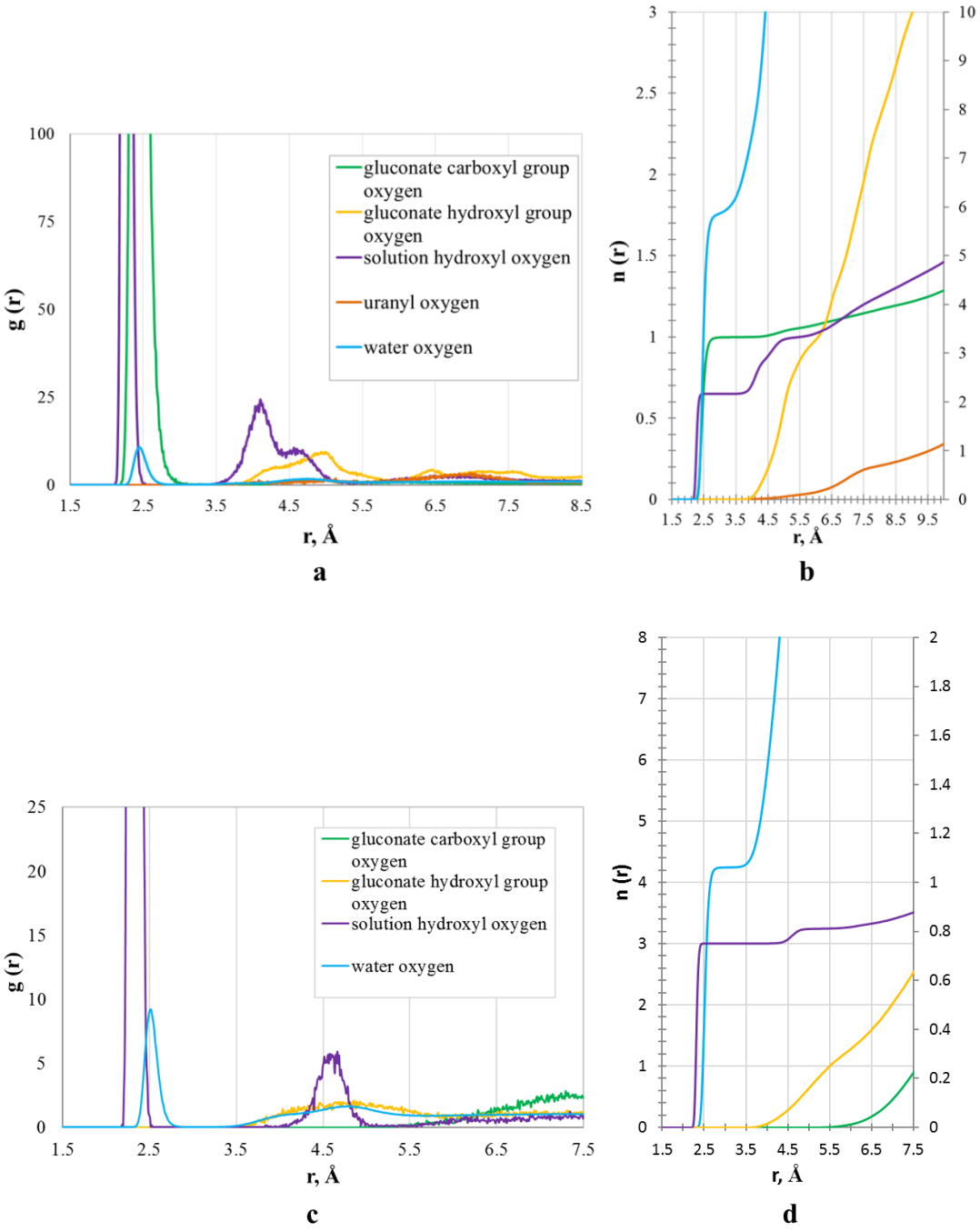

Figure 64. *Local structural properties of calcium gluconate/uranyl solution:* **(a)** *– radial distribution functions for Ca-O pairs;* **(b)** *– running coordination numbers;* **(c)** *- radial distribution functions for U-O pairs;* **(d)** *– running coordination numbers.*

For carbonated systems, a formation of calcium uranate carbonate complexes can be expected (Morse et al., 1984; Fox et al., 2006; Maher et al., 2013; Richter et al., 2016), but in the absence of CO_2 a formation of hydroxo complexes can be suggested where cations are bound with a hydroxyl "bridge".

4.2. Hydrated C-S-H surface

4.2.1. Local structural properties

Three models of substrate-water interfaces were built for each C-S-H surface of interest (Table 7).

Table 7. Atomic composition of hydrated C-S-H surface models.

Name	Ca/Si	N_{total}, atoms	Solid composition	Solution composition
CSH-0.83	0.83	15598	416 Si, 288 Ca, 48 deptonated and 168 protonated silanols, 1012 bridging oxygens	4486 H_2O, 8 aqueous hydroxyls, 24 Ca^{2+}
CSH-1.0	1.0	15510	392 Si, 288 Ca, 96 deptonated and 120 protonated silanols, 964 bridging oxygens	4490 H_2O, 8 aqueous hydroxyls, 44 Ca^{2+}
CSH-1.4	1.4	15524	360 Si, 288 Ca, 144 deptonated and 72 protonated silanols, 900 bridging oxygens	4536 H_2O, 8 aqueous hydroxyls, 64 Ca^{2+}

A comparison between them gives better insight into the possible mechanisms of interaction involved. The density profiles and other reported interfacial properties presented in this work are the averages over the time of the equilibrium production MD run for two statistically independent substrate/solution interfaces created after the C-S-H crystal cleavage for each simulation box: both surfaces are characterised by the same amount of structural defects and are in contact with the solution of the same composition (surface 1 and surface 2 in Fig. 65).

The thickness of the water layer between the two surfaces was large enough (≈ 70 Å) to ensure that the interactions at the one surface would not affect the other, and result in bulk-like solution behaviour in the middle of the model simulation box. The distance of atoms from

the surface, *d*, was calculated taking as a reference (d = 0) the average *z*-coordinates of the oxygen atoms coordinating the top-most pairing Si tetrahedra at each C-S-H surface (Fig. 65).

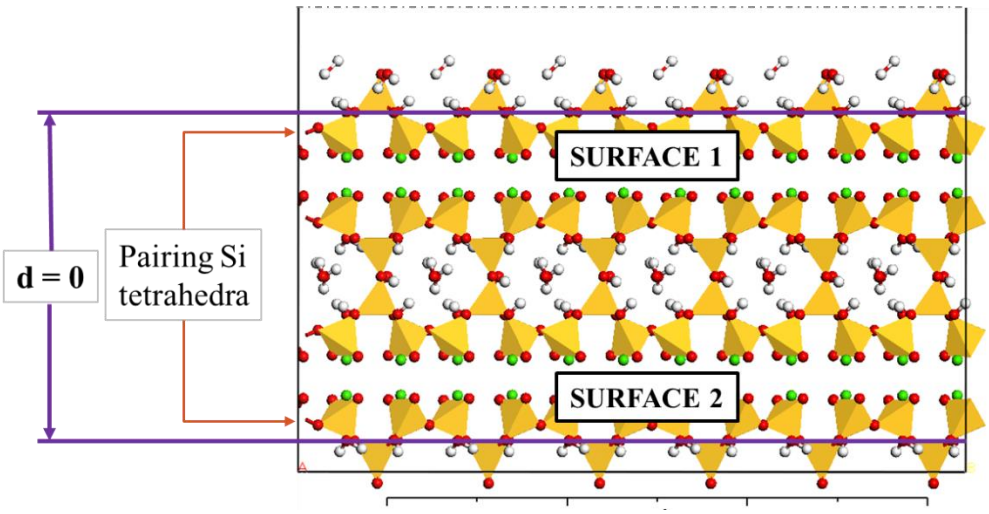

Figure 65. *The position of defined "zero" coordinate (d = 0) for the calculation of distances of atoms from the C-S-H surface.*

The interactions between the dissolved cations and the negatibvely charged surface oxygens are the key point in the structural characterisation of the adsorbed complexes.

Radial distribution functions, $g(r)$, and running coordination numbers, $n(r)$, for various pairs of atoms provide data for a quantitative description of the coordination sphere of the atom of interest and of possible complexes they can form with other ions in the system.

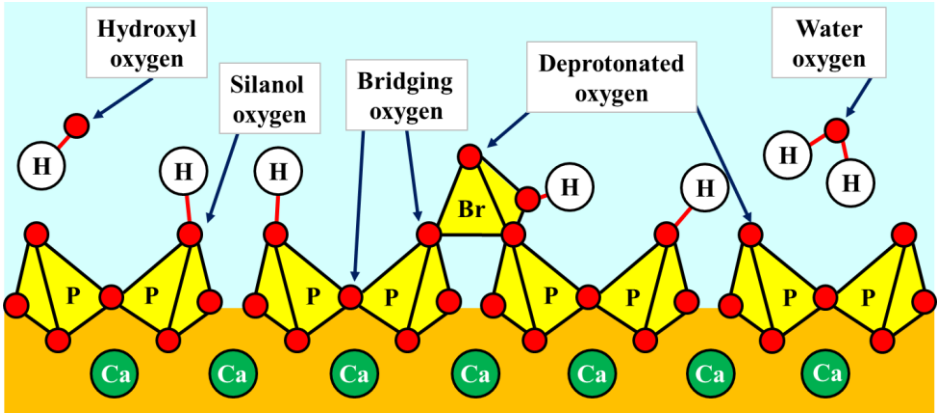

Figure 66. *Different types of oxygens present on the C-S-H/solution interface.*

ClayFF force field includes parameters for different types of oxygen atoms in hydrated mineral phases and by combining them with GAFF it is possible to differentiate between

various oxygens in organics. As a result, the interactions between ions and surface oxygens are treated separately (Fig. 66). Water oxygens are predominately present in the simulation box, so their pair distributions are shown in Fig. 67-b with a different scale for better visibility. Local structural properties of C-S-H were analysed, and radial distribution functions together with running coordination numbers for Ca-O pairs were calculated. Figure 67 presents the results for CSH-0.83 (the C-S-H surface that models Ca/Si = 0.83).

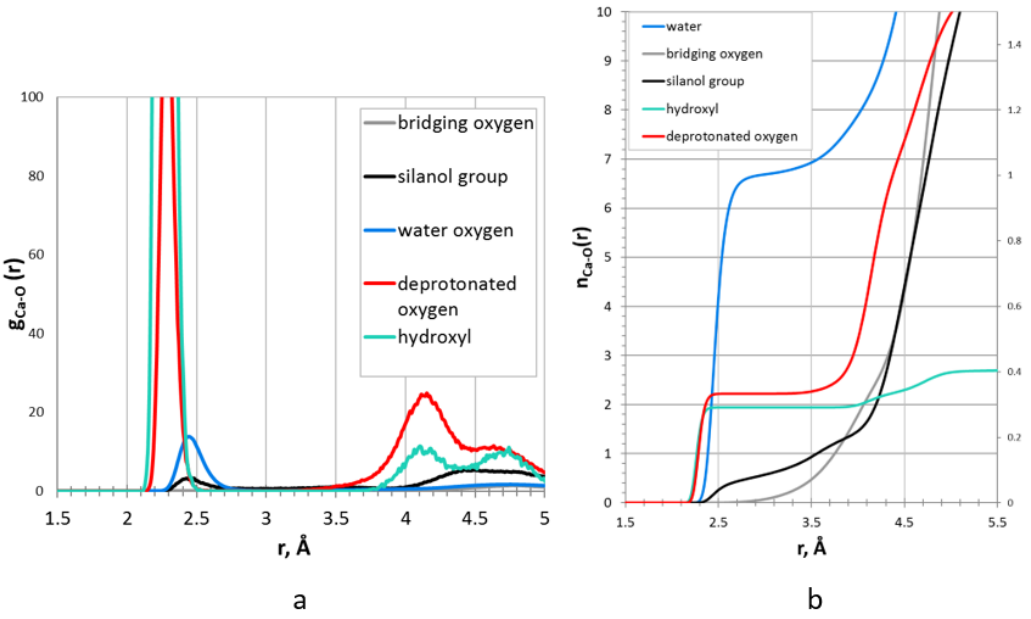

Figure 67. **(a)** – *The radial distribution functions for Ca-O pairs (CSH-0.83);* **(b)** – *the running coordination numbers for Ca-O pairs.*

From the results of bulk solution simulations, it is known that calcium cations in aqueous solution are typically coordinated with 7-8 oxygen atoms. Most of the solvation shell of calcium is composed of water molecules ($n_{Ca\text{-}O_{water}}(2.4\ Å) = 6.5$). From the calculated $g(r)$ (Fig. 67-a) it can be seen that Ca ions are sorbed on the C-S-H surface by binding to the deprotonated sites in the first coordination shell ($r \approx 2.3$ Å). The running coordination number for this pair is less than 1, and corresponds to the monodentate complexation with the surface, where Ca^{2+} coordinates only one deprotonated surface oxygen. It can also be noticed that binding to the deprotonated sites is much more preferred to the complexation with protonated silanol groups ($n_{Ca\text{-}O_{silanol}}(2.5\ Å) \approx 0.1$) and with the bridging oxygens of the surface. Solution hydroxyl groups can replace H_2O in the first solvation shell of Ca^{2+} ($r \approx 2.3$ Å).

The interface of C-S-H with Ca/Si ratio of 1.0 (CSH-1.0) shares many similar features with the CSH-0.83 surface, but there are a few differences due to its less protonated character and a larger number of missing Si tetrahedra. The modelled surface of C-S-H with the Ca/Si ratio of 1.4 (CSH-1.4) is fully deprotonated and has the highest number of structural defects (Si-O layer consists of dimers only, no bridging Si tetrahedra remain on the surface). This negatively charged surface noticeably affects the interfacial solution structure. The differences can already be noticed from the calculated RDFs and RCNs for the Ca-O pairs presented in Fig. 68, where the number of deprotonated oxygens in the first coordination shell is tripled compared to the CSH-0.83 model. Similar to other described surfaces, the complexation with protonated silanol groups is seen as less favourable.

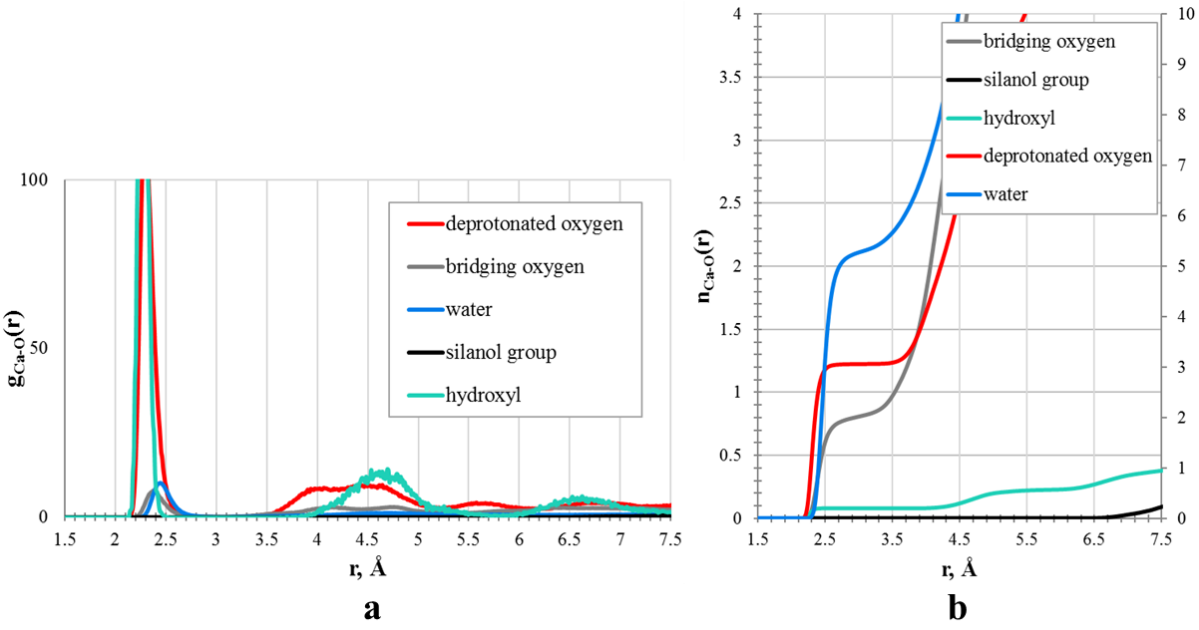

Figure 68. **(a)** – *The radial distribution functions for Ca-O pairs (CSH-1.4);* **(b)** – *the running coordination numbers for Ca-O pairs.*

4.2.2. Surface density profiles

The density profiles of water oxygen atoms (Ow) and water hydrogen atoms (Hw) as functions of their distance from the surface for all four C-S-H/solution interfaces with different Ca/Si ratios show some similar features. The typical density profiles of water oxygen and hydrogen atoms, calcium counter ions, and the oxygen atom of solution hydroxyls at the CSH-0.83 surface are presented in Fig. 69. The density profiles for the dissolved ions are shown using the secondary scale on the right for better visibility of results.

As mentioned above, the reference position (d = 0 Å) was defined via the average z-coordinate of the deprotonated silanol groups of the 'pairing' silicon tetrahedra. This choice somewhat simplifies further comparative analysis of the interfacial structures since the C-S-H surface with the highest Ca/Si ratio does not contain bridging Si tetrahedra at all.

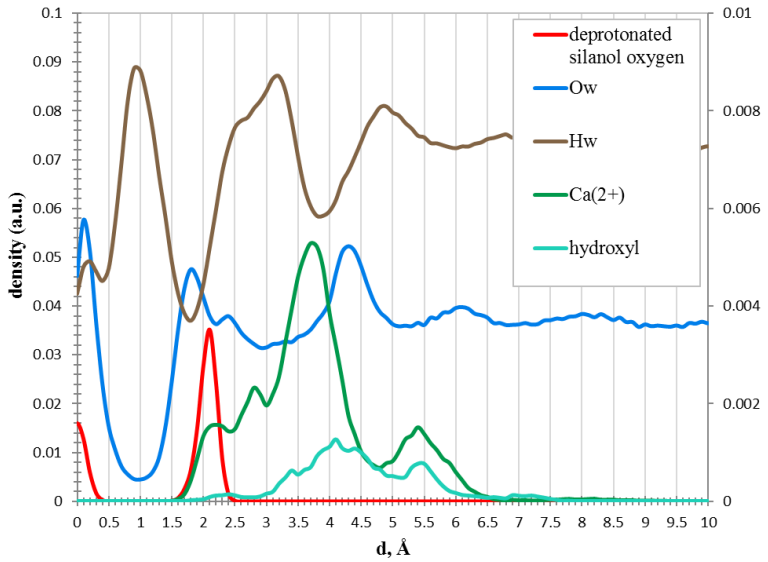

Figure 69. *The atomic density profiles of solution species near the CSH-0.83 surface.*

From the atomic density profile, three major peaks of water oxygens can be identified with correlated water hydrogen peaks of double intensity. Water forms several structured layers near the surface of C-S-H (Fig. 70). The first peak (d < 1 Å) corresponds to H_2O molecules originally present in the structure; these molecules are strongly bound to the calcium oxide layer. The second and the third peaks (1 Å < d < 3 Å and 3 Å < d < 5 Å, respectively) represent water molecules attracted to the surface and forming hydrogen bonds with it and also the molecules belonging to the hydration shell of the cations (e.g. Ca^{2+} sorbed on C-S-H).

For the CSH-0.83 model surface, there is one broad split intensity peak at d_{max} = 3.7 Å that can be seen for Ca^{2+}. Broad peaks or those split into several separate peaks with a very small distance in between (Δd is less that the diameter of one H_2O molecule) prove the existence of multiple sorption sites and several orientation possibilities for the ions. The CSH-0.83 surface is less defected, but as a result, it is more uneven which is causing oscillations on the time-averaged atom density profiles. The main peak is at the distance of 1.6 Å from the topmost deprotonated silanol group of the surface. It represents the cations that form inner-sphere complexes with the CSH-0.83 surface. Only monodentate complexes were observed for the

CSH-0.83 surface. The intensity of the peak at d = 5.5 Å in Ca^{2+} distribution corresponds to the outer-sphere complexation.

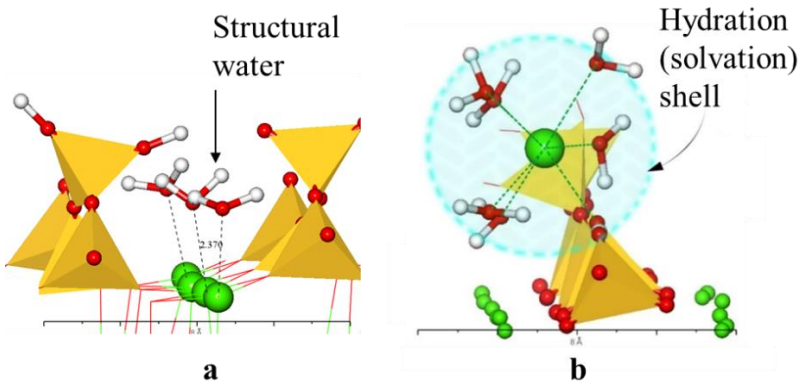

Figure 70. *Water molecules near the C-S-H surface (typical trajectory snapshots):* **(a)** *– C-S-H structural water;* **(b)** *– water in the hydration shell of Ca^{2+} ion sorbed on the surface. Colour scheme: yellow – silicon, red – oxygen, white – hydrogen, green – calcium.*

Water density profiles near the CSH-1.0 surface are almost identical for all four types of interfaces (Fig. 71). Meanwhile, the CSH-1.0 surface has less bridging silicon tetrahedra present and oxygens of pairing tetrahedra become more accessible. So, Ca^{2+} distribution is different and indicates higher probability of complexation with the deprotonated sites of pairing Si tetrahedra (the peak at d = 1 Å).

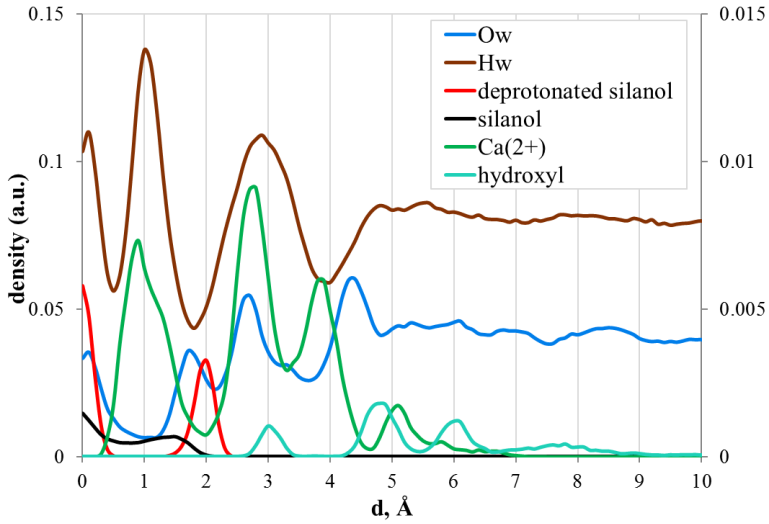

Figure 71. *The atomic density profiles near the CSH-1.0 surface. Distribution of Ow and Hw atoms is presented with a separate scale.*

H_2O molecules that are part of the CSH-1.4 structure remain the same as in the previously discussed systems. As seen in Figs. 71 and 72, both the Hw and Ow atoms of water in the first layer (d < 1 Å) are located at the same distance, parallel to the surface, while the Hw atoms of the second layer (1 Å < d < 2.5 Å) are pointed towards the surface oxygens forming hydrogen bonds.

More distinct peaks can be identified for calcium from the density profiles for the CSH-1.0 and CSH-1.4 interfaces. The results of MD simulations show that approximately half of the introduced Ca^{2+} form inner-sphere complexes with the C-S-H surfaces in which surface oxygens replace H_2O molecules in the first coordination shell of the cation.

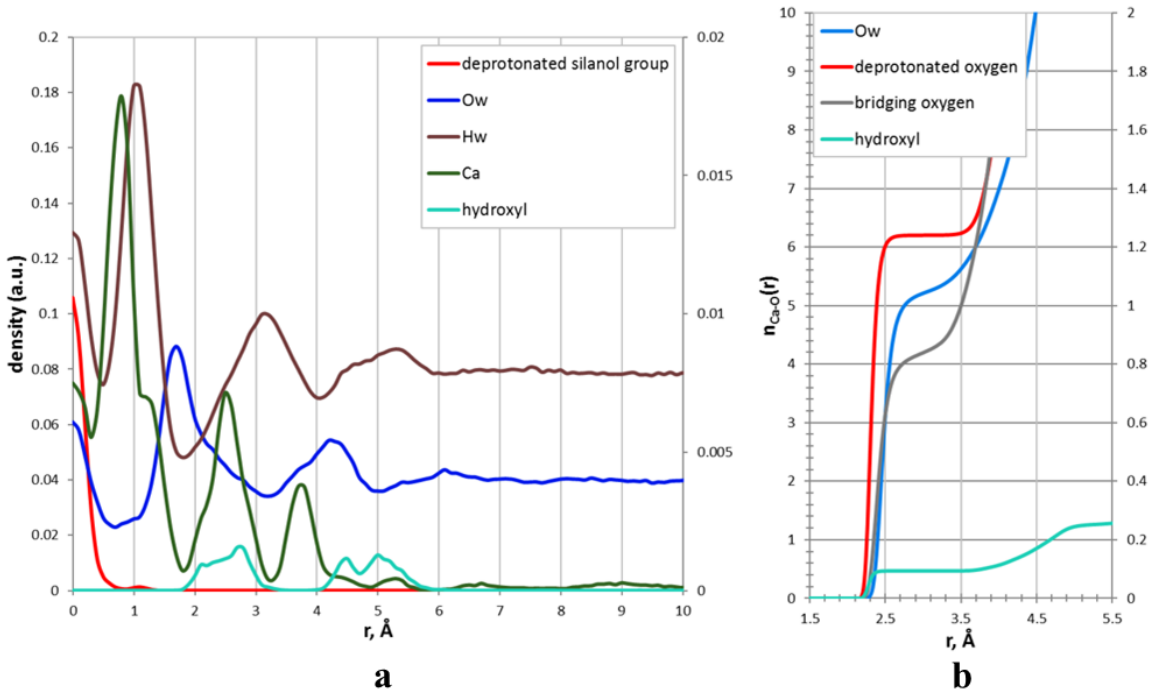

Figure 72. *The atomic density profiles near the CSH-1.4 surface* ***(a)*** *and the running coordination numbers for the pairs of* Ca^{2+} *with different oxygen atoms in the system* ***(b)****. Data for water atoms are presented on a different scale.*

Calcium cations form stronger complexes with the CSH-1.4 surface, and atoms also were shown to come much closer to the defected silicate layer (Ca^{2+} peak of the surface distribution at zero surface position, Fig. 72-a). The running coordination numbers show averages over all calcium present in the system, thus, the RCNs for the pairs (Ca^{2+} - $O_{deprotonated}$) and (Ca^{2+} - $O_{bridging}$) don't indicate directly how many oxygen atoms of the surface are involved in the complexation, but give an estimate of ~ 2 (n = 1.24 for the pair Ca^{2+} - $O_{deprotonated}$ and n = 0.86

for the pair Ca^{2+} - $O_{bridging}$). These are much higher values than the one observed for the CSH-0.83 interfaces (n (Ca^{2+} - $O_{deprotonated}$) = 0.22, no binding to bridging oxygen atoms in the first coordination shell). Together with the coordinating water molecules and solution hydroxyl groups, the total coordination number is $n \approx 7$, which is comparable with a typical coordination number for calcium cation in bulk aqueous solution. Considering that some Ca ions will form outer-sphere surface complexes, it can be assumed that the inner-sphere surface complexation should involve more than 2 oxygens. It is further confirmed by the analysis of the solution structure in selected layers parallel to the surface.

In all simulation boxes, a certain amount of OH^- ions is present in solution to compensate the total charge of the systems and to mimic the high pH of C-S-H equilibrated solutions. Hydroxyl anions have a strong affinity to metal cations; thus, they replace easily the H_2O molecules in the solvation shell. The binding of hydroxyls is strong and stable over the entire simulation time for all model systems as it can be seen from both atomic density profiles and the atomic density surface maps, as discussed below.

4.2.3. Surface maps of atomic density

Density profiles for water atoms and dissolved ions rapidly reach the value of the bulk solution (at d > 6-7 Å from the defined reference zero point), so that within one simulation box the mutual influence of one interface on another (separated by ~70 Å of aqueous solution) can be expected to be negligible, and they can both be treated as statistically independent.

The time averaged maps of atomic distribution near the surface provide useful information on the preferred sorption sites and relative mobility of the solution species on the C-S-H/solution interfaces. The surface maps of water in the first two layers are presented in Fig. 73. Atoms of the surface on the maps are presented as a reference background; they do not belong to the shown layers.

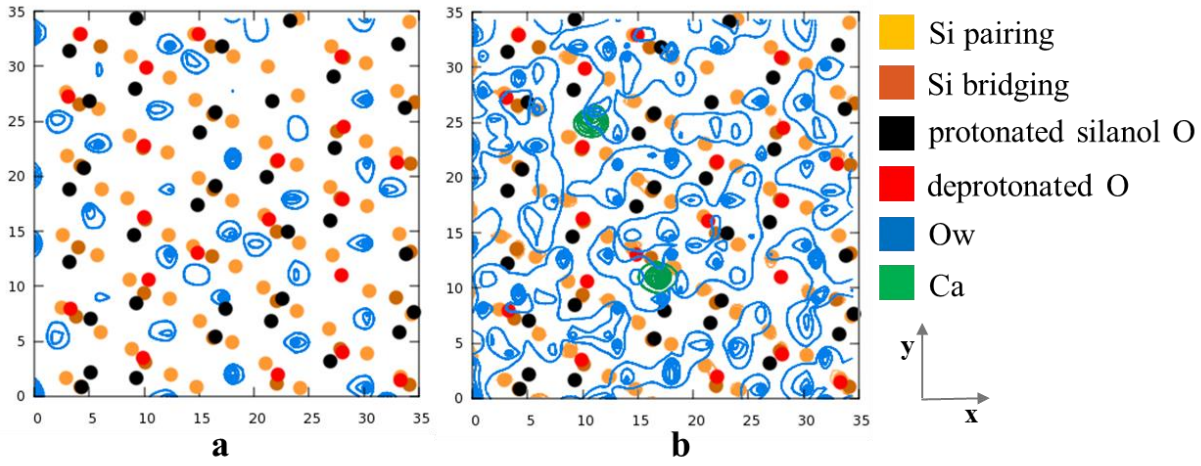

Figure 73. *The surface distribution of water oxygen atoms on the CSH-0.83 / water interface at different distances from the surface:* **(a)**– *(d < 1 Å),* **(b)** – *(1 Å < d < 3 Å).*

In Fig. 73(a) the water oxygens that are integrated into the C-S-H structure are clearly seen; while Fig. 73(b) presents water oxygen atoms coordinated around Ca^{2+} ions and also those attached to the surface.

Since the concentration of calcium is much higher, a stronger ordering of water molecules near the surface of CSH-1.0 is created (Fig. 74). Similarly to the CSH-0.83 surface, the first water layer (a) belongs to the CSH-1.0 structure, while the second layer (b) is sorbed on the surface or coordinated with the cations.

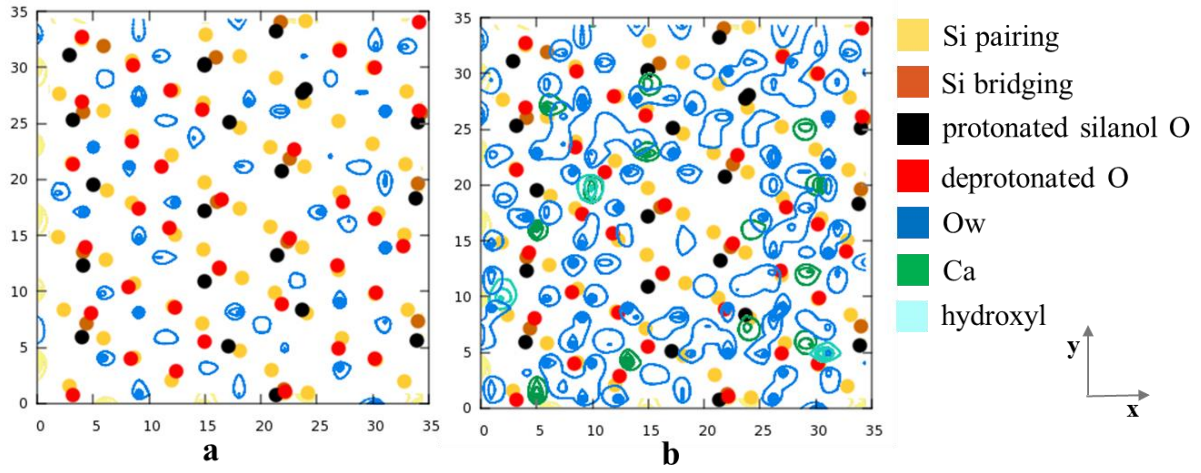

Figure 74. *The surface distribution of water oxygen atoms on the CSH-1.0 / water interface at different distance from the surface:* **(a)** *– (d < 1 Å);* **(b)** *– (1 Å < d < 2.5 Å).*

The CSH-1.4 surface has the highest amount of Ca^{2+} cations among the three modelled systems. As might be expected, even more water molecules are affected by the coordination with cations (Fig. 75). Water molecules near the surface are forming distinctive layers.

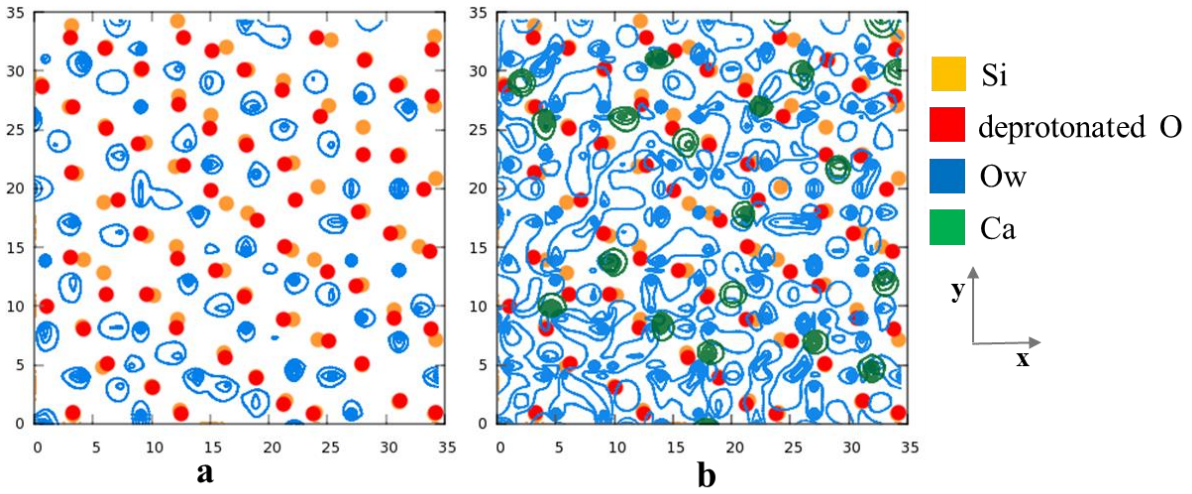

Figure 75. *The surface distribution of water oxygen atoms on the CSH-1.4 / water interface at different distance from the surface:* ***(a)*** *– (d < 1 Å),* ***(b)*** *– (1 Å < d < 2.5 Å).*

Calcium cations form strong complexes with deprotonated terminal silanol groups of C-S-H.

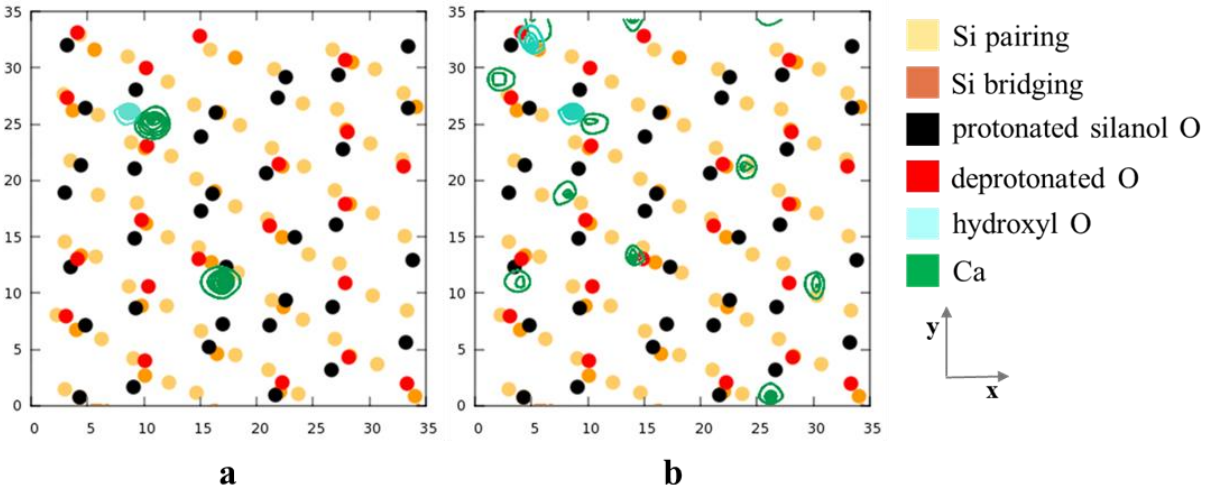

Figure 76. *The surface distribution of Ca^{2+} ions on the CSH-0.83 / water interface at different distance from the surface:* ***(a)*** *– (d < 1 Å),* ***(b)*** *– (1 Å < d < 3 Å).*

The structure of CSH-0.83 model has the least amount of surface defects and is the closest to the original mineral structure of tobermorite. Since it has most of the bridging tetrahedra in place, there are less available sites closer to the defined zero position of the surface. Two

layers of Ca^{2+} near the surface that contribute to inner-sphere complexation are identified by the calculation of surface distribution within the *xy* plane (Fig. 76). Water molecules are not shown there for image clarity. Oxygens of solution hydroxyl ions are replacing H_2O molecules in the first coordination sphere of calcium and can typically be found in the bonding proximity to the cations on the surface maps. A similar distribution is observed for CSH-1.0 (Fig. 77).

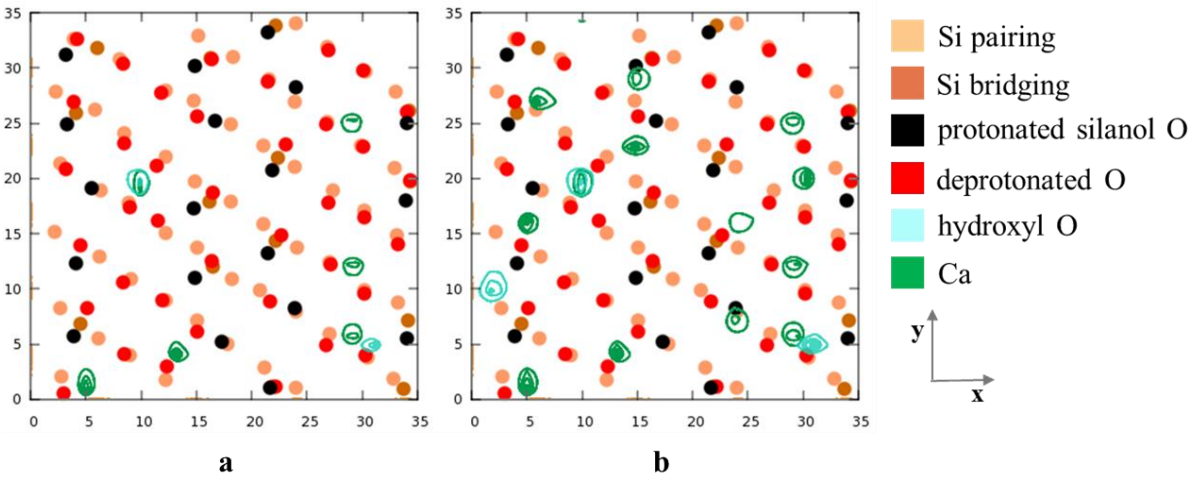

Figure 77. *The surface distribution of Ca^{2+} ions on the CSH-1.0 / water interface at different distance from the surface:* ***(a)*** *– (d < 2 Å),* ***(b)*** *– (2 Å < d < 3.5 Å).*

The distribution of calcium near the surface is similar for all three interfaces studied. The deprotonated surface has a higher negative charge and is much more attractive for the cations from solution. The Ca^{2+} cations closest to the surface are coordinated with 4 to 5 surface oxygens: typically, with 2 deprotonated sites and 2-3 bridging oxygens in the silicate layer. This complexation is strong and stable over the entire simulation time (Fig. 78).

Near the CSH-1.4 surface, the highest probability for Ca^{2+} binding is at the distance between 0.5 and 2 Å (see Fig. 71), and it represents the most typical sorption site for calcium cations. These cations are characterised by forming complexes with 3 oxygens of the surface: 2 deprotonated sites and 1 bridging oxygen atom. It is the same complexation type as the one already described for the CSH-1.0 interfaces.

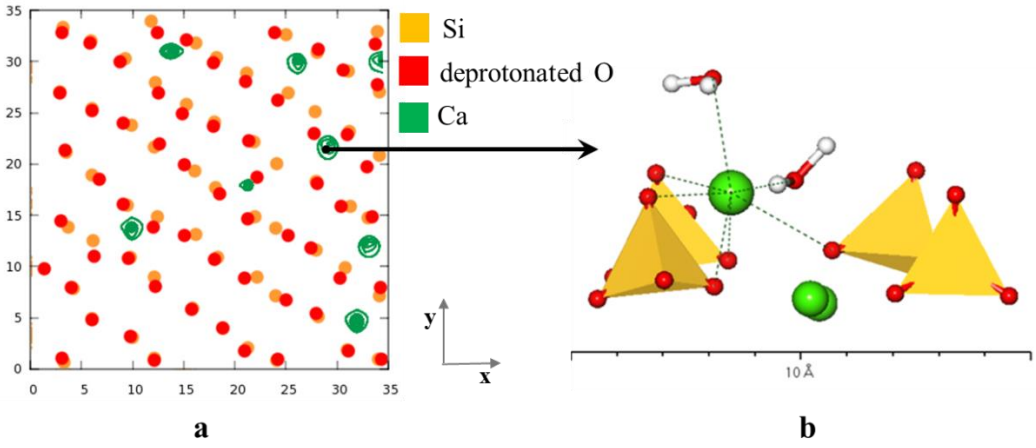

Figure 78. *Inner-sphere complex of calcium cation with CSH-1.4 surface:* **(a)** *- surface distribution of* Ca^{2+} *on the CSH-1.4 interface (distance from the surface: (-0.5) – 0.5 Å);* **(b)** *– extract from a simulation snapshot (yellow – silicon, green – calcium, red – oxygen, white – hydrogen).*

4.2.4. Preferential sorption sites and the corresponding free energy profiles

The variations in structure and surface charge distribution of the C-S-H surface models create different opportunities for the cations to bind. However, not all of the binding sites are equivalent, some of them offer better geometries for stronger binding and lower energies. A combinational analysis of the local structures, density profiles and surface maps for target atoms gives an insight of what are the preferential sorption sites on the surface.

In the case of the CSH-0.83 model, a small amount of Ca^{2+} can form monodentate complexes with deprotonated silanol groups of pairing silicon tetrahedra (1 Å < *d* < 2.5 Å, Fig. 79-a) while most of the sorbed cations are coordinated with deprotonated silanol group of bridging tetrahedra (3 Å < *d* < 4.5 Å, Fig. 79-b). The other half of cations form outer-sphere complexes (only water oxygens are present in the first coordination shell) and can be found near the surface in the layer 4.5 Å < *d* < 6.5 Å. The presence of calcium cations near the surface leads to a strong ordering of water molecules as it was noticed before.

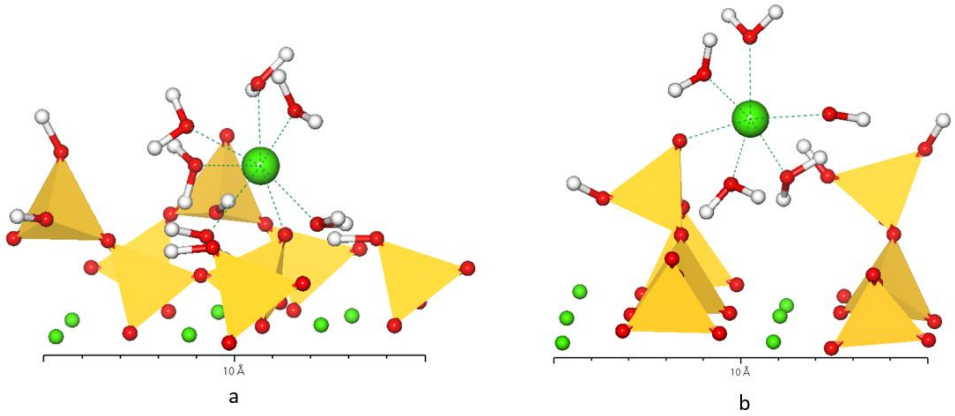

Figure 79. *Inner-sphere complexation of Ca^{2+} ions on the CSH-0.83 surface:* **(a)** *– monodentate binding to deprotonated silanol group of pairing silicon tetrahedron,* **(b)** *– monodentate binding to deprotonated silanol group of bridging silicon tetrahedron.*

In the CSH-1.0 systems, the quantity of calcium ions is much higher. All of the introduced cations were attracted to the surface and formed inner-sphere and outer-sphere complexes with the surface oxygen atoms. Calcium not only comes closer to the surface, as it was evident from the density profiles above, but also forms stronger bidentate and tridentate complexes with combinations of deprotonated sites, protonated silanol groups, and bridging oxygen atoms (Fig. 80).

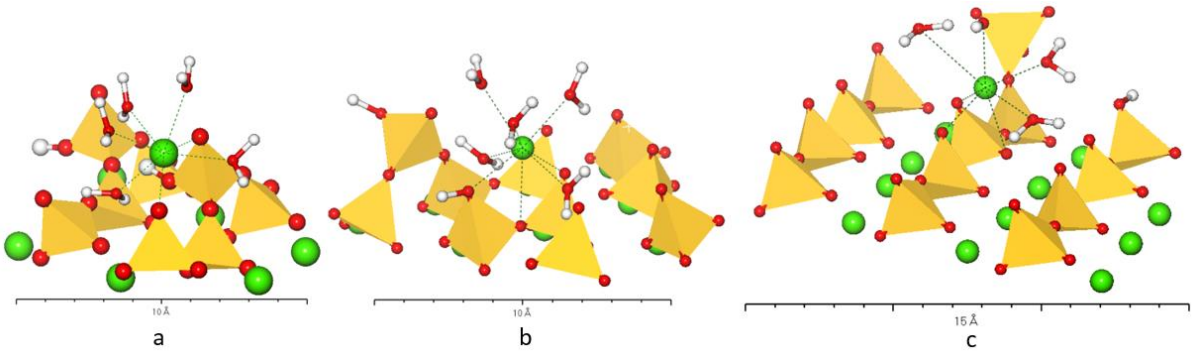

Figure 80. *Inner-sphere complexation of Ca^{2+} on the CSH-1.0 surface:* ***(a)*** *– bidentate with deprotonated oxygens of pairing and bridging silicon tetrahedra;* ***(b)*** *– tridentate with deprotonated, protonated sites of pairing tetrahedra, and bridging oxygen;* ***(c)*** *– tridentate with two deprotonated sites and a bridging oxygen.*

The CSH-1.4 surface provides much more easily accessible negatively charged sorption sites. On average, the strongest binding is expected for Ca^{2+} that is coordinated by a maximum

number of surface oxygens in the solvation shell, but statistically, the expected binding is due to the coordination with two deprotonated silanol groups.

Three most typical sorption sites for Ca^{2+} on the C-S-H surfaces were selected for constrained (biased) MD simulations and the calculations of the potential of mean force (PMF) in order to obtain quantitative information about the site-specific free energy profiles as functions of distance from the surface:

1. The deprotonated silanol group of the bridging silicon tetrahedron on the CSH-0.83 surface (Fig. 79-b).
2. The deprotonated silanol group of the pairing silicon tetrahedron on the CSH-0.83 surface (Fig. 79-a).
3. Two deprotonated silanol groups and a bridging oxygen of the pairing silicon tetrahedron on the CSH-1.4 surface (Fig. 80-b).

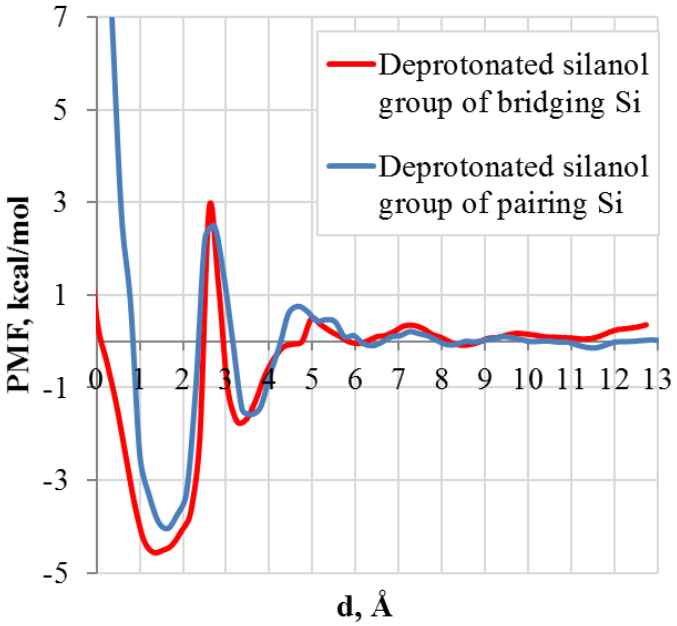

Figure 81. *The potential of mean force as a function of distance between Ca^{2+} and two chosen deprotonated silanol groups of the CSH-0.83 surface.*

The selected sorption sites are also typical for the CSH-1.0 model surface . Figure 81 shows the PMFs calculated using the umbrella sampling algorithm for Ca^{2+} above the two selected CSH-0.83 binding sites. However, Ca^{2+} is not located strictly above the selected sorption sites, so the position of the first minimum does not represent the bond distance, but shows only how close the cation is to the surface on average; the *z*-coordinate of the selected

deprotonated oxygen site is taken as a reference zero distance. The depth of the potential minimum is the same for both sorption sites sampled. The first potential well (at $d \approx 1.6$ Å) corresponds to the inner-sphere coordination to the deprotonated surface oxygen, while the second minimum (at $d \approx 3.5$ Å) to the outer-sphere coordination. The energy barrier between the inner- and outer-sphere complexes is 7.5 kcal/mol for the bridging Si site and 6.5 kcal/mol for the pairing Si site.

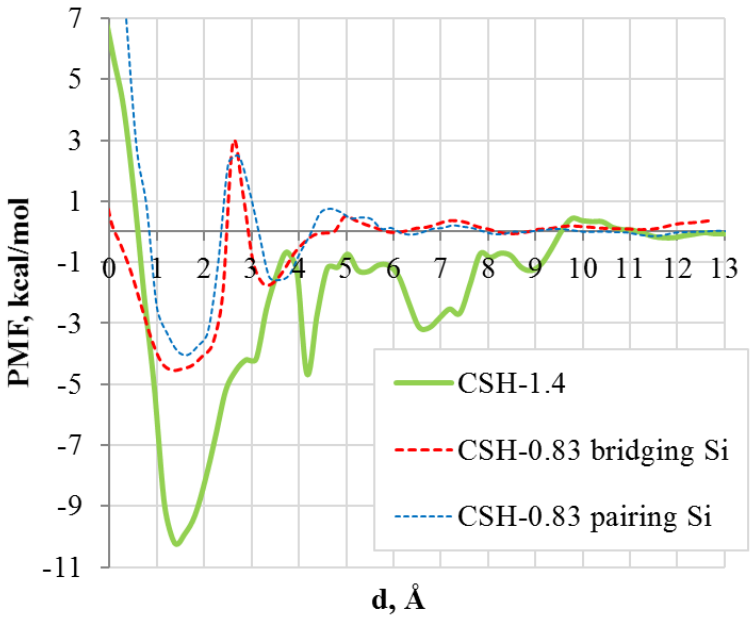

Figure 82. *The potential of mean force as a function of distance between Ca^{2+} and two deprotonated silanol groups of the CSH-1.4 surface. Dotted lines represent the results for the CSH-0.83 surface for comparison.*

Figure 82 shows the PMF calculated for Ca^{2+} coordinated with two deprotonated silanol groups and one bridging oxygen of the CSH-1.4 surface. The PMF oscillations can be associated with the local structural properties of the interface for the selected cation and sorption site (the influence of other neighbouring ions, the high negative charge of the surface and water ordering through hydrogen bonding). The complexation of Ca^{2+} with the CSH-1.4 surface sorption site is much stronger than for the other surfaces studied with the deepest free energy well of ~-10 kcal/mol and the first energy barrier of approximately 9 kcal/mol between the inner-sphere and outer-sphere coordinations.

4.3. Uranium on the C-S-H surface

4.3.1. Local structural properties

The sorption of U(VI) on C-S-H surfaces had been studied as the next step. Three interfaces were modelled (Table 8). Although the number of uranyl ions introduced to the system is limited to 8, some aqua complexes are adsorbed on the C-S-H surface. All uranyl ions adsorbed on the surface stay in a five-fold coordination with oxygens in the equatorial plane.

Table 8. The atomic composition of the simulated C-S-H/uranyl solution interfaces.

Name	**Ca/Si**	N_{total}**, atoms**	**Solution composition**
CSH-0.83U	0.83	15561	4463 H_2O, 16 aqueous hydroxyls, 22 Ca^{2+}, 6 UO_2^{2+}
CSH-1.0U	1.0	15506	4478 H_2O, 16 aqueous hydroxyls, 42 Ca^{2+}, 6 UO_2^{2+}
CSH-1.4U	1.4	15532	4533 H_2O, 16 aqueous hydroxyls, 62 Ca^{2+}, 6 UO_2^{2+}

The radial distribution functions for U(VI) – oxygen pairs and corresponding coordination numbers for C-S-H with Ca/Si = 0.83 are reported in Figure 83. Water oxygens are statistically dominating and are shown there with a different scale for clarity. The uranyl cation forms a monodentate surface complex with deprotonated sites (single peak at 2.4 Å with n (2.4 Å) ≈ 0.19) and also strongly attracts the solution hydroxyl ions (n (2.4 Å) ≈ 1). It can be seen that the binding to the protonated silanol groups of the CSH-0.83 surface in the first coordination shell is not favoured.

Previous studies have shown that the linear $[O=U=O]^{2+}$ structure is preserved upon sorption onto C-S-H or incorporation in the C-S-H structure (Harfouche et al., 2006; Tits et al., 2011; Macé et al., 2013). Furthermore, the inner-sphere coordination of UO_2^{2+} is assumed to be the predominant type of interaction with the surface.

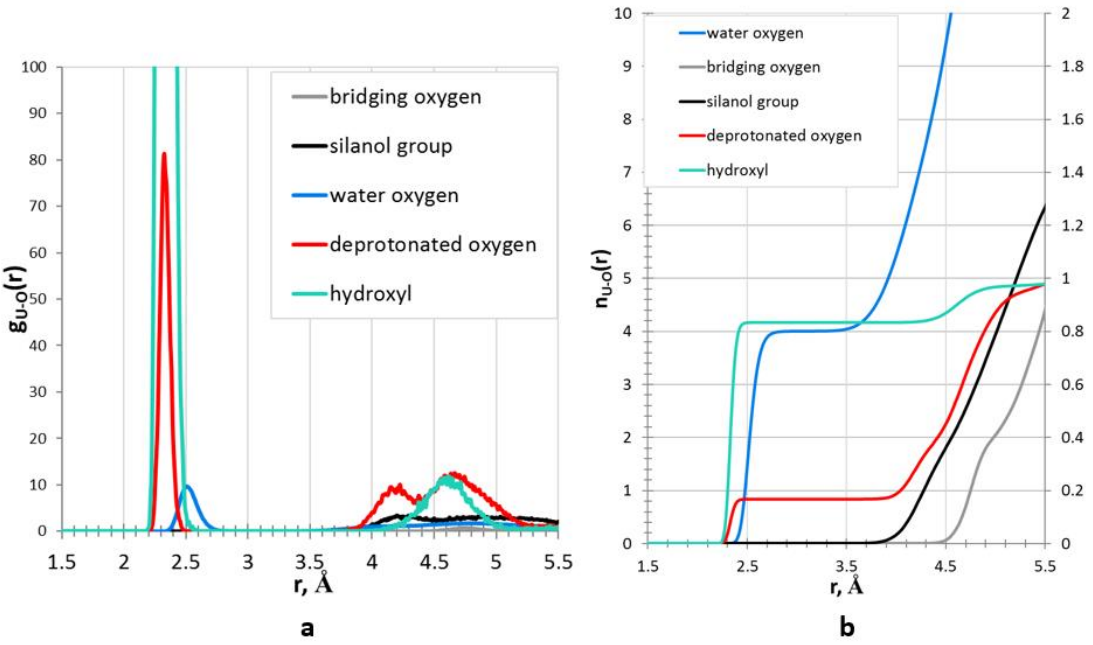

Figure 83. **(a)** – *The radial distribution functions for U-O pairs (CSH-0.83 interface);* **(b)** – *the running coordination numbers for U-O pairs.*

It can be noticed that uranyl complexation with the surface groups of pairing silicon tetrahedra is blocked by the presence of two axial oxygen atoms and a considerable number of bridging tetrahedra on the C-S-H surface at the lowest Ca/Si ratio. But differences in interaction with the CSH-1.4 surface can be seen for uranyl cations in Figure 84.

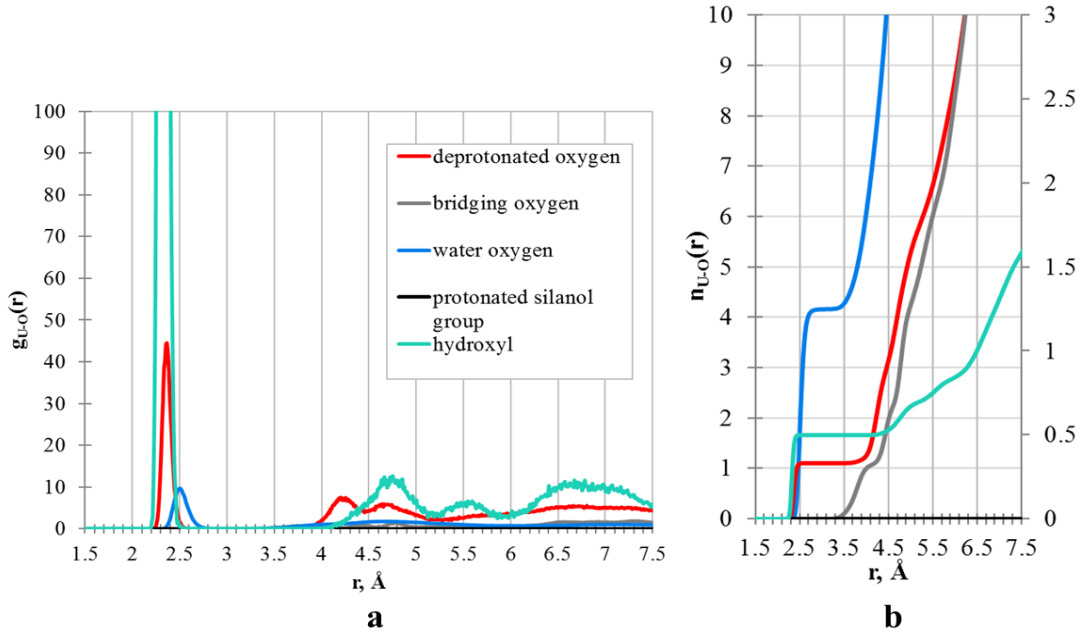

Figure 84. **(a)** – *The radial distribution functions for U-O pairs (CSH-1.4 interface);* **(b)** – *the running coordination numbers for U-O pairs.*

Since all bridging silicon tetrahedra are missing at this surface, it is much easier for uranyl cations to reach the deprotonated sites of the pairing tetrahedra and to form inner-sphere complexes. At first glance, it can be confirmed by the comparison of results on running coordination numbers in Figs. 83(b) and 84(b) that more deprotonated silanol groups are coordinated with UO_2^{2+} in the CSH-1.4 case.

4.3.2. Surface density profiles

The calculated atomic density profiles reveal clear differences in the uranyl/C-S-H coordination at two Ca/Si ratios. Two types of complexes can be seen forming at the CSH-0.83 surface (Fig. 85-a) with UO_2^{2+} peaks located, respectively, around 3-4 Å (inner-sphere surface complex) and at 5-6 Å (outer-sphere surface complex). Due to the low concentration of uranyl, its effect on the water structuring is less noticeable here than in the case of Ca^{2+}.

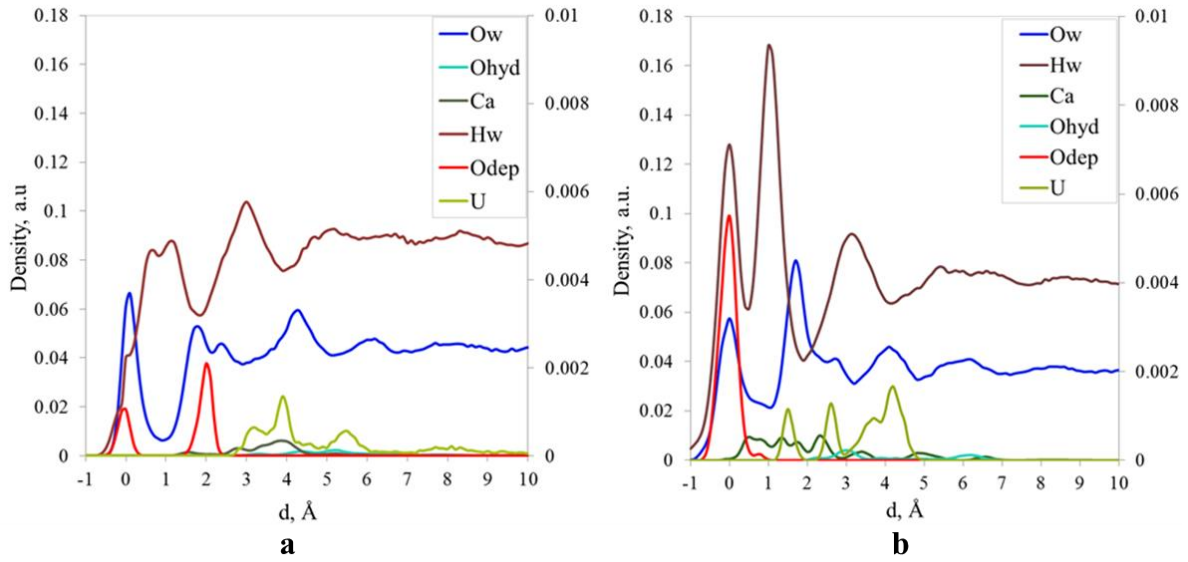

Figure 85. *The atomic density profiles of UO_2^{2+} solutions near C-S-H surfaces:* ***(a)*** *– CSH-0.83;* ***(b)*** *– CSH-1.4. The profiles of U are shown with an enlarged auxiliary scale for clarity. Abbreviations: Ow and Hw – O and H of water; Ohyd – O of the solution hydroxyl group; Odep – deprotonated silanol group of the surface.*

When the surface contains only Si dimers (as in CSH-1.4) a new sorption site can be identified. In this case, the atomic density profile of uranium distribution near the surface (Fig. 85-b) reveals three distinct peaks instead of two. The peak positions are shifted closer to the surface since all bridging Si tetrahedra are absent in this C-S-H model.

The first peak (at ~1-2 Å) corresponds to the uranyl cations complexing with two deprotonated silanol groups of the surface in their coordination sphere (bidentate coordination). A monodentate inner-sphere complexation of uranyl with the surface is evidenced by the second peak of uranyl distribution (at ~ 2-3 Å from the surface). Among them, hydroxyl bridging complexes are observed but they are not studied in detail here. Similar to other interfaces, the uranyl cations located more than 3 Å from the surface are assumed to be forming outer-sphere complexes and preserve their hydration shell almost unperturbed.

4.3.3. Surface maps of atomic density

The observed outer-sphere complexes of UO_2^{2+} with C-S-H surfaces are mostly coordinated by two deprotonated hydroxyls of the bridging Si tetrahedra. The positions of UO_2^{2+} complexes can be easily identified looking at the calculated atomic distributions within specific layers of the solution at specific distances from the surface (see Fig. 86). A bidentate complexation becomes possible for the more defected surface (Fig. 87).

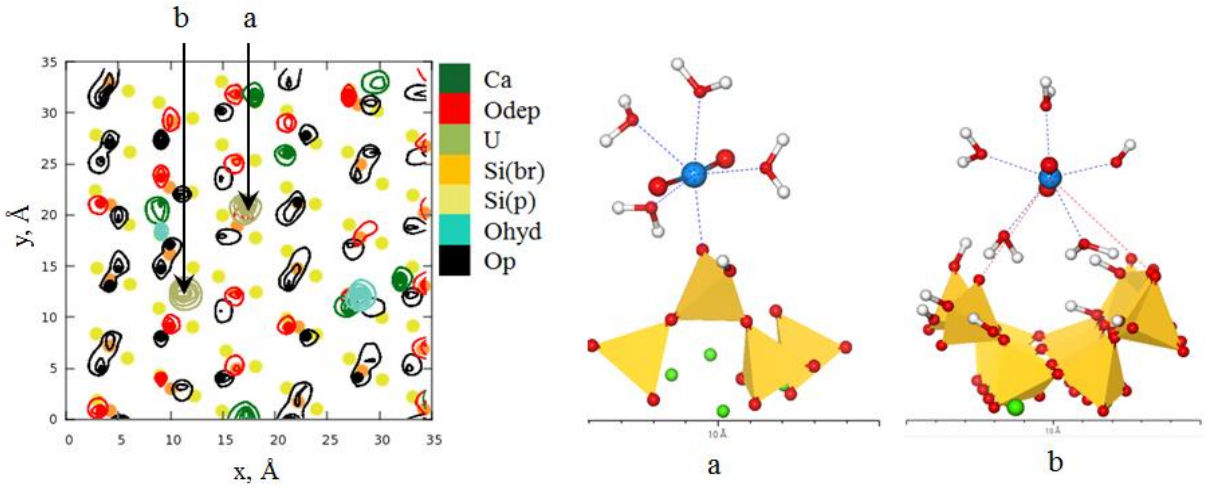

Figure 86. *The time-averaged distribution of UO_2^{2+} ions at the CSH-0.83 interface within 2.5 – 4.5 Å from the surface (the first molecular layer).* **(a)** *– the inner-sphere UO_2^{2+} surface complex;* **(b)** *– the outer-sphere UO_2^{2+} surface complex. The colour scheme: yellow – Si, red – O, white – H, blue – U.*

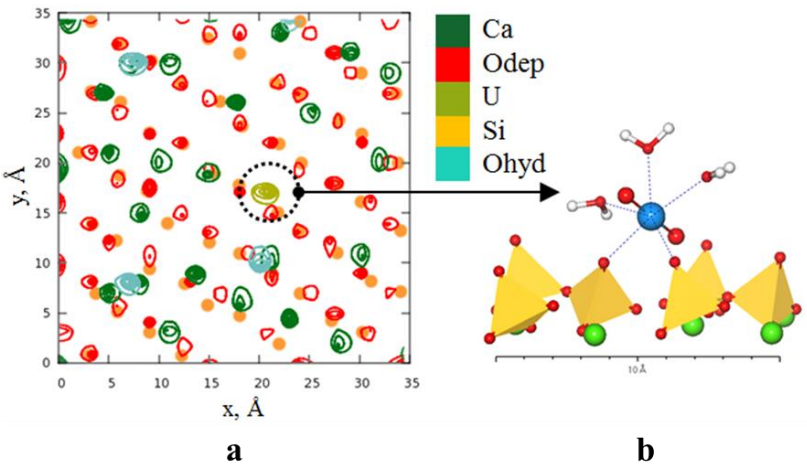

Figure 87. *The time-averaged distribution of UO_2^{2+} ions at the CSH-1.4 interface within 1.0 – 2.0 Å from the surface:* **(a)** *- the first molecular layer;* **(b)** *– the inner-sphere UO_2^{2+} surface. The colour scheme is the same as in Fig. 86.*

4.3.4. Preferential sorption sites and the corresponding free energy profiles

In general, UO_2^{2+} cations are bound to the same surface sites as Ca^{2+} cations and a competition between them can be expected (Fig. 88). There is also a preferential UO_2^{2+} sorption on deprotonated sorption sites (more negatively charged). When all of the surface silanol groups are deprotonated under high pH conditions, the bidentate adsorption configuration is strongly preferred over the monodentate configuration.

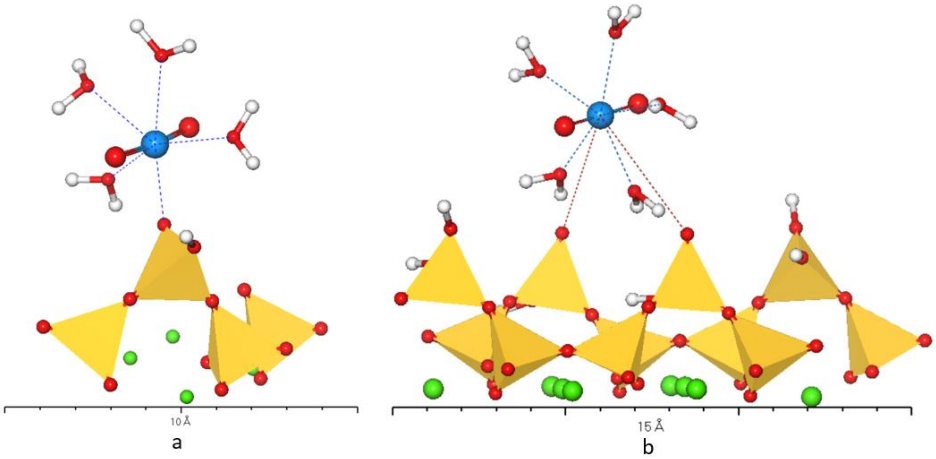

Figure 88. *The inner-sphere complexation of UO_2^{2+} ions on the CSH-0.83 surface:* **(a)** *– the monodentate binding to the deprotonated silanol group of the bridging silicon tetrahedron;* **(b)** *– the outer-sphere surface complexation. The colour scheme: yellow – silicon, red – oxygen, white – hydrogen, blue – uranium.*

In addition, hydroxyl ions in solution may form ion bridges between metal cations as it is seen in Fig. 89. The outer-sphere complexation like this can be assumed to be one of the possible binding mechanisms of UO_2^{2+} on calcium silicate hydrate surfaces.

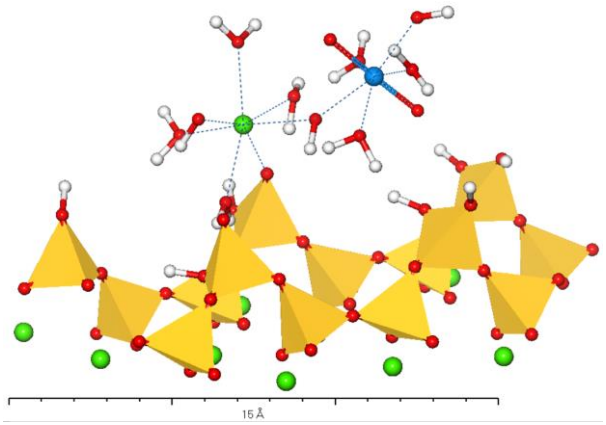

Figure 89. *The outer-sphere bridging complexation of UO_2^{2+} on the C-S-H surface.*

The free energy profile of an uranyl cation (Fig. 88-a) as a function of distance from the binding site was calculated and compared to the corresponding profile of Ca^{2+} above the same site. The results are presented in Figure 90.

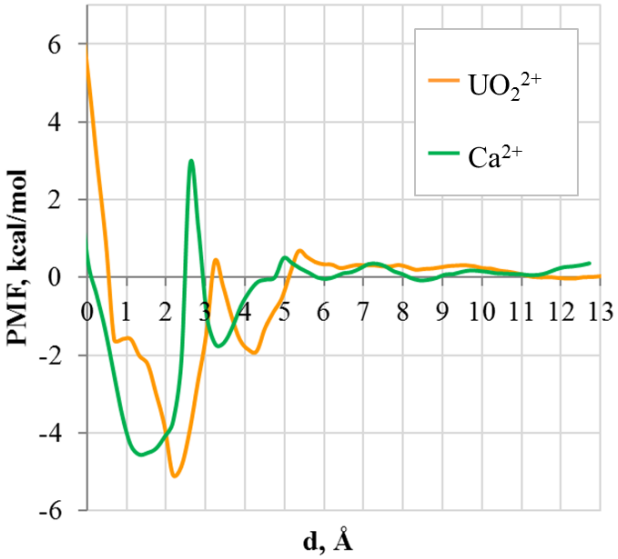

Figure 90. *The potential of mean force as a function of distance between UO_2^{2+}, Ca^{2+} and deprotonated silanol group of a bridging Si tetrahedra on the CSH-0.83 surface.*

There are two main energy minima at ~2.5 and ~4.5 Å from the surface which correspond to the formation of the inner- and outer-sphere complexes, respectively. As the comparison shows, UO_2^{2+} binds further from the surface than Ca^{2+} and the energy barrier for the transition

between two surface complexes is about 5.5 kcal/mol, which is 2 kcal/mol smaller than for Ca^{2+}.

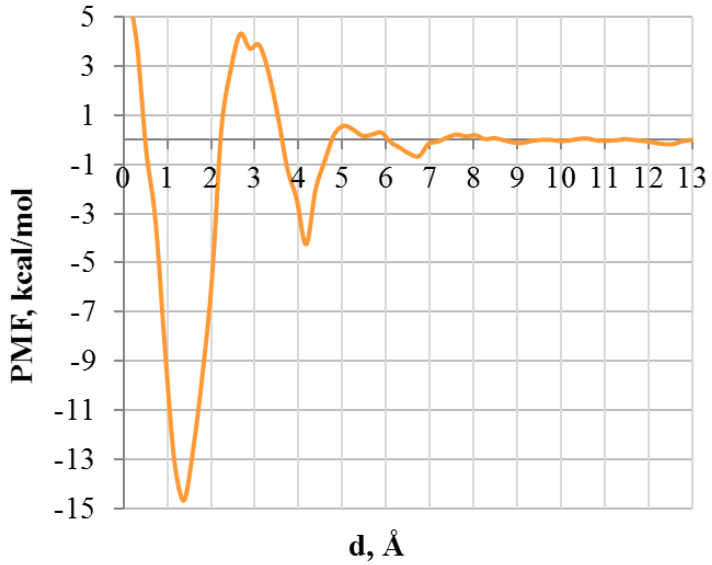

Figure 91. *The potential of mean force as a function of distance between UO_2^{2+} and deprotonated silanol groups of the CSH-1.4 surface.*

The free energy of adsorption was also evaluated for a typical sorption site on the CSH-1.4 surface (Fig. 91). In this case, the coordination of UO_2^{2+} with surface oxygens differs from the typical coordination for Ca^{2+} and does not involve bridging oxygens. Similar to the profile near the oxygen of bridging Si, the PMF profile in Fig. 91 shows two minima: around 1.5 Å and 4.0 Å from the surface. The binding to the CSH-1.4 surface is much stronger than to the CSH-0.83 surface, and the energy barrier between the inner-sphere and outer-sphere complexation is very high: approximately 18 kcal/mol. The transition from the outer-sphere surface complex to the aqueous bulk species also requires twice as much energy (4.5 kcal/mol for the CSH-1.4 surface and 2 kcal/mol for the CSH-0.83 surface).

4.4. Gluconate on the C-S-H surface

4.4.1. Local structural properties

The adsorption behaviour of the organic anion (gluconate) was also evaluated using the same C-S-H – solution models (Table 9) both for the systems with and without uranyl cations, thus modelling binary as well as ternary systems.

Table 9. Atomic composition of the simulated C-S-H/gluconate solution interfaces

Name	Ca/Si	N_{total}, atoms	Solution composition
CSH-0.83G	0.83	15685	4466 H_2O, 8 aqueous hydroxyls, 27 Ca^{2+}, 6 gluconate molecules
CSH-1.0G	1.0	15633	4282 H_2O, 8 aqueous hydroxyls, 47 Ca^{2+}, 6 gluconate molecules
CSH-1.4G	1.4	15662	4533 H_2O, 8 aqueous hydroxyls, 67 Ca^{2+}, 6 gluconate molecules
CSH-0.83GU	0.83	15649	4445 H_2O, 14 aqueous hydroxyls, 24 Ca^{2+}, 6 gluconate molecules, 6 UO_2^{2+}
CSH-1.0GU	1.0	15623	4468 H_2O, 16 aqueous hydroxyls, 45 Ca^{2+}, 6 gluconate molecules, 6 UO_2^{2+}
CSH-1.4GU	1.4	15652	4519 H_2O, 16 aqueous hydroxyls, 65 Ca^{2+}, 6 gluconate molecules, 6 UO_2^{2+}

Figure 92 shows the time-averaged radial distribution functions and running coordination numbers for Ca-O pairs in the CSH-0.83/Gluconate system. Gluconate forms stable complexes with Ca cations. Calcium coordinates carboxylic functional groups of gluconate, and the distance between Ca and oxygen atoms of the carboxyl group is comparable to the distance between Ca and Ow: ~2.5 Å.

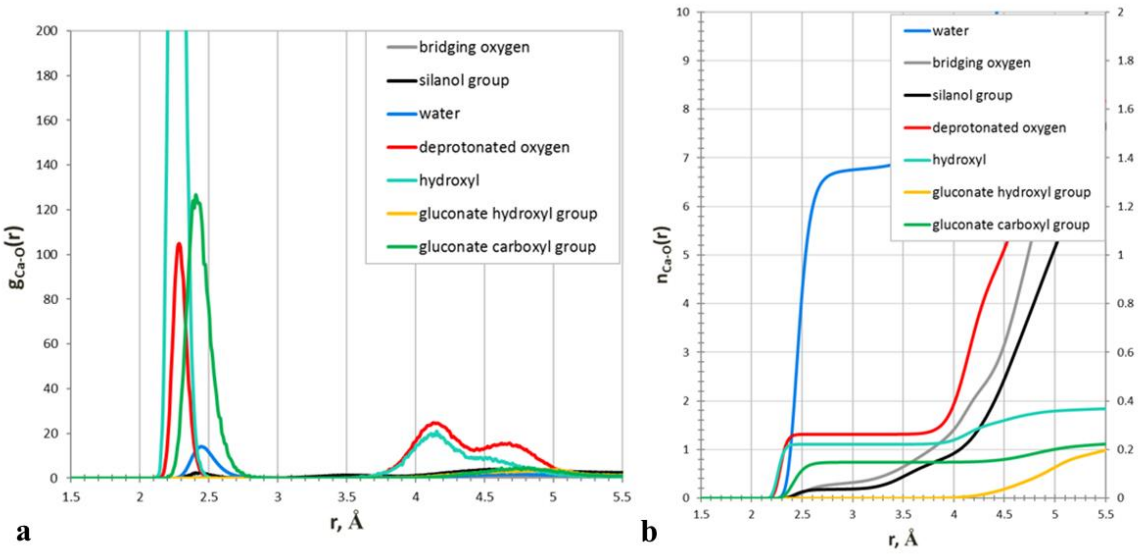

Figure 92. ***(a)*** *– The radial distribution functions for Ca-O pairs (CSH-0.83/gluconate solution) and* ***(b)*** *– the running coordination numbers for Ca-O pairs.*

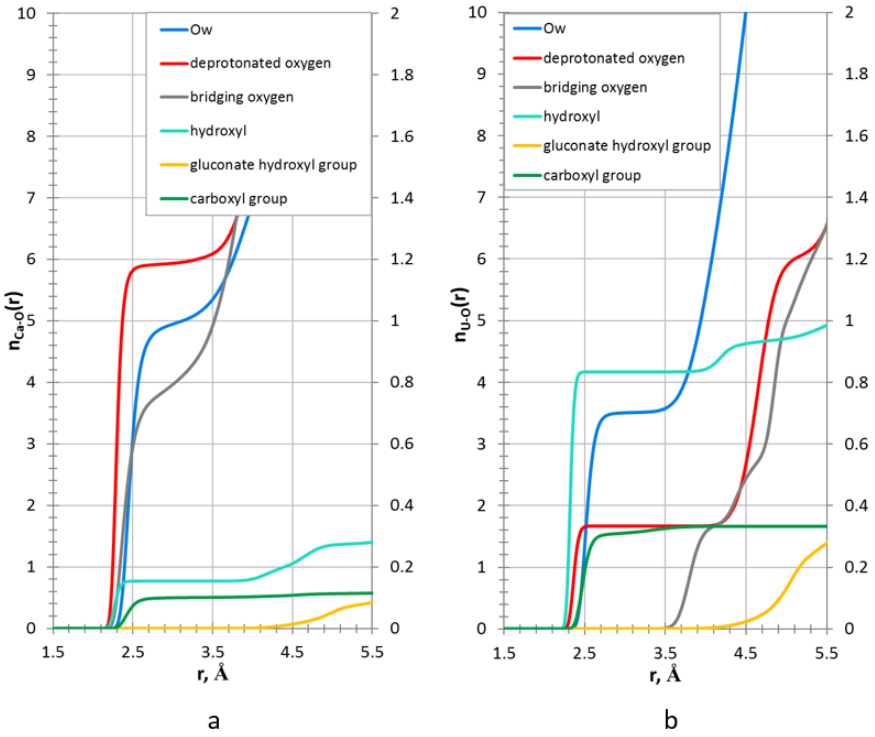

Figure 93. *The running coordination numbers for pairs of* Ca^{2+} **(a)** *and* UO_2^{2+} **(b)** *and different oxygen atoms in the CSH-1.4 interfaces (left scale for Ow).*

No major differences in the gluconate behaviour at the CSH-1.4 interface were found (Fig. 93). The organic anion forms complexes with Ca^{2+} and UO_2^{2+} cations. For both cations the carboxyl group of gluconate replaces H_2O molecules in the forst coordination shell of the cation with the bond lengths comparable to Ca-Ow (2.4 Å) and U-Ow (2.5 Å) distances in water. Gluconate anions showed stronger affinity to calcium cations than to uranyl cations; no binding to uranyl ions was observed in the unconstrained MD run for the CSH-0.83 system.

4.4.2. Surface density profiles

The molecular structure of the adsorption layers at the solution-solid interface was investigated and the results are shown in Fig. 94.

Negatively charged gluconate anions cannot form inner-sphere complexes directly with the C-S-H surface, which is also nominally negatively charged. However, as the analysis of C-S-H/gluconate interface shows, it can create complexes with Ca^{2+} ions present on the surface (cation bridging complexation). This cation bridging can be clearly identified from the calculated atomic density profiles of various species at the interface (Fig. 94): Ca^{2+} at distances of ~0.5-1.5 Å forms inner-sphere complexes with the deprotonated surface sites

(defined as d = 0 Å) and is further coordinated by carboxyl groups of gluconate (the peak of Ocarb at 2.5-3.5 Å).

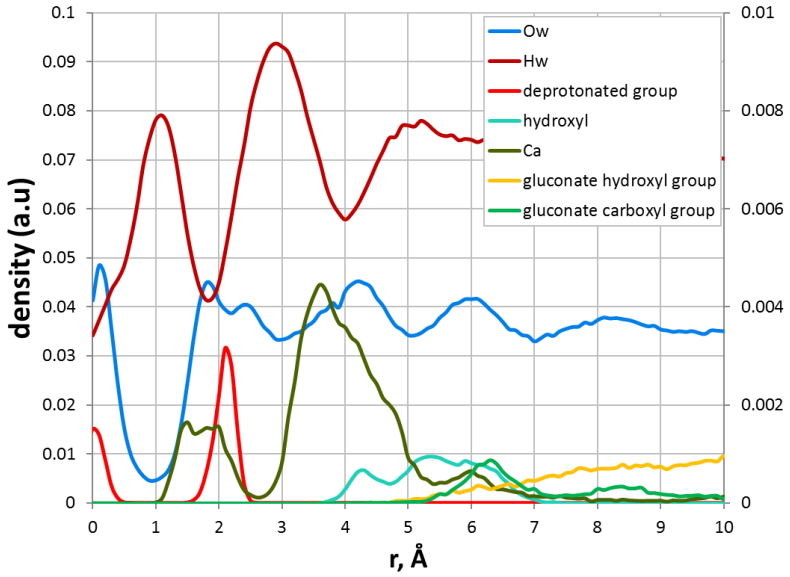

Figure 94. *Atomic density profiles near the CSH-0.83 surface for the solution containing gluconate anions.*

Like the binary surface complexes discussed above for uranyl cations, the complexation with gluconate in ternary solutions can be classified as inner-sphere and outer-sphere. The inner-sphere complexes are formed when the carboxyl group of gluconate is bound directly to the adsorbed cation (cation bridge), the weaker outer-sphere complex is formed when solvent molecules (H_2O or OH^-) are present between the carboxyl group and the surface. Both types of complexes were observed in our simulations.

4.4.3. Surface maps of atomic density

In the aqueous environment the adsorption mechanism of organic molecules changes significantly in comparison with dry surfaces. Water molecules can displace the introduced organics from the surface sites due to their interactions with the polar functional group (e.g. with gluconate hydroxyl groups). When the concentration of gluconate ions in solution is relatively low, the molecules will mostly attach to the surface through the most active functional group – deprotonated carboxyl group (a so called single-group adsorption). As it has already been seen from the RDF and RCN results, the hydroxyl groups of gluconate do not contribute to complexation.

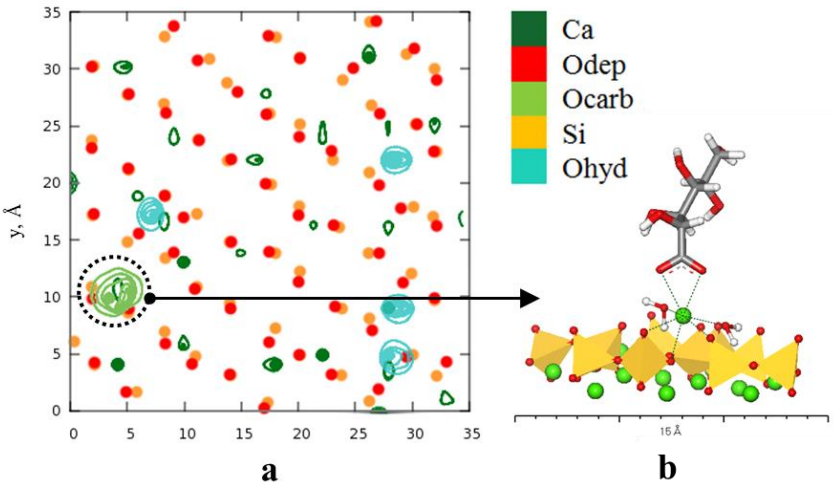

Figure 95. *The time-averaged distribution of Ca^{2+} ions and carboxyl oxygens of gluconate at the CSH-1.4 surface* **(a)**, *and a snapshot illustrating cation bridging surface complexation* **(b)**. *Ocarb – oxygen of the gluconate carboxylic group, other notations as in previous figures.*

In addition, two more types of cation bridging complexation for gluconate were detected on the CSH-1.4 surface: an outer-sphere UO_2^{2+} bridging complex (Fig. 96) and an inner-sphere Ca^{2+} bridging complex (Fig. 95). The hydroxyl groups of gluconate do not participate in complexation. To sum up, metal cations introduced to the system facilitate the sorption of organic anions from solution, and both inner-sphere and outer-sphere bridging complexation is possible. Yet the coordination with cations that are bound with 4-5 surface oxygens is less probable – no complexes of this kind were detected in the current simulations.

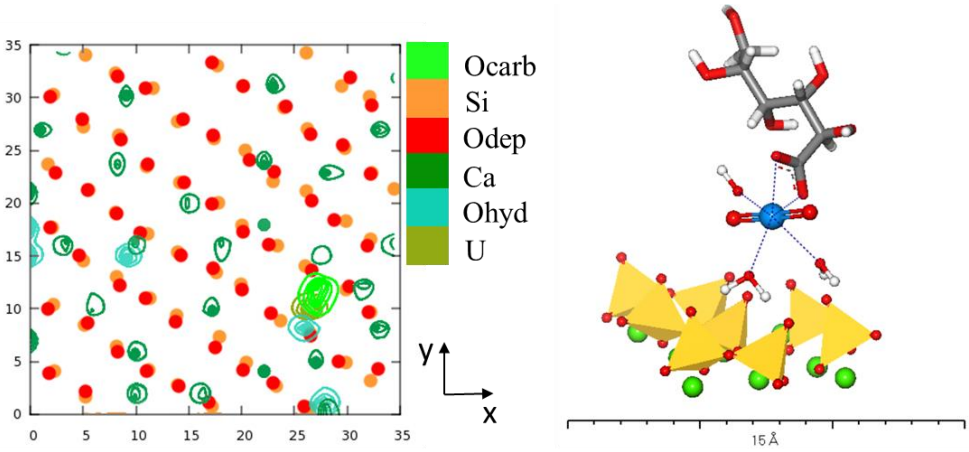

Figure 96. *The time-averaged distribution of UO_2^{2+} ions and carboxyl oxygens of gluconate at the CSH-1.4 surface* **(a)**, *and a snapshot illustrating the cation bridging surface complexation* **(b)**. *Ocarb – oxygen of the gluconate carboxylic group, other notations as in previous figures.*

4.4.4. Preferential sorption sites and the corresponding free energy profiles

Water molecules in the first solvation shell of Ca^{2+} are bound stronger to the cation than in the case of UO_2^{2+} since uranyl cation has a larger ionic radius with the same charge. Thus, it is more favourable for carboxyl oxygens to replace H_2O molecules and to form stable long-lived complexes (on the MD simulation timescales) with Ca^{2+} than with UO_2^{2+}. These results are consistent with the time-averaged structural properties of the solutions and interfaces discussed earlier.

Figure 97 shows the PMF calculated for Ca^{2+} that is bound to the deprotonated silanol of a bridging Si tetrahedron and a gluconate carboxyl group in the first coordination shell. Constrains in the simulation were applied only to the Ca^{2+} ion. The first minimum at d = 1.5 Å is due to the same inner-sphere complexation as for the organic-free system, but the energy necessary to replace surface oxygen by a water molecule is lower by half in the presence of gluconate: 3 kcal/mol. Also, the second minimum that corresponds to the outer-sphere complexation disappears here. So, the binding of Ca^{2+} becomes less strong and potentially may create higher possibility of substitution for a competing cation (UO_2^{2+}) from solution.

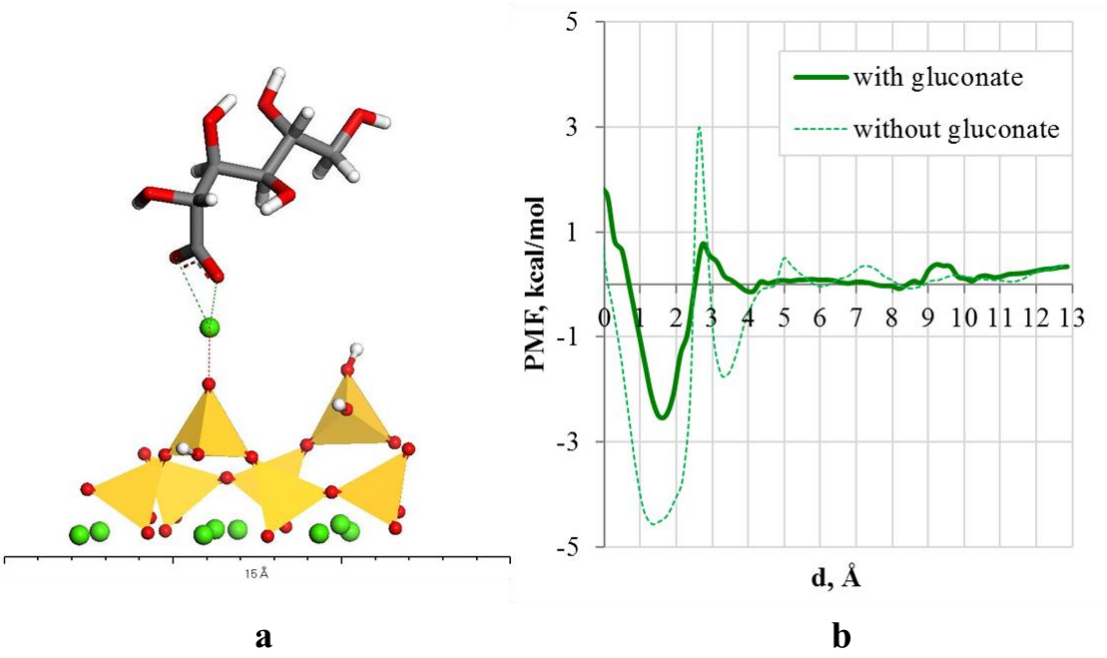

Figure 97. *The selected sorption site* **(a)** *and the potential of mean force as a function of distance between* Ca^{2+} *and a deprotonated silanol group of bridging Si tetrahedra on the CSH-0.83 surface with and without gluconate ion* **(b)**.

These results are in good agreement with observations of Nalet and Nonat (2016) that gluconate has strong calcium complexing properties and, when in contact with C-S-H phase, can cause an increase in Ca^{2+} concentration in the equilibrated solution.

4.5. Chapter conclusions

In this chapter the MD simulation results was analysed for bulk aqueous gluconate solutions, three hydrated C-S-H models that correspond to three Ca/Si ratios, and their interfaces with different solutions.

A detailed comparison of the hydrated C-S-H interfaces and the same interfaces in contact with U(VI)-containing solutions allowed us to identify and describe structurally different potential sorption sites of C-S-H as a function of the modelled Ca/Si ratio. There are several adsorption sites for uranyl cations on C-S-H surfaces. They can form monodentate and bidentate complexes with deprotonated oxygens of the surface. The same sites also adsorb Ca^{2+}, and a competition for these sites between the cations can be expected. Free energies of adsorptions were evaluated and compared for the most typical surface binding scenarios. It was found that C-S-H with Ca/Si = 0.83 has two energetically equivalent sorption sites for Ca^{2+}, and only one accessible for UO_2^{2+}. A more structurally defective C-S-H model with higher negative charge provides sites that adsorb cations much stronger, according to the calculated PMF profiles.

In aqueous solution gluconate forms complexes with Ca^{2+} and UO_2^{2+} cations, and the complexation with calcium was found to be more favourable than the complexation with uranyl cations. The resulting local structural environments for cations were shown to be in agreement with available literature data. Gluconate sorbs on the C-S-H phase via carboxyl functional group forming cation bridging inner-sphere and outer-sphere complexes with the surface. When present in the first coordination shell, gluconate affects Ca^{2+} sorption on C-S-H by lowering the bonding energy between the cation and the deprotonated silanol group of the surface.

Conclusions and Outlook

The main objective of this work was to identify the most probable molecular mechanisms of the interaction in three-component systems (C-S-H/organic additive/U(VI)) that models cement in the context of a radioactive waste repository and to characterise and describe these mechanisms quantitatively. To achieve this objective two complementary approaches were used: wet chemistry experiments and computational molecular modelling. The behaviour of the model components of binary and ternary systems were studied on different time scales to provide a better understanding of the processes involved. Gluconate (a simple well-characterized molecule) was selected as a good starting model of organic additives in cement in order to probe the interaction mechanisms on the fundamental molecular scale. Uranium (VI) was selected as a representative radionuclide because it is one of the most studied radioelements with large amounts of data on its interaction with cement already available in the literature. The real-life materials (polymer superplasticiser as an organic additive, and hydrated cement paste as cement representative) were also experimentally tested in the current work.

To answer the question of how gluconate sorbs on C-S-H surfaces and how much it is different from the sorption on hydrated cement paste, experiments on sorption and desorption of gluconate on C-S-H phases with various Ca/Si ratios were performed. The results, compared to those obtained for hydrated cement paste, showed that there is no principal difference in the gluconate adsorptive behaviour. It was confirmed that the C-S-H phase is primarily responsible for the gluconate uptake in cement. It was also shown that the gluconate sorption is a rapid process that is affected by the Ca/Si ratio of C-S-H: the sorption increases for higher Ca/Si ratios showing trends similar to the ones that could be found in the literature. This may indicate that with time, when cement degrades and when it is characterised by higher Ca/Si ratios, more organic can be released from the cement surface to the pore water and the environment.

The next question addressed was: to what extent the presence of gluconate on the surface affects the adsorption of radioelements (U(VI)) on the C-S-H phases. It was shown that the addition of gluconate ions increases significantly the sorption of U(VI). To interpret such behaviour of the studied three-component system, computational molecular modelling of these systems was additionally performed, since wet chemistry experiments typically provide only the global (macroscale) view on the possible molecular mechanisms. The structural properties of the C-S-H/solution interfaces were investigated and local adsorption

environments were identified for a range of Ca/Si ratios from 0.83 to 1.4. Several sorption sites for uranyl cations on C-S-H surfaces are identified and quantitatively characterized: monodentate and bidentate complexes with deprotonated oxygens of the surface. Moreover, a competition for these sites between the cations can be expected.

The systems including gluconate were also investigated with detailed trajectory analysis of unconstrained and several constrained MD simulations. In bulk aqueous solutions, gluconate preferably forms complexes with Ca^{2+} and, when present close to C-S-H interfaces, it sorbs via the formation of cation bridging inner-sphere and outer-sphere surface complexes with cations. In addition, the presence of gluconate in the first solvation shell of Ca^{2+} was shown to lower the cation binding energy to the surface sorption site, thus potentially facilitating its desorption and replacement with UO_2^{2+} cations.

Summarizing all the experimental (**EXP**) and molecular modelling (**MM**) results of the present work, a hypothesis can be formulated to describe the molecular mechanisms of interactions in the modelled ternary system (C-S-H/organic additive/U(VI)), as presented in Fig. 98:

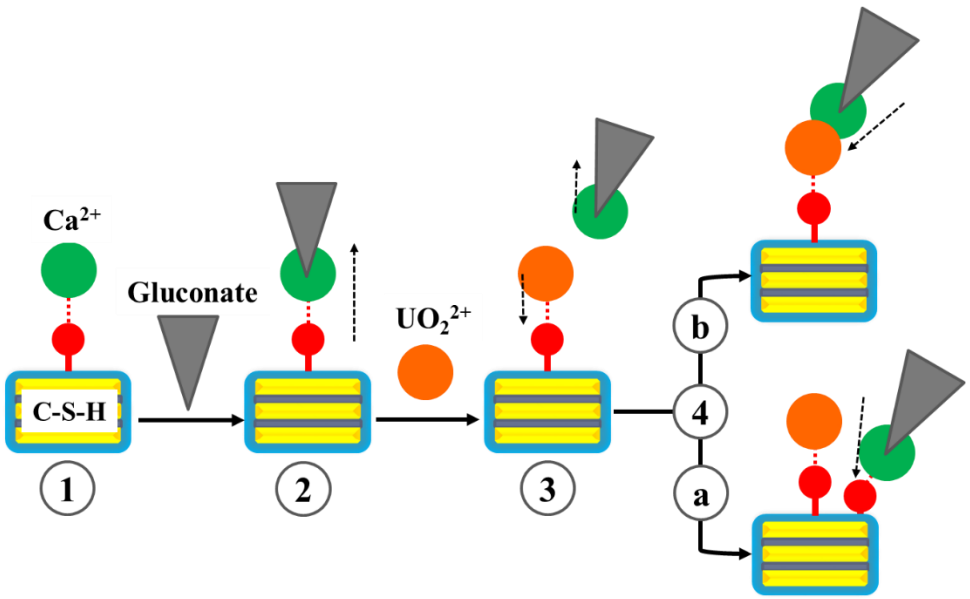

Figure 98. *The schematic representation of the hypothetical mechanism of U(VI) interaction with C-S-H surfaces in the presence of gluconate.*

1 – Specific C-S-H sorption sites were identified and described by molecular modelling (**MM**); deprotonation is defined by the pH of contact solution measured experimentally (**EXP**).

2 – Both **MM** and **EXP** confirmed the mediating role of Ca^{2+} in the sorption of gluconate. According to **MM**, there is potentially a competition for sorption sites between Ca^{2+} and UO_2^{2+}, the adsorption free energies for both cations are similar. Moreover, the addition of gluconate weakens the binding of Ca^{2+} to the surface sorption sites (**MM**).

3 – The decreased free energy of adsorption of calcium gluconate complex may facilitate the exchange with UO_2^{2+} on the same sorption site (**MM**). The **EXP** results confirm that the presence of gluconate enhances sorption of U(VI) on C-S-H.

4 – The **EXP** results showed that the concentration of gluconate in equilibrated solution does not change significantly after the addition of U(VI). Also, no release of Ca^{2+} had been observed. It can be suggested that calcium gluconate complex remains bound to the surface: ***4a*** – it can form multinuclear hydroxo complexes with sorbed uranyl cations (**MM**); ***4b*** – it sorbs on another unoccupied sorption site that is less favourable for UO_2^{2+} binding (**MM**).

To further investigate and characterise the proposed molecular mechanisms, additional studies need to be performed to understand the role of hydroxyl ions in the solvation shell of the cations and their effect on the adsorption of organics and the formation of multinuclear surface complexes that include organic ligands. Also, thermodynamical modelling can be performed to serve as an additional link between the molecular scale theoretical results and the macroscopic scale experimental observations.

Gluconate is a small molecule and a good starting model for the investigation of C-S-H/organic interaction mechanisms on the molecular scale. However, it can be questioned if the same mechanisms work for more complex organic molecules. Therefore, a system involving polycarboxylate superplasticiser (PCE), representative of a typical industrial cement admixture, was tested here for comparison. It was confirmed experimentally that the interaction of PCE and C-S-H is also mostly electrostatic and driven by the attraction to Ca^{2+} cation present on the surface. In contrast to gluconate, PCE does not affect the sorption of U(VI) on C-S-H. A separate study might be necessary to investigate the influence of molecular mass and structure of the organic additives on the U(VI) sorption mechanisms. Moreover, PCE isotopically labelled with ^{14}C can be potentially synthesised to perform experiments at particularly low polymer concentrations in order to exclude interactions of organic molecules with each other.

The proposed model and approach certainly have natural limitations. First of all, gluconate ion is quite a simple and small proxi molecule that cannot fully represent all the diversity of organic-cement interactions. At the same time, studying the interactions only with larger polymeric molecules brings multiple complications both for wet chemistry experiments (instrumental limitations) and for molecular modelling (e.g., determination of the exact molecular structure and atomic composition).

Moreover, the residual concentrations of organics in the cement pore water can be very low and the surface will be unsaturated with respect to the adsorbed organic additives (Glaus et al., 2006). Thus, there may be sorption sites available for adsorption of other molecules. In addition, classical molecular dynamics simulations can only be used to study the physisorption behaviour of ions at the interface but the modelling of the chemisorption behaviour, i.e., the incorporation of organic molecules or metal cations into the C-S-H structure, is a much more difficult problem, requiring quantum chemical methods rather than the force-field based approaches.

And finally, C-S-H definitely plays the key role in cement chemistry, but in any real-life scenario the presence of other cement mineral phases may have additional important effects on the processes. Moreover, there are many other factors to consider, such as redox conditions, the presence of other dissolved ions (carbonate ions, particularly), the presence of bacteria, elevated temperatures, radiation damage to materials, organic degradation, etc. Therefore, even though this work has successfully addressed several important questions concerning the effects of organic additives in cement on the adsorption and mobility of radionuclides in cementitious systems, and has qualitatively and even semi-quantitatively clarified several important issues related to these process, it should be kept in mind that only simplified model systems were considered here and the conclusions of this work should be extrapolated for the prediction of real field-scale processes with a proper caution.

Bibliography

Aaberg, M., Ferri, D., Glaser, J., Grenthe, I., 1983. Structure of hydrated dioxouranium(VI) ion in aqueous solution. An x-ray diffraction and proton NMR study. Inorganic Chemistry 22 (26), 3986–3989.

Allen, A.J., Thomas, J.J., Jennings, H.M., 2007. Composition and density of nanoscale calcium-silicate-hydrate in cement. Nature Materials 6, 311-316.

Alonso, M.M., Palacios, M., Puertas, F., 2013. Compatibility between polycarboxylate-based admixtures and blended-cement pastes. Cement & Concrete Composites 35, 151–162.

Altmann S., 2008. 'Geo'chemical research: A key building block for nuclear waste disposal safety cases. Journal of Contaminant Hydrology 102, 174–179.

Autier, C., Azema, N., Taulemesse, J.-M., Clerc, L., 2013. Mesostructure evolution of cement pastes with addition of superplasticizers highlighted by dispersion indices. Powder Technology 249, 282–289.

Barret, P., Bertrandie, D., Casabonne-Masonnave, J.M., Damidot, D., 1992. Short term processes of radionuclide immobilization in cement: a chemical approach. Applied Geochemistry, Suppl. 1, 109-124.

Baston, G.M.N., Berry, J.A., Bond, K.A., Brownsword, M., Linklater, C.M., 1992. Effects of organic degradation products on the sorption of actinides. Radiochimica Acta 58/59, 349–356.

Baston, G.M.N., Berry, J.A., Bond, K.A., Boult, K.A., Brownsword, M., Linklater, C.M., 1994. Effects of cellulosic degradation products on uranium sorption in the geosphere. Journal of Alloys and Compounds 213/214, 475–480.

Bauchy, M., Abdolhosseini Qomi, M. J., Ulm, F.-J., Pellenq, R. J.-M., 2014. Order and disorder in calcium–silicate–hydrate. The Journal of Chemical Physics 140, 214503.

Beaudoin, J.J., Raki, L., Alizadeh, R., 2009. A 29Si MAS NMR study of modified C–S–H nanostructures. Cement & Concrete Composites 31, 585-590.

Bell, I.S., Coveney, P.V., 1998. Molecular modelling of the mechanisms of action of borate retarders on hydrating cements at high temperatures. Molecular Simulation 20, 331–356.

Bentz, D.P., 1997. Three-dimensional computer simulation of Portland cement hydration and microstructure development. Journal of American Chemical Society 80 (1), 3–21.

Biagioni, C., Merlino, S., Bonaccorsi, E., 2015. The tobermorite supergroup: a new nomenclature. Mineralogical Magazine 79 (2), 485–495.

Birks, J.B., 2013. The Theory and Practice of Scintillation Counting: International Series of Monographs in Electronics and Instrumentation. Elsevier, Oct 22, 2013 – Technology & Engineering - 684 pages.

Bonnaud, P.A., Labbez, C., Miura, R., Suzuki, A., Miyamoto, N., Hatakeyama, N., Miyamoto, A., Van Vliet, K.J., 2016. Interaction grand potential between calcium–silicate–hydrate nanoparticles at the molecular level. Nanoscale 8, 4160–4172.

Bowers, J.M., Kirkpatrick, R.J., 2009. Natural Abundance 43Ca NMR Spectroscopy of Tobermorite and Jennite: Model Compounds for C–S–H. Journal of American Ceramic Society 92, 545-548.

Brunet, F., Bertani, Ph., Charpentier, Th., Nonat, A., Virlet, J., 2004. Application of ^{29}Si homonuclear and ^{1}H-^{29}Si heteronuclear NMR correlation to structural studies of calcium silicate hydrates. Journal of Physical Chemistry B 108, 15494–15502.

Buhl, M., Kabrede, H., Diss, R., Wipff, G., 2006. Effect of hydration on coordination properties of Uranyl(VI) complexes. A first-principles molecular dynamics study. Journal of American Chemical Society 128, 6357–6368.

Bullard, J.W., Jennings, H.M., Livingston, R.A., Nonat, A., Scherer, G.W., Schweitzer, J.S., Scrivener, K.L., Thomas, J. J., 2011. Mechanisms of cement hydration. Cement and Concrete Research 41 (12), 1208–1223.

Cappelletto, E., Borsacchi, S., Geppi, M., Ridi, F., Fratini, E., Baglioni, P., 2013.Comb-shaped polymers as nanostructure modifiers of Calcium Silicate Hydrate: a ^{29}Si solid-state NMR investigation. Journal of Physical Chemistry C 117, 22947−22953.

Chen, J.J., Thomas, J.J., Taylor, H.F.W., Jennings, H.M., 2004. Solubility and structure of calcium silicate hydrate. Cement and Concrete Research 34, 1499-1519.

Churakov, S.V., Labbez, C., Pegado, L., Sulpizi, M., 2014. Intrinsic acidity of surface sites in calcium silicate hydrates and its implication to their electrokinetic properties. Journal of Physical Chemistry C 118, 11752−11762.

Classification of Radioactive Waste. General Safety Guide. IAEA Safety Standards Series No. Gsg-1 International Atomic Energy Agency Vienna, 2009.

Colàs, E., Grivé, M., Rojo, I., 2013. Complexation of Uranium(VI) by gluconate in alkaline solutions. Journal of Solution Chemistry 42, 1545–1557.

Colombet, P., Zanni, H., Grimmer, A.-R., Sozzani, P., (Eds.), 1998. Nuclear Magnetic Resonance Spectroscopy of Cement-based Materials, Springer Berlin Heidelberg, Berlin, Heidelberg, 1998.

Cong, X., Kirkpatrick, R.J., 1996. ^{29}Si MAS NMR study of the structure of calcium silicate hydrate, Advanced Cement Based Materials 3, 144–156.

Cygan, R.T., Liang, J.-J., Kalinichev, A.G., 2004. Molecular Models of Hydroxide, Oxyhydroxide, and Clay Phases and the Development of a General Force Field. Journal of Physical Chemistry B 108, 1255–1266.

Dario, M., Molera, M., Allard, B., 2004. Effects of cement additives on radionuclide mobility. Materials Research Society Symposium – Proceedings 807, 639–644.

De Stefano, C., Gianguzza, A., Pettignano, A., Piazzese, D., Sammartano, S., 2011. Uranium(VI) sequestration by polyacrylic and fulvic acids in aqueous solution. Journal of Radioanalytical and Nuclear Chemistry 289 (3), 689–697.

Delhorme, M., Labbez, C., Turesson, M., Lesniewska, E., Woodward, C.E., Jönsson, B., 2016. Aggregation of Calcium Silicate Hydrate nanoplatelets. Langmuir 32 (8), 2058–2066.

Dolado, J.S., van Breugel, K., 2011. Recent advances in modeling for cementitious materials. Cement and Concrete Research 41 (7), 711–726.

Druchok, M., Bryk, T., Holovko, M. A molecular dynamics study of uranyl hydration. Journal of Molecular Liquids 120 (1-3), 11–14.

Elakneswaran, Y., Nawa, T., Kurumisawa, K., 2009. Zeta potential study of paste blends with slag. Cement and Concrete Composites 31,72–76.

Faucon, P., Delaye, J.M., Virlet, J., Jacquinot, J.F., Adenot, F., 1997. Study of the structural properties of the C-S-H(I) by molecular dynamic simulation. Cement and Concrete Research 27 (10), 1581–1590.

Ferrari, L., Kaufmann, J., Winnefeld, F., Plank, J., 2010. Interaction of cement model systems with superplasticizers investigated by atomic force microscopy, zeta potential, and adsorption measurements. Journal of Colloid and Interface Science 347, 15–24.

Ferrenberg, A.M., Swenden, R.H., 1989. Optimized Monte Carlo data Analysis. Physical Review Letters 63, 1195–1198.

Flatt, R.J., Houst, Y.F., 2001. A simplified view on chemical effects perturbing the action of superplasticizers. Cement and Concrete Research 31, 1169–1176.

Fox, P.M., Davis, J.A., Zachara, J.M., 2006. The effect of calcium on aqueous uranium(VI) speciation and adsorption to ferrihydrite and quartz. Geochimica and Cosmochimica Acta 70, 1379–1387.

Freeman, C.L., Harding, J.H., Cooke, D.J., Elliott, J.A., Lardge, J.S., Duffy, D.M., 2007. New force fields for modeling biomineralization processes. Journal of Physical Chemistry C 111 (32), 11943–11951.

Gaona, X., Kulik, D.A., Macé, N., Wieland, E., 2012. Aqueous–solid solution thermodynamic model of U(VI) uptake in C–S–H phases. Applied Geochemistry 27, 81–95.

Gelardi, G., Mantellato, S., Marchon, D., Palacios, M., Eberhardt, A.B., Flatt, R.J., 2015. Science and Technology of Concrete Admixtures, Woodhead Publishing, 666 pages.

Giraudeau, C., d'Espinose de Lacaillerie, J.-B., Souguir Z., Nonat, A., Flatt, R. J., 2007. Surface and intercalation chemistry of polycarboxylate copolymers in cementitious systems. Journal of the American Ceramic Society 92 (11), 2471–2488.

Glasser, F.P., Marchand, J., Samson, E., 2008. Durability of concrete – degradation phenomena involving detrimental chemical reactions. Cement and Concrete Research 38 (2), 226–246.

Glaus, M.A., Laube, A., Van Loon, L.R., 2006. Solid–liquid distribution of selected concrete admixtures in hardened cement pastes. Waste Management 26, 741–751.

Gmira, A., Zabat, M., Pellenq, R.J.-M., Van Damme, H., 2004 Microscopic physical basis of the poromechanical behavior of cement-based materials. Materials and Structures / Concrete Science and Engineering 37, 3–14.

Grangeon, S., Claret, F., Lerouge, C., Warmont, F., Sato, T., Anraku, S., Numako, C., Linard, Y., Lanson, B., 2013. On the nature if structural disorder in calcium silicate hydrate with a calcium/silicon ratio similar to tobermorite. Cement and Concrete Research 52, 31–37.

Grangeon, S., Claret, F., Linard, Y., Chiaberge, C., 2013. X-ray diffraction: a powerful tool to probe and understand the structure of nanocrystalline calcium silicate hydrates. Acta Crystallographica Section B 69, 465–473.

Greenfield, B.F., Ilett, D.J., Ito, M., McCrohon, R., Heath, T.G., Tweed, C.J., Williams, S.J., Yui, M., 1998. The effect of cement additives on radionuclide solubilities. Radiochimica Acta 82, 27–32.

Groenewold, G.S., de Jong, W.A., Oomens, J., Van Stipdonk, M.J., 2010. Variable denticity in carboxylate binding to the uranyl coordination complexes. Journal of the American Society for Mass Spectrometry 21 (5), 719–727.

Grossfield, A, "WHAM: an implementation of the weighted histogram analysis method", http://membrane.urmc.rochester.edu/content/wham/, version 2.0.9.

Guilbaud, P., Wipff, G., 1993. Hydration of uranyl (UO22+) cation and its nitrate ion and 18-crown-6 adducts studied by molecular dynamics simulations. Journal of Physical Chemistry 97 (21), 5685–5692.

Guilbaud, P., Wipff, G., 1996. Force field representation of the UO_2^{2+} cation from free energy MD simulations in water. Tests on its 18-crown-6 and NO_3^- adducts, and on its calix[6]arene^{6-} and CMPO complexes. Journal of Molecular Structure: THEOCHEM 366 (1-2), 55–63.

Gutowski, K.E., Dixon, D.A., 2006. Predicting the energy of the water exchange reaction and free energy of solvation for the uranyl ion in aqueous solution. Journal of Physical Chemistry A 110 (28), 8840–8856.

Grambow, B., 2016. Geological disposal of radioactive waste in clay. Elements 12, 239–245.

Grangeon, S., Claret, F., Lerouge, C., Warmont, F., Sato, T., Anraku, S., Numako, C., Linard, Y., Lanson, B., 2013. On the nature if structural disorder in calcium silicate hydrate with a calcium/silicon ratio similar to tobermorite. Cement and Concrete Research 52, 31–37.

Hagberg, D., Karlström, G., Roos, B.O., Gagliardi, L., 2005. The coordination of uranyl in water: a combined quantum chemical and molecular simulation study. Journal of American Chemical Society 127 (41), 14250–14256.

Hamid, S.A., 1981. The crystal structure of the 11 Å natural tobermorite $Ca_{2.25}[Si_30_{7.5}(OH)_{1.5}] \cdot 1\ H_20$, Zeitschrift flir Kristallographie 154, 189–198.

Hanehara, S., Yamada, K., 1999. Interaction between cement and chemical admixture from the point of cement hydration, absorption behaviour of admixture, and paste rheology. Cement and Concrete Research 29, 1159–1165.

Harfouche, M., Wieland, E., Dähn, R., Fujita, T., Tits, J., Kunz, D., Tsukamoto, M., 2006. EXAFS study of U(VI) uptake by calcium silicate hydrates. Journal of Colloid and Interface Science 303, 195–204.

Herterich, U., Volland, G., Krause, G., Hansen, D., 2003. Determination of concrete admixtures in concrete by NMR spectroscopy. Otto-Graf-Journal 14, 101–114.

Hong, S.-Y., Glasser, F.P., 1999. Alkali binding in cement pastes Part I. The C-S-H phase. Cement and Concrete Research 29, 1893–1903.

Hoover, W.G., 1985. Canonical dynamics: Equilibrium phase-space distributions. Phys. Rev. A. American Physical Society. 31 (3), 1695–1697.

Hou, D., Ma, H., Yu, Z., Li, Z., 2014. Calcium silicate hydrate from dry to saturated state: Structure, dynamics and mechanical properties. Acta Materialia 67, 81–94.

Houst, Y.F., Bowen, P., Perche, F., 2007. Adsorption of Superplasticizers on a Model Powder. Proceedings of the 12th International Congress on the Chemistry of Cement, vol. ISBN: 978-0-660-19695-4. Montréal: Conseil national de recherches du Canada, 2007.

Houst, Y.F., Bowen, P., Perche, F., Kauppi, A., Borget, P., Galmiche, L., Le Meins, J.-F., Lafuma, F., Flatt, R.J., Schober, I., Banfill, P.F.G., Swift, D.S., Myrvold, B.O., Petersen, B.G., Reknes, K., 2008. Design and Function of novel superplasticizers for more durable high performance concrete (superplast project). Cement and Concrete Research 38, 1197–1209.

Isaacs, M. PhD thesis – personal communication.

Jalilehvand, F., Spångberg, D., Lindqvist-Reis, P., Hermansson, K., Persson, I., Sandström, M., 2001. Hydration of the Calcium ion. An EXAFS, large-angle X-ray scattering, and molecular dynamics simulation study. Journal of American Chemical Society 123 (3), 431–441.

Jennings, H.M., 2008. Refinements to colloid model of C-S-H in cement: CM-II. Cement and Concrete Research 38 (3), 275–289.

Jolicoeur, C., Simard, M.-A., 1998. Chemical Admixture-Cement Interactions: Phenomenology and Physico-Chemical Concepts. Cement and Concrete Composites 20, 87–101.

Jonssön, B., Nonat, A., Labbez, C., Cabane, B., Wennerström, H., 2005. Controlling the Cohesion of Cement Paste. Langmuir 21, 9211–9221.

Kakihana, M., Nagumo, T., Okamoto, M., Kakihana, H., 1987. Coordination structures for uranyl carboxylate complexes in aqueous solution studied by IR and ^{13}C NMR spectra. Journal of Physical Chemistry 91, 6128–6136.

Kalinichev, A.G., Kirkpatrick, R.J., 2002. Molecular dynamics modeling of chloride binding to the surfaces of calcium hydroxide, hydrated calcium aluminate, and calcium silicate phases. Chemistry of Materials 14, 3539–3549.

Kalinichev, A.G., Wang, J., Kirkpatrick, R.J., 2007. Molecular dynamics modeling of the structure, dynamics and energetics of mineral–water interfaces: Application to cement materials. Cement and Concrete Research 37, 337–347.

Kalinichev, A.G., 2014. Molecular Structure and Dynamics of Nano-Confined Water: Computer Simulations of Aqueous Species in Clay, Cement, and Polymer Membranes, in: L. Mercury, N. Tas, M. Zilberbrand (Eds.) Transport and Reactivity of Solutions in Confined Hydrosystems, Springer Netherlands, Dordrecht, 2014, pp. 103–115.

Kirkpatrick, R.J., Kalinichev, A.G., Hou, X., Struble, L., 2005. Experimental and molecular dynamics modeling studies of interlayer swelling: Water incorporation in kanemite and ASR gel. Materials and Structures 38, 449–458.

Kastner, J., 2011. Umbrella sampling. John Wiley & Sons, Ltd. WIREs Computational Molecular Science 1, 932–942. DOI: 10.1002/wcms.66.

Kauppi, A., Andersson, K.M., Bergström, L., 2005. Probing the effect of superplasticizer adsorption on the surface forces using the colloidal probe AFM technique. Cement and Concrete Research 35, 133–140.

Keith-Roach, M., 2008. The speciation, stability, solubility and biodegradation of organic co-contaminant radionuclide complexes: A review. Science of the Total Environment 396, 1–11.

Kosmatka, S.H., Kerkhoff, B., Panarese, W.C., 2002. Design and Control of Concrete Mixtures Portland Cement Association 14th edition, 358 p.

Kovačević, G., Persson, B., Nicoleau, L., Nonat, A., Veryazov, V., 2015. Atomistic modeling of crystal structure of $Ca_{1.67}SiH_x$. Cement and Concrete Research 67, 197–203.

Ku, H.H., 1966. Notes on the Use of Propagation of Error Formulas. Journal of Research of the National Bureau of Standards - C. Engineering and Instrumentation 70C, 263–273.

Kumar, S., Bouzida, D., Swendsen, R.H., Kollmann, P.A., Rosenberg, J.M., 1992. The weighted histogram analysis method for free-energy calculations on biomolecules. I. The method. Journal of Computational Chemistry 13, 1011–1021.

Kumar, P.P., Kalinichev, A.G., Kirkpatrick, R.J., 2007. Molecular dynamics simulation of the energetics and structure of layered double hydroxides intercalated with carboxylic acids. Journal of Physical Chemistry C 111, 13517–13523.

Labbez, C., Pochard, I., Jönsson, B., Nonat. A., 2011. C-S-H/solution interface: Experimental and Monte Carlo studies. Cement and Concrete Research 41, 161–168.

Larreur-Cayol, S., Bertron, A., Escadeillas, G., 2011. Degradation of cement-based materials by various organic acids in agro-industrial waste-waters. Cement and Concrete Research 41 (8), 882–892.

Lequeux, N., Morau, A., Philippot, S., Boch, P., 1999. Extended X-ray absorption fine structure investigation of Calcium Silicate Hydrates. Journal of the American Ceramic Society 82 (5), 1299–1306.

Lesage, K., Özlem, C., Desmet, B., Vantomme, J., De Schutter, G., Vandewalle, L., 2015. Plasticising mechanism of sodium gluconate combined with PCE. Advances in Cement Research 27 (3), 163–174.

Littleton, C.D., 1953. A structure determination of the gluconate ion. Acta Crystallographica 6, 775–781.

Liu, M., Lei, J., Guo, L., Du, X., Li, J., 2015. The application of thermal analysis, XRD and SEM to study the hydration behavior of tricalcium silicate in the presence of a polycarboxylate superplasticizer. Thermochimica Acta 613, 54–60.

Loganathan, N., Kalinichev, A.G., 2017. Quantifying the mechanisms of site-specific ion exchange at an inhomogeneously charged surface. J. Phys. Chem. C 121, 7829-7836.

Lothenbach, B., Nonat, A., 2015. Calcium silicate hydrates: Solid and liquid phase composition. Cement and Concrete Research 78, 57–70.

Lys, T., 1984. Structure of sodium D-gluconate, Na[C6H11O7]. Acta Crystallographica C 40, 376–378.

Macé, N., Wieland, E., Dähn, R., Tits, J., Scheinost, A. C., 2013. EXAFS investigation on U(VI) immobilization in hardened cement paste: influence of experimental conditions on speciation. Radiochimica Acta 101, 379–389.

Maher, K., Bargar, J.R., BrownJr., G.E., 2013. Environmental speciation of actinides. Inorganic Chemistry 52 (7), 3510–3532.

Massiot, D., Fayon, F., Capron, M., King, I., Le Calvé, S., Alonso, B., Durand, J.-O., Bujoli, B., Gan, Z., Hoatson, G., 2002. Modelling one- and two-dimensional solid-state NMR spectra, Magnetic Resonance in Chemistry 40, 70–76.

McCrohon, R., Williams, S.J., 1997. Effect of Sikament 10 Superplasticiser on Radionuclide Solubility. UK Nirex Ltd, Didcot, Oxfordshire, UK, report.

Mendes, A., Gates, W.P., Sanjayan, J.G., Collin, F., 2011. NMR, XRD, IR and synchrotron NEXAFS spectroscopic studies of OPC and OPC/slag cement paste hydrates. Materials and Structures 44, 1773–1791.

Merlino, S., Bonaccorsi, E., Armbruster, T., 1999. Tobermorites: Their real structure and order-disorder (OD) character. American Mineralogist 84, 1613–1621.

Milestone, N.B., 2006. Reactions in cement encapsulated nuclear wastes: need for toolbox of different cement types. Advances in Applied Ceramics 1, 13–20.

Mollah, M.Y.A., Adams, W.J., Schennach, R., Cocke, D.L., 2000. A review of cement-superplasticizer interactions and their models. Advances in Cement Research 12 (4), 153-161.

Morse, J.W., Shanbhag, P.M., Saito, A., Choppin, G.R., 1984. Interaction of uranyl ions in carbonate media. Chemical Geology 42 (1-4), 85–99.

Nalet, C., Nonat, A., 2016-a. Ionic complexation and adsorption of small organic molecules on calcium silicate hydrate: Relation with their retarding effect on the hydration of C_3S. Cement and Concrete Research 89, 97–108.

Nagele, E., 1986. The Zeta-Potetial of Cement. P.II. Effect of Ph-Value. Cement and Concrete Research 16(6), 853–863.

Nguyen-Trung, C., Begun, G.M., Palmer, D.A., 1992. Aqueous Uranium Complexes: 2. Raman-spectroscopic study of the complex-formation of the dioxouranium(VI) ion with a variety of inorganic and organic ligands. Inorganic Chemistry 31, 5280–5287.

Nonat, A., Lecoq, X., 1998. The structure, stoichiometry and properties of CSH prepared by C_3S hydration under controlled conditions, in: P. Grimmer, A.-R. Grimmer, H. Zanni, P. Sozzani (Eds.). Nuclear Magnetic Resonance Spectroscopy of Cement-Based Materials, Springer, Berlin, 197–207.

Nosé, S., 1984. A unified formulation of the constant temperature molecular-dynamics methods". Journal of Chemical Physics 81 (1), 511–519.

Ochs, M., Pointeau, I., Giffaut, E., (2006). Caesium sorption by hydrated cement as a function of degradation state: experiments and modelling. Waste Management 26, 725.

Pallagi, A., Csendes, Z., Kutus, B., Czeglédi, E., Peintler, G., Forgo, P., Pálinkó, I., Sipos, P., 2013. Multinuclear complex formation in aqueous solutions of Ca(II) and heptagluconate ions. Dalton Transactions 42, 8460–8467.

Pallagi, A., Bajnóczi, É.G., Canton, S.E., Bolin, T., Peintler, G., Kutus, B., Kele, Z., Pálinkó, I., Sipos, P., 2014. Multinuclear complex formation between Ca(II) and gluconate ions in hyperalkaline solutions. Environmental Science and Technology 48, 6604−6611.

Pane, I., Hansen, W., 2005. Investigation of blended cement hydration by isothermal calorimetry and thermal analysis. Cement and Concrete Research 35 (6), 1155–1164.

Papageorgiou, A., Tzouvalas, G., Tsimas, S., 2005. Use of inorganic setting retarders in cement industry. Cement and Concrete Composites 27 (2), 183–189.

Pellenq, R.J.-M., Kushima, A., Shahsavari, R., Van Vliet, K.J., Buehler., M.J., Yip, S., Ulm, F.-J., 2009. A realistic molecular model of cement hydrates. PNAS 106 (38), 16102–16107.

Perez, J-Ph., 2007. The mechanism of action of sodium gluconate on the fluidity and set of Portland cement. Proceedings of the 12th International Congress on the Chemistry of Cement, Montreal.

Phan, T.H., Chaouche, M., Moranville, M., 2006. Influence of organic admixtures on the rheological behaviour of cement pastes. Cement and Concrete Research 36 (10), 1807–1813.

Phillips, J.C., Braun, R., Wang, W., Gumbart, J., Tajkhorshid, E., Villa, E., Chipot, C., Skeel, R.D., Kale, L., Schulten, K., 2005. Scalable molecular dynamics with NAMD. Journal of Computational Chemistry 26, 1781–1802.

Plank, J., Pöllmann, K., Zouaoui, N., Andres, P.R., Schaefer, C., 2008. Synthesis and performance of methacrylic ester based polycarboxylate superplasticizers possessing hydroxy terminated poly(ethylene glycol) side chains. Cement and Concrete Research 38, 1210–1216.

Plank, J., Schroefl, C., Gruber, M., Lesti, M., Sieber, R., 2008. Effectiveness of polycarboxylate superplasticizersin ultra-high strength concrete: the importance of PCE compatibility with silica fume. Journal of Advanced Concrete Technology 7 (1), 5–12.

Plank, J., Winter, Ch., 2008. Competitive adsorption between superplasticizer and retarder molecules on mineral binder surface. Cement and Concrete Research 38, 599–605.

Plank, J., Sachsenhauser, B., de Reese, J., 2010. Experimental determination of the thermodynamic parameters affecting the adsorption behaviour and dispersion effectiveness of PCE superplasticizers. Cement and Concrete Research 40, 699–709.

Plimpton, S., 1995. Fast Parallel Algorithms for Short-Range Molecular Dynamics. J Comp Phys 117, 1-19.

Pointeau, I., Landesman, C., Giffaut, E., Reiller, P., 2004. Reproducibility of the uptake of U(VI) onto degraded cement pastes and calcium silicate hydrate phases. Radiochimica Acta 92, 645–650.

Pointeau, I., Reiller, P., Macé, N., Landesman, C., Coreau, N., 2006. Measurement and modeling of the surface potential evolution of hydrated cement pastes as a function of degradation. Journal of Colloid and Interface Science 300, 33–44.

Pointeau, I., Coreau, N., Reiller, P.E., 2006. Uptake of anionic radionuclides onto degraded cement pastes and competing effect of organic ligands. Radiochimica Acta 96, 367–374.

Popova, A., Geoffroy, G., Renou-Gonnord, M.-F., Faucon, P., Gartner, E., 2000. Interactions between Polymeric Dispersants and Calcium Silicate Hydrates. Journal of the American Ceramic Society 83 (10), 2556–2560.

Pourchet, S., Comparet, C., Nonat, A., Maitrasse, P., 2006. Influence of three types of superplasticizers on tricalciumaluminate hydration in presence of gypsum. 8th CANMET/ACI International Conference on Superplasticizers and other chemical admixtures in concrete, Sorrento: Italy, 2006.

Probst, M.M., Radnai, T., Heizinger, K., Bopp, P., Rode, B.M., 1985. Molecular dynamics and x-ray investigation of an aqueous calcium chloride solution. Journal of Physical Chemistry 89 (5), 753–759.

Quiles, F., Burneau A., 1998. Infrared and Raman spectroscopic study of uranyl complexes: hydroxide and acetate derivatives in aqueous solution. Vibrational Spectroscopy 18, 61–75.

Richardson, I.G., Groves, G.W., 1992. Models for the composition and structure of calcium silicate hydrate (C-S-H) gel in hardened tricalcium silicate pastes. Cement and Concrete Research 22, 1001–1010.

Richardson, I. G., Skibsted, J., Black, L., Kirkpatrick, R.J., 2010. Characterization of cement hydrate phases by TEM, NMR and Raman spectroscopy. Advances in Cement Research 22 (4), 233–248.

Richter, C., Muller, K., Drobot, B., Steudtner, R., Großmann, K., Stockmann, M., Brendler, V., 2016. Macroscopic and spectroscopic characterization of Uranium(VI) sorption onto orthoclase and muscovite and the influence of competing Ca^{2+}. Geochimica et Cosmochimica Acta 189, 143–157.

Ridi, F., Fratini, E., Baglioni, P., 2011. Cement: A two thousand old nano-colloid. Journal of Colloid and Interface Science 357, 255–264.

Roosz, C., 2016. Propriétes thermodynamiques des phases cimentaires hydratées C-S-H, C-A-H et M-S-H, Ph.D. thesis University of Poitiers (France).

Rottstegge, J., Wilhelm, M., Spiess, H.W., 2006. Solid state NMR investigations on the role of organic admixtures on the hydration of cement pastes. Cement and Concrete Composites 28 (5), 417–426.

Roux B., 1995. The calculation of the potential of mean force using computer simulations. Computer Physics Communications 91, 275–282.

Sáez del Bosque, I.F., Martín-Pastor, M., Sobrados, I., Martínez-Ramírez, S., Blanco-Varela, M.T., 2016. Quantitative analysis of pure triclinic tricalcium silica and C-S-H gels by ^{29}Si NMR longitudinal relaxation time. Construction and Building Materials 107, 52–27.

Sanchez, F., Sobolev, K., 2010. Nanotechnology in concrete - A review. Construction and Building Materials 24, 2060-2071.

Scrivener, K.L., Füllmann, T., Gallucci, E., Walenta, G., Bermejo, E., 2004. Quantitative study of Portland cement hydration by X-ray diffraction/Rietveld analysis and independent methods. Cement and Concrete Research 34 (9), 1541–1547.

Scrivener, K.L., Juilland, P., Monteiro, P.J.M., 2015. Advances in understanding hydration of Portland cement. Cement and Concrete Research 78 (Part A), 38–56.

Šeputytė-Jucikė, J., Kligys, M., Sinica, M., 2016. The effects of modifying additives and chemical admixtures on the properties of porous fresh and hardened cement paste. Construction and Building Materials 127, 679–691.

Shahsavari, R., Pellenq, R.J.-M., Ulm, F.-J., 2011. Empirical force fields for complex hydrated calcio-silicate layered materials. Physical Chemistry Chemical Physics 13, 1002–1011.

Smith, K.F., Bryan, N.D., Swinburne, A.N., Bots, P., Shaw, S., Natrajan, L.S., Mosselmans, J.F.W., Livens, F.R., Morris, K., 2015. U(VI) behaviour in hyperalkaline calcite systems. Geochimica et Cosmochimica Acta 148, 343-359.

Souaille, M., Roux. B., 2001. Extension to the weighted histogram analysis method: combining umbrella sampling with free energy calculations. Computer Physics Communications 135, 40–57.

Stade, H., 1989. On the reaction of C–S–H(di, poly) with alkali hydroxides. Cement and Concerete Research 19, 802–810.

Sylwester, E. R., Allen, P. G., Zhao, P., Viani, B. E., 2000. Interactions of uranium and neptunium with cementitious materials studied by XAFS. Materials Research Society Symposium Proceedings 608, 307–312.

Szczerba, M., Kalinichev, A., 2016. Intercalation of ethylene glycol in smectites: several molecular simulation models verified by X-ray diffraction data. Clays and Clay minerals 64 (4), 488–502.

Tajuelo Rodriguez, E., Richardson, I.G., Black, L., Boehm-Courjault, E., Nonat, A., Skibsted, J., 2015. Composition, silicate anion structure and morphology of calcium silicate hydrates (C-S-H) synthesised by silica-lime reaction and by controlled hydration of tricalcium silicate (C_3S). Advances in Applied Ceramics 114 (7), 362–371.

Taylor, H.F.W. Cement Chemistry. Academic Press: London, 1990.

Teich-McGoldrick, S.L., Greathouse, J.A., Cygan, R.T., 2014. Molecular dynamics simulations of uranyl adsorption and structure on the basal surface of muscovite. Molecular Simulation 40, 610-617.

Tits, J., Fujita, T., Tsukamoto, M., Wieland, E., 2008. Uranium (VI) uptake by synthetic calcium silicate hydrates, Proceedings of the Material Research Society 1107, 467–474.

Tits, J., Geipel, G., Macé, N., Eilzer, M., Wieland, E., 2011. Determination of uranium (VI) sorbed species in calcium silicate hydrate phases: a laser-induced luminescence spectroscopy and batch sorption study. J. Colloid Interf. Sci. 359, 248-256.

Tits, J., Walther, C., Stumpf, T., Macé, N., Wieland, E., 2015. A luminescence line-narrowing spectroscopic study of the Uranium(VI) interaction with cementitious materials and titanium dioxide. Dalton Transactions 44, 966–976.

Tommaso, D.D., Ruiz-Agudo, E., de Leeuw, N.H., Putnis, A., Putnis, C.V., 2014. Modelling the effects of slat solution on the hydration of calcium ions. Physical Chemistry Chemical Physics 16, 7772–7785.

Torrie, G.M., Valleau, J.P., 1974. Monte Carlo free energy estimates using non-Boltzmann sampling: Application to the sub-critical Lennard-Jones fluid. Chemical Physics Letters 28, 578–581.

Torrie, G.M., Valleau, J.P., 1977. Nonphysical sampling distributions in Monte Carlo free-energy estimation: Umbrella sampling. Journal of Computational Physics 23, 187–199.

Turesson, M., Nonat, A., Labbez, C., 2014. Stability of negatively charged platelets in calcium rich anionic copolymer solutions. Langmuir 30, 6713–6720.

Trauchessec, R., Mechling, J.-M., Lecomte, A., Roux, A., Le Rolland, B., 2015. Hydration of ordinary Portland cement and calcium sulfoaluminate cement blends. Cement and Concrete Composites 56, 106–114.

Van Loon, L.R., Glaus, M.A., Stallone, S., Laube, A., 1997. Sorption of isosaccharinic acid, a cellulose degradation product, on cement. Environmental Science and Technology 31 (4), 1243–1245.

Verlet, L. 1967. Computer ‘experiments’ on classical fluids: I. Thermodynamical properties of Lennard-Jones molecules, Physical Review, 159 (1), 98–103.

Viallis, H., Faucon, P., Petit, J.-C., Nonat, A., 1999. Interaction between salts (NaCl, CsCl) and Calcium Silicate Hydrates (C−S−H). Journal of Physical Chemistry B 103 (25), 5212–5219.

Viallis-Terrisse, H., Nonat, A., Petit, J.-C., 2001. Zeta-potential study of Calcium Silicate Hydrates interacting with alkaline cations. Journal of Colloid and Interface Science 244, 58–65.

Wang, J., Wolf, R.M., Caldwell, J.W., Kollman, P.A., Case, D.A., 2004. Development and Testing of a General Amber Force Field. Journal of Computational Chemistry 25, 1157-1174.

Warwick, P., Evans, N., Vines, S., 2006. Studies on metal gluconic acid complexes. IN: Isheghem, Van P. (ed.). Scientific Basis for Nuclear Waste Management XXIX (Materials Resource Society Symposium Proceedings, 932, Warrendale, PA), 959–966.

Wieland, E., Macé, N., Dähn, R., Kunz, D., Tits, J., 2010. Macro- and micro-scale studies on U(VI) immobilization in hardened cement paste. Journal of Radioanalytical and Nuclear Chemistry 286, 793–800.

Winnefeld, F., Becker, S., Pakusch, J., Götz, T., 2007. Effects of the molecular architecture of comb-shaped superplasticizers on their performance in cementitious systems. Cement and Concrete Composites 29, 251–262.

Won, J.-P., Choi, B.-R., Lee, J.-W., 2012. Experimental and statistical analysis of the alkali–silica reaction of accelerating admixtures in shotcrete. Construction and Building Materials 30, 330–339.

Yamada, K., Takahashi, T., Hanehara, S., Matsuhisa, M., 2000. Effects of the chemical structure on the properties of polycarboxylate-type superplasticizer. Cement and Concrete Research 30, 197–207.

Yamada, K., Ogawa, S., Hanehara, S., 2001. Controlling of the adsorption and dispersing force of polycarboxylate-type superplasticizer by sulfate ion concentration in aqueous phase. Cement and Concrete Research 31, 375–383.

Yoshioka, K., Tazawa, E., Kawai, K., Enohata, T., 2002. Adsorption characteristics of superplasticizers on cement component minerals. Cement and Concrete Research 32, 1507–1513.

Young, A.J., Warwick, P., Milodowski, A.E., Read, D., 2013. Behaviour of radionuclides in the presence of superplasticiser. Advances in Cement Reasearch 25(1), 32–43.

Yu, P., Kirkpatrick, R.J., Poe, B., McMillan, P.F., Cong, X., 1999. Structure of Calcium Silicate Hydrate (C-S-H): Near-, Mid-, and Far-Infrared Spectroscopy. Journal of the American Ceramic Society 82 (3), 742–748.

Zhang, Z., Helms, G., Clark, S.B., Tian, G., Zanonato, P.L., Raoc, L., 2009. Complexation of Uranium(VI) by gluconate in acidic solutions: a thermodynamic study with structural analysis. Inorganic Chemistry 48, 3814–3824.

Zhu, J., Li, Z., Yang, R., Zhang, Y., 2014. Organic Additive Implantation onto Cement Hydration Products. Journal of Wuhan University of Technology-Mater. Sci. Ed., 527-533.

Zingg, A., Winnefeld, F., Holzer, L., Pakusch, J., Becker, S., Gauckler, L., 2008. Adsorption of polyelectrolytes and its influence on the rheology, zeta potential, and microstructure of various cement and hydrate phases. Journal of Colloid and Interface Science 323, 301–312.

Zuo, Y., Zi, J., Wei, X., 2014. Hydration of cement with retarder characterized via electrical resistivity measurements and computer simulation. Construction and Building Materials 53, 411–418.

Annexes

Annexe 1 Liquid scintillation counting

The Tri-Carb® 3170TR/SL is a computer-controlled benchtop liquid scintillation analyzer, specially configured for detection of extremely low level alpha and beta radioactivity. Counting time of 1 hour has been used. The sensitive LSC detection method requires specific cocktails to absorb the energy into detectable light pulses. In general, the detection method can be described by the scheme shown in Fig. 99.

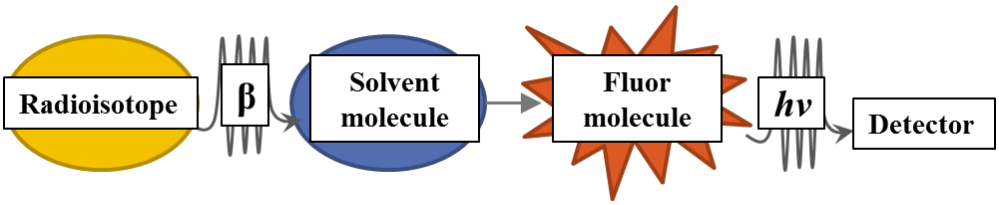

Figure 99. *The scheme of the main principle of liquid scintillation detection.*

Ultima Gold LLT is a multipurpose liquid scintillation cocktail for a wide range of aqueous samples. It is characterised by quench resistance, high flash point (150 ºC), the absence of permeation through plastic, and low toxicity (LD_{50} > 3000 mg/kg). The cocktail contains an organic aromatic solvent (2,6-di-isopropylnaphtaline), scintillator and emulsifier for aqueous samples since aqueous samples are completely insoluble in the pure organic solvents and scintillators.

Because of the broad spectrum of β-particle energies emitted by a given radionuclide sample, beta decays can be easily recognised by the distinct broad spectral pattern (Fig. 100). The efficiency of counting in the sample depends on how the decay events are producing light flashes in the media that are further detected and quantified by the instrument.

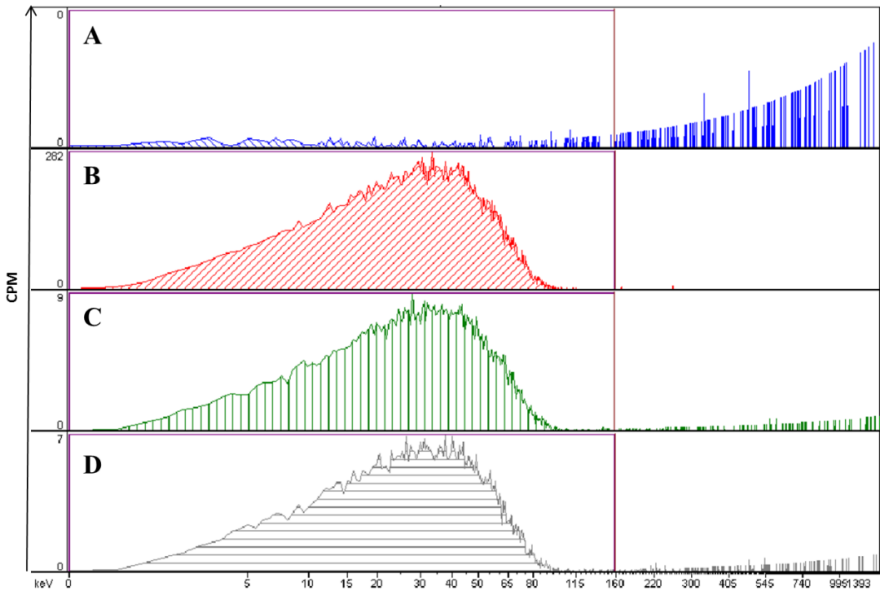

Figure 100. *Typical spectra of liquid scintillation counting analysis of ^{14}C-gluconate: A – background signal; B - standard solution, spike of labelled gluconate in C-S-H equilibrated solution; C and D – gluconate sorption on C-S-H (Ca/Si = 1.0) for* $[Gluconate]_{initial} = 7.00 \cdot 10^{-9}$ *mol/l and* $[Gluconate]_{initial} = 1.73 \cdot 10^{-8}$ *mol/l respectively.*

Annexe 2 Ion exchange chromatography (IC)

Ion exchange chromatography is an analytical technique in which molecules are separated and determined based on their affinity to the charged solid chromatographic support. The separation is controlled by electrostatic interactions when charged molecules form an ionic complex with functional groups of opposite charge on the support. In this work, the cation and anion exchange chromatography analysis have been performed to identify and quantify ionic species in the studied system: Ca, Na and gluconate. The general scheme is presented in Fig. 101.

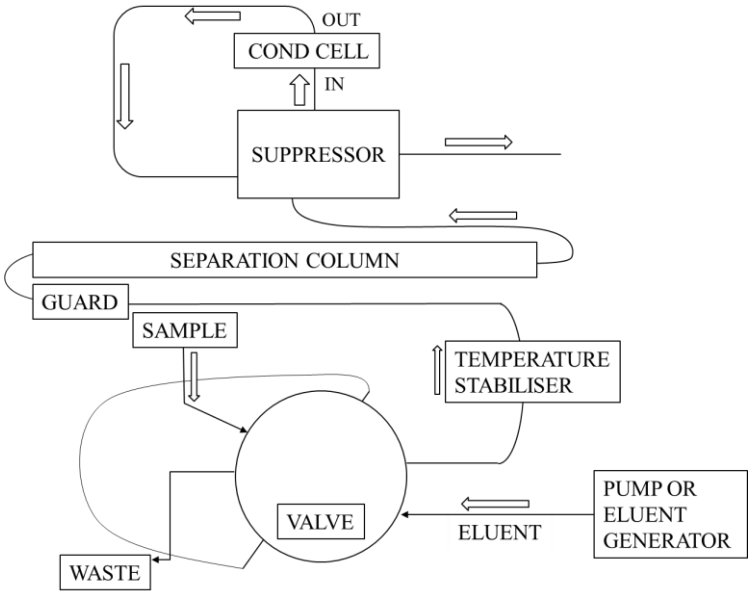

Figure 101. *The general instumental set-up of ion chromatography procedure.*

A sample is injected into the system with an autosampler into a sample loop of known volume (in this work: 100 µl for anion-exchange and 25 µl for cation-exchange analysis). A buffered aqueous solution (or eluent, mobile phase) brings the sample into a separation column that contains ion-exchange stationary phase material where the target analytes are retained. Further, the eluted ions are detected by conductivity.

In cation exchange chromatography stationary phase contains negatively charged functional group that retain positively charged cations of the mobile phase:

$-R^{-}X^{+} + Ct^{+}An^{-} \leftrightarrow -R^{-}\ Ct^{+} + X^{+} + An^{-}$,

where, $-R^{-}$ is a negatively charged groups of stationary chromatographic phase, X^{+} is an exchanged cation (e.g. Na^{+}, H^{+}, K^{+}), Ct^{+} is a cation of interest, An^{-} is a counterion.

In anion exchange chromatography stationary phase contains positively charged functional group that retain negatively charged cations:

$-R^+X^- + Ct^+An^- \leftrightarrow -R^+ An^- + X^- + Ct^+$,

where, $-R^+$ is a positively charged groups of stationary chromatographic phase (e.g. hydroxide-selective anion-exchange phase of IonPac AS18 column used in this work, Fig. 102), X^- is an exchanged cation (e.g. OH^-,), An^- is an anion of interest, Ct^+ is a counterion.

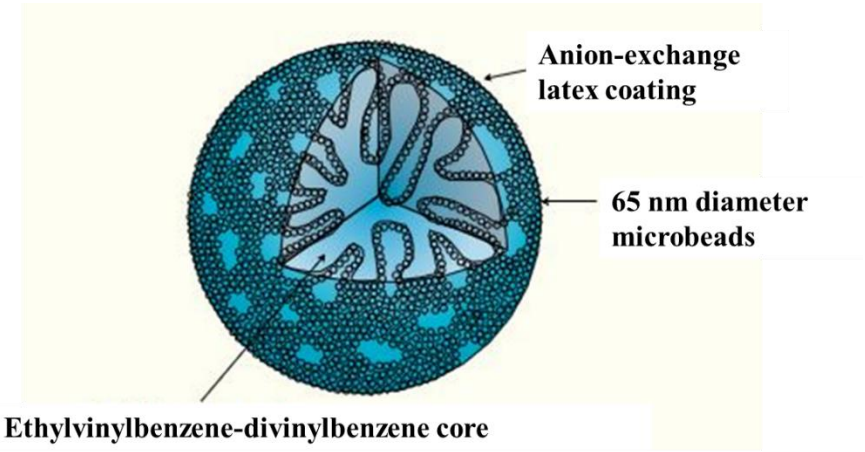

Figure 102. *Packing particle of IonPac AS18 hydroxide-selective anion-exchange column.*

The typical chromatogram for gluconate detection can be seen in Fig. 103.

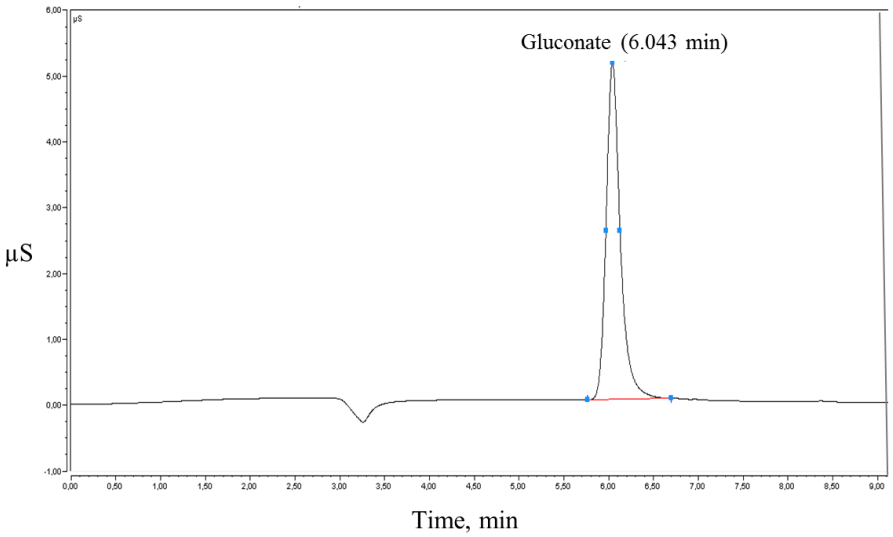

Figure 103. *Typical chromatogram for gluconate identification by anion-exchange chromatography in the C-S-H equilibrated solution.*

Annexe 3 Inductively coupled plasma mass spectrometry

Inductively coupled plasma mass spectrometry (abbreviated as ICP-MS) is an analytical technique used to determine elements and their concentrations in samples. The inductively coupled plasma source transform metals of interest into ions that further separated, identified and quantified by the mass spectrometer.

The general scheme of ICP-MS analysis is presented in Fig. 104. First, a sample is injected into nebuliser where it is transformed into the fine aerosol. The aerosol is further transmitted to the plasma torch. The solution is dehydrated and the solid sublimates into gas phase before entering ICP. In the plasma, the analytes are ionised and directed towards the quadrupole mass analyser, where only ions of the selected m/z ratio pass through to the detector.

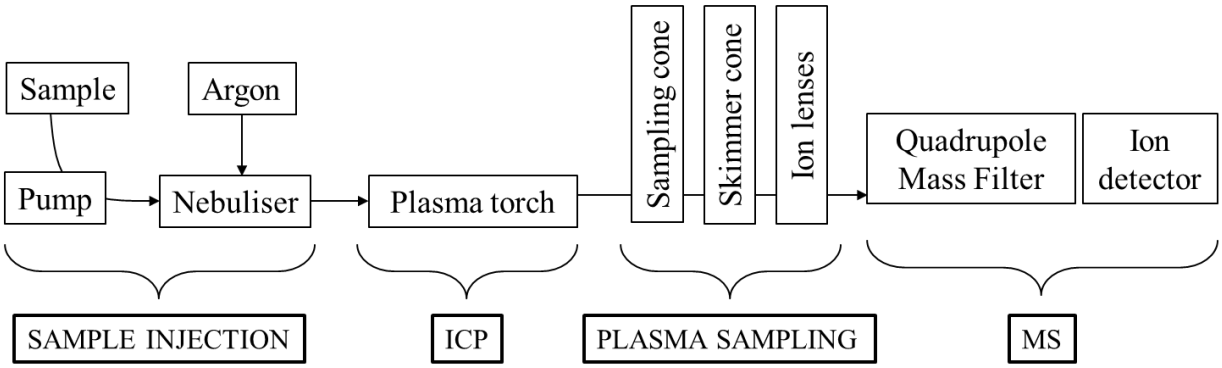

Figure 104. *The general scheme of ICP-MS analysis.*

Annexe 4 Total organic carbon (TOC) analysis

Total organic carbon (abbreviated as TOC) is the content of organic carbon in measured media.

The general scheme of TOC analysis is shown in Fig. 105 (TOC-V_{CSH}, Shimadzu). Carrier gas (flow rate of 150 mL/min) is passing through an oxidation combustion tube (T = 680°C). When the sample is injected into the combustion tube, the total carbon (TC) is oxidised or decomposes to producing CO_2. The combustion products in the gas are further cooled and dehumidified in before passing via the halogen scrubber into the sample cell of the non-dispersive infrared detector (NDIR), where CO_2 is detected. The NDIR analogue signal forms a peak, and the data processor calculates the peak area. To measure the TC concentration of the sample, the relationship between the TC concentration and peak area (calibration curve) is predetermined using a TC standard solution, to express the peak area as a ratio of the TC concentration;

TC (Total Carbon) = TOC (Total Organic Carbon) + IC (Inorganic Carbon)

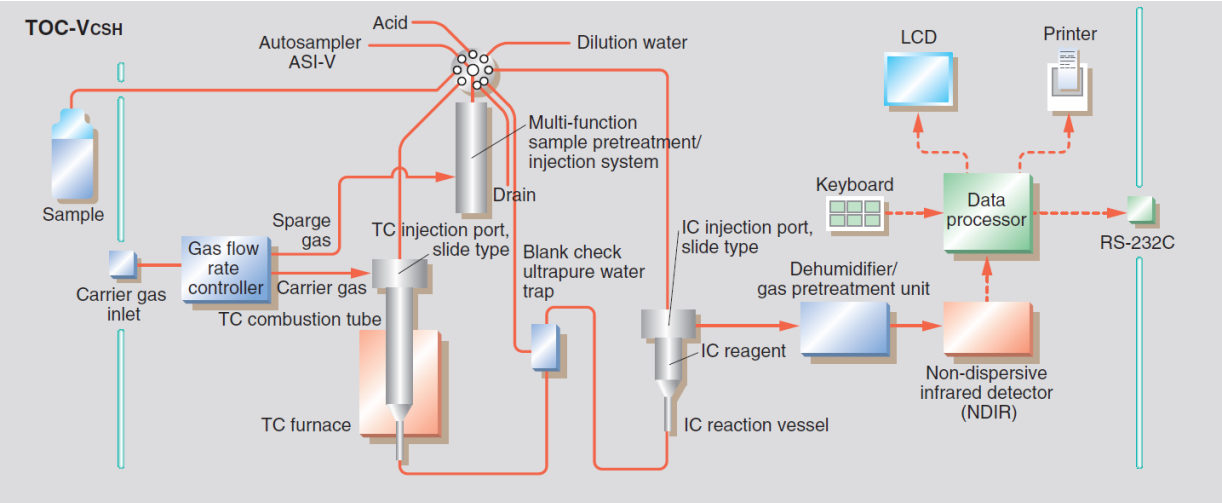

Figure 105. *Measurement flow line diagram (TOC-V_{CSH}, Shimadzu).*

To quantify the amount of inorganic carbon (IC), the acidified sample is sparged with the carrier gas to convert only the IC in the sample to CO2 (detected by the NDIR). The IC is a combination of carbonate and bicarbonate. Thus, it is possible to calculate the content of total organic carbon (TOC) in the sample: TOC = TC – IC

Annexe 5 Tabulated experimental data (Chapter 3)

Table A-1. Kinetics of gluconate adsorption on C-S-H phases (0.83, 1.0, 1.4), S/L = 20 g/l.

	Ca/Si = 0.83		Ca/Si = 1.0		Ca/Si = 1.4	
Time, days	[Gluconate]eq, mmol/l	σ, mmol/l	[Gluconate]eq, mmol/l	σ, mmol/l	[Gluconate]eq, mmol/l	σ, mmol/l
0	1.03E+00	5.15E-02	1.03E+00	5.15E-02	1.03E+00	5.15E-02
0.5	9.92E-01	4.96E-02	7.98E-01	3.99E-02	2.82E-01	1.41E-02
1	9.74E-01	4.87E-02	7.60E-01	3.80E-02	2.34E-01	1.17E-02
3	9.82E-01	4.91E-02	7.81E-01	3.91E-02	2.22E-01	1.11E-02
7	9.89E-01	4.95E-02	7.61E-01	3.81E-02	2.19E-01	1.10E-02
15	9.69E-01	4.85E-02	7.48E-01	3.74E-02	2.41E-01	1.21E-02
30	9.80E-01	4.90E-02	7.65E-01	3.83E-02	2.17E-01	1.09E-02

Table A-2. Isotherms of gluconate adsorption on C-S-H phases (0.83, 1.0, 1.4), S/L = 20 g/l.

Ca/Si = 0.83					
	$[Gluconate]_{eq}$, mmol/l	σ, mmol/l	$[Gluconate]_{sorbed}$, mmol/mol of Si	σ, mmol/mol of Si	Rd, l/kg (σ = 20%)
^{14}C-labelled gluconate	6.45E-06	3.22E-07	6.08E-08	6.68E-09	4.29
	1.61E-05	8.05E-07	1.34E-07	1.47E-08	3.78
	3.49E-05	1.75E-06	3.36E-07	3.70E-08	4.38
	7.39E-05	3.69E-06	5.90E-07	6.49E-08	3.63
	1.02E-04	5.10E-06	9.03E-07	9.93E-08	4.03
	2.89E-04	1.44E-05	3.04E-06	3.34E-07	4.79
	6.85E-04	3.42E-05	4.94E-06	5.44E-07	3.29
	9.69E-04	4.85E-05	7.69E-06	8.46E-07	3.61
	2.86E-03	1.43E-04	2.64E-05	2.90E-06	4.19
	6.86E-03	3.43E-04	4.09E-05	4.50E-06	2.71
	2.85E-02	1.42E-03	2.72E-04	2.99E-05	4.34
	6.45E-06	3.22E-07	6.08E-08	6.68E-09	4.34
Inactive gluconate	9.49E-03	4.74E-04	8.95E-05	9.84E-06	4.40
	2.74E-02	1.37E-03	3.88E-04	4.27E-05	6.43
	6.79E-02	3.40E-03	4.79E-04	5.27E-05	3.19
	2.81E-01	1.40E-02	3.22E-03	3.54E-04	5.20
	6.37E-01	3.18E-02	9.58E-03	1.05E-03	6.73
	9.78E-01	4.89E-02	5.99E-03	6.58E-04	2.76
	2.86E+00	1.43E-01	2.76E-02	3.04E-03	4.20
	6.42E+00	3.21E-01	9.96E-02	1.10E-02	6.27
	9.10E+00	4.55E-01	1.52E-01	1.67E-02	6.73
Ca/Si = 1.0					

	$[Gluconate]_{eq}$, mmol/l	σ, mmol/l	$[Gluconate]_{sorbed}$, mmol/mol of Si	σ, mmol/mol of Si	Rd, l/kg (σ = 20%)
^{14}C-labelled gluconate	1.33E-05	6.65E-07	3.71E-07	1.85E-08	15.96
	2.08E-05	1.04E-06	1.58E-06	7.89E-08	15.14
	4.09E-05	2.05E-06	3.53E-06	1.76E-07	41.18
	6.67E-05	3.33E-06	4.00E-06	2.00E-07	46.82
	1.97E-04	9.86E-06	1.10E-05	5.50E-07	32.63
	4.42E-04	2.21E-05	2.64E-05	1.32E-06	30.30
	6.10E-04	6.10E-06	3.95E-05	1.97E-06	32.43
	1.81E-03	1.81E-05	1.19E-04	5.96E-06	35.19
	2.24E-02	1.12E-03	7.96E-04	3.98E-05	35.87
	7.82E-02	3.91E-03	2.31E-03	1.15E-04	29.06
	4.57E-03	2.29E-04	2.45E-04	1.22E-05	19.00
Inactive gluconate	1.82E-02	4.55E-03	1.19E-03	1.19E-04	
	5.03E-02	5.03E-03	2.03E-03	2.03E-04	
	6.82E-02	6.82E-03	3.23E-03	3.23E-04	
	2.04E-01	2.04E-02	9.85E-03	9.85E-04	
	4.96E-01	4.96E-02	2.11E-02	2.11E-03	
	7.63E-01	7.63E-02	2.51E-02	6.26E-03	
	2.18E+00	2.18E-01	8.62E-02	8.62E-03	
	5.41E+00	5.41E-01	1.76E-01	1.76E-02	
	7.47E+00	7.47E-01	2.77E-01	2.77E-02	
Ca/Si = 1.4					
	$[Gluconate]_{eq}$, mmol/l	σ, mmol/l	$[Gluconate]_{sorbed}$, mmol/mol of Si	σ, mmol/mol of Si	Rd, l/kg (σ = 20%)
^{14}C-labelled gluconate	1.05E-06	5.25E-08	6.43E-07	3.21E-08	283.54
	2.84E-06	1.42E-07	1.56E-06	7.82E-08	254.47
	5.89E-06	2.94E-07	3.46E-06	1.73E-07	272.33
	1.18E-05	5.90E-07	7.28E-06	3.64E-07	285.97
	2.79E-05	1.40E-06	8.89E-06	4.44E-07	147.33
	5.27E-05	2.64E-06	2.85E-05	1.43E-06	250.17
	1.15E-04	5.77E-06	6.63E-05	3.32E-06	266.30
	1.64E-04	8.22E-06	9.45E-05	4.72E-06	266.11
	5.06E-04	2.53E-05	2.81E-04	1.40E-05	256.62
	1.18E-03	5.91E-05	6.53E-04	3.27E-05	255.98
	5.53E-03	2.77E-04	2.75E-03	1.37E-04	283.54
	2.10E-02	1.05E-03	8.88E-03	4.44E-04	230.02
Inactive gluconate	7.18E-03	3.59E-04	2.57E-03	1.28E-04	165.66
	1.47E-02	7.36E-04	6.21E-03	3.11E-04	195.46
	1.33E-02	6.67E-04	9.71E-03	4.85E-04	337.07
	4.41E-02	2.21E-03	2.87E-02	1.43E-03	301.07
	1.45E-01	7.23E-03	6.24E-02	3.12E-03	199.81
	2.19E-01	1.10E-02	8.79E-02	4.39E-03	185.41
	6.92E-01	3.46E-02	2.60E-01	1.30E-02	173.64
	2.38E+00	1.19E-01	5.24E-01	2.62E-02	101.50
	3.55E+00	1.77E-01	7.33E-01	3.67E-02	95.43

Table A-3. Evolution of Ca and Si concentrations in C-S-H eq. solution as a function of gluconate concentration at permanent state.

Ca/Si = 0.83					
$[Glu]_{eq}$, mmol/l	σ, mmol/l	Ca, mmol/l	σ, mmol/l	Si, mmol/l	σ, mmol/l
9.49E-03	4.75E-04	1.17	0.11	2.74	0.27
6.79E-02	3.40E-03	1.17	0.11	2.98	0.29
1.02E-01	5.10E-03	1.15	0.11	3.02	0.30
2.81E-01	1.41E-02	1.22	0.12	3.11	0.31
9.78E-01	4.89E-02	1.30	0.18	3.12	0.43
2.86E+00	1.43E-01	1.49	0.14	3.05	0.30
6.42E+00	3.21E-01	1.84	0.18	3.37	0.33
2.65E+01	1.33E+00	3.21	0.32	4.06	0.40
Ca/Si = 1.0					
$[Glu]_{eq}$, mmol/l	σ, mmol/l	Ca, mmol/l	σ, mmol/l	Si, mmol/l	σ, mmol/l
1.08E-02	5.40E-04	2.06	0.20	0.35	0.03
5.03E-02	2.52E-03	1.85	0.18	0.24	0.02
6.82E-02	3.41E-03	2.00	0.20	0.24	0.02
2.04E-01	1.02E-02	1.81	0.18	0.34	0.03
7.63E-01	3.82E-02	1.93	0.19	0.31	0.03
2.18E+00	1.09E-01	2.03	0.20	0.43	0.04
5.41E+00	2.71E-01	1.70	0.20	0.68	0.08
2.29E+01	1.15E+00	2.78	0.27	0.80	0.08
1.08E-02	5.40E-04	2.06	0.20	0.35	0.03
Ca/Si = 1.4					
$[Glu]_{eq}$, mmol/l	σ, mmol/l	Ca, mmol/l	σ, mmol/l	Si, mmol/l	σ, mmol/l
1.36E-02	1.36E-03	11.2	0.56	0.028	0.003
1.47E-02	1.47E-03	12.75	0.63	0.034	0.004
1.33E-02	1.33E-03	11.22	0.56	0.034	0.004
4.41E-02	4.41E-03	12.67	0.63	0.031	0.003
2.19E-01	2.19E-02	11.47	0.80	0.035	0.004
6.92E-01	6.92E-02	11.35	0.56	0.038	0.004
2.38E+00	2.38E-01	9.02	0.72	0.053	0.006
1.54E+01	1.54E+00	9.70	0.58	0.070	0.008

Table A-4. Sorption of Na^+ on C-S-H with different Ca/Si ratios

Ca/Si = 0.83			
[Na]eq, mol/l	σ, mol/l	[Na]s, mol/kg	σ, mol/kg
4.19E-05	6.29E-06	6.81E-04	1.02E-04
8.47E-05	1.27E-05	1.32E-03	1.98E-04
4.22E-04	6.32E-05	6.70E-03	1.01E-03
8.69E-04	1.30E-04	1.21E-02	1.82E-03
4.20E-03	6.30E-04	6.78E-02	1.02E-02
8.55E-03	1.28E-03	1.28E-01	1.92E-02
Ca/Si = 1.0			

[Na]eq, mol/l	σ, mol/l	[Na]s, mol/kg	σ, mol/kg
4.59E-05	6.89E-06	4.81E-04	7.21E-05
8.97E-05	1.35E-05	1.07E-03	1.61E-04
4.70E-04	7.06E-05	4.26E-03	6.38E-04
9.70E-04	1.46E-04	7.06E-03	1.06E-03
4.34E-03	6.52E-04	6.06E-02	9.09E-03
9.07E-03	1.36E-03	1.02E-01	1.53E-02
Ca/Si = 1.4			
[Na]eq, mol/l	σ, mol/l	[Na]s, mol/kg	σ, mol/kg
5.47E-05	8.20E-06	4.37E-05	6.55E-06
1.08E-04	1.63E-05	1.34E-04	2.01E-05
5.45E-04	8.17E-05	5.28E-04	7.92E-05
5.33E-03	8.00E-04	1.10E-02	1.66E-03
1.05E-02	1.57E-03	3.23E-02	4.84E-03

Table A-5. Ca concentration and pH values in the C-S-H eq. solution as a function of the Na^+ addition

Ca/Si = 0.83				
[Na], mol/l	σ, mol/l	pH (σ = 0.01)	Ca, mmol/l	σ, mmol/l
8.28E-05	4.14E-06	10.31	1.17E+00	5.86E-02
1.13E-04	5.64E-06	10.25	1.22E+00	6.12E-02
1.45E-04	7.27E-06	10.32	1.23E+00	6.16E-02
4.22E-04	2.11E-05	10.29	1.27E+00	6.33E-02
8.17E-04	4.08E-05	10.41	1.34E+00	6.69E-02
3.89E-03	1.95E-04	10.26	1.75E+00	8.77E-02
8.03E-03	4.01E-04	10.31	2.10E+00	1.05E-01
Ca/Si = 1.0				
[Na], mol/l	σ, mol/l	pH (σ = 0.01)	Ca, mmol/l	σ, mmol/l
1.12E-04	5.60E-06	11.49	1.56E+00	7.82E-02
1.39E-04	6.95E-06	11.52	1.50E+00	7.51E-02
1.79E-04	8.97E-06	11.52	1.44E+00	7.19E-02
4.70E-04	2.35E-05	11.56	1.55E+00	7.74E-02
9.26E-04	4.63E-05	11.60	1.42E+00	7.10E-02
4.02E-03	2.01E-04	11.55	1.38E+00	6.88E-02
8.33E-03	4.17E-04	11.65	1.55E+00	7.76E-02
Ca/Si = 1.4				
[Na], mol/l	σ, mol/l	pH (σ = 0.01)	Ca, mmol/l	σ, mmol/l
1.52E-04	7.61E-06	12.35	9.90E+00	4.95E-01
1.86E-04	9.31E-06	12.25	1.12E+01	5.62E-01
2.34E-04	1.17E-05	12.46	1.07E+01	5.35E-01
6.38E-04	3.19E-05	12.31	1.06E+01	5.30E-01
1.17E-03	5.83E-05	12.33	1.09E+01	5.45E-01
5.23E-03	2.62E-04	12.46	1.09E+01	5.45E-01
1.03E-02	5.14E-04	12.45	1.06E+01	5.30E-01

Table A-6. The kinetics of gluconate desorption from C-S-H phases with three Ca/Si ratio (0.83, 1.0, 1.4), S/L = 20 g/l

	Ca/Si = 0.83		Ca/Si = 1.0		Ca/Si = 1.4	
Time, days	[Gluconate]eq, mmol/l	σ, mmol/l	[Gluconate]eq, mmol/l	σ, mmol/l	[Gluconate]eq, mmol/l	σ, mmol/l
0.5	1.63E-02	5.72E-03	8.35E-02	1.25E-02	7.48E-02	1.12E-02
1	2.41E-02	8.43E-03	8.10E-02	1.22E-02	7.96E-02	1.19E-02
3	2.06E-02	7.22E-03	8.96E-02	1.34E-02	8.08E-02	1.21E-02
7	1.76E-02	6.17E-03	9.68E-02	1.45E-02	1.05E-01	1.58E-02
15	2.62E-02	9.18E-03	8.46E-02	1.27E-02	9.86E-02	1.48E-02
30	2.15E-02	7.53E-03	9.01E-02	1.35E-02	9.67E-02	1.45E-02

Table A-7. Isotherms of gluconate desorption from C-S-H phases with three Ca/Si ratio (0.83, 1.0, 1.4), S/L = 20 g/l

Ca/Si = 0.83			
$[Gluconate]_{des.eq.}$, mmol/l	σ, mmol/l	$[Glu]_{desorption}$, mmol/mol of Si	σ, mmol/mol of Si
2.09E-07	3.14E-08	6.05E-08	2.12E-08
6.80E-07	1.02E-07	1.33E-07	4.66E-08
1.07E-06	1.61E-07	3.35E-07	1.17E-07
2.32E-06	3.49E-07	5.88E-07	2.06E-07
2.92E-06	4.38E-07	9.00E-07	3.15E-07
9.68E-06	1.45E-06	3.03E-06	1.06E-06
2.05E-05	3.07E-06	4.92E-06	1.72E-06
3.08E-05	4.62E-06	7.66E-06	2.68E-06
9.54E-05	1.43E-05	2.63E-05	9.20E-06
1.61E-04	2.42E-05	4.07E-05	1.43E-05
8.37E-04	1.26E-04	2.71E-04	9.50E-05
Ca/Si = 1.0			
$[Gluconate]_{des.eq.}$, mmol/l	σ, mmol/l	$[Glu]_{desorption}$, mmol/mol of Si	σ, mmol/mol of Si
1.71E-06	2.57E-07	3.69E-07	1.29E-07
5.84E-06	8.76E-07	1.57E-06	5.50E-07
1.18E-05	1.78E-06	3.51E-06	1.23E-06
1.51E-05	2.27E-06	3.99E-06	1.40E-06
4.35E-05	6.53E-06	1.10E-05	3.83E-06
9.83E-05	1.47E-05	2.63E-05	9.21E-06
1.53E-04	2.29E-05	3.93E-05	1.38E-05
4.57E-04	6.86E-05	1.19E-04	4.16E-05
3.57E-03	5.36E-04	7.92E-04	2.77E-04
1.30E-02	1.95E-03	2.29E-03	8.03E-04
9.58E-04	1.44E-04	2.44E-04	8.53E-05
Ca/Si = 1.4			
$[Gluconate]_{des.eq.}$, mmol/l	σ, mmol/l	$[Glu]_{desorption}$, mmol/mol of Si	σ, mmol/mol of Si
5.48E-07	8.23E-08	6.42E-07	2.25E-07

1.40E-06	2.11E-07	1.56E-06	5.47E-07
2.95E-06	4.43E-07	3.46E-06	1.21E-06
6.27E-06	9.41E-07	7.28E-06	2.55E-06
9.59E-06	1.44E-06	8.88E-06	3.11E-06
2.55E-05	3.83E-06	2.85E-05	9.97E-06
5.69E-05	8.53E-06	6.63E-05	2.32E-05
8.31E-05	1.25E-05	9.44E-05	3.30E-05
2.57E-04	3.85E-05	2.80E-04	9.81E-05
5.41E-04	8.11E-05	6.53E-04	2.29E-04
3.18E-03	4.77E-04	2.74E-03	9.61E-04
1.08E-02	1.62E-03	8.87E-03	3.10E-03

Table A-8. The isotherm of gluconate adsorption on hydrated cement paste (CEM I, S/L=20 g/l)

$[Gluconate]_{eq}$, mol/l	σ, mol/l	$[Gluconate]_{sorbed}$, mol/kg	σ, mol/kg
4.99E-10	2.50E-11	2.73E-06	4.10E-07
2.47E-09	1.24E-10	1.35E-05	2.03E-06
5.90E-09	2.95E-10	3.16E-05	4.74E-06
2.61E-08	1.31E-09	1.38E-04	2.07E-05
5.98E-08	2.99E-09	3.19E-04	4.78E-05
2.47E-07	1.23E-08	1.21E-03	1.82E-04
5.80E-07	2.90E-08	2.82E-03	4.24E-04
3.19E-06	1.59E-07	1.21E-02	1.81E-03
1.17E-05	5.86E-07	2.80E-02	4.20E-03
4.03E-03	2.02E-04	1.59E-01	2.38E-02
9.27E-02	4.64E-03	1.10E+00	1.64E-01
2.20E-04	1.10E-05	1.16E-01	1.74E-02

Table A-9. The isotherm of ^{14}C-labelled gluconate desorption from the hydrated cement paste (S/L = 20 g/l)

$[Gluconate]_{des\cdot eq}$, mol/l	σ, mol/l	$[Gluconate]_{desorption}$, mol/kg	σ, mol/kg
2.53E-10	3.79E-11	2.73E-06	5.47E-07
2.52E-09	3.78E-10	1.35E-05	2.71E-06
3.80E-09	5.71E-10	3.16E-05	6.32E-06
1.67E-08	2.50E-09	1.38E-04	2.76E-05
9.01E-07	1.35E-07	3.18E-04	6.36E-05
1.46E-07	2.19E-08	1.21E-03	2.42E-04
5.12E-07	7.68E-08	2.82E-03	5.65E-04
2.25E-06	3.37E-07	1.21E-02	2.42E-03
7.83E-06	1.17E-06	2.80E-02	5.60E-03
4.50E-05	6.74E-06	1.59E-01	3.17E-02
1.63E-03	2.44E-04	1.09E+00	2.19E-01
1.77E-04	2.66E-05	1.16E-01	2.32E-02

Table A-10. The kinetics of PCE adsorption on C-S-H

	Ca/Si = 1.0		Ca/Si = 1.4	
Time, days	[PCE]s, g/kg	σ, g/kg	[PCE]s, g/kg	σ, g/kg
1	1.55E+01	7.73E-01	1.65E+01	8.25E-01
3	1.55E+01	7.74E-01	1.83E+01	9.17E-01
7	1.55E+01	7.74E-01	1.91E+01	9.57E-01
14	1.75E+01	8.77E-01	1.89E+01	9.47E-01
28	1.51E+01	7.54E-01	1.85E+01	9.25E-01

Table A-11. Adsorption of PCE on C-S-H.

Ca/Si ratio	$PCE_{solution}$, g/l	σ, g/l	PCE_{sorbed}, g/kg	σ, kg/l
1.0	3.44E-03	1.16E-04	5.78E-01	1.16E-01
	2.27E-02	2.73E-04	1.37E+00	2.73E-01
	1.25E-02	5.75E-04	2.88E+00	5.75E-01
	7.61E-03	1.42E-03	7.12E+00	1.42E+00
	4.06E-01	2.94E-03	1.47E+01	2.94E+00
	7.34E-01	7.66E-03	3.83E+01	7.66E+00
	1.37E+00	1.63E-02	8.16E+01	1.63E+01
1.4	4.64E-03	5.36E-05	2.68E-01	5.36E-02
	7.03E-03	2.30E-04	1.15E+00	2.30E-01
	3.03E-03	6.70E-04	3.35E+00	6.70E-01
	3.36E-02	6.64E-04	3.32E+00	6.64E-01
	2.63E-02	2.74E-03	1.37E+01	2.74E+00
	3.28E-01	3.72E-03	1.86E+01	3.72E+00
	3.75E-01	6.25E-03	3.13E+01	6.25E+00
	1.23E+00	1.77E-02	8.84E+01	1.77E+01

Table A-12. pH values of the C-S-H equilibrated solution as a function of the PCE concentration in stable state

Ca/Si = 1.0			Ca/Si = 1.4		
$PCE_{solution}$, g/l	σ, g/l	pH	$PCE_{solution}$, g/l	σ, g/l	pH
3.44E-03	1.16E-04	11.2	4.64E-03	5.36E-05	12.1
2.27E-02	2.73E-04	11.5	7.03E-03	2.30E-04	12.2
1.25E-02	5.75E-04	11.6	3.03E-03	6.70E-04	12.1
7.61E-03	1.42E-03	11.5	3.36E-02	6.64E-04	12.1
6.92E-03	2.93E-03	11.5	2.63E-02	2.74E-03	12.1
4.06E-01	2.94E-03	11.4	3.28E-01	3.72E-03	12.3
7.34E-01	7.66E-03	11.3	3.75E-01	6.25E-03	12.0
1.37E+00	1.63E-02	11.5	1.23E+00	1.77E-02	12.3
5.63E+00	1.38E-02	11.5	6.72E+00	2.81E-03	12.2
9.22E+00	7.81E-03	11.3	7.53E+00	2.47E-02	12.1

Table A-13. The isotherm of U(VI) adsorption on C-S-H with Ca/Si = 1.4, S/L = 20 g/l.

$[U]_{eq}$, mol/l	σ, mol/l	$[U]_{sorbed}$, mmol/mol of Si	σ, mmol/mol of Si
2.10E-10	1.05E-11	8.96E-05	7.17E-06
2.77E-10	1.38E-11	1.51E-04	1.21E-05
1.65E-09	8.27E-11	6.05E-04	4.84E-05
3.94E-09	1.97E-10	1.19E-03	9.50E-05
1.89E-08	9.45E-10	3.02E-03	2.42E-04
4.15E-08	2.07E-09	8.96E-03	7.17E-04
4.89E-08	2.44E-09	1.19E-02	9.50E-04

Table A-14. pH, Si and Ca concentrations in the C-S-H equilibrated solution as a function of U(VI) concentration in equilibrium (C-S-H with Ca/Si = 1.4)

[U] in equilibrium, mmol/l	pH values	[Ca] in equilibrium, mmol/l	[Si] in equilibrium, mmol/l
(2.10±0.11)×10-7	12.35±0.05	8.93±0.45	0.028±0.0.002
(2.71±0.14)×10-7	12.29±0.05	7.72±0.39	0.030±0.0.002
(1.63±0.08)×10-6	12.25±0.05	8.09±0.40	0.029±0.0.002
(3.90±0.19)×10-6	12.36±0.05	8.48±0.42	0.029±0.0.002
(1.92±0.09)×10-5	12.23±0.05	11.03±0.55	0.028±0.0.002
(4.21±0.20)×10-5	12.31±0.05	11.15±0.56	0.031±0.0.002
(4.91±0.25)×10-5	12.35±0.05	12.07±0.60	0.030±0.0.002

Table A-15. pH, Si and Ca concentrations in the C-S-H equilibrated solution as a function of U(VI) concentration in equilibrium in the presence of gluconate (C-S-H with Ca/Si = 1.4)

[U] in equilibrium, mmol/l	pH values	[Ca] in equilibrium, mmol/l	[Si] in equilibrium, mmol/l
(8.40±0.81)x10-9	12.35±0.05	8.89±0.47	0.026±0.0.002
(1.68±0.45)x10-8	12.23±0.05	8.70±0.42	0.030±0.0.002
(1.68±0.42)x10-8	12.25±0.05	9.08±0.41	0.029±0.0.002
(2.52±0.19)x10-8	12.36±0.05	8.93±0.46	0.028±0.0.002
(3.36±0.35)x10-8	12.23±0.05	8.71±0.55	0.028±0.0.002
(6.72±0.55)x10-8	12.22±0.05	8.36±0.56	0.031±0.0.002
(5.88±0.61)x10-8	12.35±0.05	8.52±0.61	0.030±0.0.002
(8.40±0.79)x10-8	12.14±0.05	8.84±0.60	0.028±0.0.002
(1.93±0.09)x10-7	12.23±0.05	7.93±0.68	0.030±0.0.002
(4.62±0.46)x10-7	12.37±0.05	8.75±0.60	0.029±0.0.002
(6.30±0.46)x10-7	12.35±0.05	10.90±0.72	0.031±0.0.002
(8.40±0.87)x10-7	12.27±0.05	12.92±0.75	0.027±0.0.002

Table A-16. The isotherm of U(VI) adsorption on C-S-H with Ca/Si = 1.4 (S/L = 20 g/l) in the presence of gluconate and PCE (ternary systems).

Gluconate				PCE			
$[U]_{eq}$, mmol/l	σ, mmol/l	$[U]_{sorbed}$, mmol/mol of Si	σ, mmol/mol of Si	$[U]_{eq}$, mmol/l	σ, mmol/l	$[U]_{sorbed}$, mmol/mol of Si	σ, mmol/ mol of Si
8.40E-09	8.40E-10	8.96E-05	4.48E-06	4.14E-07	4.14E-08	8.96E-05	4.48E-06
1.68E-08	1.68E-09	1.19E-04	5.94E-06	4.50E-07	4.50E-08	1.19E-04	5.94E-06
1.68E-08	1.68E-09	1.51E-04	7.56E-06	8.37E-07	8.37E-08	1.51E-04	7.55E-06
2.52E-08	2.52E-09	3.02E-04	1.51E-05	9.32E-07	9.32E-08	3.02E-04	1.51E-05
3.36E-08	3.36E-09	6.05E-04	3.02E-05	1.19E-06	1.19E-07	6.05E-04	3.02E-05
6.72E-08	6.72E-09	8.96E-04	4.48E-05	3.40E-06	3.40E-07	8.96E-04	4.48E-05
5.88E-08	5.88E-09	1.19E-03	5.94E-05	4.54E-06	4.54E-07	1.19E-03	5.94E-05
8.40E-08	8.40E-09	1.51E-03	7.56E-05	6.44E-06	6.44E-07	1.51E-03	7.56E-05
1.93E-07	1.93E-08	3.02E-03	1.51E-04	1.27E-05	1.27E-06	3.02E-03	1.51E-04
4.62E-07	4.62E-08	6.05E-03	3.02E-04	2.84E-05	2.84E-06	6.04E-03	3.02E-04
6.30E-07	6.30E-08	8.96E-03	4.48E-04	3.82E-05	3.82E-06	8.96E-03	4.48E-04
8.40E-07	8.40E-08	1.19E-02	5.94E-04	4.61E-05	4.61E-06	1.19E-02	5.94E-04

Table A-17. The concentration of gluconate in the C-S-H equilibrated solution as a function of U(VI) addition ($[Gluconate]_{initial}$=0.35 mmol/l.

[U]eq, mol/l	σ, mol/l	[Gluconate]sorbed, mmol/mol of Si	σ, mmol/mol of Si
8.40E-12	4.20E-13	2.82E-02	1.41E-03
1.68E-11	8.40E-13	2.49E-02	1.24E-03
1.68E-11	8.40E-13	2.82E-02	1.41E-03
2.52E-11	1.26E-12	2.90E-02	1.45E-03
3.36E-11	1.68E-12	2.82E-02	1.41E-03
6.72E-11	3.36E-12	2.82E-02	1.41E-03
5.88E-11	2.94E-12	2.78E-02	1.39E-03
8.40E-11	4.20E-12	2.84E-02	1.42E-03
1.93E-10	9.66E-12	2.84E-02	1.42E-03
4.62E-10	2.31E-11	2.84E-02	1.42E-03
6.30E-10	3.15E-11	2.99E-02	1.50E-03
8.40E-10	4.20E-11	3.19E-02	1.59E-03

UNIVERSITE BRETAGNE LOIRE

IMT Atlantique
Bretagne-Pays de la Loire
École Mines-Télécom

Thèse de Doctorat

Iuliia ANDRONIUK

Effets des additifs organiques du ciment sur l'adsorption des ions uranyles sur de silicate de calcium hydraté : détermination expérimentale et modélisation moléculaire

Effects of cement organic additives on the adsorption of uranyl ions on calcium silicate hydrate phases: experimental determination and computational molecular modelling

Résumé

Les matériaux cimentaires sont largement utilisés dans la conception et la construction des sites de stockage de déchets radioactifs. Une des manières d'améliorer leur performance est d'introduire des adjuvants organiques dans la structure. La présence de matière organique dans l'eau porale peut affecter la mobilité des radionucléides: les molécules organiques forment des complexes solubles et peuvent être en compétition avec les radionucléides au niveau des sites de sorption. Ce travail avait pour but de comprendre les mécanismes de telles interactions au niveau moléculaire. Le système modèle a trois composantes. D'abord, des phases C-S-H ont été choisies en tant que modèles du ciment. Ensuite, le gluconate est sélectionné en tant que modèle d'additif organique pour sonder les mécanismes d'interaction à l'échelle moléculaire. Un système plus complexe impliquant un superplastifiant (PCE) a été testé. La troisième espèce, U(VI), est représentative d'un radionucléide de la série des actinides. Le développement de la description des effets de postproduction des espèces organiques pour les applications de stockage des déchets radioactifs était l'objectif principal de ce travail. L'étude des systèmes binaires fournit des données de référence pour l'investigation de systèmes ternaires C-S-H/matière organique/U(VI) plus complexes. Des cinétiques et des isothermes de sorption/désorption pour les espèces sur les C-S-H sont mesurés. En parallèle, des modèles atomiques ont été développés pour les interfaces d'intérêt. Les aspects structuraux, énergétiques et dynamiques des processus de sorption sur les surfaces de ciment sont modélisés par la technique de la dynamique moléculaire.

Mots clés
Silicate de calcium hydraté (C-S-H), Uranium (VI); gluconate; adsorption; dynamique moléculaire

Abstract

Cementitious materials are extensively used in the design and construction of radioactive waste repositories. One of the ways to enhance their performance is to introduce organic admixtures into the cement structure. However, the presence of organics in the pore water may affect the radionuclide mobility: organic molecules can form water-soluble complexes and compete for sorption sites. This work was designed to get detailed understanding of the mechanisms of such interactions on the molecular level. The model system has three components. First, pure C-S-H phases with different Ca/Si ratios were chosen as a cement model. Secondly, gluconate (a simple well-described molecule) is selected as a good starting organic additive model to probe the interaction mechanisms on the molecular scale. A more complex system involving polycarboxylate superplasticizer (PCE) was also tested. The third, U (VI), is a representative of the actinide radionuclide series. The development of description of the effects of organics for radioactive waste disposal applications was the primary objective of this work. The study of binary systems provides reference data for the investigation of more complex ternary (C-S-H/organic/U (VI)). The interactions are studied by means of both experimental and computational molecular modelling techniques. Data on sorption and desorption kinetics and isotherms for additives and for U (VI) on C-S-H are acquired in this work. In parallel, atomistic models are developed for the interfaces of interest. Structural, energetic, and dynamic aspects of the sorption processes on surface of cement are quantitatively modeled by molecular dynamics technique.

Key Words
Calcium silicate hydrate (C-S-H); Uranium (VI); gluconate; adsorption; molecular dynamics